

---

***Processing and Interpretation of Multichannel Seismic Reflection  
Data Acquired off Isfjorden, Svalbard***

---

Master of Science in Earth Science

Güney Dinçtürk



Department of Earth Science

University of Bergen

October 2022





## ABSTRACT

The Svalbard archipelago has been complexly deformed during its billions of years-long evolution history, where fault zones, other deformation structures and hard seafloor morphology have emerged. This research project has aimed to characterize the main geological structures in the study area located on the western shelf of Spitsbergen by processing and interpreting of four 2D marine seismic reflection profiles.

The quality of the seismic data has been influenced by several sorts of noise, dominantly surface-related multiples due to the hard seafloor in the study area, where the velocities of primary waves are approximately 5500 m/s and often escalate up to 6500 m/s at shallow depths. A total of five different processing workflows have been applied to a seismic profile in order to remove the multiples from the data. The multiple extraction & adaptive subtraction approach has been determined as the most effective remedy for multiple attenuation among the tested methods, as it enhanced the signal-to-noise ratio the most. Thanks to that approach, and many other essential processing sequences, including post-stack time migration in the main workflow, the seismic datasets have become almost multiple-free.

Seismic interpretation of the four processed profiles has been done to distinguish the main geological setting in the study area. Nine seismic horizons interpreted between the seabed and basement, as well as several major faults, allowed the division into five stratigraphic units, being the Quaternary, Cenozoic, Mesozoic-Paleozoic, Devonian sedimentary successions and the crystalline basement (so-called Hecla Hoek). The thickness and 2D - 3D surface maps including faults have supported the identification of the main structures in the study area: the Hornsund Fault Zone and a Devonian Graben. The interpretation implies a new model describing the development of a N-S trending fault-bounded rift basin, named Devonian Graben structure, as a product of the collapsed Caledonian mountain range due to continental extension. The development was followed by reactivation in an oblique extensional regime in Cenozoic, which is also associated with seafloor spreading between Greenland and Svalbard. The oblique

extension deformed the basement in the Hornsund Fault Zone, interpreted as an area of NNW-SSE trending down-faulted, westward dipping blocks, impacted by W-E trending strike-slip faults. An NNW-SSE trending horst structure has also been distinguished between the Hornsund Fault Zone and Devonian Graben.

# ACKNOWLEDGMENT

I would like to honestly dedicate this thesis project to Atatürk and those individuals being a part of my ultimate success and never stop believing in me for years.

I would have not broadened my geoscientific knowledge without priceless guidance and assistance from my advisor Prof. Rolf Mjelde and co-advisor Bent Ole Ruud. I am so lucky to study this research project with them!

I also appreciate Prof. Stephane Rondenay for his amazing teaching of signal theory and seismic studies, and Thomas Theunissen for his cooperation during my teaching assistant period in the course GEOV113 at the UiB. Of course, special thanks to those: Prof. Haflidi Haflidason for welcoming me to the Nordfjord study project onboard R/V Nansen, Stein Sandven and Hanne Sagen for accepting me to the research school on board the Norwegian Coast Guard icebreaker KV Svalbard that has been the greatest experience in my life! Emilie Randeberg for her countless logistic and motivational supports since I was accepted to this master's program at the UiB. I cannot forget to thank all my master fellows, especially Kingsley Ofoedu, Ingrid Haugland, Henry Ravndal, Nil Eryilmaz and Muhammad Usman. Millions of thanks go to University of Bergen and Norway for the most amazing experience in my life for those 26 months!

I am grateful to my scholar fellows and colleagues Mert Kiraz and Efan Kabaca that we all have advanced our academic journeys abroad thanks to our scholarship program by the Ministry of National Education, Turkey. My deepest and very special thanks go to my advisor Asli Zeynep Yavuzoglu in MTA (General Directorate of Mineral Research and Exploration, Turkey).

The last but not least, "canım anam" my mom Biriz and family in Turkey, Mert Irmak and Brookes family in Canada, Mert, Burak, Isil and Onur and all my friends around the world, and my girlfriend Lisa; I truly appreciate your priceless support during my master journey and your existence in my life. Together, the force is strong with us always...

PS. "Ata'm izindeyim!"

Güney Dinçtürk

Bergen, Norway

October 2022



# TABLE OF CONTENTS

ABSTRACT .....	I
ACKNOWLEDGMENT.....	III
TABLE OF CONTENTS.....	V
LIST OF ABBREVIATIONS .....	IX
<b>1 INTRODUCTION .....</b>	<b>1</b>
1.1 STUDY AREA.....	1
1.2 MARINE SEISMIC DATA .....	1
1.3 RESEARCH SCOPES.....	3
<b>2 GEOLOGICAL BACKGROUND .....</b>	<b>5</b>
2.1 TECTONIC EVOLUTION .....	5
2.2 MAIN TECTONIC STRUCTURES OF THE WESTERN SPITSBERGEN.....	7
2.2.1 <i>The Hornsund Fault Complex</i> .....	7
2.2.2 <i>West Spitsbergen Fold and Thrust Belt</i> .....	11
2.2.3 <i>The Bellsund Graben</i> .....	12
2.3 STRATIGRAPHY OF THE WESTERN SPITSBERGEN .....	12
2.3.1 <i>Hecla Hoek</i> .....	13
2.3.2 <i>Devonian Old Red Sediments</i> .....	13
2.3.3 <i>Cenozoic Sedimentary Wedge</i> .....	14
<b>3 METHODS .....</b>	<b>15</b>
3.1 SEISMIC DATA ACQUISITION .....	15
3.1.1 <i>Seismic Data Principles</i> .....	15
3.1.2 <i>Marine Seismic Data</i> .....	17
3.1.3 <i>Ray Paths of Multiple and Ghost Reflections</i> .....	18
3.1.4 <i>Source</i> .....	21
3.1.4.1 <i>Airgun and Bubble Pulses</i> .....	21
3.1.4.2 <i>Source Signature and Array Tuning</i> .....	22
3.1.4.3 <i>Near- and Far-Field Source Signatures</i> .....	22
3.1.5 <i>Receiver</i> .....	24
3.1.5.1 <i>Streamer</i> .....	24
3.1.5.2 <i>Single and Multichannel Seismic</i> .....	25
3.1.6 <i>Recording and Storing</i> .....	26

3.2	SEISMIC DATA PROCESSING .....	27
3.2.1	<i>Pre-processing</i> .....	27
3.2.1.1	Data Loading .....	27
3.2.1.2	Resampling.....	28
3.2.1.3	Fourier Transform .....	29
3.2.1.4	Geometry Calculation .....	30
3.2.1.5	Gain Recovery .....	33
3.2.1.6	Spherical Divergence Correction.....	33
3.2.1.7	Spatial Amplitude Smoothing .....	35
3.2.1.8	Band-pass Filtering.....	36
3.2.1.9	Convolution.....	38
3.2.1.10	Deconvolution.....	38
3.2.1.11	Signature Deconvolution .....	40
3.2.1.12	<i>f-x</i> Projective Filtering .....	40
3.2.1.13	<i>f-k</i> Filtering .....	40
3.2.1.14	Single Trace Section .....	43
3.2.2	<i>2D Spatial Trace Interpolation</i> .....	44
3.2.3	<i>Muting</i> .....	44
3.2.3.1	Inner and Top Mutes.....	44
3.2.3.2	Surgical Mute .....	45
3.2.3.3	NMO Stretch Mute.....	45
3.2.3.4	Top Mute from Incidence Angle .....	46
3.2.4	<i>Seismic Velocity Modelling &amp; Analysis</i> .....	46
3.2.4.1	Types of Seismic Velocity .....	46
3.2.4.2	Velocity Modelling .....	48
3.2.4.3	Velocity Analysis .....	48
3.2.5	<i>NMO Correction</i> .....	49
3.2.5.1	NMO Stretch .....	51
3.2.6	<i>Multiple Modelling and Extraction</i> .....	52
3.2.7	<i>Adaptive Subtraction</i> .....	53
3.2.7.1	Autocorrelation to Adaptive Subtraction for QC.....	55
3.2.8	<i>DMO Correction</i> .....	56
3.2.9	<i>Stacking</i> .....	58
3.2.9.1	Brute-Stack for QC Purposes .....	58
3.2.10	<i>Post-Stack Time Migration</i> .....	59
3.2.10.1	Finite-Difference Migration Approach .....	61
3.2.10.2	Omega-X Algorithm.....	62
3.2.10.3	The Factors Impacting the FD Migration Algorithm .....	63

3.3	SEISMIC INTERPRETATION .....	65
3.3.1	<i>Seismic Attributes</i> .....	65
3.3.1.1	Acoustic Impedance .....	65
3.3.1.2	Reflection Coefficient.....	65
3.3.1.3	Seismic Response .....	66
3.3.2	<i>Structural Analysis</i> .....	67
3.3.3	<i>Stratigraphic Analysis</i> .....	67
<b>4</b>	<b>RESULTS.....</b>	<b>71</b>
4.1	SEISMIC DATA ACQUISITION .....	71
4.2	SEISMIC DATA PROCESSING .....	77
4.2.1	<i>Pre-processing</i> .....	80
4.2.1.1	Data Loading and QC.....	80
4.2.1.2	Trace Length Reducing.....	81
4.2.1.3	Band-pass Filtering – Butterworth .....	82
4.2.1.4	Resampling.....	82
4.2.1.5	Spatial Amplitude Smoothing (with noise attenuation option) .....	83
4.2.1.6	Geometry Calculation .....	83
4.2.1.7	QC - 1 Spherical Divergence Correction .....	84
4.2.1.8	QC - 2 Near-Trace Section .....	84
4.2.1.9	Signature Deconvolution .....	85
4.2.1.10	<i>f-x</i> Projective Filtering .....	86
4.2.1.11	Spherical Divergence Correction.....	87
4.2.1.12	Spatial Amplitude Smoothing .....	87
4.2.1.13	<i>f-k</i> Filter.....	88
4.2.1.14	QC - 3 Near-Trace Section .....	89
4.2.1.15	Water Bottom Library .....	91
4.2.2	<i>2D Spatial Trace Interpolation</i> .....	91
4.2.3	<i>Velocity Modelling</i> .....	93
4.2.4	<i>1st Velocity Analysis</i> .....	95
4.2.5	<i>Multiple Extraction &amp; Adaptive Subtraction</i> .....	98
4.2.5.1	Step 1 - NMO Correction.....	98
4.2.5.2	Step 2 – Generating the 1st Dataset .....	99
4.2.5.3	Step 3 – Generating the 2nd Dataset: Multiple Modelling .....	100
4.2.5.4	Step 4 - Adaptive Subtraction: .....	100
4.2.6	<i>QC Applications for Adaptive Subtraction Result</i> .....	102
4.2.7	<i>2nd Velocity Analysis</i> .....	104
4.2.8	<i>DMO Correction</i> .....	105

4.2.9	<i>NMO Correction &amp; Stacking</i> .....	106
4.2.10	<i>Post-Stack Processing Sequences Before the Migration</i> .....	108
4.2.10.1	Band-pass Filtering.....	108
4.2.10.2	<i>f-k</i> Filtering.....	108
4.2.10.3	Amplitude Scaling .....	109
4.2.11	<i>Post-Stack Time Migration</i> .....	109
4.2.12	<i>Seg-y Format Extracting</i> .....	112
4.3	SEISMIC INTERPRETATION .....	118
4.3.1	<i>Horizon and Fault Interpretation</i> .....	120
4.3.2	<i>Surface Maps</i> .....	128
4.3.2.1	Seabed .....	128
4.3.2.2	Upper Regional Unconformity .....	129
4.3.2.3	The HFZ Westward Dipping Layer 5 .....	130
4.3.2.4	Top Devonian .....	131
4.3.2.5	Top Hecla Hoek .....	131
4.3.3	<i>Stratigraphic Units</i> .....	132
4.3.3.1	Unit 1: From Seabed to URU .....	133
4.3.3.2	Unit 2: From URU to The HFZ Westward Dipping Layer 5.....	134
4.3.3.3	Unit 3: From The HFZ Westward Dipping Layer 5 & URU to Top Hecla Hoek .....	135
4.3.3.4	Unit 4: From Top Devonian to Top Hecla Hoek.....	136
4.3.3.5	Unit 5: Hecla Hoek .....	137
<b>5</b>	<b>DISCUSSIONS</b> .....	<b>139</b>
5.1	SEISMIC DATA ACQUISITION .....	139
5.2	SEISMIC DATA PROCESSING .....	139
5.3	SEISMIC INTERPRETATION .....	153
<b>6</b>	<b>CONCLUSIONS</b> .....	<b>163</b>
6.1	SEISMIC DATA PROCESSING .....	163
6.2	SEISMIC INTERPRETATION .....	166
	<b>REFERENCES</b> .....	<b>169</b>
	<b>FIGURE REFERENCE</b> .....	<b>171</b>
	<b>APPENDIX A</b> .....	<b>173</b>
	<b>APPENDIX B</b> .....	<b>211</b>
	<b>APPENDIX C</b> .....	<b>233</b>



## LIST OF ABBREVIATIONS

2D: Two Dimensional

3D: Three Dimensional

AI: Acoustic Impedance

Ave: Average

BG: Bellsund Graben

CDP: Common-depth point

CMP: Common-midpoint

CRG: Common-receiver gather

CSG: Common-shot gather

CSW: Cenozoic Sedimentary Wedge

dB: Decibel

DMO: Dip Moveout

FD: Finite-Difference

FG: Forlandsundet Graben

$f$ - $k$ : Frequency-wavenumber domain

$f$ - $x$ : Frequency-space domain

GF: Greenland Fracture Zone

GI: Generator/Injector

HFC: Hornsund Fault Complex

HFZ: Hornsund Fault Zone

Hz: Hertz

Ins: Instantaneous

INT: Interval

KR: Knipovich Ridges

Ma: Mega-annum/One million years

MFZ: Molloy Fracture Zone

MR: Molloy Ridge  
Ms: Millisecond  
NMO: Normal Moveout  
NTNU: Norwegian University of Science and Technology  
Ny: Nyquist  
Oct: Octave  
PC: Personal Computer  
QC: Quality Control  
RC: Reflection Coefficient  
RMS: Root-Mean-Square  
R/V: Research Vessel  
SEG: Society of Exploration Geophysics  
SpFZ: Spitsbergen Fracture Zone  
SQL: Structured Query Language  
SS: Strike-slip  
S/N: Signal-to-noise  
Tau-p ( $\tau$ - $p$ ): Intercept time-ray parameter domain  
TWT: Two-way travel time  
 $t$ - $x$ : Time-distance domain  
UiB: University of Bergen  
UiS: University of Stavanger  
UiT: University of Tromsø  
UNIS: The University Centre in Svalbard  
URU: Upper Regional Unconformity  
UTM: Universal Transverse Mercator  
VM: Van Mijenfjorden  
VSP: Vertical Sensor Profile  
WSFTB: West Spitsbergen Fold and Thrust Belt  
YP: Yermak Plateau

# 1 INTRODUCTION

## 1.1 STUDY AREA

Svalbard is the official Norwegian name of an Arctic archipelago and administrative area, located between 74 - 81 °N and 10 - 35 °E. Spitsbergen is Svalbard's largest and only permanently populated island. The other larger islands are Nordaustlandet, Barentsøya and Edgeøya, while the remote islands are Bjørnøya, Hopen and Kong Karls Land (Dallmann, 2015).

The Svalbard archipelago has been uplifted as the Barents Sea by tectonic forces related to varying compressional and extensional regimes from Precambrian until present (Dallmann, 2015). These tectonic regimes have been reactivated over and over again for millions of years and are associated with the following processes: continental rifting, crustal thinning, orogen collapse, erosion, fold and thrust belt formation, strike-slip movements, faulting, seafloor spreading, and ice advances-retreatments that mainly formed the western shelf of Spitsbergen (Blinova et al., 2009; Dallmann, 2015), where the study area is located (Figure 1.1.A).

## 1.2 MARINE SEISMIC DATA

The 2D multichannel marine seismic reflection data used in this thesis project were acquired on the shelf between Isfjorden and Van Mijen Fjorden during the student course SVALEX 2002. From the SVALEX survey in 2002 a set of eight seismic profiles is called leg-2 (Mjelde, 2003), of which four seismic profiles have been used in this thesis (Figure 1.1.B). Seismic lines 6, 7 and 8 are trending WSW-ENE, while seismic line 2 is an NW-SE oriented cross-section.

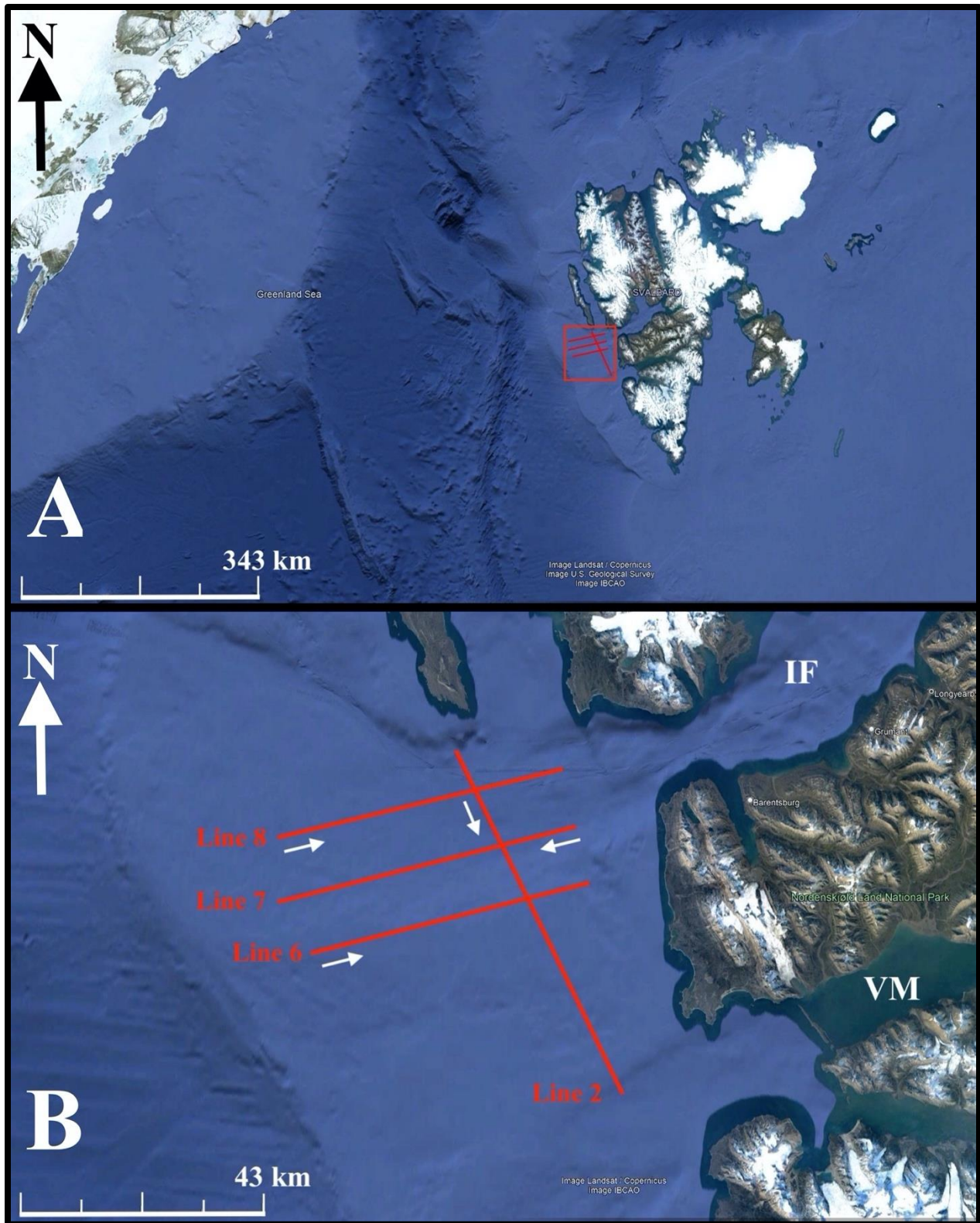


Figure 1.1 Satellite image of Svalbard (A) with the study area (inside the red frame) and 4 seismic profiles (red lines). The satellite image of the study location in western Spitsbergen (B) with seismic lines and their acquisition directions. IF: Isfjorden, VM: Van Mijenfjorden, displayed by Google Earth Pro and redesigned InkSpace.

### 1.3 RESEARCH SCOPES

The 2D multichannel marine seismic profiles will first be processed to obtain noise- and multiple-free data, with maximum effort. Then the processed seismic data will be interpreted to distinguish the geology of the study area. This research thesis will also clarify the relationships between acquisition, processing, and interpretation of marine multi-channel seismic data in general. The two main goals of this research project are:

- To implement the most effective data processing sequences attenuating the multiples and other types of noise, while increasing the signal-to-noise ratio, which will provide better and more certain imaging of the very complex subsurface in the study area.
- To characterize the stratigraphic units and identify the main geological structures and fault zones, which will build relationships between the many tectonic events and the development histories of the study area.



## 2 GEOLOGICAL BACKGROUND

In this chapter, the geological background of Svalbard and the Arctic Ocean will be generally explained with reference to earlier studies, to comprehend the tectonic evolution and geological history, the tectonic structures, and the stratigraphy of the research area.

### 2.1 TECTONIC EVOLUTION

Svalbard archipelago is located between the southeast of the Yermak Plateau (YP) shelf and the uplifted northwestern corner of the Barents Sea shelf presented in Figure 2.1 (Dallmann, 2015). One of the longest sheared margin segments in the world is located along the western coast of Spitsbergen and the western Barents Sea extending about 1500 km from the Norwegian Margin. The margin formation started in the Early Cenozoic related to the North Atlantic evolution, which can be evaluated with the three main stages: anomalies 27-24 (Paleocene), anomalies 24-13 (Eocene) and anomaly 13 (Oligocene-present). Greenland and Svalbard were connected by a land bridge since Greenland was located at the Eurasian plate before the Norwegian and Greenland Seas were opened in the Paleocene (magnetic anomalies 27-24) (Blinova et al., 2009). The margin formation has been defined as having a progressive propagation from SE to N and from N to NW directions, which started spreading the seafloor in the North Atlantic and Arctic Oceans. Therefore, Svalbard and the shelf of the Barents Sea to Greenland began to tectonically extend into the Arctic Ocean during the Eocene (anomaly 24). A continental transform fault system, the De Geer Fault/Fracture Zone, which is part of the present the Hornsund Fault Complex/Zone (HFZ) and the Greenland Fracture Zone (GF), was impacted by the separation. The De Geer Fault Zone was associated with the evolution of the West Spitsbergen Fold and Thrust Belt (WSFTB), which was followed by the development of the offshore graben structures Forlandsundet (FG) and the Bellsund (BG) (Blinova et al., 2009; Dallmann, 2015). From the early Oligocene (anomaly 13) to present, Svalbard was completely rifted from Greenland and thus a passive and rifted continental margin developed (Dallmann, 2015).



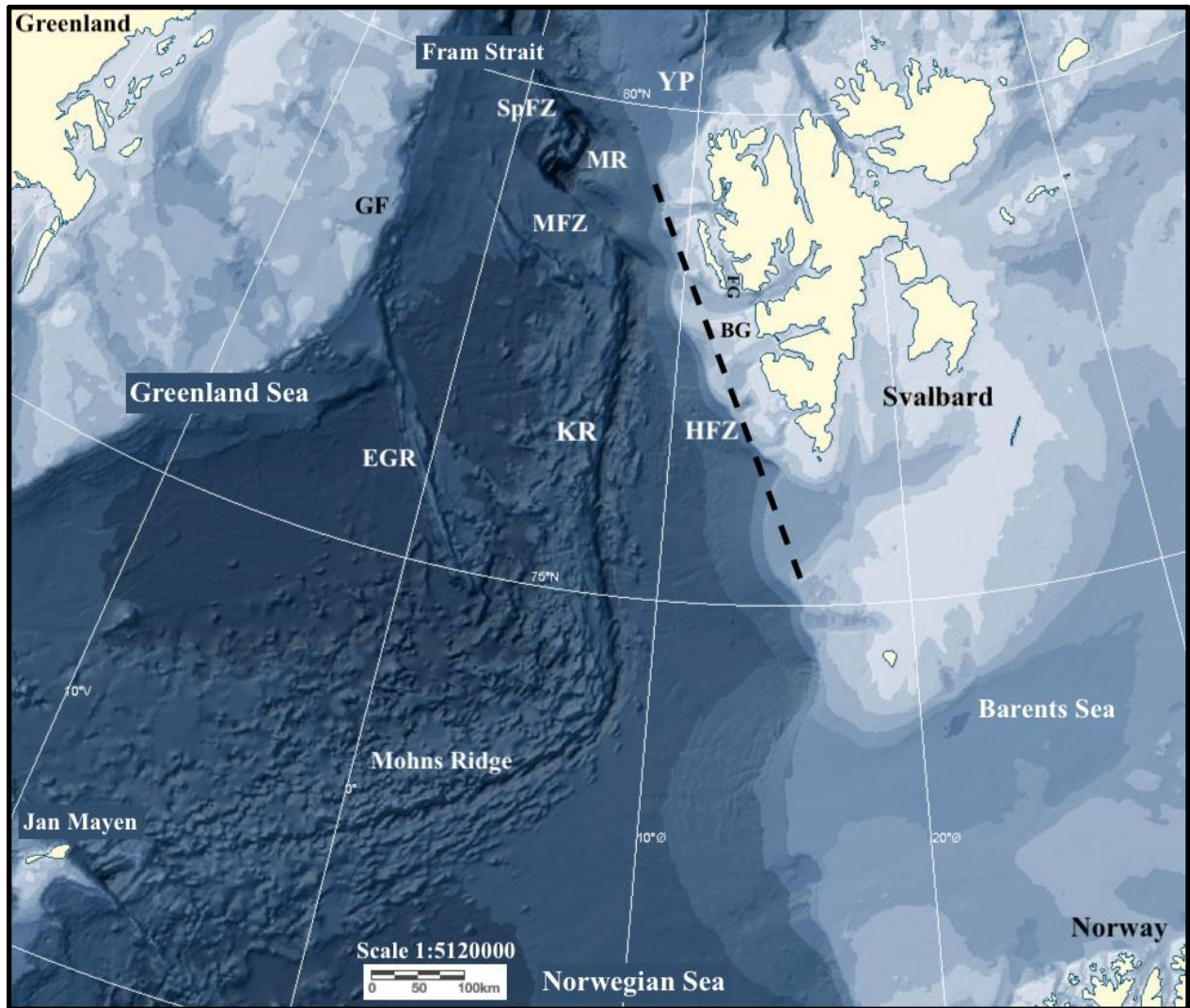


Figure 2.1 The bathymetric map of the North Atlantic, adapted from Svalbardkartet (2022). Yermak Plateau (YP), Spitsbergen Fracture Zone (SpFZ), Molloy Ridge (MR), Molloy Fracture Zone (MFZ), Greenland Fracture Zone (GF), the Forlansundet Graben (FG), the Bellsund Graben (BG), Knipovich Ridge (KR), the Hornsund Fault Zone (HFZ) along the dashed line, East Greenland Ridge (GR) (Blinova et al., 2009; Dallmann, 2015).

Since the extension stopped in the Baffin Bay, northwest of Greenland, in the late Eocene (35 Ma), the plate boundary between North America and Eurasia has become the North Atlantic ridge system, which is subdivided by transform faults into the Reykjanes, Kolbeinsey, Mohns and Knipovich Ridges (KR). The Mohns and Knipovich Ridges have rugged reliefs up to a few thousands meters, which are part of the mid-ocean spreading ridges. The deepest part is the Molloy Deep, 5669 m deep, in the Fram Strait. The west coast of Svalbard is separated from the Knipovich Ridge by a 40-80 km wide shelf. The central part of that ridge is separated by the newly developed



transform faults, named the Spitsbergen Fracture Zone (SpFZ) and Molloy Fracture Zone (MFZ) where Molloy Ridge (MR) is situated between these two. The fault zones have been triggered by extensional and compressional motions (Dallmann, 2015).

## 2.2 MAIN TECTONIC STRUCTURES OF THE WESTERN SPITSBERGEN

During long geological periods, the geology of Svalbard has been characterized by major old fault zones, striking approximately N-S to NNW-SSE. The western Spitsbergen continental sheared margin has been mostly influenced by the extensional and compressional forces during the North Atlantic evolution since the late Cretaceous. These tectonic forces led to uplifting of Svalbard. In addition, a complex interplay of strike-slip (SS) motion has a significant role in the margin formation. The North Atlantic evolution affected WSFTB from magnetic anomaly 24 to 13 when Svalbard had passed the North Atlantic spreading zone. WSTFB development was accompanied by the formation of offshore graben structures by extensional deformation. The Forlandsundet and Bellsund Grabens are cut off by the dextral transverse faults off Isfjorden. These main faults are part of the Hornsund Fault Zone off the western coast of Spitsbergen (Blinova et al., 2009; Dallmann, 2015).

### 2.2.1 The Hornsund Fault Complex

The continental transform fault Hornsund Fault Complex, also known as The De Geer Fracture Zone, was active between Greenland and the Barents Sea Shelf and Svalbard during the Eocene (anomalies 24-13). The name De Geer Fracture Zone is used to define the activities during the Eocene with three tectonic stages (anomalies 27-24, 24-13 and 13), whereas the HFC usually refers to the present structure and the younger activities engaged with the fracture zone. Before HFC affected the area during the North Atlantic evolution, the Eurokean compressive deformation affected the area at the tectonic stage described as the pre-Eurekan situation at anomaly 31 (Figure 2.2.A) (Blinova et al., 2009; Dallmann, 2015).

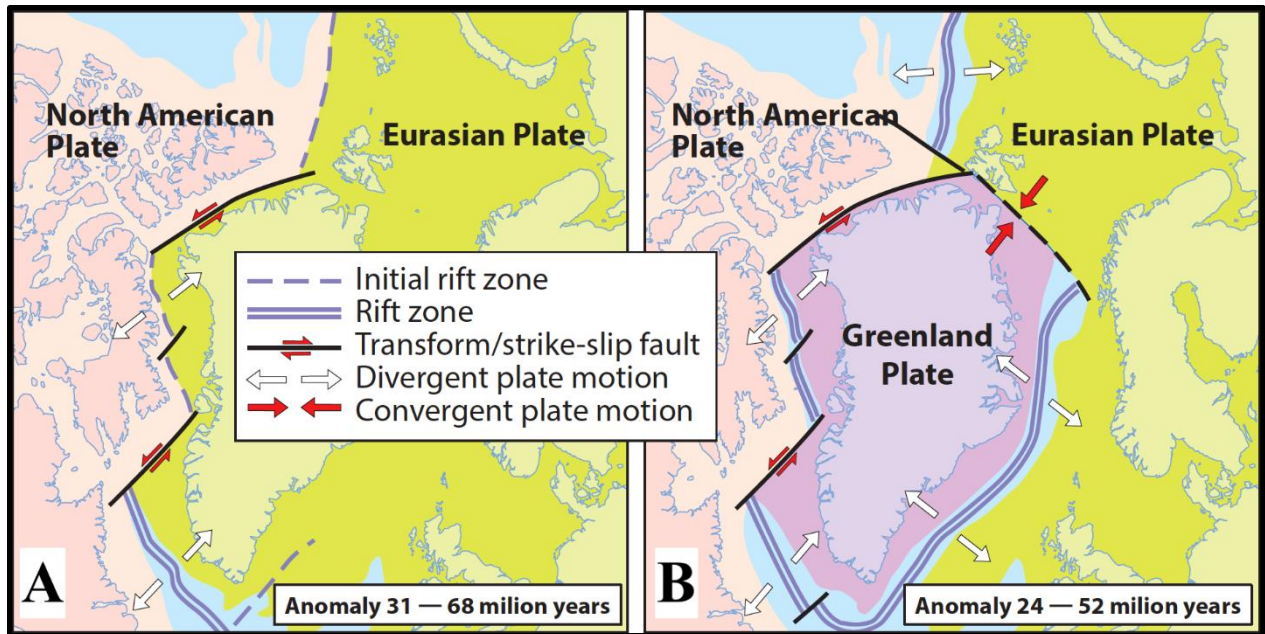


Figure 2.2 Pre-Eurekan situation at anomaly 31 (A) and first stage of Eurekan deformation at anomaly 24 (B), modified from Dallmann (2015).

During the first period of seafloor spreading in the North Atlantic and the Eurasian Basin (Figure 2.3), the HFC segmented the area already deformed by the earliest Eocene Eurekan (anomaly 21). When the seafloor spreading stopped at the Eocene-Oligocene transition (around anomaly 13), the transform fault movement of the HFC ceased, which was followed by the development of the new transform faults at the center of the Knipovich Ridge: Spitsbergen and Molloy fracture zones (Dallmann, 2015).

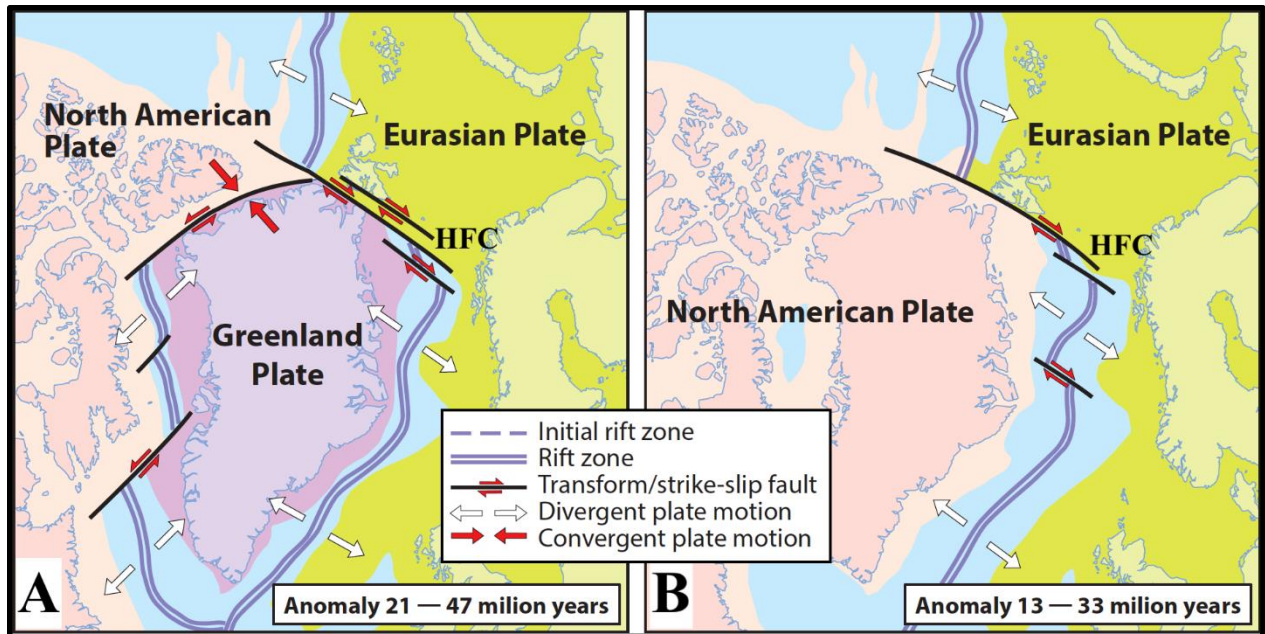


Figure 2.3 Second Eureka stage at anomaly 21 (A), post-Eureka situation at anomaly 31 (B), modified from Dallmann (2015).

The HFC is part of a large transform fracture system related to strike-slip faults in northern Greenland. Strike-slip is a horizontal tectonic block motion that can be a dextral or sinistral. Dextral movement (right-lateral) is used when the opposite block is moving toward the right, while sinistral movement means that the opposite block is moving toward the left. The block movement of De Geer Fracture Zone was identified as dextral wrench movement during the Eocene. Fjords in the west of Svalbard that are oriented east-west seem to be controlled by strike-slip systems (Dallmann, 2015).

Since the Early Oligocene (anomaly 13 - present), the sheared margin of the western Spitsbergen has been obliquely rifted and became a passive margin, which is associated with the Hornsund Fault Zone being parallel to the western Spitsbergen (Figure 2.4). The HFZ is defined by Blinova et al. (2009) as a down-faulted block zone extending from NNW to SSE direction along the central and outer continental shelf, and overlaid by the Tertiary sedimentary wedge. Its eastern boundary is the beginning of this down-faulted block zone with the westward-dipping faults. This boundary is located west of the Forlandsundet Graben and Bellsund Graben. The area of west of the Bellsund Graben was defined by Blinova et al. (2009) as a horst structure covered by a Tertiary

sedimentary wedge down to the underlying pre-Devonian crystalline basement in this study area (Figure 2.4).

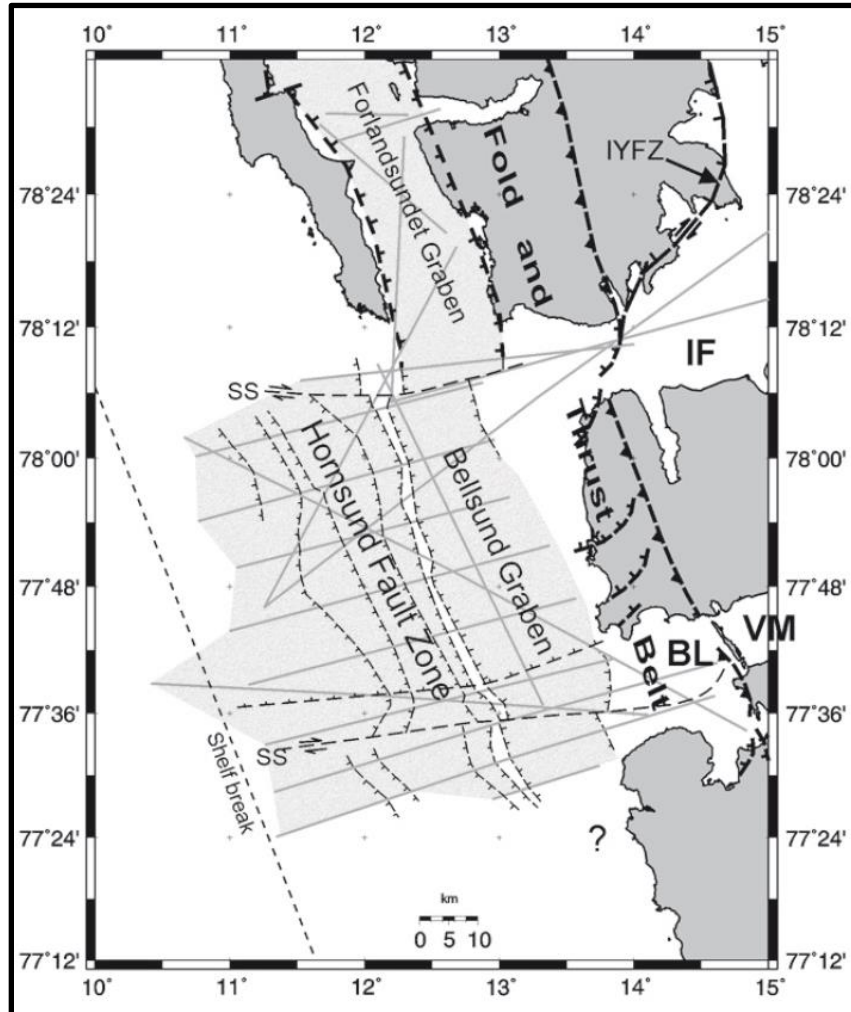


Figure 2.4 The map of the continental shelf off Spitsbergen (dark grey area) and the margin's main structural system (light grey area): Isfjorden-Ymerbukta Fault Zone (IYFZ), Forlansundet Graben (FG), The Bellsund Graben (BG), The Hornsund Fault Zone (HFZ), strike-slip faults (SS) Isfjorden (IF) and Van Mijenfjorden (VM). Acquired and interpreted seismic profiles (grey lines) from different surveys is also shown, extracted from Blinova et al. (2009).



## 2.2.2 West Spitsbergen Fold and Thrust Belt

The Old Red sedimentary strata deformed during the Caledonian Orogeny was impacted by the fold and thrust belt in northern Svalbard during the early Carboniferous. During the early Eocene

(magnetic anomaly 24), the margin deformation of the western part of Spitsbergen was dominated by east-northeast directed folding and thrusting locally named the West Spitsbergen Fold and Thrust Belt. WSFTB affected west Spitsbergen from Kongsfjorden in the north to Sørkapp Land in the south (Figure 2.5). Unlike many other fold belts, WSFTB is not the consequence of a plate collision. It is assumed that it is a component of an intra-plate structure from anomaly 24 to 21 when seafloor spreading occurred in the Labrador Sea, Baffin Bay, west of Greenland. The Hornsund Fault Zone was related to this transform movement in West Spitsbergen which ceased at anomaly 13 after Svalbard formed as an obliquely rifted passive continental margin (Dallmann, 2015).

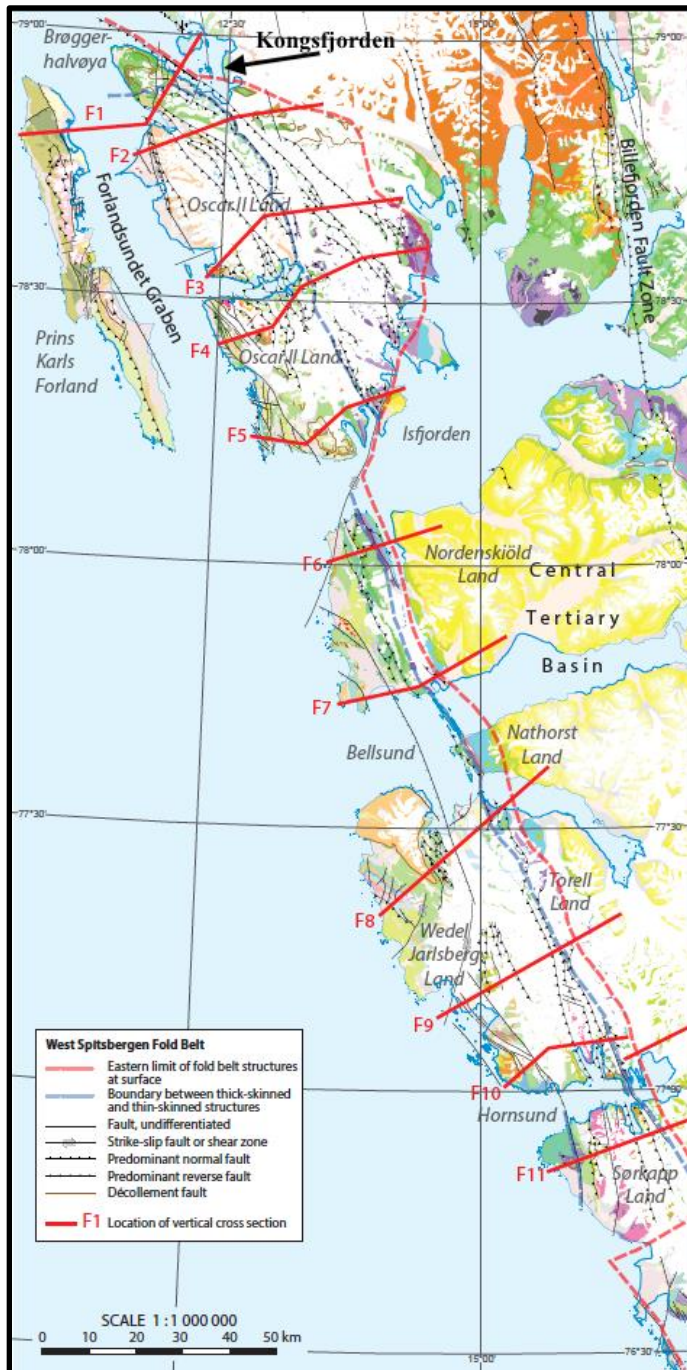


Figure 2.5 The map of the western Svalbard showing the WSFTB and main fault structures, modified from Dallmann (2015).

### 2.2.3 The Bellsund Graben

According to Blinova et al. (2009) there was no solid agreement for a hypothesis about the evolution of the graben structures along the western part of WSFB. However, it is mentioned by Dallmann (2015) that the development of the graben structures in the West Spitsbergen was essentially impacted by the dextral strike-slip regime and seafloor spreading between Greenland and Norwegian seas during the North Atlantic evolution and the WSFTB advancement. The Bellsund Graben was distinguished as a southern continuation of the Forlandsundet Graben (Blinova et al., 2009). The Forlandsundet and Bellsund grabens were dissected by a dextral strike-slip fault motion off Isfjorden in the E-W direction (Figure 2.4). The length of BG is about 70 km limited by the W-E trending dextral strike-slip faults off Isfjorden and Van Mijenfjorden. The evolution of the BG has been explained with three stages by Blinova et al. (2009):

1. Latest Paleocene - Early Eocene (?): Initial sedimentation within the local synsedimentary extensional structures, possibly on the top of an uplifted area during the main compressional regime.
2. Latest Eocene: Graben formation due to initial transtensional movements in the area, possibly developed as a pull-apart structure during a dextral strike-slip regime accompanied by local compression.
3. Oligocene: Normal faulting and final graben development caused by a transtensional regime corresponding to seafloor spreading between Svalbard and Greenland.

## 2.3 STRATIGRAPHY OF THE WESTERN SPITSBERGEN

Svalbard is rich with countless rock formations representing different periods of geological history varying from Precambrian to Quaternary. However, due to the several hiatuses during the geological history of Svalbard, a few rock formations completely disappeared, such as part of the Permian and upper-Cretaceous. The fault zones also interrupted and displaced the normal stratigraphic succession in several locations in Svalbard. Thus, the fault zones have been likely the other main cause of the distribution of the sediment depositions in the north and west Svalbard during its geological history, due to the varying extensional and compressional regimes. In general, the sedimentation in western Svalbard has been impacted by these factors: uplifting,

erosion, deformation, repeated deglaciations, ice retreatments, glacial erosions, debris flow and ocean currents. The westernmost part of Svalbard has been mostly dominated by the Cenozoic sediment accumulation (Dallmann, 2015). The stratigraphic units from the study area will be presented in this chapter with their given local unit names.

### 2.3.1 Hecla Hoek

Hecla Hoek is a commonly used name for the basement rock groups in Svalbard from Precambrian to early Devonian. The term for the bedrock of Svalbard varies between different studies. Some studies distinguished the name as pre-Caledonian basement, since the basement was deformed during the development of the Caledonian Orogeny when magmatic and metamorphic rocks were deformed and deposited (Dallmann, 1999). It was emphasized by Dallmann (2015) that the pre-Caledonian basement also refers to the oldest and most altered rocks in Svalbard, so the basement name is the crystalline basement, which also comprises sedimentary bedrock with a cumulative thickness of up to 8000 m. The sedimentary rocks exposed in the western and northern parts of Svalbard was deposited from Devonian to Palaeogene times.

### 2.3.2 Devonian Old Red Sediments

During the collision of the predecessor continents Laurentia and Baltica, the Caledonian mountain chain developed and created the so-called Old Red Continent that refers to the Old Red Molasse sediments. These sediments are erosional products of the post-Caledonian mountain range, accumulated in Devonian depositional basins during the continental extension and orogenic collapse. The mineral haematite and a ferrous oxide mineral ( $\text{Fe}_2\text{O}_3$ ) led to the distinctive red colour of these siliciclastic sediments (Dallmann, 2015). According to Blinova et al. (2009), the accumulation of the Old Red molasse likely occurred from the Latest Silurian to Late Devonian, while it may have lasted until the early Carboniferous period by Dallmann (2015). During the deformation in early Carboniferous, the Old Red sedimentary strata in Svalbard were impacted by the compressional west trending folding and thrusting. Thus, they were separated by an

angular unconformity from the overlying Carboniferous rocks, sandstones and siltstones (Blinova et al., 2013; Dallmann, 2015).

### 2.3.3 Cenozoic Sedimentary Wedge

The Cenozoic Sedimentary Wedge (CSW) has been described as an unconformably deposited unit overlying the down-faulted block of the Hecla Hoek unit in the HFZ (Blinova et al., 2009). The glacial deposition of the unit has emphasized its occurrence in the last 2.7 million years. CSW consists of multiple sequences divided by countless unconformities. A major unconformity, named Upper Regional Unconformity (URU), was formed by the glacial erosion of the entire shelf during the repeated glacial extensions (Dallmann, 2015; Faleide et al., 1996). URU splits the Cenozoic sediment wedge into two main units. The overlying sedimentary unit divided by URU is a relatively flat stratum parallel to the seafloor, while the underlying sedimentary unit is westward dipping. The overlying unit is thinner than the underlying unit, which was impacted by the thinning of the continental crust of the western Svalbard margin due to the extension (Blinova et al., 2009).



### 3 METHODS

The methods of this research consist of three fundamental applications; seismic data acquisition, seismic data processing and seismic data interpretation, which are detailly explained in this chapter. Those seismic methods are applied to investigate layered sequences to reveal geological structures beneath the seafloor by acquiring seismic data; then improving the signal quality of seismic data by processing; and next interpreting the final version of seismic images.

#### 3.1 SEISMIC DATA ACQUISITION

##### 3.1.1 Seismic Data Principles

Multichannel reflection seismic data is measured in two-way travel time (TWT) as seismic waves propagates from a source/sources along and/or reflecting back from reflection boundaries, also known as interfaces of acoustic impedance contrast, to a receiver/receivers. To give an example in a simple two-layer model with a flat reflector where seismic velocities of mediums are  $V_1 < V_2$  in Figure 3.1, a direct wave propagates from near-surface source to surface receivers along the surface. The travel time of the direct wave is given by

$$t_{dir} = \frac{x}{V_1} \quad (3.1)$$

where  $x$  is offset between source and receiver. The travel time of reflected wave obliquely propagating from the source and reflecting on the interface is given by

$$t_{refl} = \frac{(x^2 + 4z^2)^{1/2}}{V_1} \quad (3.2)$$

where  $z$  is the depth between the surface and the interface. The refracted wave is obliquely propagating downward in upper medium  $V_1$ , then propagating along the interface with  $V_2$ , and

then propagating upward to the receiver with  $V_1$ . The travel (or arrival) time of the refracted wave is given by

$$t_{refr} = \frac{x}{V_2} + \frac{2z \cos \theta_c}{V_1} \quad (3.3)$$

and

$$\frac{\sin \theta_c}{V_1} = \frac{1}{V_2} \quad (3.4)$$

where  $\theta_c$  represents critical angle, also known as incident angle,  $\vartheta_i$  explained by Snell's Law (Kearey et al., 2002).

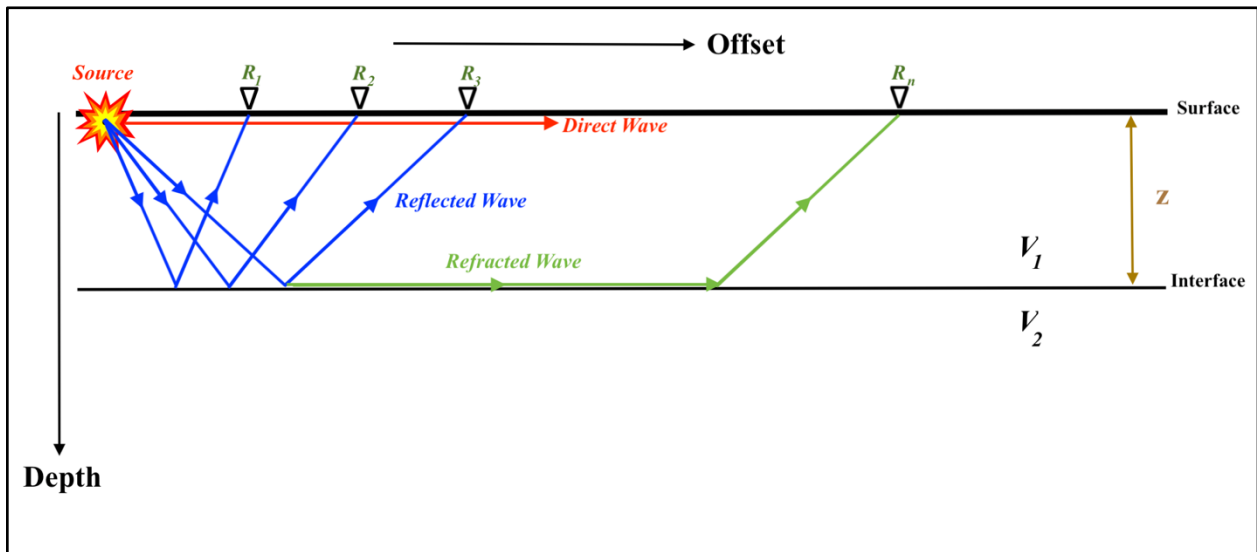


Figure 3.1 The schematic illustration of two-layer model with a flat interface. The model shows ray paths for direct (red), reflected (blue) and refracted (green) waves from near surface to surface receivers where velocity of mediums represented by  $V_1$  and  $V_2$  respectively downward and  $V_1 < V_2$ , created by Inkspace.

The refracted wave loses its energy by longer travel time and several physical factors while propagating downward into the medium, along the interfaces and then back up to the surface. However, collecting reflected wave is beneficial regarding the energy preservation carrying significant information for seismic studies and less complexity of data processing to attenuate

the noise, while increasing the signal-to-noise (S/N) ratio. For decades, the recorded reflection seismic has been processed with common-midpoint (CMP) gathers for academical and industrial purposes such as imaging both near-surface geology for exploration of valuable resources and the crustal structure down to the Moho (Yilmaz, 2001). Therefore, the marine seismic reflection was used in this research area to enable detail investigation of geological structures.

### 3.1.2 Marine Seismic Data

The signal in marine seismic exploration is always generated in seawater by a controlled-source yielding pressure wave (p-wave). The p-wave compress and decompress the water molecules while three-dimensionally traveling as sound waves from the source through the water column. Their pressures are recorded by hydrophones. The sound velocity of the water in exploration areas changes by the physical properties of the ocean such as density, salinity, and temperature (Dondurur, 2018). Marine seismic data can be acquired by various surveys (Figure 3.2) regarding different purposes. Then, the recorded data as 2D or 3D seismic is processed to obtain seafloor and subsurface image (Landrø & Amundsen, 2018).

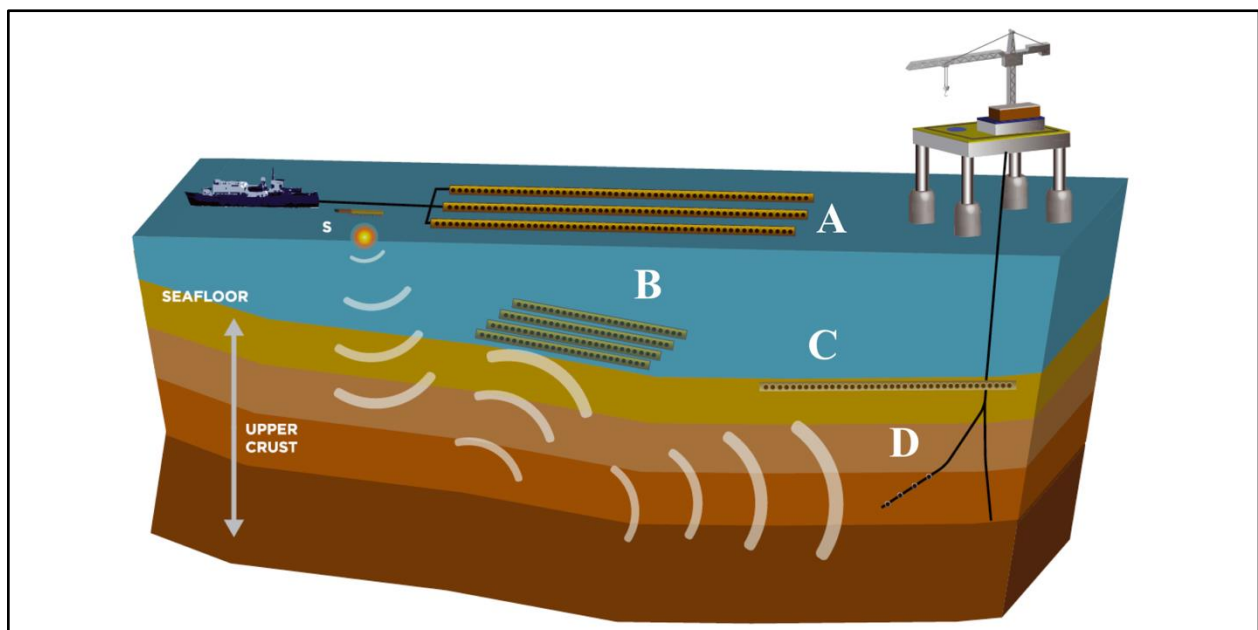


Figure 3.2 The illustration of all marine seismic surveys with a towed source (s). A: towed streamers (cables) acquisition; B: ocean-bottom acquisition on the seafloor; C: an array of sensors buried in the seafloor; D: a VSP (Vertical Sensor Profile) survey where the streamers are positioned in a well, modified from Landrø & Amundsen (2018).

The S/N ratio of marine seismic data can be drastically reduced due to some destructive marine noise. The dominant type of noise in marine seismic is multiple reflections regarding their amplitudes and complex ray paths, compared to other sorts of noise in marine. Since the multiple reflections have lower amplitudes than primary reflections, they can easily be determined by comparison with primary reflections in the seismic processing sense (Dondurur, 2018; Kearey et al., 2002). However, the amplitude of sea surface-related multiples may be stronger than primary reflections from deeper subsurface. Therefore, they are mostly identified based on their travel time and NMO velocity (equation 3.28).

### 3.1.3 Ray Paths of Multiple and Ghost Reflections

Seismic energy reflected from an interface one time and traveling along a particular ray path is called a primary reflection. However, multiple reflections can travel along the same ray path multiple times appearing on the zero-offset shot gathers and stack sections as repetitions of the primary reflection with lower amplitude (Dondurur, 2018; Kearey et al., 2002). Distinctive multiple reflections occur only at the interfaces which have the largest impedance contrast. Two sorts of multiple can be distinguished as short- and long-path multiples. A short-path multiple arrives earlier than a long-path multiple due to the traveling time along different reflectors. As ray-paths of the long-path multiples are longer than the paths of their associated primary events from the same reflector, long-path multiples, also called water layer multiples, are recorded as separate events (Sheriff & Geldart, 1995). The multiples propagating with various ray paths between different interfaces are illustrated in Figure 3.3 such as surface-related, peg-leg and interbed multiples.

Surface-related multiples are easily recognized in trace and stacked sections thanks to their periodic travel time being the same as the arrival time of primary reflection between a reflection boundary and a free surface, which are the seabed and the sea-surface in marine seismic, respectively. They travel through the water column by going down from a source, reflecting from the seabed and going up, and then going down again reflecting more than one time from the sea-surface to the seabed to the receiver. Interbed multiples, also known as internal multiples or

short-period multiples, occur when their downward reflections repeated themselves between the seabed and a subsurface interface, or between two subsurface interfaces. Peg-leg multiples, also called long-period multiples, are generated at a high amplitude reflective boundary in the subsurface such as the acoustic basement. They are traveling from the source to this strong reflective boundary and then travel upward to the sea-surface where the signal reflected again from the sea-surface through the water column. Thus, they appear in the seismic sections as a phantom interface mimicking the strong reflective interface with the time interval that always equal to the water depth. Pegleg multiples can also be combined by the ray paths of the internal multiples and the surface-related multiples (Dondurur, 2018; Dragoset & Jeričević, 1998; Sheriff & Geldart, 1995).

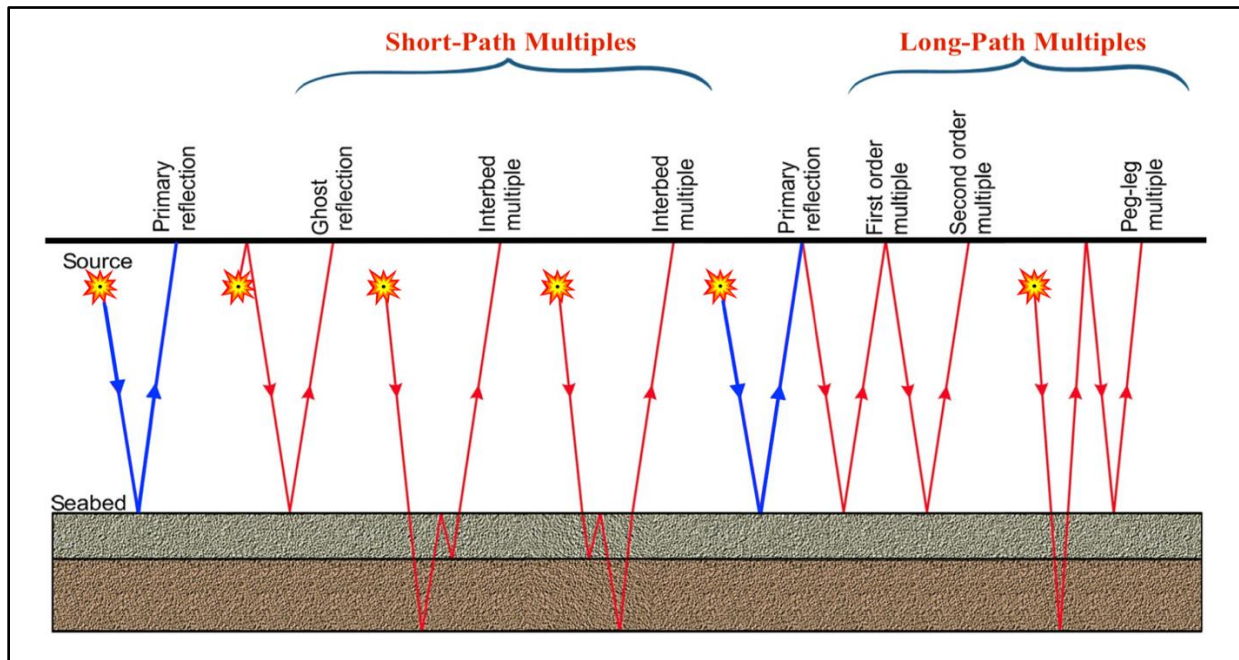


Figure 3.3 The schematic illustration of ray paths of primary reflections (blue) within various sort of multiple reflections (red), modified from Dondurur (2018).

Ghost reflections in marine seismic are the delayed version of the primary signal with the opposite phase, which is directly downgoing through the water column, due to the reflection coefficient of the sea-surface being approximately -1. In a towed streamer acquisition, the ghost reflections can appear both at the source and receiver sides. They can arrive at the streamers

with 3 different ray paths for a single reflection between a shot and a receiver (Figure 3.4). Ghost reflections impact the composite signal yielding constructive and destructive interference. The frequency band of the signal is limited by these interferences. Thus, the amplitudes of certain frequency bands are periodically attenuated, called ghost notches in Figure 3.5 (Dondurur, 2018; Sheriff & Geldart, 1995).

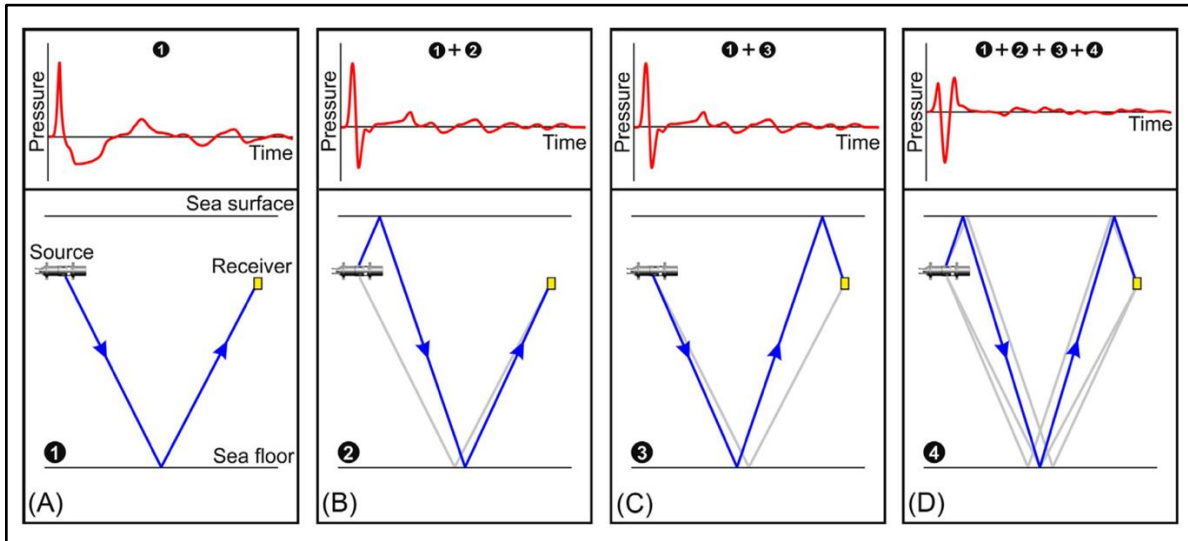


Figure 3.4 The schematic illustration of the ray paths (blue) of a primary (A) and 3 different ghost reflections. Their signals received from a single shot (red). The combined signal of source ghost with primary reflection (B) is represented by 1+2. The combined signal of primary reflection and receiver ghost (C) is represented by 1+3. The combined signal of source ghost and receiver ghost with primary reflection (D) is represented by 1+2+3+4, extracted from Dondurur (2018).

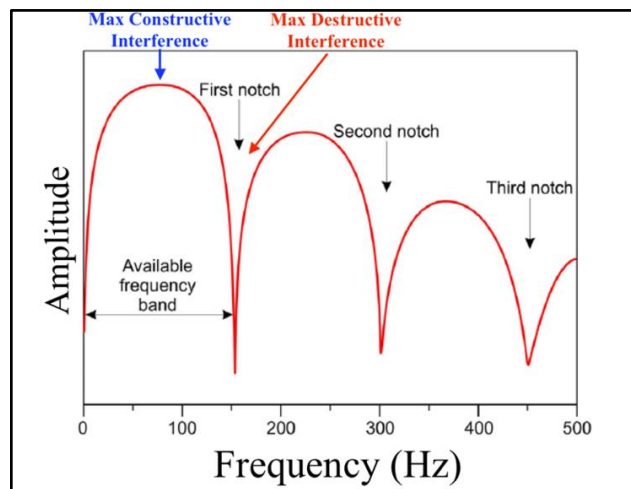


Figure 3.5 The amplitude spectrum of the combined signal. Constructive and destructive interference and the periodic ghost notches on the amplitude spectrum due to ghost interference, modified from Dondurur (2018).

### 3.1.4 Source

For different purposes, seismic sources in marine seismic exploration can be chemical explosives, impulsive sources, marine vibrators, electrical sources, and airguns to generate high amplitude acoustic signals in the conventional marine exploration (Mjelde, 2011). SVALEX data were acquired by airgun string (5 guns) with one additional gun system as an example in Figure 3.6 (Mjelde, 2003).



*Figure 3.6 The photo of the airgun used onboard R/V Håkon Mosby during the SVALEX 2002, extracted from Mjelde (2011).*

#### 3.1.4.1 Airgun and Bubble Pulses

Airgun is the common marine source that injects the highly compressed air from the air chambers to water creating a primary bubble traveling in the water column in three dimensions. Therefore, generated energy depends on the air volume, air pressure and water depth. It is used as a single source, or a cluster of airguns closely placed into an airgun string in order to increase the energy providing a broad frequency band. Once an airgun is fired, it generates a primary seismic signal in a bubble (Figure 3.7.A). The primary bubble travels through water column by periodically expanding and collapsing. This periodic movement causes the new signals with opposite polarity (Figure 3.7.B, C and D), called bubble effect or bubble noise. In acquisition, the bubble noise problem can be attenuated by using an airgun cluster or a sort of special airgun, named

generator/injector (GI). Otherwise, it can be attenuated by signature deconvolution in the data processing (3.2.1.11).

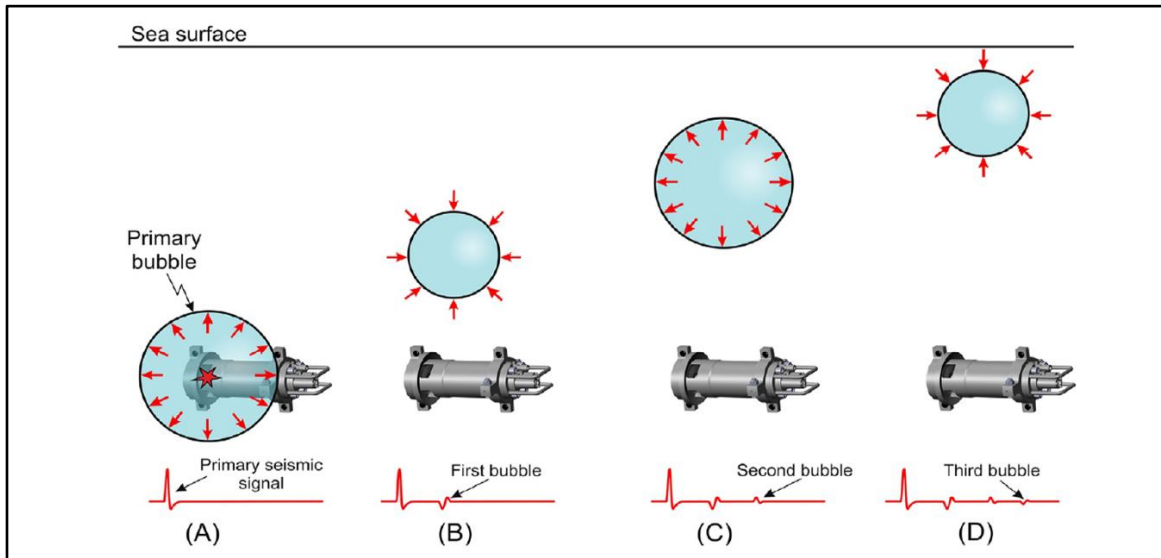


Figure 3.7 The illustration of a fired airgun and the periodical movement of primary signal (A) causing the first bubble noise (B), the second bubble noise (C), and third bubble noise (D) in the source signature, extracted from Dondurur (2018).

### 3.1.4.2 Source Signature and Array Tuning

The combination of a primary signal and its ghost signal creates a composite signal, called the source signature (Figure 3.8), which presents the characteristic pressure shape as a function of time in the far-field. The primary and its ghost signal cannot be separated from the composite signal. However, to control the destructive part of the signal, the airguns array can be tuned (Dondurur, 2018).

### 3.1.4.3 Near- and Far-Field Source Signatures

In marine seismic acquisition, the source signature can be measured in the near-field ( $r$ ) where the distance is between the physical size of an airgun ( $d$ ) and wavelength of the signal ( $\lambda$ ). On the other hand, bandwidth of the source signature can be measured in the far-field, which provides the signature of the composite signal at a certain depth ( $R$ ) below the airgun. The near- and far-field signature and the measurement is illustrated in Figure 3.9 (Dondurur, 2018).



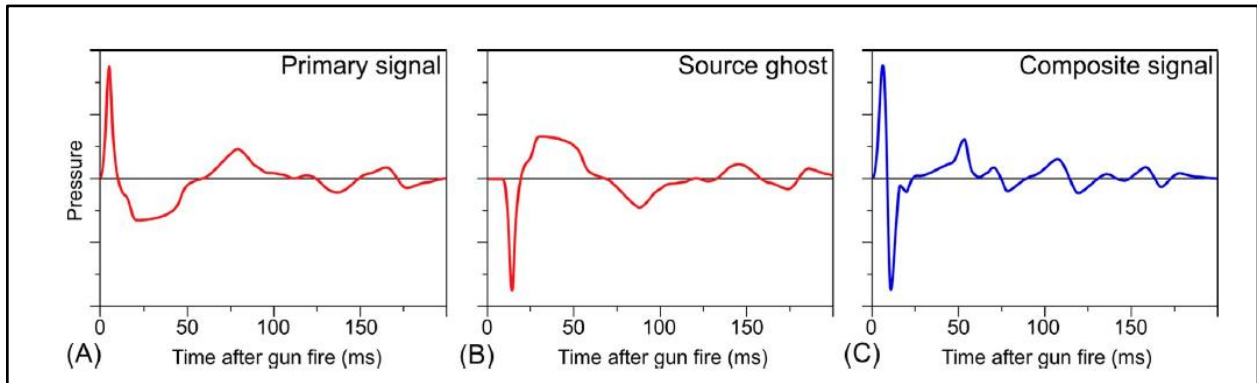


Figure 3.8 shows the far-field source signature as composite signal (C). It is a combination of the primary signal produced by an airgun (A) and the ghost reflection of the source (B) arriving a short time after the primary signal as identical version of primary signal with opposite polarity, extracted from Dondurur (2018).

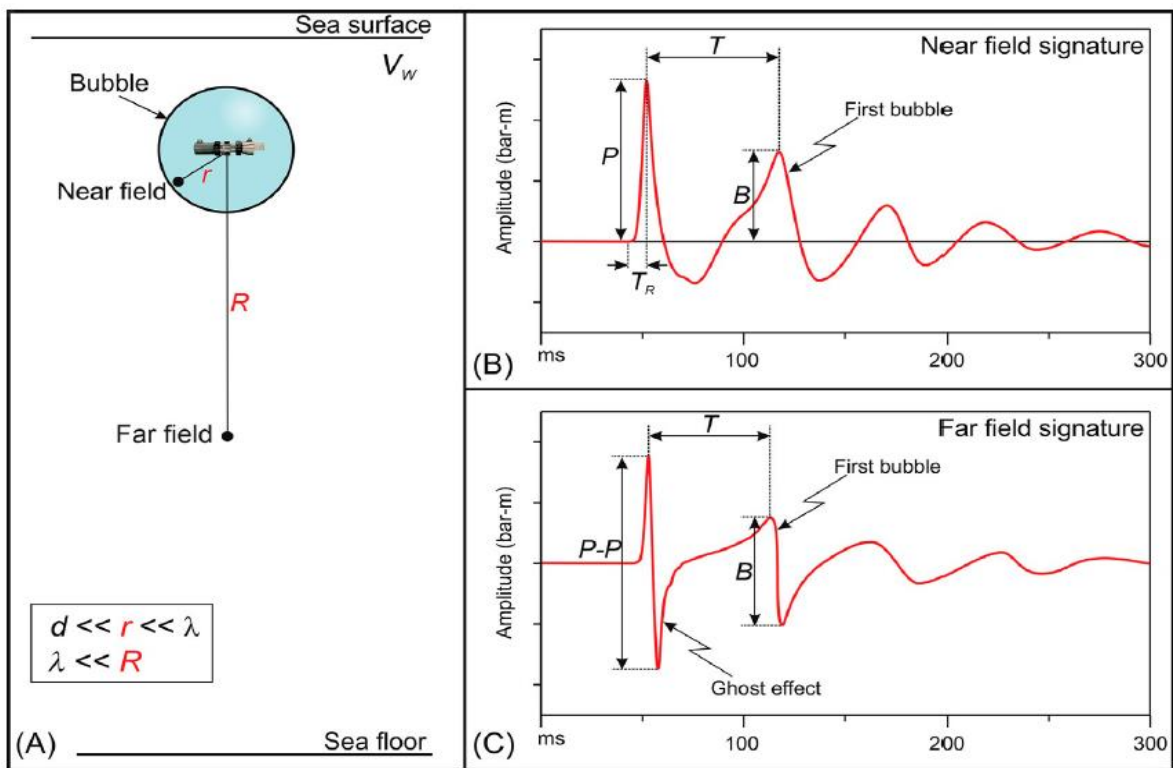


Figure 3.9 shows the illustration of marine seismic source with its near- and far-field zones. Near-field signature (B) and far-field signature (C).  $V_w$ : water velocity;  $P$ : Peak amplitude of the primary wave in near-field;  $P-P$ : Amplitude of the primary wave in far-field;  $B$ : Amplitude of the first bubble pulse;  $T$ : bubble period;  $T_R$ : is the rise time, extracted from Dondurur (2018).

### 3.1.5 Receiver

Information of a signal reflecting or refracting from the earth is sensed by an instrument, named receiver or sensor, which is geophone on land and hydrophone in marine towed streamer acquisition. A piezoelectric hydrophone is a common instrument in marine research, composed of piezoelectric ceramic element. The hydrophone senses pressure variations in the water column as well as the one-way streamer acceleration towards the towing direction. Two identical piezoelectric elements are polarized in the hydrophone to cancel the effect of acceleration. A group of hydrophones is added into a single or multiple streamers to collect high-resolution seismic data (Kearey et al., 2002; Sheriff & Geldart, 1995). In addition, de-ghosting during the acquisition stage is also possible by assembling extra sensors into the towed streamers in addition to the conventional pressure hydrophones (1C). This is called multi-sensor recording (2C and 3C) that provides higher resolution broad-band seismic data (Dondurur, 2018).

#### 3.1.5.1 Streamer

A streamer, or marine cable, is a specially designed plastic tube consisting of numerous coupled piezoelectric elements and filled with liquid, such as oil. A schematic example of the data acquisition by the towed streamer system can be seen in Figure 3.2. Marine seismic data acquisition can be done by a single or multiple streamers with the aim of 2D or 3D seismic data acquisition, respectively. The main difference basically between them is that the 3D seismic acquisition provides high-resolution data quality thanks to the acquisition from various azimuth angles such as wide-, medium- and narrow-azimuth while the 2D seismic acquires only a single-azimuth along the survey line. During a seismic operation, streamer depth is controlled by instruments named birds. A single series of interconnected hydrophones are grouped in a streamer, called a hydrophone group. The center of each hydrophone group in a streamer is engaged with a particular recording channel. The distance between these recording channels is called group interval. Although larger group length provides higher S/N ratio as well as stronger directivity, spatial resolution becomes lower. Modern streamers are commonly made up of 3.125 or 6.25 m for high-resolution seismic and 12.5 m group intervals for conventional 2D/3D seismic surveys. For 6.25 and 12.5 m group intervals, a 100 streamer section contains 16 or 8 channels,

respectively. (Dondurur, 2018; Mjelde, 2011). To obtain 2D multichannel seismic reflection data, a single streamer was used during SVALEX 2002, whose brand was WesternGeco Nessie3 digital streamer (Figure 3.10), 3000 m long with 240 channel and 12.5 m group length (Mjelde, 2003).



*Figure 3.10 The streamer photo used onboard R/V Håkon Mosby during the SVALEX 2002, extracted from Mjelde (2011).*

### 3.1.5.2 Single and Multichannel Seismic

Marine seismic reflection data with a streamer can be acquired by single channel design where there is only one source and one recording channel towed by ship (Figure 3.11.A) providing zero-offset acquisition geometry (also explained in 3.2.1.4). Thus, the single channel acquisition technique only provides single-fold coverage with low resolution whereas multichannel seismic acquisition (Figure 3.11.B) can obtain folds of more than one from seismic reflectors. The fold number is also known as the number of traces in CMP gathers. The fold relies on the survey geometry such as shot and channel intervals, and channel and streamer numbers (Dondurur, 2018; Yilmaz, 2001). Single-channel seismic is also simpler regarding subsurface geology without the complex data processing sequences for multichannel seismic due to the requirement of time correction by normal moveout (NMO) and stacking for instance.

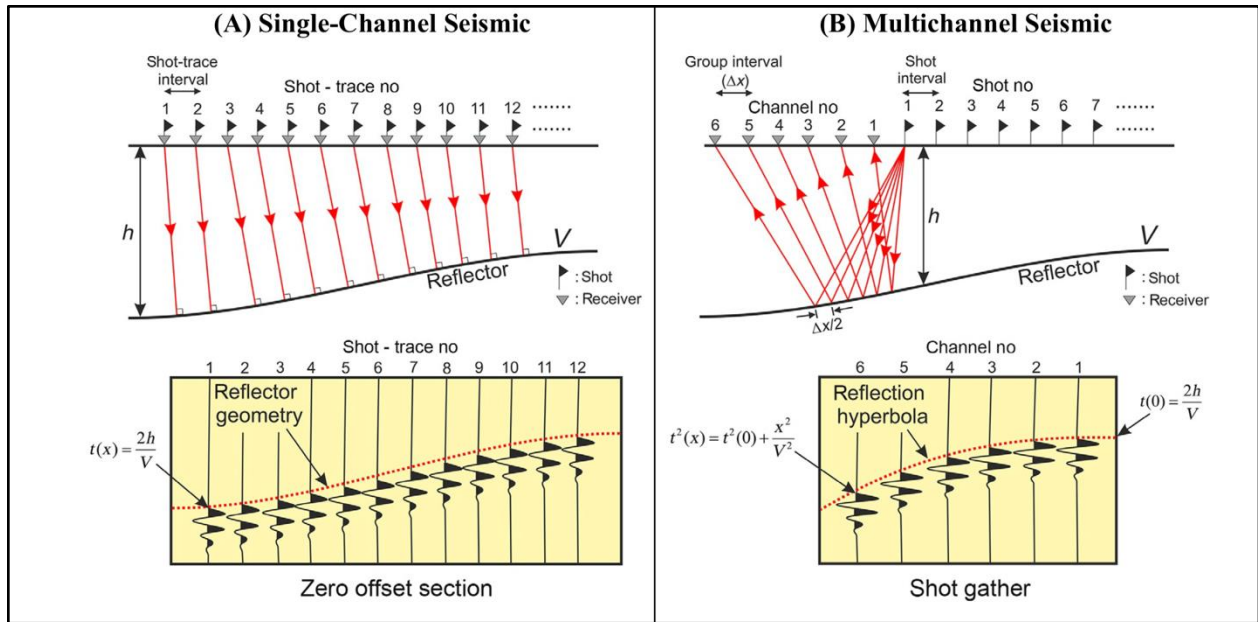


Figure 3.11 Comparison of single- and multichannel seismic data acquisition.  $t(x)$  arrival time of reflected waves are different in those two type of acquisition design due to reflection hyperbola between near- and far-offsets.  $\Delta x/2$  represents CMPs where reflector is not flat, modified from Dondurur (2018).

Multichannel reflection seismic provides high-resolution images due to higher fold coverage in the target area. It also enables attenuation of the multiples, which are the most dominant problem in the study area, by various techniques. Therefore, the streamer was designed for multichannel reflection data acquisition in SVALEX 2002 (Mjelde, 2003).

### 3.1.6 Recording and Storing

Seismic data are digitally recorded and saved in tape or hard disk drivers as SegD format, which is the standard recording format of field data defined by the Society of Exploration Geophysics (SEG). In seismic operation, navigational parameters should be saved in a metric system. The geographical coordinate can be converted to the metric system by using projection systems. The Universal Transverse Mercator (UTM) coordinate system is the most common projection (Dondurur, 2018). Triacq recording system was used to obtain seismic data and saved them as SegD format in tapes. The geographical coordinate of the SVALEX 2002 operation was collected by GPS antenna (72 m offset) and saved in plain text format as metric (easting and northing) represented by a particular projection within UTM-zone 33X (Mjelde, 2003).

## 3.2 SEISMIC DATA PROCESSING

This chapter briefly explains the most essential concepts of seismic data, signal theory, some mathematical operations such as the Fourier transform and convolution, various seismic trace gathers within geometry calculation, pre-processing and advanced processing steps used in this research.

Acquired seismic traces measured in time are summation of both desired information from target points beneath the surface, such as their density and elastic moduli, and undesired noise and destructive factors. Seismic data processing is done by commercial and/or academic software in order to attenuate the noise, while keeping the valuable information. Furthermore, remedies can be determined and suggested for the best signal-to-noise ratio improvement which provides interpreters or earth scientists with clear seismic images (Dondurur, 2018; Kearey et al., 2002; Yilmaz, 2001; Zhou, 2014).

### 3.2.1 Pre-processing

Pre-processing is the initial processing sequence where the seismic data is prepared for the main processing sequences. It consists of data loading, trace selection, geometry calculation, header definition, trace editing, band-pass filtering, gain recovery, muting,  $f$ - $k$  filter and brute stack (Dondurur, 2018). In addition to these pre-processing steps, signature deconvolution and noise attenuations were also added in the processing workflow.

#### 3.2.1.1 Data Loading

Raw seg-y data used as input data for the processing should be converted to a specific media where seismic processing is done (Gadallah & Fisher, 2009). The binary data format of the recorded raw seismic datasets in this research is seg-y used as input.

### 3.2.1.2 Resampling

A continuously recorded signal might be analogue as a function of time or distance. The signal can be digitized by picking the values at specific times (Figure 3.12), which is also called sampling (Kearey et al., 2002). The sampled signal  $s(t)$  can be given as

$$s(t) = [s(t_0), s(t_1), s(t_2), s(t_3), \dots] \quad (3.5)$$

where the picked values of time are defined by the sampling interval ( $\Delta t$ ).

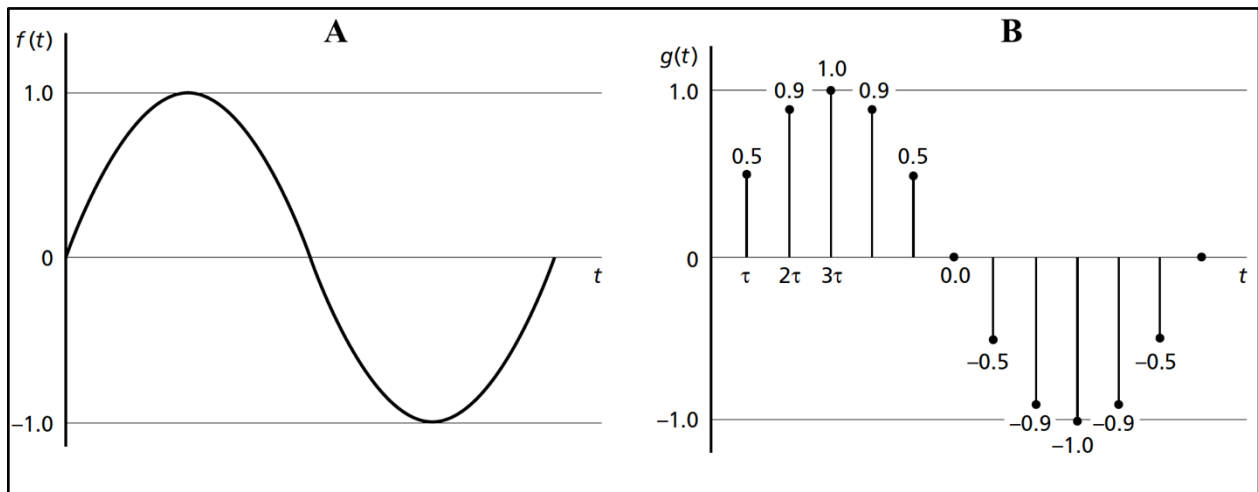


Figure 3.12 A continuously recorded signal as a function of time is sampled from an analogue record (A) to digitized one (B), modified from Kearey et al. (2002).

The accuracy of a sampled signal relies on the sampling interval (or sampling frequency) and amplitude measurement expressed as dynamic range. Dynamic range (unit in dB) is a ratio of the maximum measurable amplitude ( $A_{max}$ ) to minimum measurable amplitude ( $A_{min}$ ) given by

$$20\log_{10} (A_{max} / A_{min}) = [dB] \quad (3.6)$$

The sampled data can be aliased which is a distortion of the recorded signal due to undersampling. All frequencies of the sampled data can be preserved up to half of the sampling frequency. This frequency is defined as the Nyquist frequency ( $f_{NY}$ ) given by

$$f_{NY} = 1/(2\Delta t) \quad (3.7)$$

where  $\Delta t$  is sampling interval. Once the sampled data contains frequencies above the Nyquist frequency, the sampled data is aliased. If a signal is aliased, there is no way of recovering the original signal. Therefore, the sampling interval should be chosen carefully. In order to prevent aliasing, the signal should be oversampled, or an anti-alias filter should be applied to the processing sequence.

### 3.2.1.3 Fourier Transform

To study amplitude and phase variation of a signal, the waveform should be analyzed both in time and frequency domain (Kearey et al., 2002). Periodic functions of cosine and sine signals can be obtained by Fourier series whereas non-periodic functions cannot be expressed (Dondurur, 2018). Thus, the frequency component of a non-periodic signal in the time domain  $f(t)$  can be approached by forward Fourier transform calculated with the given Fourier integral:

$$F(\omega) = \int_{-\infty}^{\infty} f(t)e^{-i\omega t} dt \quad (3.8)$$

where  $i = \sqrt{-1}$ ,  $f(t)$  is function of time;  $F(\omega)$  is function of the angular frequency for a non-periodic 1D signal and  $\omega = 2\pi f$ . Once analyzing is done in the frequency domain, the function of the angular frequency can be reversed the function of the original signal in the time domain by inverse Fourier transform calculated with the given Fourier integral:

$$f(t) = \frac{1}{2\pi} \int_{-\infty}^{\infty} F(\omega)e^{i\omega t} d\omega \quad (3.9)$$

Eventually, Fourier transform pair of a waveform can be also shown (Figure 3.13) in the time domain  $g(t)$  and the frequency domain  $G(f)$  with Fourier transform given by

$$g(t) \leftrightarrow G(f) \quad (3.10)$$

where open-headed arrow stands for Fourier transform pair.

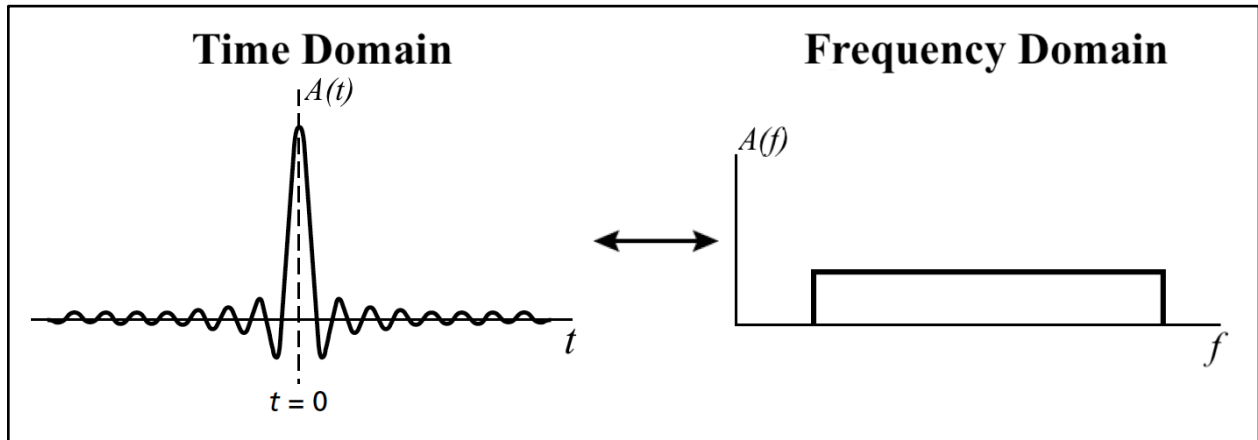


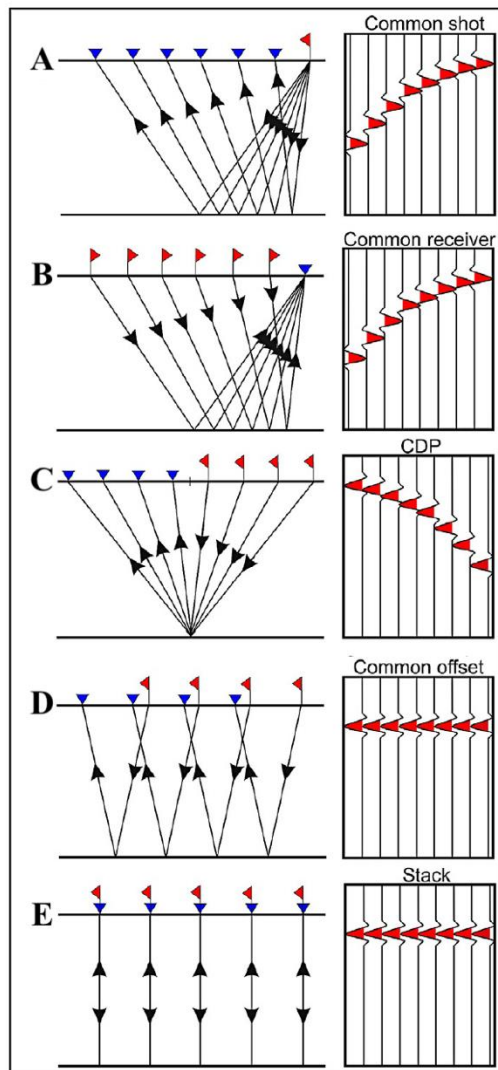
Figure 3.13 The schematic Fourier Transform illustrates amplitude spectra of a zero-phase waveform in the time and the frequency domains, modified from Kearey et al. (2002).

#### 3.2.1.4 Geometry Calculation

Geometry calculation relies on field documentations such as a cruise report, where shot and receiver positions are saved as well as their intervals through survey design. Some errors related to static corrections and velocity analysis might result from a wrong geometry definition. So, after header definitions within their geometry calculations, QC should be done to avoid further errors, since these cannot be removed later (Gadallah & Fisher, 2009).

Geometry calculation is done by header uploading and defining shot and receiver intervals of the data acquisition regarding how seismic traces are going to be grouped. Thus, they can be displayed through various traces groups for different processing and QC purposes (Figure 3.14). Therefore, seismic traces can be defined by different types of geometric sorting (Dondurur, 2018). It is also important to mention offset as a term within survey design and therefore geometry calculation, since it defines the distance between source and receiver/receivers.





A group of seismic traces expressing propagation from their common single shot point to all receiver points can be displayed by a common-shot gather (CSG) (Figure 3.14.A). Similarly, a common-receiver gather (CRG) shows the propagation of a group of seismic traces from all shot points where they recorded at a common receiver point (Figure 3.14.B). In multichannel seismic acquisition, numerous seismic traces are reflected from the same midpoints. A common-depth point gather (CDP) displays those common reflection points of a group of seismic traces propagated between different shots and different receivers (Figure 3.14.C). A common-offset section (Figure 3.14.D), also known as a single trace section, gives information about a group of seismic traces recorded at the same channels having common offset from all shot points. A stack section (Figure 3.14.E) shows a group of seismic traces stacked all traces at their associated CDP gathers by normal move out correction (explained in chapter 3.2.5).

Figure 3.14 The schematic illustration of different group of trace gathers for CSG (A), CRG (B), CDP (C), common offset section(D), and stack section (E) within their ray paths between shot (red flags) and receiver points (blue triangles), modified from Dondurur (2018).

Since conventional seismic data is processed in midpoint-offset coordinates, shot-receiver coordinates must be transformed by sorting the recorded data. That can be called CDP sorting or CMP sorting in case ray paths are reflected on a flat interface (Figure 3.15). However, in reality, there are reflection events from dipping surfaces, where CDP gather is not equivalent to CMP gather (Figure 3.16). Thus, they should be called as CMP gather (Yilmaz, 2001).

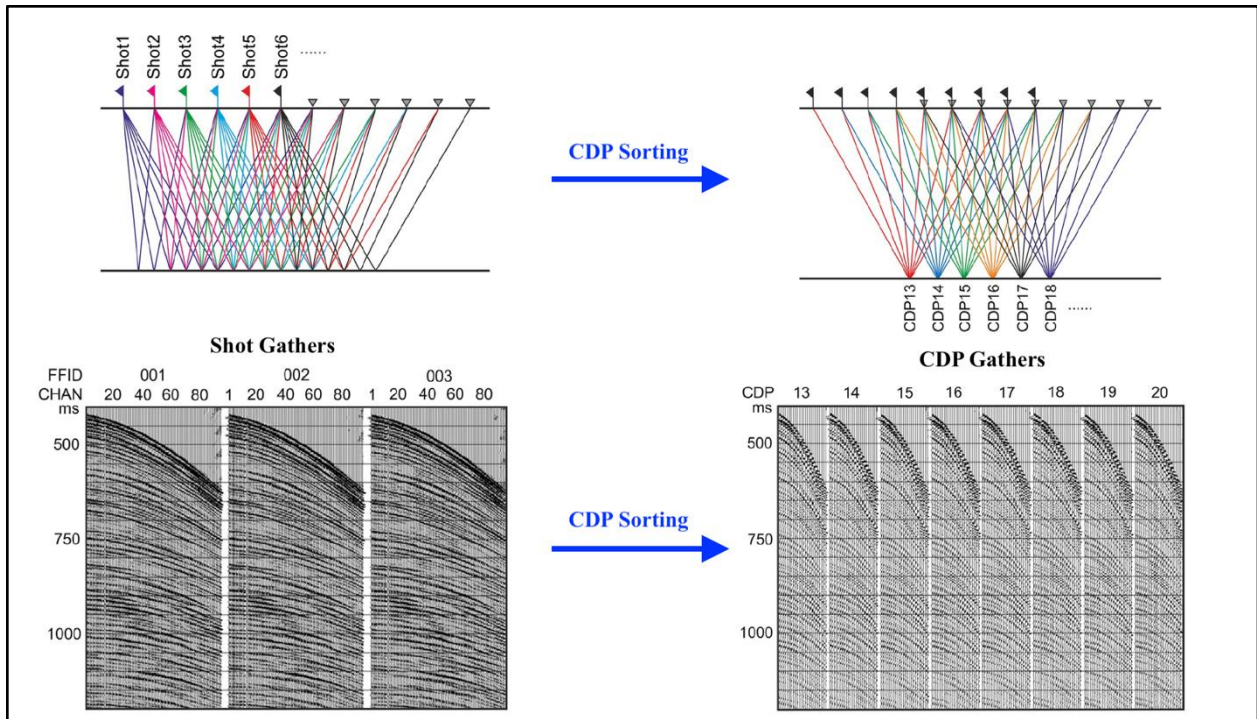


Figure 3.15 The illustration of CDP sorting reveals how trace geometry changes with a flat reflector. Ray paths for shot gathers and their records in the left before CDP sorting; ray paths for CDPs and their constructed CDP gathers to the right, modified from Dondurur (2018).

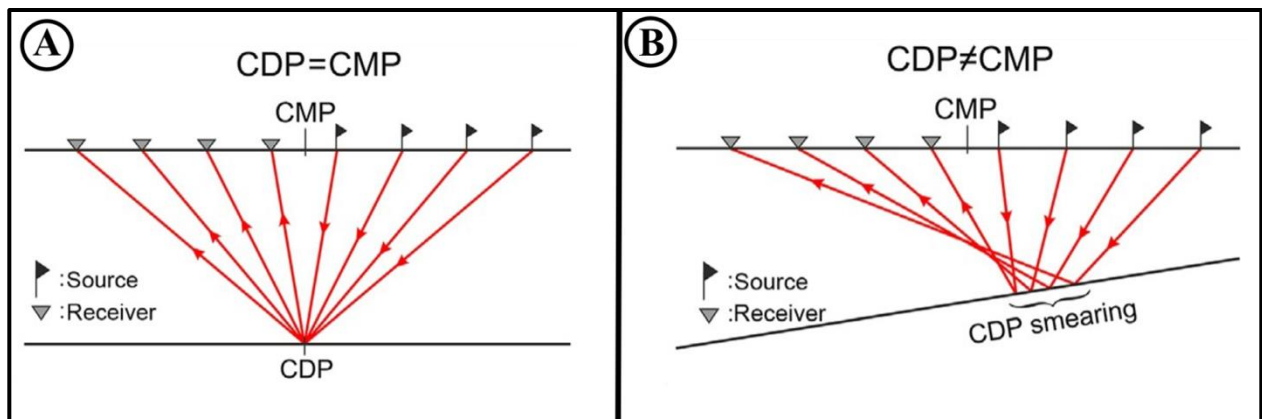


Figure 3.16 The schematic illustration of ray paths for CMP gathers with a flat surface where  $CDP = CMP$  (A) and dipping surface where  $CDP \neq CMP$  due to CDP smearing, modified from Dondurur (2018).

In order to complete a CDP calculation, the fold numbers should be calculated from information of survey geometry. The fold refers to the number of traces on a common-mid point gather. Maximum fold calculation for a 3D seismic survey is done by:

$$\text{Maximum Fold Number} = \text{Inline Fold } (F_I) \times \text{Crossline Fold } (F_C) \quad (3.11)$$

and

$$F_I = \frac{\text{number of channels} \times \Delta_R}{2 \times \Delta_S} \quad (3.12)$$

where  $\Delta_R$  is group interval and  $\Delta_S$  is shot interval. It should be underlined that  $F_C$  is 1, for a 2D seismic marine acquisition. Number of channels per streamer is calculated by

$$\text{Number of channels per streamer} = \frac{\text{streamer length}}{\Delta_R} \quad (3.13)$$

### 3.2.1.5 Gain Recovery

The acquired seismic amplitudes contains reflection coefficients which are affected by several factors such as geometrical spreading, absorption and amplitude change vs offset. These sorts of phenomena influence the data by having inconsistent amplitudes in the shallow and deep part of the seismic traces along the time axis. For instance, amplitudes of early arrivals from shallow reflectors are higher than amplitudes from late arrivals. Gain recovery is applied in the processing to provide consistent amplitudes, which preserve the reflection coefficients, including information about the subsurface in both shallow and deep parts (Dondurur, 2018; Liner, 2016).

### 3.2.1.6 Spherical Divergence Correction

In a homogenous medium, an acoustic wave loses its energy (Figure 3.17) while propagating the square of distance from a source through the geometrical spreading of the wave fronts becoming larger (Gadallah & Fisher, 2009). The proportion of the energy density ( $E$ ) to the square of the amplitude ( $A$ ) by distance ( $r$ ) is

$$E(r) \propto A^2(r) \quad (3.14)$$

Amplitude as a function of distance is given by

$$A \propto \frac{1}{r} \quad (3.15)$$

and that can provide the amplitude variation by distance due to the spherical divergence effect by:

$$A_0 r_0 = A_1 r_1 \quad (3.16)$$

where  $A_1$  is the deducted amplitude by distance between  $r_1$  and  $r_0$  compared to  $A_0$  the amplitude at  $r_0$  distance from the source (Liner, 2016).

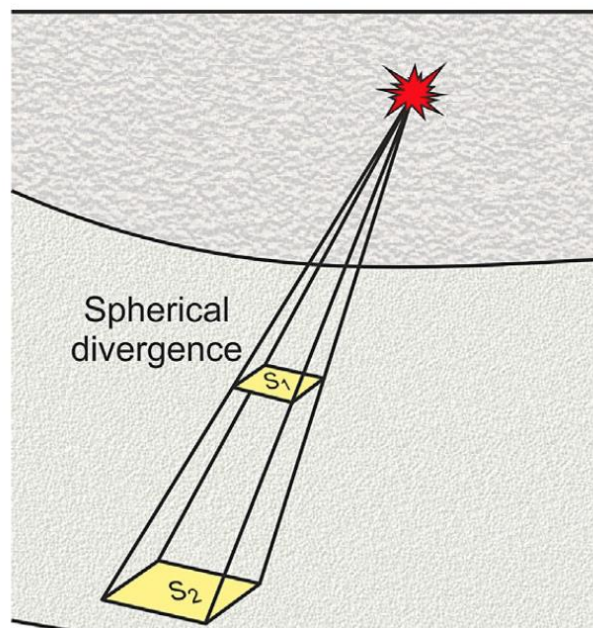


Figure 3.17 Amplitude reduction caused by spherical divergence. The energy density in different surfaces are represented by  $S_1$  &  $S_2$ , where  $S_1 < S_2$ , modified from Dondurur (2018).

Time raised to a power correction method was applied to recover this energy loss for the spherical divergence problem. The method operates a gain function ( $t^p$ ) to the samples of traces by multiplication of seismic amplitudes,



$$g(t) = (t^P) \quad (3.17)$$

Where  $t$  is the recording time of the sample and  $P$  is a constant which can be a positive or negative integer or real number. The amplitude is increased with time for  $P > 0$  and decreased with time for  $P < 0$ . For the positive numbers of  $P$ , it is suggested to be varied from 0.5 to 4.0 (Figure 3.18).  $t^P$  enhances the amplitudes of late arrivals for  $t > 1.0$ , while reducing the amplitudes of early arrivals for  $t < 1.0$ s (Dondurur, 2018).

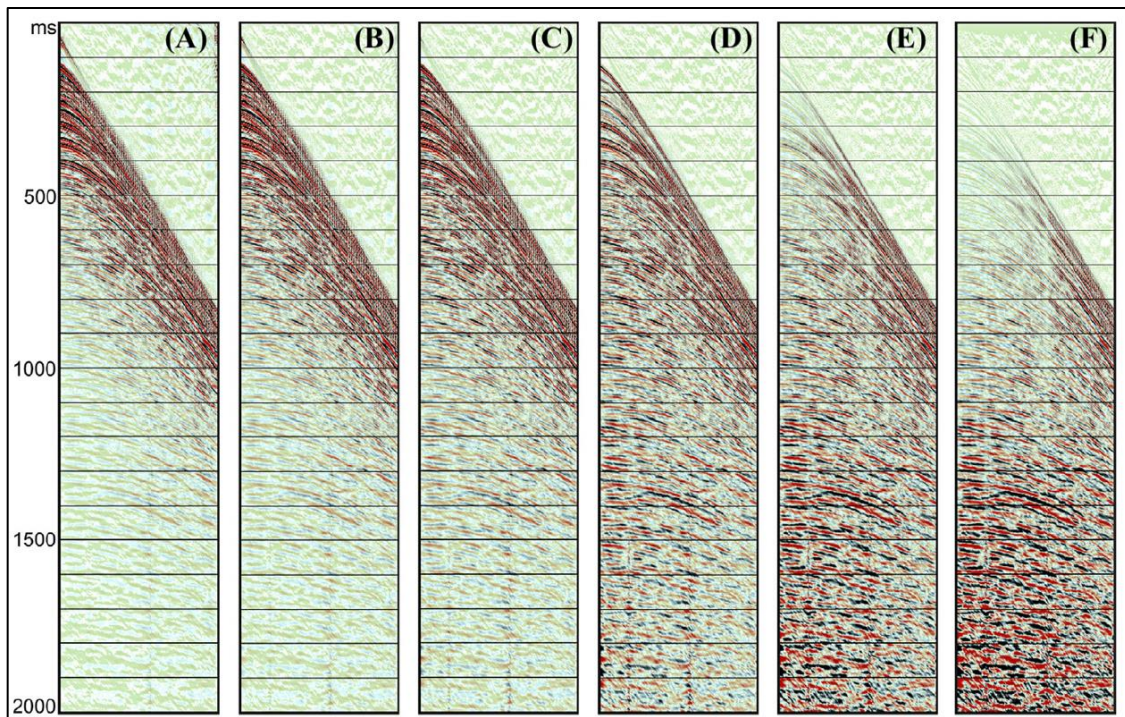


Figure 3.18 shows the amplitude changes by different  $t^P$  gain functions on shot gathers for  $P=0$  (A),  $P=0.5$  (B),  $P=1.0$  (C),  $P=2.0$  (D),  $P=3.0$  (E), and  $P=4.0$  (F), modified from Dondurur (2018).

### 3.2.1.7 Spatial Amplitude Smoothing

During the seismic processing, amplitudes of seismic noise may be burst as a side effect of any processing steps. For instance, correcting the spherical divergence problem also strengthens the amplitudes of seismic noise (CGGVeritas, 2008b). Therefore, spatial amplitude smoothing was

applied several times in different processing stages by the determined parameters and various operations such as with or without the noise attenuation option.

### 3.2.1.8 Band-pass Filtering

Swell noise, which is known as the dominant ambient noise type in recorded marine seismic data, consisting of large amplitude and low-frequency content, which should be attenuated in the pre-processing stage by a frequency filtering. Typical low-cut filter for swell noise attenuation should be applied from 4 to 8 Hz at 18 dB/Oct (Dondurur, 2018). Raw data also includes high frequency noise due to other vessels, ocean waves, wind and from operational noise, for instance streamer noise.

Therefore, band-pass filtering can be the most practical method to attenuate those type of noise by removing their undesired low and high frequencies, while keeping the frequencies between the specified cut-off values to improve the vertical resolution of the seismic data. Since both desired low and high frequencies rely on that improvement, band-pass filtering provides significant enhancement of the vertical resolution. However, the filtering should not be designed too narrow to prevent to lower the resolution (Yilmaz, 2001). It is applied by determining 4 cut-off frequencies (Figure 3.19.B) to set the slopes having a trapezoid-shaped band-pass range instead of box-car shaped (Figure 3.19.A). This reduces the Gibbs effects from the data (Dondurur, 2018).

Furthermore, the Butterworth band-pass filter (Figure 3.20) relies on low-cut ( $f_1$ ) and high-cut ( $f_2$ ) frequency values as well as two slope values ( $S_1$  and  $S_2$ ) which leads to a smooth tapering. In order to determine the frequency parameters for a band-pass filter, the data is converted from shot gathers to the amplitude spectrum by the Fourier transform (3.8). Once filtering is applied, the output is reconverted from the frequency domain to the time domain by the inverse Fourier transform (3.9) (Yilmaz, 2001).

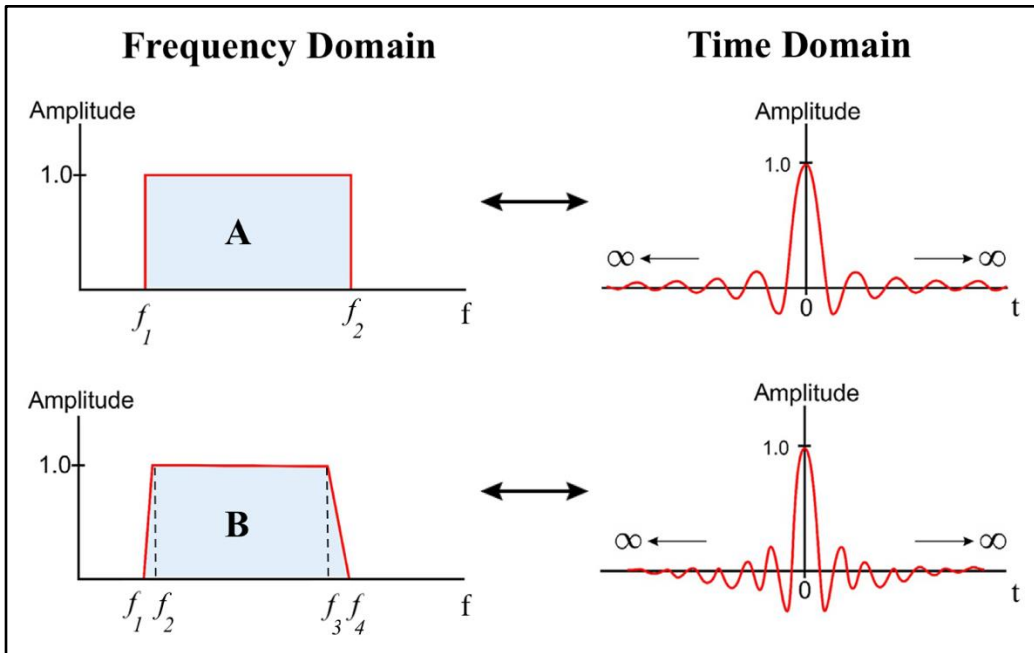


Figure 3.19 Comparison of band-pass filter design in the amplitude spectrum with box-car design (A) with 2 frequency limits and trapezoid-shaped design (B) with 4 frequency limits in the frequency domain. The impact of different designs in the time domain after Fourier transform to the right. Trapezoid-shaped design provides narrower filter operator in the time domain, modified from Dondurur (2018).

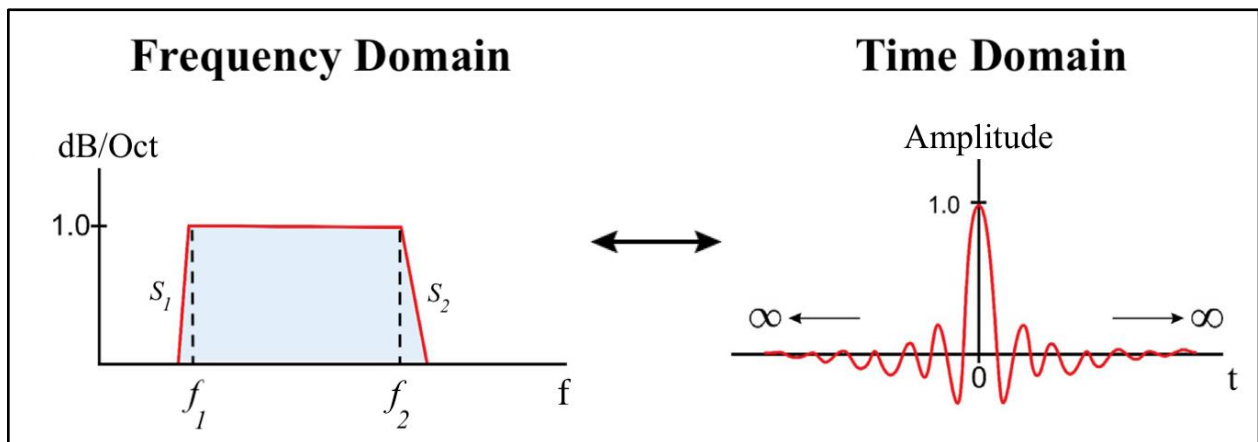


Figure 3.20 Schematic illustration shows the amplitude spectrum for trapezoid-shaped band-pass design by Butterworth requiring limits of 2 frequencies, and 2 slope values in the frequency domain, which impacts the waveform in the time domain, modified from Dondurur (2018).

### 3.2.1.9 Convolution

A waveform reshaped after a single filtering process includes noise as well. To define the alteration of shape caused by filtering effects, a mathematical operation is applied, named convolution. For example, a seismic source generates a seismic pulse that is used as a spike input in a filter, both in the ground and in the recording system (Figure 3.21) while generating an impulse response as output (Kearey et al., 2002).

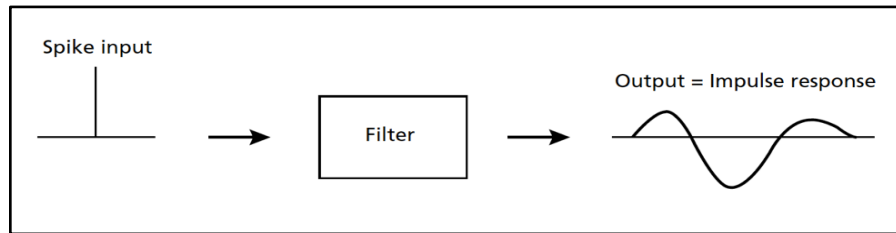


Figure 3.21 illustrates a spike input and its impulse response as an output through filtering, modified from Kearey et al. (2002).

In a mathematical operation, if this spike input as a function of a signal;  $g(t)$  convolves with a filter's impulse response  $f(t)$ , known as the convolution operator, the output from a filtered signal  $y(t)$  can be generated:

$$y(t) = g(t) \star f(t) \quad (3.18)$$

where the asterisk stands for the convolution operation. This is basically how a seismic trace is shaped by convolution of filtering with a signal from a source.

### 3.2.1.10 Deconvolution

Deconvolution is the inverse operation of convolution (given in 3.18), also known as inverse filtering (Kanasewich, 1981). If a signal's response output  $y(t)$  and its filter describing the earth's reflectivity in depth  $f(t)$  are known, the input waveform / wavelet  $g(t)$  can be recovered if  $y(t)$  is convolved with the deconvolution operator  $f'(t)$



$$g(t) = y(t) \star f'(t) \tag{3.19}$$

The substitution of the given equations (3.18) and (3.19) provides that

$$g(t) = g(t) \star f(t) \star f'(t) \tag{3.20}$$

where  $f(t) \star f'(t)$  can be replaced by a spike function  $\delta(t)$  given by

$$g(t) = g(t) \star \delta(t) \tag{3.21}$$

The spike function is a unit amplitude at zero time. If  $\delta(t)$  is convolved with a time function  $g(t)$ , it produces unchanged convolution output (Kearey et al., 2002). In seismic data processing, this unchanged convolution output is aimed to be obtained throughout the deconvolution of the spike function where the exact  $f(t)$  has a minimum delay. Perfect deconvolution is possible only if the filter has minimum delay property.

Briefly, deconvolution is applied to remove the parts of the source signal from the seismic trace recorded at a station. As a result, the seismic wavelet is compressed or replaced in the data while the multiple reflections are eliminated. Deconvolution both widens the amplitude in the frequency domain (Figure 3.22) and improves the vertical resolution (Dondurur, 2018).

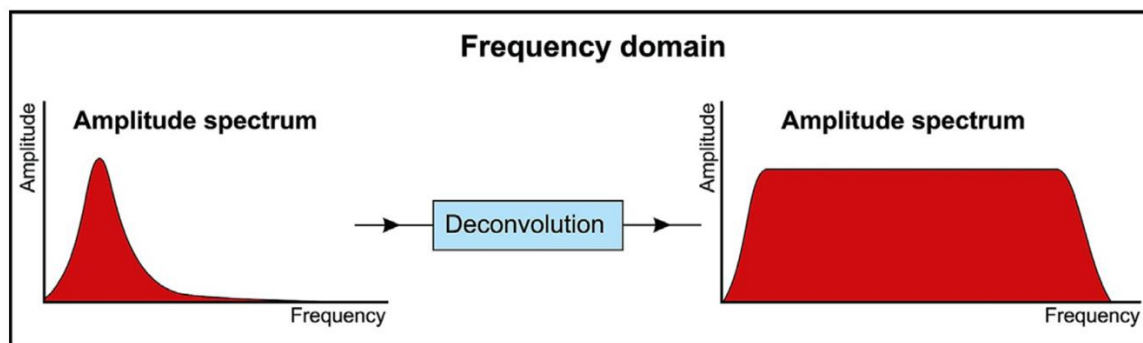


Figure 3.22 shows amplitude widening of deconvolution in the frequency domain, extracted from Dondurur (2018).

### 3.2.1.11 Signature Deconvolution

Signature deconvolution is applied to remove bubble noise, or bubble pulses, and the interference of ghost reflections from airgun signals, appearing as reversed polarity recurrent amplitudes on shot gathers and near trace sections. The signature deconvolution applied in this thesis was designed using statistical methods such as in predictive deconvolution to reshape the input wavelet which is the source signature extracted from the data. The operator length should be designed by reshaping the input wavelet into zero or minimum-phase wavelet as output in this deconvolution operation (Dondurur, 2018; Kearey et al., 2002). It is important to apply signature deconvolution to shot gathers in the pre-processing since the energy of the seismic source may change slightly from shot to shot during the acquisition.

### 3.2.1.12 $f$ - $x$ Projective Filtering

Incoherent noise, also known as random noise, lacks a systematic consistency between the traces, which can be specified such as swell noise, bird noise created by the depth controllers on the streamer, powerline interference, spikelike noise, marine mammals, and other marine vessels.  $f$ - $x$  projective filtering is used to attenuate those types of noise to preserve the signal quality in the frequency-space domain ( $f$ - $x$ ). The projective filtering separates the input signal by predicting it in  $x$  from non-predictable noise (or incoherent noise). The signal passes through the filter with 0 or 1 spectrum values, which ensures that the signal is preserved (Dondurur, 2018).

### 3.2.1.13 $f$ - $k$ Filtering

Coherent noise, such as swell noise or direct and diffracted waves appearing as linear events, can be simply removed by  $f$ - $k$  filters since distinguishing them related to their different dips in the frequency-wavenumber domain ( $f$ - $k$ ) is quite simple. Considering a seismic wavefront travelling at angle ( $\alpha$ ) to the horizontal surface,  $\alpha$  can be calculated from its traveling velocity ( $\mathcal{V}$ ) and the apparent velocity ( $\mathcal{V}_\alpha$ ) propagating across a spread of detectors (Figure 3.23.A) given by

$$\mathcal{G}_\alpha = \frac{v}{\sin \alpha} \quad (3.22)$$

Every sinusoidal component of the pulse along the spread direction has an apparent wavenumber ( $k_\alpha$ ) corresponding to the individual frequency ( $f$ ) given by

$$f = \mathcal{G}_\alpha \cdot k_\alpha \quad (3.23).$$

A  $f$ - $k$  plot for the pulse (Figure 3.23.B) creates a straight-line curve with an inclination of  $\mathcal{G}_\alpha$  (Kearey et al., 2002).

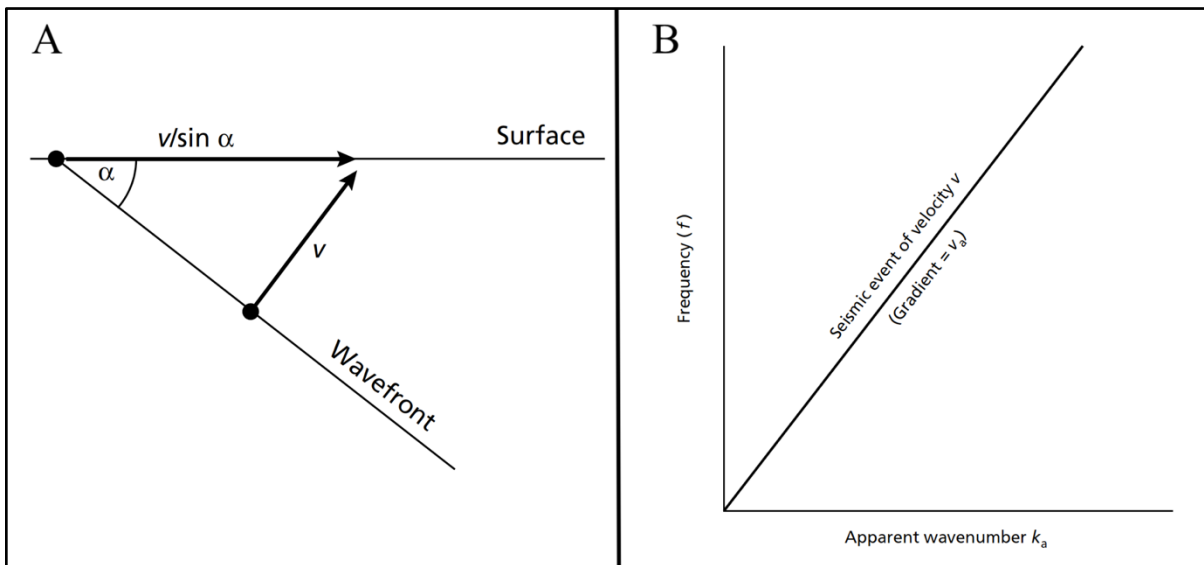


Figure 3.23 The schematic illustration of a seismic wavefront travelling with the velocity  $v$  and crossing the surface at an angle  $\alpha$  (A); its apparent velocity  $\mathcal{G}_\alpha$  in the  $f$ - $k$  plot (B), modified from Kearey et al. (2002).

Then, to analyze these dipping events and define the filtering limits in  $f$ - $k$  spectrum (Figure 3.24), the data is converted from the time-distance domain ( $t$ - $x$ ) to the  $f$ - $k$  domain by 2D Fourier transform. Once the filtering is done, the data is returned from the  $f$ - $k$  to the  $t$ - $x$  domain by the inverse Fourier transform.

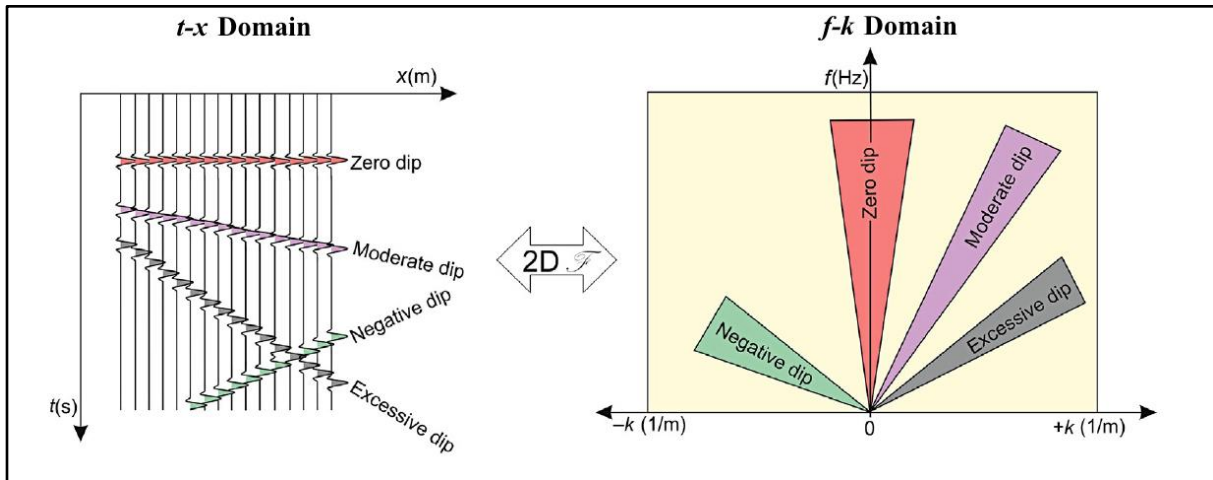


Figure 3.24 The various dipping events in the time-distance ( $t$ - $x$ ) domain and their correspondence in the frequency-wavenumber ( $f$ - $k$ ) domain by the 2D Fourier transform, modified from Dondurur (2018).

The  $f$ - $k$  spectrum is made up of negative and positive panels. Amplitudes of negative dipping events appear on the negative panel, while amplitudes of positive dipping events appear on the positive panel. However, certain dip values appear passing through the origin of the spectrum (Dondurur, 2018). Figure 3.25 illustrates the common events in marine seismic data both in the  $t$ - $x$  and the  $f$ - $k$  domains.

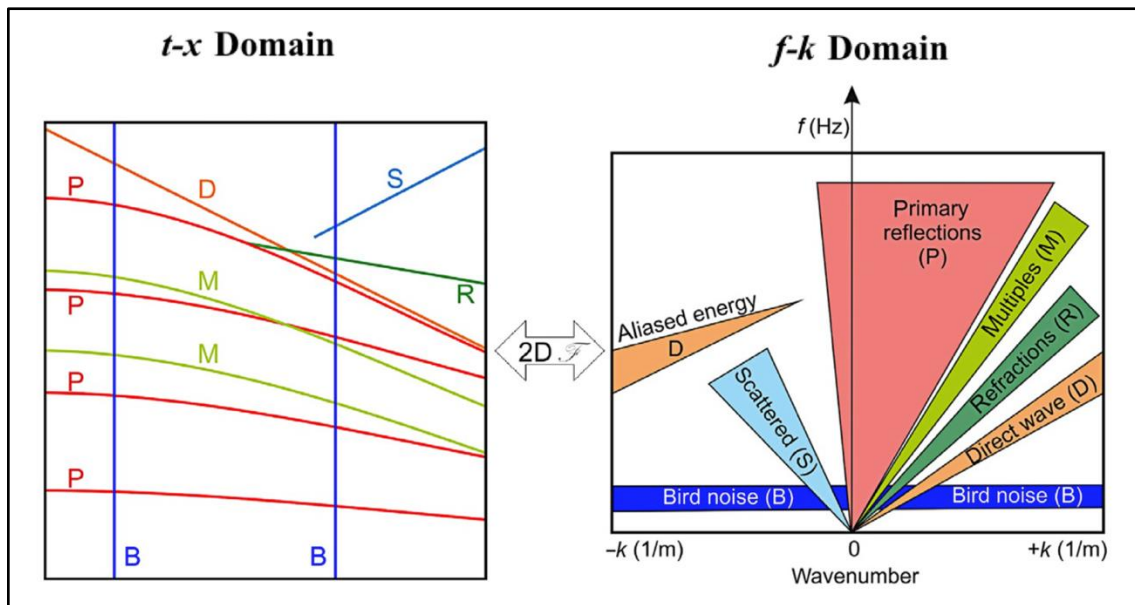


Figure 3.25 The schematic illustrations of reflection events and noise in the  $t$ - $x$  domain (left) and the  $f$ - $k$  domain (right) by 2D Fourier transform: P: primary reflection; D: direct wave; R: refracted wave; M: multiple reflections; B: bird noise; S: scattered (negative) dip events, modified from Dondurur (2018).

### 3.2.1.14 Single Trace Section

Single trace sections can be generated as common-offset gathers (Figure 3.26.A) by selecting a certain offset from every single shot gathers, either relying on near-offset or far-offset information. Since near-offset data have shorter arrival times than far-offset data owing to normal moveout (NMO) (Figure 3.26.B), common-offset gathers should be constructed using first channel information (near trace) from multichannel seismic data, especially during pre-processing application (Dondurur, 2018).

That procedure in this thesis was used during the data processing mostly for QC purpose in order to quickly display the near-trace sections after the major seismic processing applications. It is very beneficial to apply QC with a single trace section in some critical job folders to investigate the impact of the applied processing steps and their associated parameters, such as bandpass and  $f-k$  filters and gain recovery.

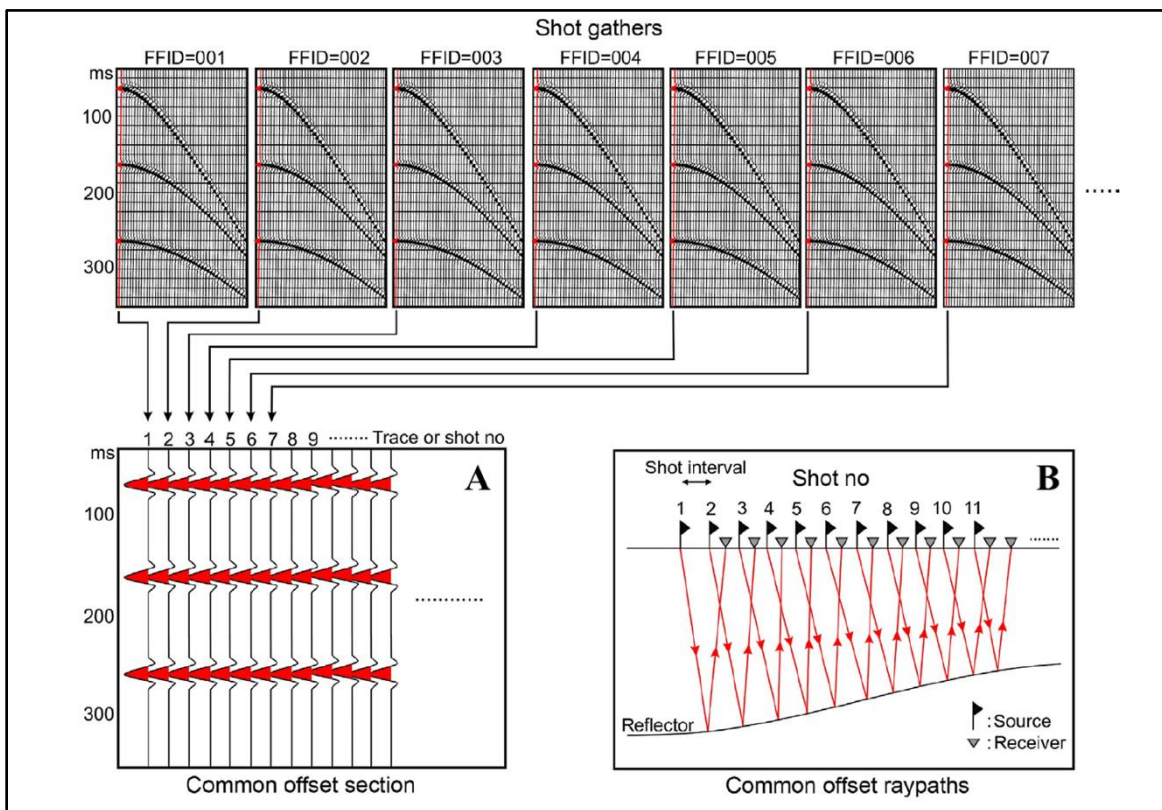


Figure 3.26 Schematic illustration shows a single trace section constructed by every shot gather (A); common minimum offset reflections and their ray paths (B), modified from Dondurur (2018).

### 3.2.2 2D Spatial Trace Interpolation

In this research, seismic traces in the CMP gathers have been spatially interpolated to improve the results from different processing approaches for multiple attenuation (chapter B.2) done by  $f$ - $k$  filtering and  $\tau$ - $P$  transforms since the higher number of traces in the CMP gathers would reduce the undesired effects of the sharp truncation in the data processing. The 2D spatial interpolation of a seismic traces only generates extra traces that does not recover the frequencies lost by the original sampling. However, it measures the defined dip for the unaliased frequencies and applies the dip information to interpolate both aliased and unaliased frequencies. Therefore, in addition to the dip information, interpolation also relies on the frequency threshold for spatial aliasing (CGGVeritas, 2008b; Yilmaz, 2001).

### 3.2.3 Muting

The amplitudes of various types of noise can be removed in seismic data with multiplication by 0 throughout the defined arrival times for undesired areas. Muting may be applied several times to the seismic data processing with different muting methods (Dondurur, 2018).

#### 3.2.3.1 Inner and Top Mutes

Inner mute, also known as *tail mute*, is applied to data to remove ground rolls (in land seismic) having low apparent velocities. Top mute, also known *external* and *outer mute*, is used to remove first arrivals from the seismic data. Top mute is a common term in marine seismic studies to remove the undesired first arrivals above seabed such as direct and refracted waves. It zeroes out all amplitudes before the seabed arrival time (Figure 3.27.A). Unless top muted is applied to those arrivals in pre-processing, they can impact velocity analysis for the velocity of seabed reflections. Top mute can also be applied to the data in different processing sequences such as before stacking process and after migration process (Dondurur, 2018; Zhou, 2014).



### 3.2.3.2 Surgical Mute

The particular noisy zones inside the dataset can be muted out by a designed polygon (Figure 3.27.B). Since this muting method is surgically applied to undesired zone in the shot or CDP gathers, it is called as surgical mute as well as polygon mute. Even though the surgical muting approach is effective due to the precise application into undesired portion of the whole data, it might also mute the significant reflection events within the mute zones (Dondurur, 2018; Zhou, 2014).

### 3.2.3.3 NMO Stretch Mute

In order to prevent the NMO stretching (explained in chapter 3.2.5.1), NMO stretch muting is automatically applied to the frequency disruption zone (Figure 3.27.C) during the NMO correction in CDP gathers, where early arrivals of far-offset traces are muted out (Dondurur, 2018).

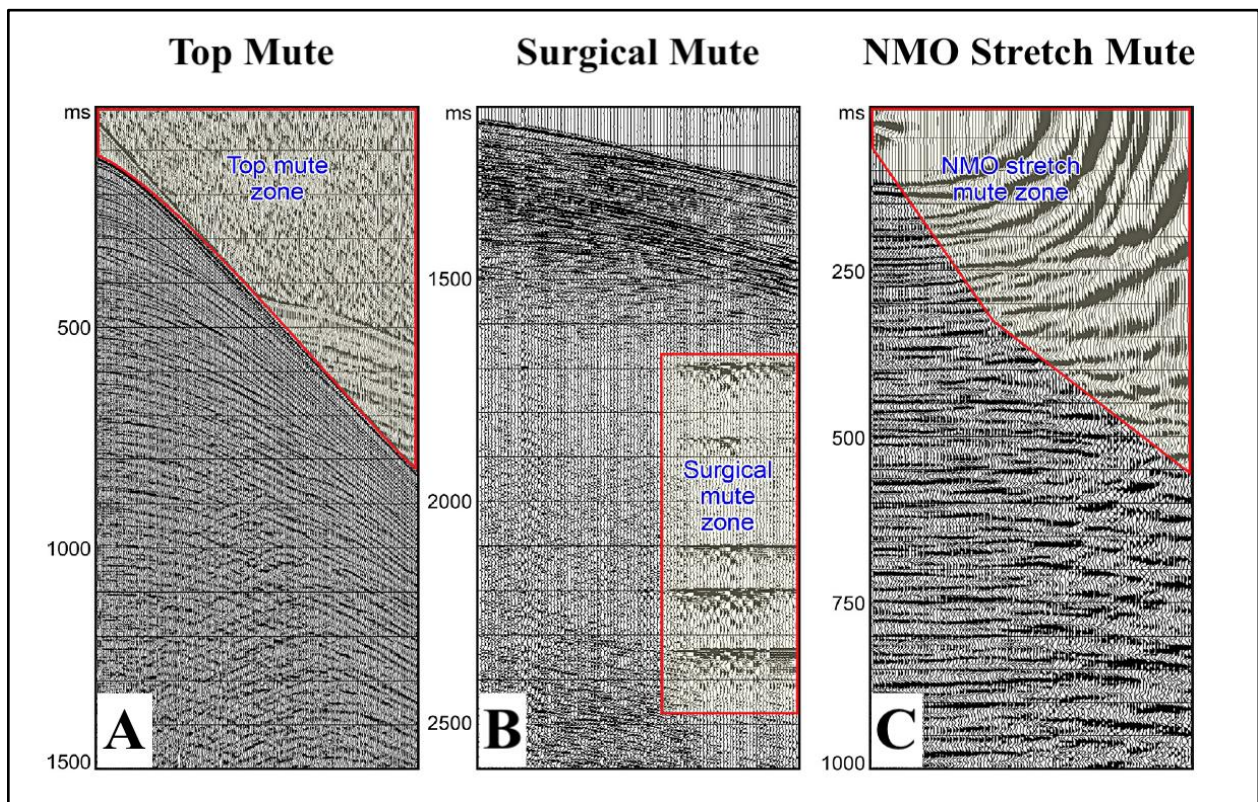


Figure 3.27 The different muting applications are shown in shot and CDP gathers as examples: top (external) muting (A), surgical (tail) muting (B) and NMO stretch muting (C), modified from Dondurur (2018).

### 3.2.3.4 Top Mute from Incidence Angle

The incidence angles larger than the critical angles at reflectors distorts the waveform of seismic reflections due to phase shifts. The distorted reflections can be attenuated by the top muting the traces using their incidence/critical angles, where the larger reflection angles than the incidence angle are removed.

## 3.2.4 Seismic Velocity Modelling & Analysis

### 3.2.4.1 Types of Seismic Velocity

The velocity in seismic usage means the propagation rate in time of a seismic wave relying on the properties of a medium. Thanks to the velocities of the mediums, depth, dip and horizontal locations can be identified. The velocity may vary for the same rocks in different locations due to frequency of the seismic signal during the acquisition, lithology, temperature, density, age, saturation, fluid type, fractures, pore shape and pressure and consolidation of the rocks. There are several terms for the seismic velocity related to seismic data processing (Sheriff, 2002).

**Instantaneous Velocity:** It is speed of measured at specific location by given differentiations of the depth (h) regarding the one-way travel time (t) defined by

$$V_{ins} = \frac{dh}{dt} = \frac{h_2 - h_1}{t_2 - t_1} \quad (3.24)$$

where  $V_{ins}$  is the instantaneous velocity.  $h_2$  and  $h_1$  are the different depths of reflector locations whereas  $t_2$  and  $t_1$  their associated times (Dondurur, 2018).

**Average Velocity:** If a seismic velocity in a marine surface survey is measured by the ratio of the distance from the sea surface to the target, its average velocity is given by

$$V_{ave} = \frac{h_1 + h_2 + h_3 + \dots + h_n}{t_1 + t_2 + t_3 + \dots + t_n} = \frac{\sum h_i}{\sum t_i} \quad (3.25)$$



where  $h_i$  is the total thickness of the layers and  $t_i$  is the total travel time (one-way) for each layer (Dondurur, 2018).

**Interval Velocity:** It is the average velocity of the  $n$  number of the interfaces, usually over a single layer. It can be measured for the  $n$ th interval by  $V_{RMS}$ , which uses the DIX' formula that is

$$V_{int, n} = \sqrt{\frac{(V_{RMS, n}^2 t_n) - (V_{RMS, n-1}^2 t_{n-1})}{t_n - t_{n-1}}} \quad (3.26)$$

where  $V_{int, n}$  is the interval velocity between the  $(n-1)$ th and  $n$ th reflection.  $t_n$  and  $t_{n-1}$  reflected ray travel times and  $V_{RMS, n}$  and  $V_{RMS, n-1}$  are the RMS velocities for the  $n$ th and  $(n-1)$ th reflectors (Kearey et al., 2002).

**Root-Mean-Square (RMS) Velocity:** It is obtained from the velocity analysis used in NMO correction.  $V_{RMS}$  for the  $n$  number of layers can be given by

$$V_{RMS, n} = \sqrt{\frac{\sum_i^n V_i^2 t_i}{\sum_i^n t_i}} \quad (3.27)$$

where  $V_i$  is the interval velocity and  $t_i$  the one-way travel time for the number of  $n$  layer.  $V_{RMS}$  is a few percentage greater than the corresponding  $V_{ave}$  (Dondurur, 2018; Sheriff, 2002).

**NMO (or Stacking) Velocity:** The velocity for the normal-move out correction (explained in 3.2.5) is applied to CDP gathers to correct the traces to zero-offset time before the stacking

$$V_{NMO} = \sqrt{\frac{x^2}{t_x^2 - t_0^2}} \quad (3.28)$$

where  $t_x$  is the TWT time and  $t_0$  is the zero-offset time of a reflected signal corresponding to the same offset  $x$ . RMS velocity can be used as NMO velocity for isotropic horizontal layers in theory (Dondurur, 2018; Sheriff, 2002) given by

$$V_{NMO} \approx V_{RMS} \quad (3.29).$$

### 3.2.4.2 Velocity Modelling

In general sense, a seismic velocity model is generated to map depth and thickness of interpreted subsurface layers by velocity information from both seismic data and well logs. Thanks to the velocity model of target area subsurface geology can be imaged more accurately after the seismic data processing (AlAli & Anifowose, 2022; Zhou, 2014).

In this research, velocity models are generated for different purposes by calculated the RMS velocity from estimated interval velocity of refracted waves and the RMS velocity from velocity analysis. Before the velocity analysis the model has been generated for QC purpose to evaluate the model visually whether the CDP gathers are ready for the analysis. The most reliable velocity model can only be provided by an accurately obtained RMS velocities from the velocity analysis.

### 3.2.4.3 Velocity Analysis

Velocity analysis is necessary to gather RMS velocities from picked velocities in semblance plot to use in an adequate NMO correction as input, which provides correct stacking velocities as a function of reflection time. The velocity analysis also enables us to achieve a reliable subsurface velocity model from multichannel seismic data (Dondurur, 2018; Kearey et al., 2002).

Velocity analysis is done in semblance plots, which are generated from the CDP gathers, by picking the velocity of primary reflections. During velocity picking on the semblance plots, it should be taken into consideration to avoid the picking velocities of multiples which otherwise would become stronger after the stacking sequence. Multiples can be easily ignored as their velocities lower than the primary reflections. For instance, the velocity of long period multiples

such as surface-related multiples can be assume between 1480 and 1500 m/s due to the ray travel path in the water column. In case of obvious enhancement for S/N ratio in the autocorrelation sections (explained in 3.2.7.1) after a multiple suppression method, velocity analysis can be applied more than one time to seismic data, which can enable us to generate more accurate velocity model (Dondurur, 2018).

### 3.2.5 NMO Correction

In recorded seismic data, time differences occur between the receivers along the residual offset distance which must be moved to their original time by normal moveout (NMO) correction before stacking the traces. Since the NMO correction can be explained as the function of the two-way travel time ( $t_0$  and  $t_x$ ), velocity ( $V_{RMS} \approx V_{NMO}$ ) and depth ( $z$ ), the reflection time (TWT) of a wave from a single horizontal layer should be taken into consideration at first. The two-way travel time ( $t_x$ ) of the reflected wave at an offset distance  $x$  previously given in equation (3.2) can also be written as

$$t_x^2 = \frac{x^2}{V^2} + \frac{4z^2}{V^2} \quad (3.30).$$

Moreover, the two-way vertical travel time ( $t_0$ ) of the reflected wave at zero-offset ( $x = 0$ ) can be found

$$t_0 = \frac{2z}{V} \quad (3.31).$$

The equation (3.31) can be replaced in the equation (3.32)

$$t_x^2 = \frac{x^2}{V^2} + t_0^2 \quad (3.32).$$

Therefore, NMO at the offset  $x$  can be described as the difference in travel time ( $\Delta t_{NMO}$ ) (Figure 3.28) given by

$$\Delta t_{NMO} = t_x - t_0 \quad (3.33)$$

and the equation (3.32) can be replaced in (3.33) which gives

$$\Delta t_{NMO} = \sqrt{\frac{x^2}{V^2} + t_0^2} - t_0 = \sqrt{\frac{x^2}{V_{NMO}^2} + t_0^2} - t_0 \quad (3.34)$$

that corrects the time shifting on the offsets to their corresponding zero-offset time (Kearey et al., 2002). RMS velocities from the picked velocities during velocity analysis are used in the NMO correction. If these obtained RMS velocities are higher than their real values, the NMO under-corrects the trace by bending downwards. On the contrary, the traces are over-corrected with NMO by bending upwards if the lower RMS velocities are applied.

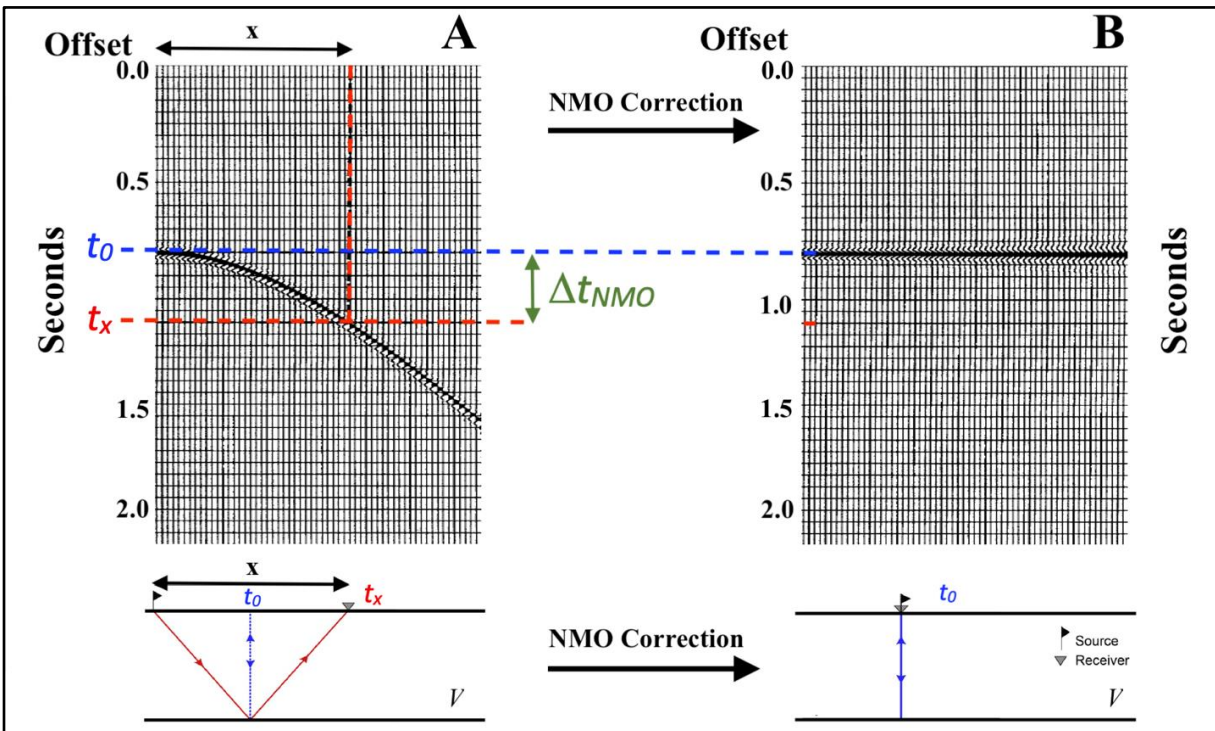


Figure 3.28 The illustration of a reflected wave from a single horizontal layer yielding a time-distance curve in the CMP gathers due to the time difference ( $\Delta t_{NMO}$ ) along the increasing offset (A); results after the NMO correction (B), modified from Dondurur (2018); Yilmaz (2001).

Furthermore, to obtain the NMO time for a single dipping reflector (Figure 3.29), travel time for a dipping reflector model can be expressed by the Levin equation

$$t_x^2 = \frac{x^2 \cos^2 \Phi}{V^2} + t_0^2 \quad (3.35)$$

where  $\Phi$  is inclination angle of the dipping reflector and  $V$  is the velocity of the upper medium (Yilmaz, 2001). From equation (3.33),  $\Delta t_{NMO}$  can be expressed as

$$\Delta t_{NMO} = \sqrt{\frac{x^2 \cos^2 \Phi}{V^2} + t_0^2} - t_0 = \sqrt{\frac{x^2 \cos^2 \Phi}{V_{NMO}^2} + t_0^2} - t_0 \quad (3.36).$$

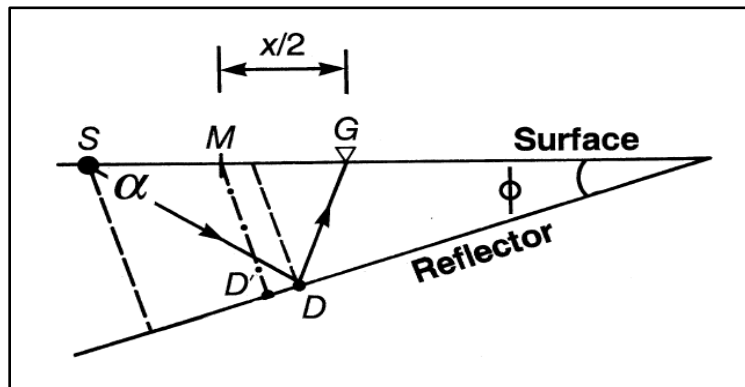


Figure 3.29 The illustration of NMO geometry for a single dipping reflector. SDG is the nonzero-offset ray path from source (S) to reflection point (D) and to receiver (G), normal incidence ray path MD' at midpoint M.  $\alpha$  is the incidence angle  $\Phi$  is inclination angle of the dipping reflector, extracted from Yilmaz (2001).

### 3.2.5.1 NMO Stretch

After NMO correction, a frequency distortion occurs in the shallow parts of the CDP gathers, which is called NMO stretching. The frequency distortion leads to lower frequency contents of the traces in the far off-set, which can also be compared between before and after the NMO correction for the dominant periods  $t_A$  and  $t_B$ , respectively in Figure 3.30. Briefly, the NMO stretching has higher impact on far-offsets than near-offsets. Therefore, early arrivals of the far-offset traces are automatically removed from the data by NMO stretch mute, which leads to NMO stretch mute gap at the start-of-line in a stack image (Dondurur, 2018).

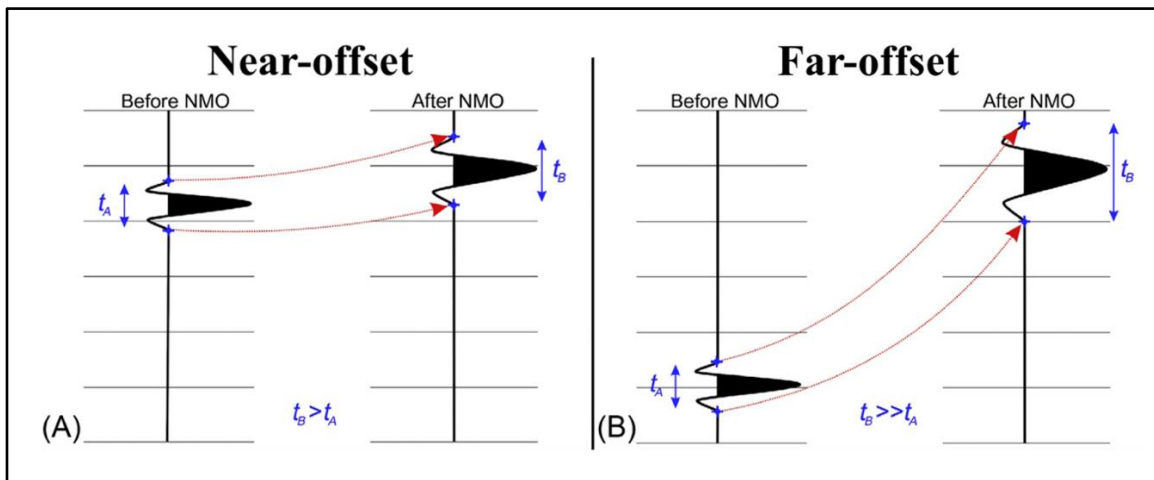


Figure 3.30 The schematic illustrations of the NMO stretching impact after the NMO correction in near-offset (A) and far-offset (B) in the CDP gathers.  $t_B > t_A$  in near-offset and  $t_B \gg t_A$  in far-offset, modified from Dondurur (2018).

### 3.2.6 Multiple Modelling and Extraction

Surface-related multiples can be modelled by a forward modeling approach where the source signature and the surface reflectivity are estimated by an iterative inversion process (deconvolution). Then, all surface-related multiples can be modelled in the time domain by convolving the total down-going primary response with the subtraction of the reflected total response from the original source signature which is given by Verschuur (2013). However, the surface-related multiple dataset can be obtained and subtracted from the original dataset by alternative approaches to the wave field multiple modeling explained above, such as multiple extraction and subtraction in the  $z-p$  domain by predictive deconvolution (**Error! Reference source not found.**), extracting multiple-free dataset in  $f-k$  filtering (6.2B.2.4), multiple extraction within  $f-k$  filtering and adaptively subtraction them from the recorded data (Dondurur, 2018; Verschuur, 2013).

For the subtraction, a dataset keeping the multiple reflections should be obtained by either modelling or extraction. To extract a group of traces keeping only the surface-related multiples, an  $f-k$  filter can be utilized with NMO corrected dataset, where the hyperbolas of the multiples are bent downwards, while the reflection hyperbolas of the primaries are bent upwards in the

CDP gathers. That can be achieved by applying a predicted velocity percentage of picked velocities from the spectrum. Then next, velocities of the primaries and multiples can be estimated in a  $f-k$  spectrum to design a filter polygon where the velocity of the primary events are removed, while the velocity of the multiples are passed. Therefore, the dataset keeps only the multiples.

### 3.2.7 Adaptive Subtraction

Sea surface-related multiples can be attenuated by several subtraction methods, such as subtraction in the  $\tau$ - $P$  domain or subtraction in the time domain by least-square approaches. Attenuation of the multiples can be done by a simple subtraction (Figure 3.31.C), or adaptive subtraction (Figure 3.31.D) of the predicted multiples in a modelled dataset (Figure 3.31.B) from reflection events in a recorded dataset (Figure 3.31.A). In case of the simple subtraction, the energy may be even larger than the energy in the subtracted input data. Thus, the preferred adaption might be the one which synchronizes the energy differences between the model data and recorded data before the subtraction. Therefore, adaptive subtraction is a two-step iterative procedure (Verschuur, 2013; Yilmaz, 2001).

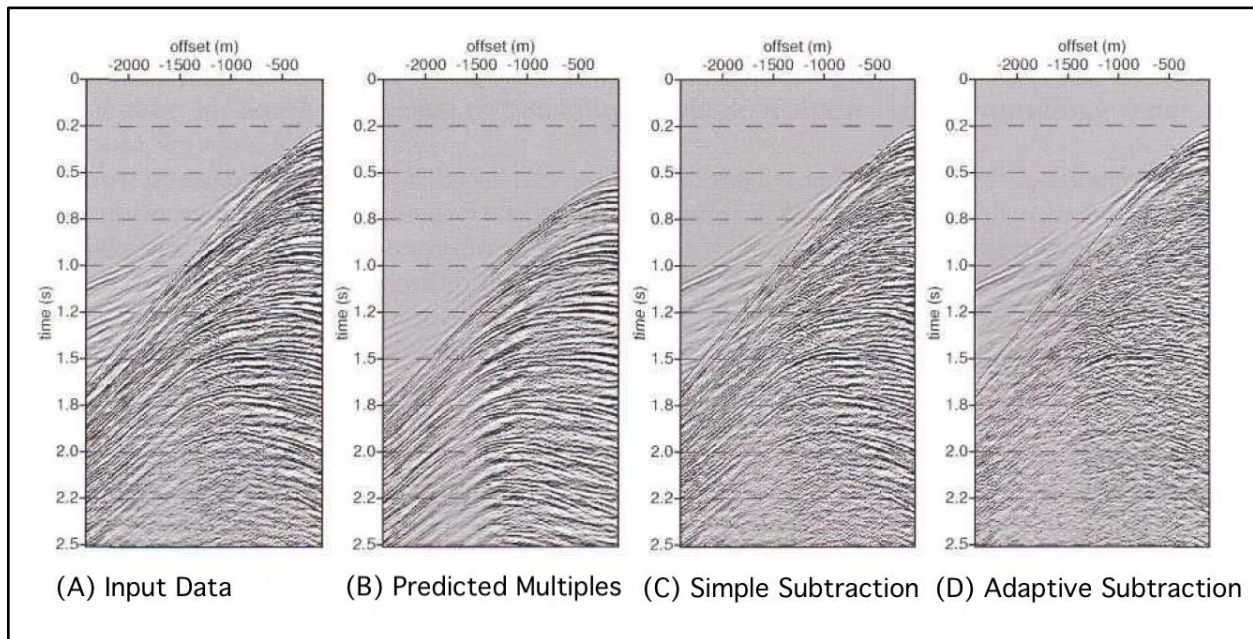


Figure 3.31 The illustration of a simple subtraction and an adaptive subtraction of a predicted multiples from an input data in shot gathers acquired offshore Scotland, modified from Verschuur (2013).

Modelled data may have different amplitudes, frequencies and phases compared to the recorded data. There may be several steps as components of the subtraction method can be applied to model multiple data in order to adapt those differences between the model and the recorded data. The energy difference in the unscaled model dataset is minimized in the least-square approach as a first step of two-step iterative process where the energy difference is minimized in the time domain given by

$$E_{min} = \sum_{x_r, x_s, t} [P(x_r, x_s, t) - a(t) \star M(x_r, x_s, t)]^2 \quad (3.37)$$

where  $x_r$  and  $x_s$  are the (discrete) receiver and source positions of the seismic traces.  $P(x_r, x_s, t)$  represents the original dataset having both multiple and primary reflections. The asterisk stands for the multi-dimensional convolution operation between the match operator  $a(t)$  and the unscaled multiples  $M(x_r, x_s, t)$ . The operator can be expressed by source and receiver energy transfer functions as frequency in a diagonal matrix (Verschuur & Berkhout, 1997). In the second step of the two-step iterative procedure, adapted multiple model data by multi-dimensional convolution of the operator can be adaptively subtracted from the input dataset in the time domain given by

$$P_0^{(i)}(x_r, x_s, t) = P(x_r, x_s, t) - a(t) \star M(x_r, x_s, t) \quad (3.38)$$

and the deconvolution of the operator with the unscaled multiple dataset gives the adapted multiple dataset  $M_0^{(i)}(x_r, x_s, t)$  given by

$$M_0^{(i)}(x_r, x_s, t) = a(t) \star M_0(x_r, x_s, t) \quad (3.39)$$

and this can be replaced in the given subtraction (3.38) that

$$P_0^{(i)}(x_r, x_s, t) = P(x_r, x_s, t) - M_0^{(i)}(x_r, x_s, t) \quad (3.40)$$

where  $P_0^{(i)}(x_r, x_s, t)$  is the adaptively subtracted input dataset (Figure 3.31.D) (Verschuur, 2013).



### 3.2.7.1 Autocorrelation to Adaptive Subtraction for QC

The effectiveness of the different sort of multiple attenuation applications, such as deconvolution,  $f$ - $k$  filtering in NMO-corrected CMP gathers and adaptive subtraction can be analyzed by CDP gathers, autocorrelation and brute-stack sections (explained in 3.2.9.1). To be able to analyze the autocorrelated outputs of the adaptive subtraction in this study, autocorrelation should be explained.

To comprehend autocorrelation, firstly, the cross-correlation of two digital waveforms should be expressed briefly. The individual elements of the waveforms are cross-multiplied by each other's elements by sliding one waveform over the other one using a time shift, called lag  $\tau$ . Then, these cross-multiplication products are summed. The cross-correlation as a function of the lag value is given by

$$\phi_{xy}(\tau) = \sum_{i=1}^{n-\tau} x_{i+\tau}y_i ; (-m < \tau < +m) \quad (3.41)$$

where  $x_i$  and  $y_i$  are the finite length of the two waveforms of finite lengths, which can be  $i = 1, 2, \dots, n$ . Tau ( $\tau$ ) is the lag and  $m$  is the maximum lag value of the function (Kearey et al., 2002).

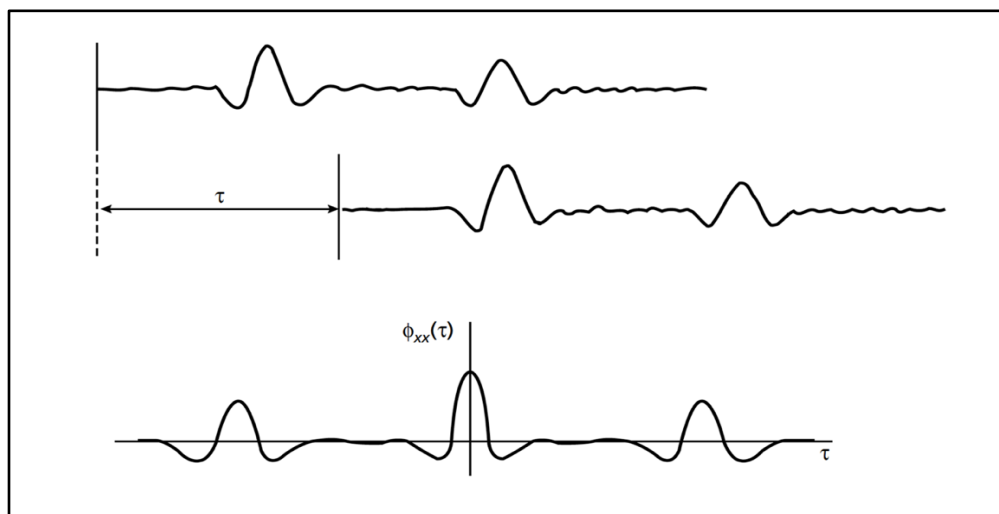


Figure 3.32 Illustrates the autocorrelation of a waveform producing a symmetrical waveform about zero lag ( $\tau$ ). As it seems the maximum value for the products of autocorrelation is at  $\tau=0$ , extracted from Kearey et al. (2002).

Autocorrelation is a cross-correlation of an input function with itself. An autocorrelation as a function of the lag value is symmetrical about zero-lag (Figure 3.32) because it produces a zero-phase waveform. It is therefore a commutative operation given by

$$\phi_{xx}(\tau) = \phi_{xx}(-\tau) = \sum_{i=1}^{n-\tau} x_{i+\tau}x_i ; (-m < \tau < +m) \quad (3.42)$$

where  $\tau$  is operation lag. In the case of minimum lag ( $\tau=0$ ), the maximum value of the autocorrelation is preserved (Figure 3.33), which is significant for the QC purposes to obtain exact autocorrelation efficiency (Dondurur, 2018).

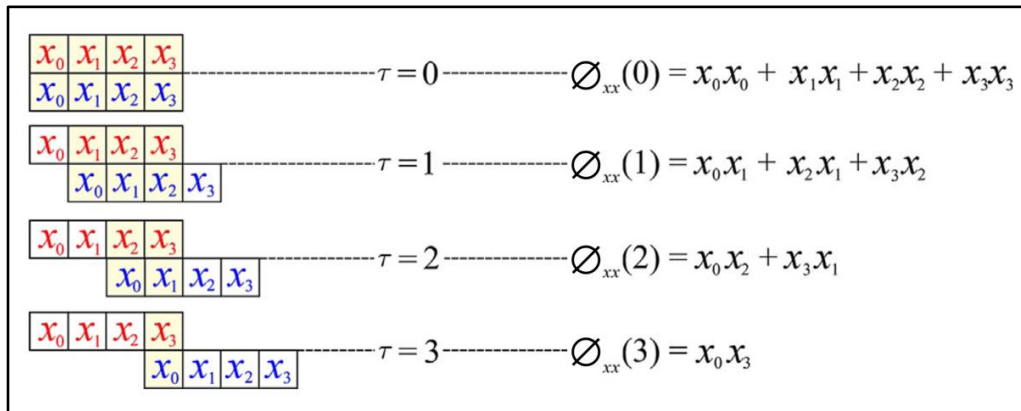


Figure 3.33 The schematic illustration of an autocorrelation operation of a given function with 4 elements. The autocorrelated products from minimum lag to maximum are represented, modified from Dondurur (2018).

### 3.2.8 DMO Correction

Reflection points shift upslope along the dipping subsurface leading to CDP smearing, where CMP gathers do not coincide (Figure 3.16), and limitation by DIX' formula that  $V_{NMO}$  cannot be correctly converted to  $V_{int}$ . To overcome this dipping issue, pre-stack migration or dip moveout (DMO) correction is applied. DMO is also called pre-stack partial migration. If pre-stack migration is not preferred during the seismic data processing, DMO correction is applied to CMP gathers, which moves the reflection events along the dipping layer to their correct zero-offset distances

(Dondurur, 2018; Liner, 2016). Practically, the reflections located at the source-receiver mid-point position are moved to their true zero-offset distances displayed in Figure 3.34.

If the equality  $\sin^2 \Phi + \cos^2 \Phi = 1$  is substituted in the previously given Levin equation (3.35), it can be divided into 2 parts representing NMO and DMO terms expressed by

$$t_x^2 = \underbrace{t_0^2}_{\text{NMO}} + \underbrace{\frac{x^2 \sin^2 \Phi}{v^2}}_{\text{DMO}} \quad (3.43)$$

where  $\Phi$  is inclination angle of the dipping reflector and  $V$  is the velocity of the upper medium. First NMO and then DMO correction can be applied to seismic data using equation (3.35) (Dondurur, 2018).

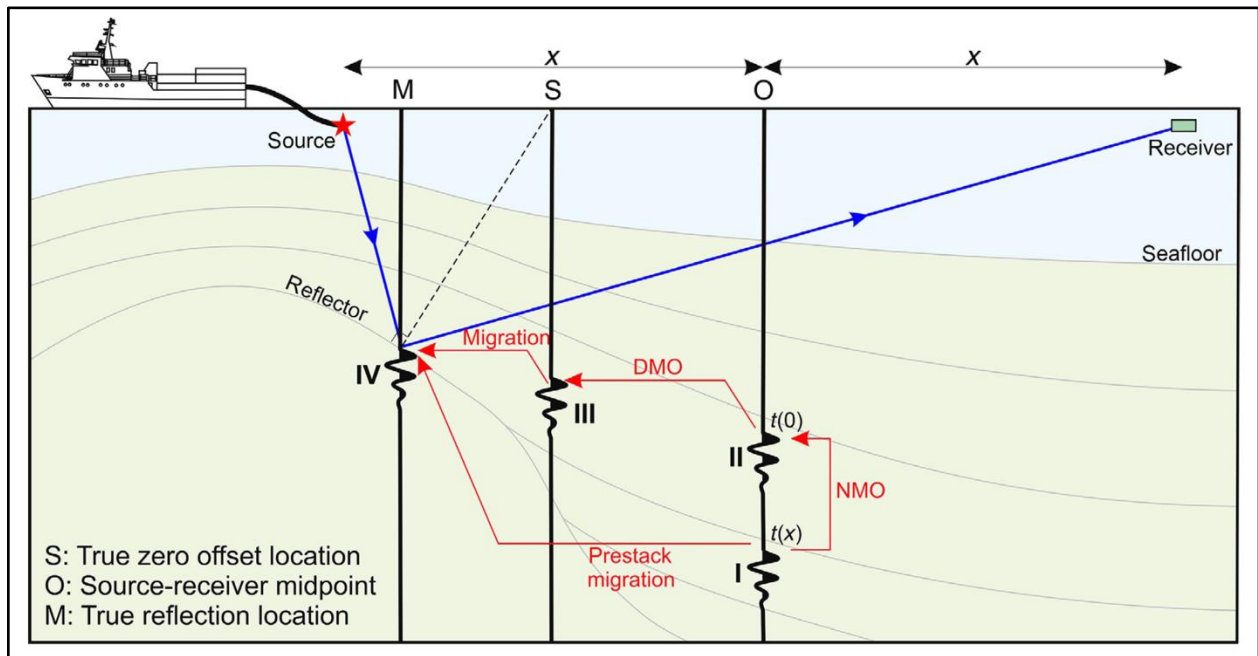


Figure 3.34 The schematic illustration of the NMO and DMO corrections and post-stack migration and their comparison with pre-stack migration. Time shifting at the source-receiver mid-point (O) is moved from arrival time ( $t_x$ ) to true zero-offset time ( $t_0$ ) by NMO correction. Location of the NMO corrected reflections (O) are moved to their true zero-offset location (S) by DMO correction. The reflection event is moved from true zero-offset location (S) to true reflection location (M) by post-stack migration, extracted from Dondurur (2018).

### 3.2.9 Stacking

After correction for normal moveout, all traces in CMP gathers are constructively summed up and averaged by a stacking process known as *mean stacking*  $S(t)$  for a certain time sample given by

$$S(t) = \frac{1}{N} \sum_{i=1}^N A_i(t) \quad (3.44)$$

where  $N$  is the number of input traces, also known as the fold number, and  $A_i$  is the amplitude value for the  $i$ th trace in the CMP gathers. As a result of the stacking process, composite traces are obtained at common midpoints (Figure 3.35) having balanced and higher amplitude content by dividing the output amplitude at individual samplings corresponding to fold number. Furthermore, random noise is tended to be attenuated, which leads to an important enhancement in S/N ratio by a factor  $\sqrt{N}$  (Dondurur, 2018; Hübscher & Gohl, 2013; Liner, 2016).

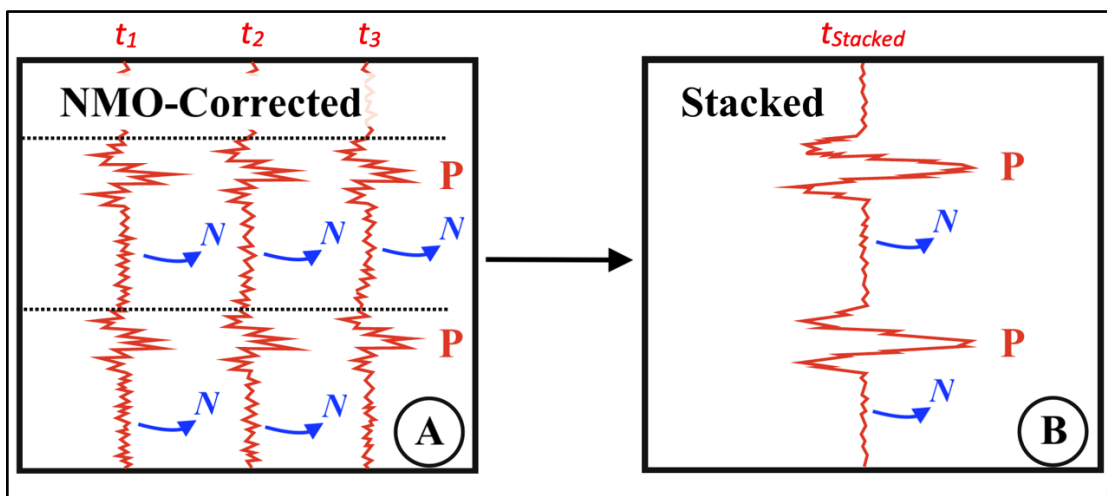


Figure 3.35 The schematic illustration of the NMO corrected traces before (A) and after (B) stacking process. After the stacking, amplitudes of the primaries (P) are increased, while the random noise (N) is attenuated, modified from Hübscher & Gohl (2013).

#### 3.2.9.1 Brute-Stack for QC Purposes

Brute stack is applied for quality control (QC) purposes in data processing just after the essential processing steps are applied such as band-pass filtering, deconvolution, f-k filtering, etc. It can be

used for determination of various parameters. Then, the results can be compared regarding the improvement of the S/N ratio (Gadallah & Fisher, 2009). For instance, to find the ideal parameters for band-pass filtering, impacts of the different values on brute stacked images can be compared rapidly omitting the time-consuming processing applications such as muting, velocity analysis and migration. Instead of the RMS velocity from velocity analysis, a constant velocity for sea column (approx. 1480m/s for Spitsbergen) or a single velocity function linearly rising can be applied to CDP gathers for NMO correction for the brute-stack processing sequence. Therefore, seismic traces can be summed up by one of those velocity models (Dondurur, 2018).

### 3.2.10 Post-Stack Time Migration

Stacked seismic data with zero-offset traces only allows to image horizontal reflectors in their correct subsurface locations. However, in case dipping and undulated layers exist in a subsurface model (Figure 3.36.A), their reflection events in the seismic data (zero-offset section) look incorrect and artificial effects occur, such as bow-tie (Figure 3.36.B). To give an example in the figure below, dipping layers are displaced in the up-dip direction, synclines are narrower, and anticlines are broader in the unmigrated seismic section. Furthermore, in the presence of fault blocks along the survey line (the plane of the section), their edges become new point sources causing hyperbolic artificial events, named diffractions (Dondurur, 2018; Kearey et al., 2002).

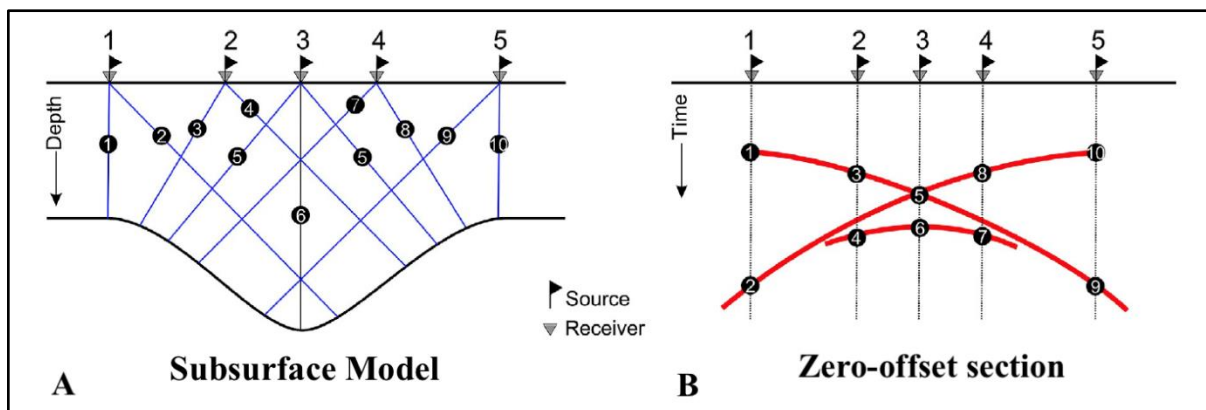


Figure 3.36 The schematic illustration of five zero-offset source and receiver for a subsurface model (A) and a zero-offset section (B). Their ray paths reflecting at the subsurface model and their incorrect reflection events recorded at the same receivers in the stack section yielding the bow-tie effect (B). Only reflection points 1 & 10 are correctly located beneath at their mid-point since their reflectors are horizontal, modified from Dondurur (2018).

The seismic migration process collapses the energy of diffractions while moving the dipping reflectors from their recorded positions to their true subsurface positions both in space and time (Figure 3.34). This increases the lateral resolution and enables to image the subsurface accurately. Therefore, anticlines become narrower, synclines are broader and bow-tie effects are solved (Figure 3.36.B). The migration also moves the recorded dipping reflectors into their correct up-dip direction, while shortening their length and steepening their dipping angle (Dondurur, 2018; Kearey et al., 2002; Yilmaz, 2001). The impact of the migration process on an unmigrated dipping reflector can be given as an example in Figure 3.37.

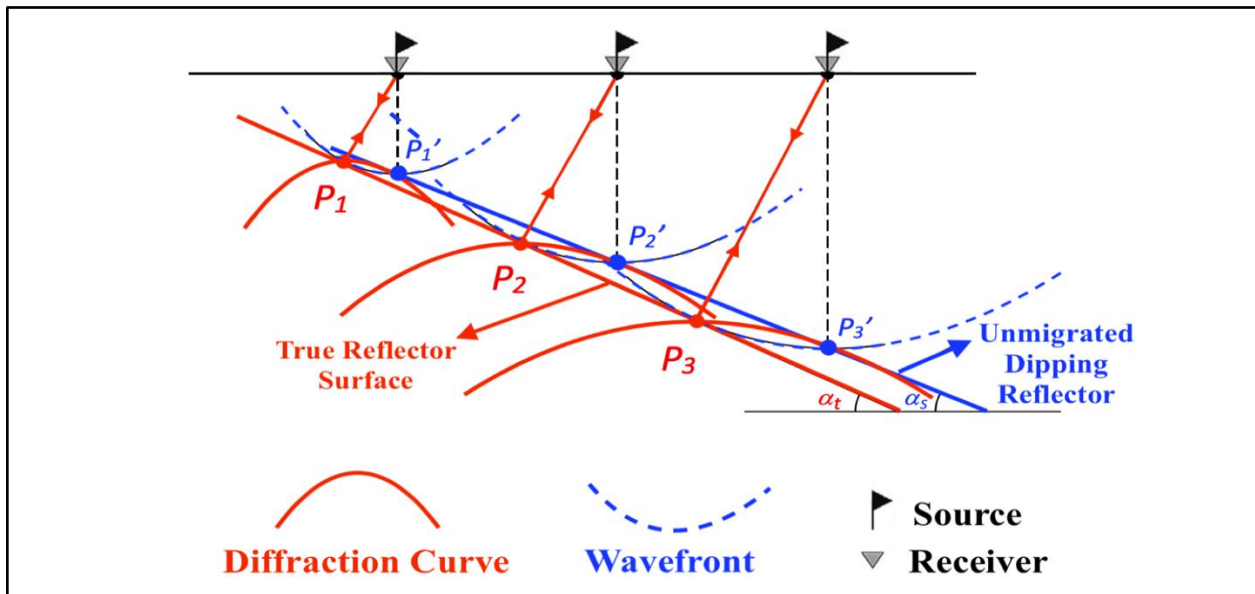


Figure 3.37 The schematic illustration of the zero-offset ray paths on an unmigrated dipping reflector (blue line) with wavefronts and diffraction curves intersecting at two points, where  $P_1'$ ,  $P_2'$  and  $P_3'$  are the apparent reflection points in seismic data before migration;  $P_1$ ,  $P_2$  and  $P_3$  are the true reflection points after migration. These points are the apexes of the diffraction and wavefront curvatures. The red inclined reflector is the true geological surface after migration. Migration also yield  $\alpha_t > \alpha_s$ , where  $\alpha_s$  is the dipping angle of the recorded surface and  $\alpha_t$  is the dipping angle of the true reflector, redesigned from Dondurur (2018); Kearey et al. (2002) and created by InkSpace.

Before performing a migration process, the multiples must be eliminated from the data keeping the only primary events. S/N ratio should be as high as possible, especially spike noise should be attenuated in the stacked data. The velocity field should be accurately known at every location of the samples to be used by the migration algorithm. If the high-amplitude spike noise is not

removed from the data, migration algorithm will highly transform them into the migration impulse of a semicircle (smiling). The 2D seismic data should also be free of side-sweep reflections, which are the diffractions from out-of-plane scattering leading to the smiling effect after the migration process. The greater S/N ratio with coherent noise-, multiples, and spikes-free data before the migration may have provided more accurate migration image with less smiling effects. The migration process can be applied before or after stacking the seismic data, which are called pre-stack and post-stack migrations, respectively. Their migration algorithm can compute the data either in the time or in the depth domain, which produces a seismic section with time information in the vertical dimension, or depth information converted from the time by velocity information of the particular locations. In addition, the NMO stretch mute gaps at the start-of-line in the stacked sections which are zero mute zones causes unique noise in the migrated images called swings. However, they can also occur at the end-of-line due to either the muted amplitudes or the weakened amplitudes by data acquisition or tapering the edge effects (Dondurur, 2018). Since the dipping conflicts would be corrected by DMO correction and the seismic data would be stacked in order to provide the migration algorithm with the increased S/N ratio, the post-stack time migration by the finite-difference approach is the chosen migration type in this thesis.

### 3.2.10.1 Finite-Difference Migration Approach

The finite-difference (FD) migration is a deterministic processing method solving scalar wave equation by the finite-difference approach that the receivers are theoretically moved downwards in finite depth steps to collapse the diffraction hyperbolas. It is thought in theory that the receivers along the surface record signals as diffraction hyperbolas from a point source at a particular depth. Since the downward movement of the receivers and the downward continuation of the recorded wave field are the same, the receivers can collapse these diffraction hyperbolas when they meet at the apex of the hyperbolas with the wavefield information in finite depth steps. The process should be stopped when the hyperbolas are collapsed at the apex (Figure 3.38.C). If the downward movement of the receivers surpasses the depth of the apex, which is called over-migration, a mirror image of the diffraction hyperbola occurs (Figure 3.38D

and E). The other way round, if downward movement does not reach the apex depth, undermigration emerges (Figure 3.38A and B).

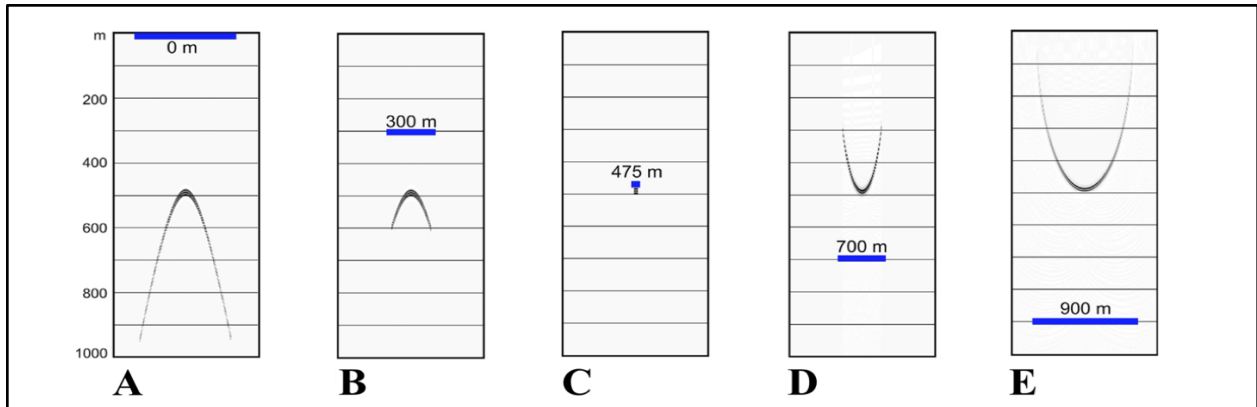


Figure 3.38 The schematic illustration of collapsing the diffraction hyperbola by the downward continuation of the zero-offset wavefield owing to the receivers moved downward from 0 m to 900m (A to E), where the blue line represents the total spread length. The spread length becomes narrower when by the downward continuation of the receivers (from A to C). The diffraction hyperbola collapses when the receiver is at the correct location meeting with the apex of the diffraction curve (C). Once downward continuation surpasses the ideal location to collapse the diffraction, the receivers yield the mirror images (D and E), modified from Dondurur (2018).

### 3.2.10.2 Omega-X Algorithm

The FD time migration approach can be performed with an explicit or implicit algorithm that recalculates the section to solve an approximation of the wave equation. Even though these algorithms can solve the lateral velocity variations relatively faster than other algorithms in the time domain, they are limited to up to 35° steep-dipping layers owing to dispersion, undermigration, and the bandlimited seismic data, which are the common limitations (Yilmaz, 2001). Nevertheless, the FD time migration approach can be implemented by a specific implicit algorithm solving the wave equation in the frequency-space ( $f-x$ ) domain, which is also known as the *omega-x* algorithm and the steep-dip FD algorithm, in order to improve the steep-dip layers up to 70°. The algorithm also performs without difficulties against both vertical and horizontal velocity variations (Dondurur, 2018). Therefore, the FD time migration with *omega-x* algorithm has been initiated as the last processing sequence in this thesis.



The *omega-x* algorithm works as a two-step iterative processing. The first phase is done for each downward-continuation step (depth step), which is also called partial migration (Figure 3.39.A). A linear phase shifting is applied to a one-way pressure wavefield  $P(x,z,w)$ . Then, the retarded wavefield is computed by implicit extrapolation for each frequency components of the wavefield. This extrapolated discrete section is thus imaged.  $V_{int}(x,t)$  is then used to proceed with the velocity of the medium at the particular depth step during the partial migration. In the second phase (Figure 3.39.B), the partial migration is repeated for each depth step to build their discrete images, while summing up their single image to achieve the whole migrated section (Yilmaz, 2001). How this algorithm has been computed regarding the data processing software used in this research will be detailedly explained in chapter 4.2.11.

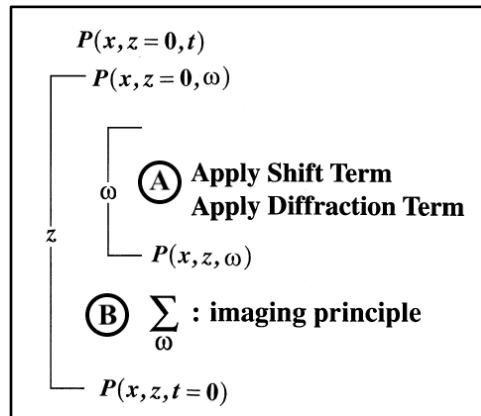


Figure 3.39 The schematic illustration of the two-step algorithm framework (A and B), where  $P$  is the pressure wave;  $x$ : the depth point axis;  $t$ : the record time axis;  $w$ : the  $w$  time axis, extracted from Yilmaz (2001).

### 3.2.10.3 The Factors Impacting the FD Migration Algorithm

#### 1) Depth Step Size

The effectiveness of the FD migration is related to the computation of the wave fields moving downward by discrete depth steps creating time slices where diffraction hyperbolas are collapsed. Each time slices towards depth build up the whole migration section. The minimum depth step size means the sampling rate of the zero-offset section as input. Large depth step sizes cannot remove diffraction hyperbolas yielding frowns due to under-migration of steep-dips

(Figure 3.40). Thus, smaller depth steps are convenient for the steep-dips (Dondurur, 2018; Yilmaz, 2001).

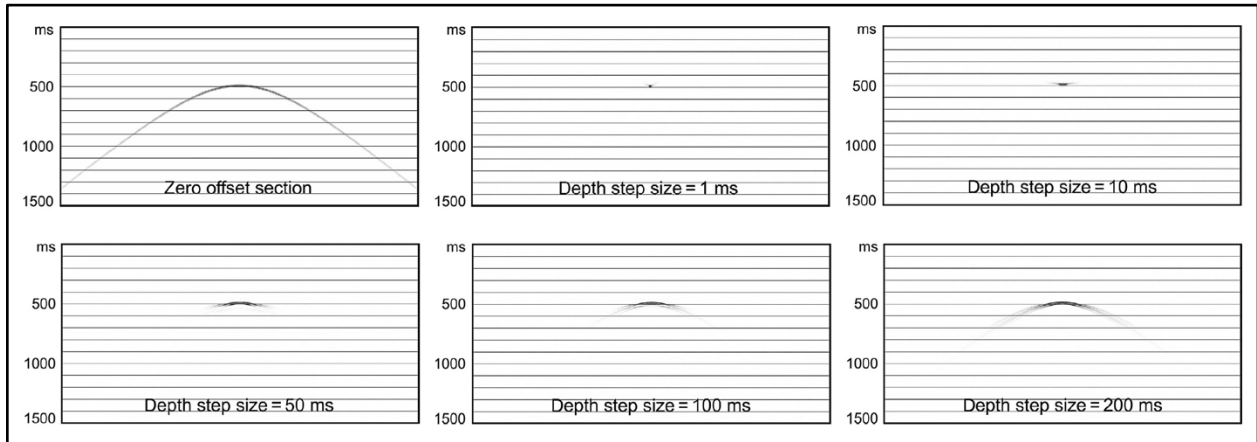


Figure 3.40 shows the impacts of the correct and the incorrect depth step size in a constant velocity medium. The sampling rate of the zero-offset section is 1ms while the diffraction hyperbola collapses at 10 ms depth step size, modified from Dondurur (2018).

## 2) Velocity

After the migration, semicircular artifacts can occur in case of an incorrect velocity model used during the migration (Figure 3.41). For example, if the velocity is slower than it is supposed to be, the artifact will look like a frown in the under-migrated image. The other way round, a smiling will appear in the over-migrated image if the velocity is faster (Dondurur, 2018; Yilmaz, 2001).

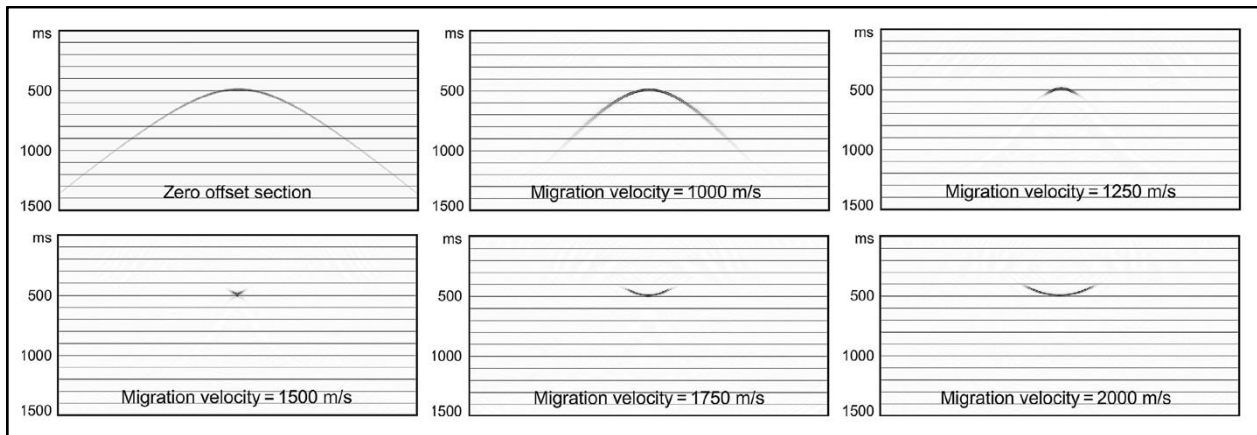


Figure 3.41 shows the impacts of the correct and the incorrect migration velocities in a constant velocity medium. The diffraction hyperbola is collapsed by correct migration velocity as 1500 m/s, which is same as zero-offset section velocity, modified from Dondurur (2018).

### 3.3 SEISMIC INTERPRETATION

This chapter briefly explains the principles of seismic interpretation and the analysis techniques used in this thesis research. Seismic interpretation is an analysis of processed seismic data to obtain reasonable subsurface models to distinguish geological structures and subsurface and build possible histories of evolution in research areas (Herron, 2011; Sheriff, 2002). After processing recorded seismic data, the interpretation is done including different methods such as structural and stratigraphic analysis. There are various types of interpretation software used in both industry and academy, such as Petrel (Schlumberger) used for 2D seismic interpretation in this study.

#### 3.3.1 Seismic Attributes

##### 3.3.1.1 Acoustic Impedance

Acoustic impedance AI is a product of P-wave velocity ( $V$ ) with density ( $\rho$ ) in a homogeneous, isotropic rock (Figure 3.42) that provides the interpreters with valuable information about lithology (Zhou, 2014), which is given by

$$AI = V \times \rho \quad (3.45).$$

##### 3.3.1.2 Reflection Coefficient

Reflection coefficient (RC) is a ratio of the amplitude of a reflected wave ( $A_1$ ) to the amplitude of an incident wave ( $A_0$ ) which is used to measure the impact of an interference, an AI contrast (Kearey et al., 2002). The ratio can be given by

$$RC = A_1 / A_0 \quad (3.46).$$

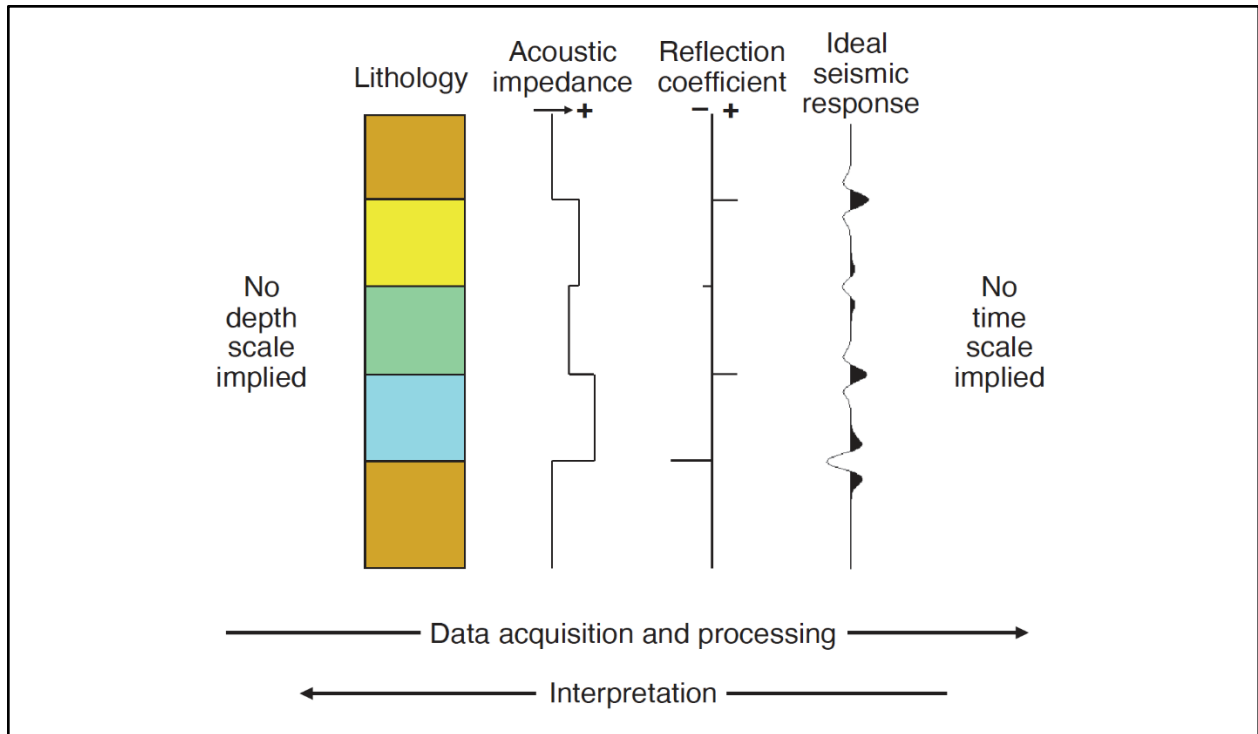


Figure 3.42 The schematic illustration of relationship between acoustic impedance, reflection coefficient and seismic response, extracted from Herron (2011).

### 3.3.1.3 Seismic Response

Seismic waves reflect the compression and expansion of a body-mass as they travel through mediums. The shape or character of seismic waves can change due to the propagation through different acoustic impedance zones (Figure 3.42). That differentiation of a seismic wavelet at acoustic impedance contrasts in the subsurface is measurable and called seismic response. The seismic response can be described by reflection amplitude, seen as phase and polarity changes on the seismic profiles (Herron, 2011; Sheriff & Geldart, 1995). Phase is a description of the motion of a seismic wave motion on the AI contrast. In a seismic interpretation, casual or noncausal wavelets can be used. The noncausal wavelet is symmetrical around zero-time also called a zero-phase wavelet, while the causal wavelet starts at zero-time called a minimum-phase wavelet (Figure 3.43). Zero-phase does not exist as a response to AI contrast, but it can be generated during seismic processing (Herron, 2011; Sheriff, 2002). In this thesis research, the zero-phase has been used during the interpretation in Petrel. A seismic wavelet is displayed by positive and negative polarities through positive and negative RC changes, which are called peaks

and troughs, respectively. During the interpretation of seismic reflectors, the peaks and troughs can be determined as blue or red colors by interpreters (Herron, 2011; Sheriff & Geldart, 1995).

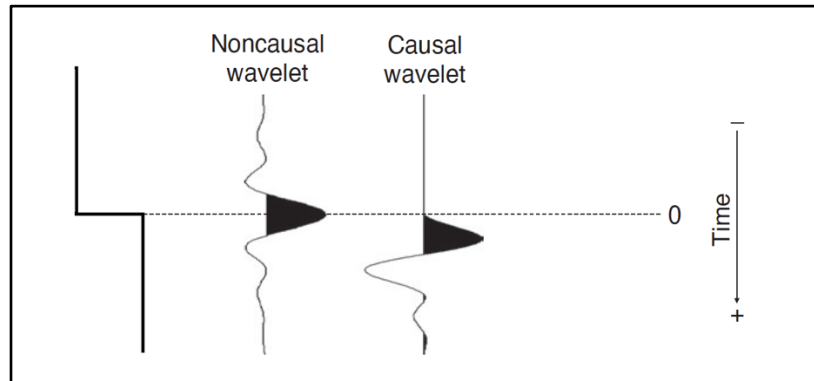


Figure 3.43 The schematic illustration of noncausal wavelet (zero-phase) and causal wavelet (minimum-phase), modified from Herron (2011).

### 3.3.2 Structural Analysis

Structural analysis is done to identify the geometry of the seismic reflectors by correlating them with the seismic horizons. The continuity of the seismic horizons can be tracked while changing patterns of reflections can be recognized. Recognizing discontinuities of offset or seismic patterns indicates some sorts of changes in the geometry of geological structures. For instance, fault blocks, terminated edges, horst and graben structures are easily defined during the structural analysis. For fault interpretation, first major faults are done, then minor faults or fractures can be predicted (Herron, 2011). During the most structural interpretation, depth- or time-structure maps can be generated to demonstrate the geometry of a seismic horizon. Moreover, isopach maps can be generated from two interpreted seismic horizons by calculating the thickness in two-way time (Kearey et al., 2002).

### 3.3.3 Stratigraphic Analysis

A stratigraphic analysis is done to predict lithology and depositional environment by using the reflection boundaries and patterns. The analysis is done by subdividing the stratigraphic units (Kearey et al., 2002). A horizon/seismic horizon is a geological boundary separating two different

rock layers depending on the AI contrast. The horizon interpretation or horizon pickings is the initial step of the analysis to differentiate the top and bottom geological boundaries of the seismic units (Figure 3.44), which is also called seismic sequence analysis (Herron, 2011).

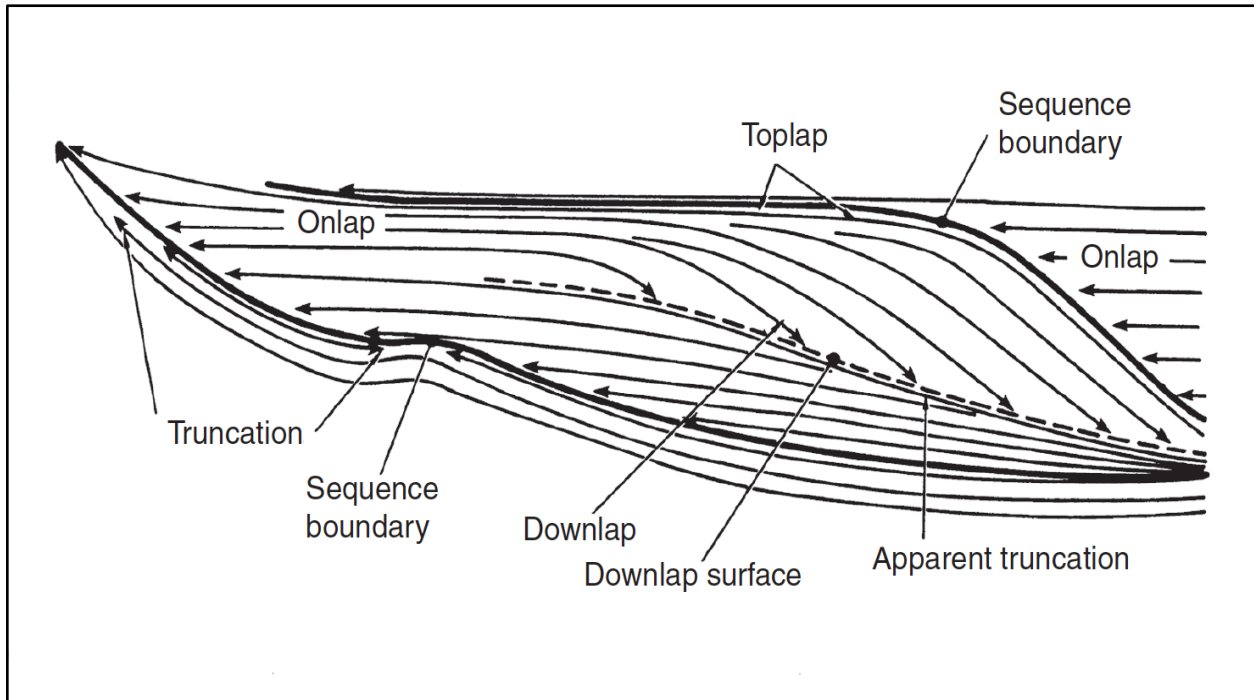


Figure 3.44 The illustration of different types of geological boundaries (straight lines) and termination patterns (dashed lines) through sedimentary strata, modified from Liner (2016).

Another part of the analysis is seismic facies analysis depending on the quality of reflection character. The reflection characters (Figure 3.45) are often described as parallel, subparallel, and chaotic, which are mostly related to these parameters: amplitude, continuity, frequency, etc. (Kearey et al., 2002; Mitchum Jr et al., 1977). The reflection amplitudes can be expressed as weak, low, moderate, high, or strong depending on the AI contrast. A seismic reflector can be continuous and discontinuous due to the abrupt changes of the acoustic impedance relying on the elastic properties and/or density (Herron, 2011; Kearey et al., 2002; Sheriff, 2002).

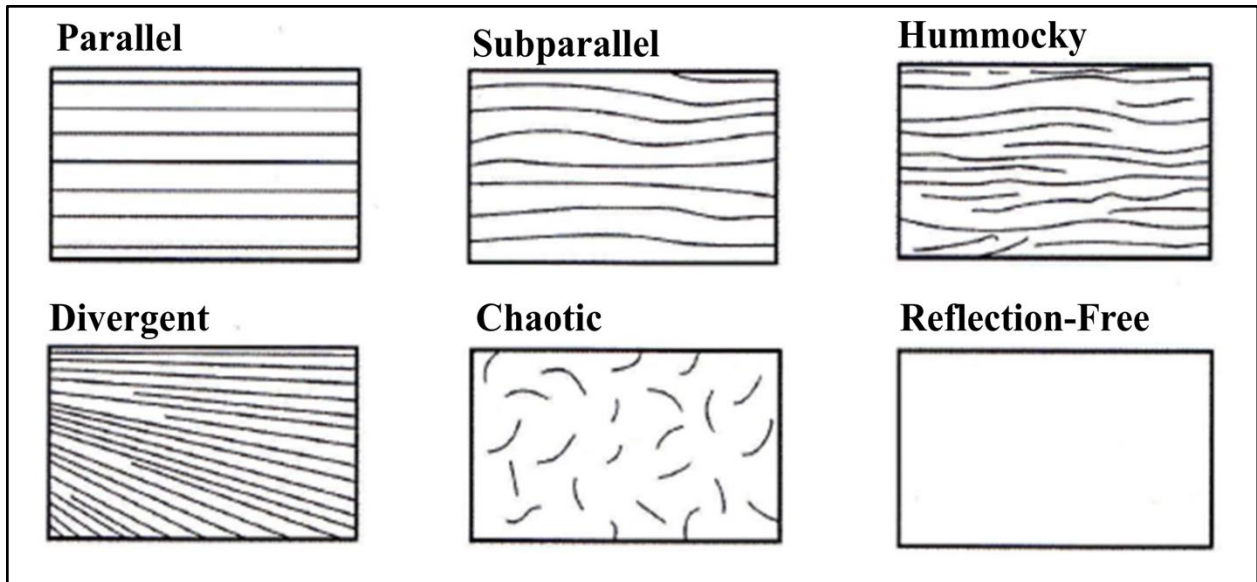


Figure 3.45 The illustration of general reflection characters used to describe seismic facies, modified from Mitchum Jr et al. (1977).





## 4 RESULTS

### 4.1 SEISMIC DATA ACQUISITION

2D Multichannel marine seismic reflection data acquisition results from SVALEX 2002 presented in this chapter was obtained from the cruise report for leg-2 by Mjelde (2003). 8 profiles of multichannel seismic reflection data (leg-2) were acquired on the shelf between Isfjorden and Van Mijen Fjorden (Figure 4.1) by use of the GEO (UiB) source system airgun string (5guns) with one additional gun and the WesternGeco Nessie3 streamer and the Triacq recording system. The SVALEX 2002 acquisition on board R/V Håkon Mosby was operated from September 4th to September 6th, 2002, with cooperation between several institutes: NTNU, UiB, UiS, UiT, UNIS, the Norwegian Petroleum Directorate and Equinor (formerly Statoil).

A total of 456 km of seismic data were acquired during leg-2 west of Svalbard. Only 4 of those seismic profiles (detailedly showed in Table 4.1) were used in this thesis for processing and interpretation methods. In the table, their UTM coordinates and geographical positions are shared together with the offset correction between antenna and the source, which is 72 m. Line 6 and Line 8 were acquired from west-south-west to east-north-east, while Line 7 was acquired in the opposite direction. These three lines are parallel to each other, whereas Line 2 is a cross-section profile acquired from north-west to south-east.

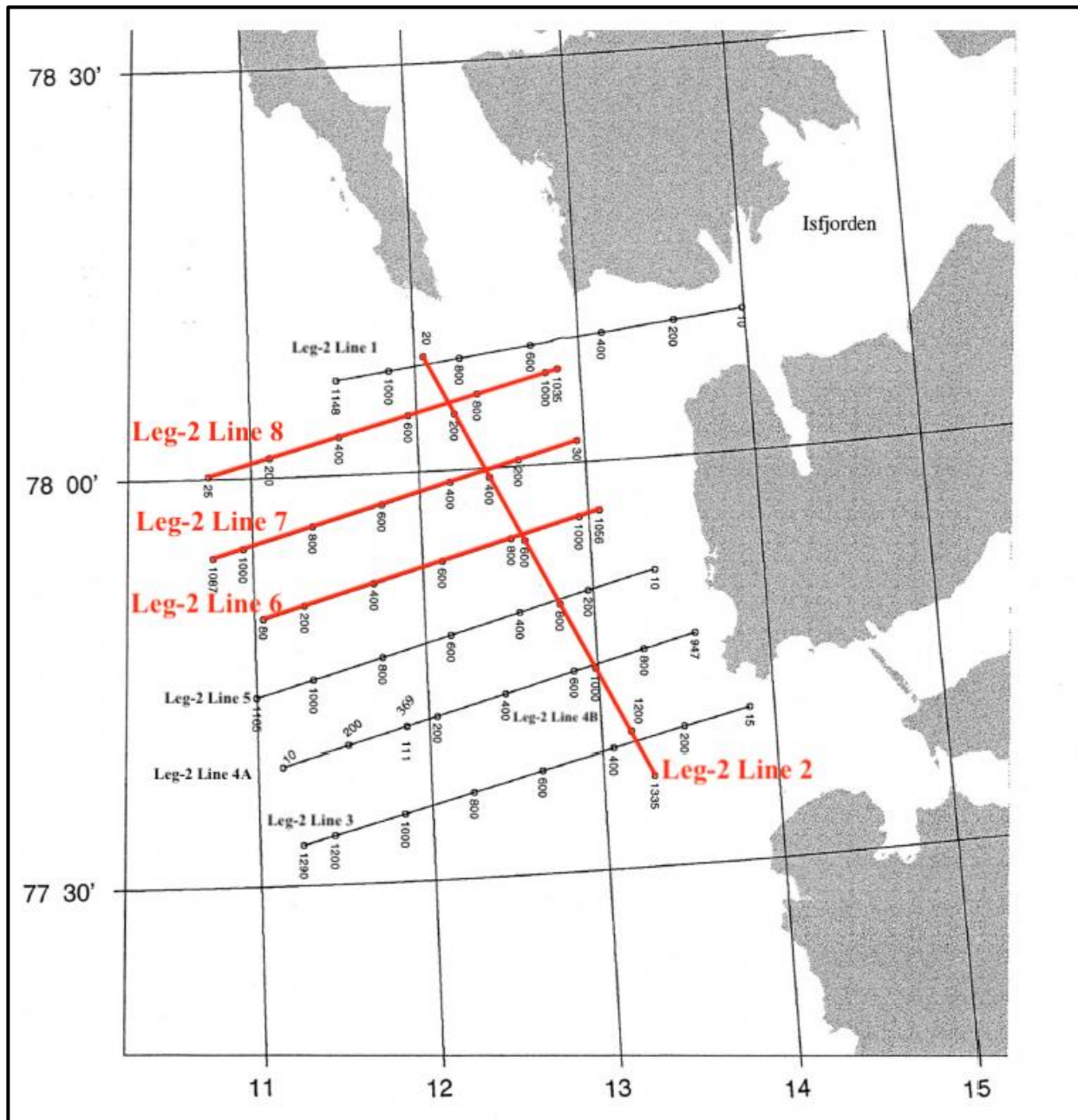


Figure 4.1 Location map of SVALEX-2002, Leg-2. The map shows 8 seismic profiles within their shot numbers. The red lines represent the chosen ones for processing and interpretation of seismic data in this thesis project, modified from Mjelde (2003).

Seismic Profile	Shot Number	Time	Year	UTM - Northing	UTM - Easting	N°	E°	Length (km)
Leg-2 Line 2	20	06:41:51	2002	8690112.13	706850.00	78	12	65.75
	1335	14:51:04	2002	8636674.15	745157.27	77	13	
Leg-2 Line 6	80	00:32:52	2002	8651965.61	688833.73	77	11	48.80
	1056	06:29:35	2002	8671712.86	733514.49	77	13	
Leg-2 Line 7	30	07:55:29	2002	8680906.36	729559.72	78	12	52.85
	1087	14:21:11	2002	8659538.50	681222.13	77	10	
Leg-2 Line 8	25	16:00:31	2002	8670507.70	679176.28	78	10	50.50
	1035	22:05:04	2002	8690352.64	725669.50	78	12	

Table 4.1 Seismic profiles and their start and end points of recorded shots with geographical positions and coordinates in UTM zone33X, before offset correction for antenna, extracted from Mjelde (2003).

Line-6 and Line-8 had some mis-fired shots in shooting sequences where the problems occurred between the distance of two consecutive shots 100 m and once 150 m (otherwise the shot interval was 50 m). However, these problems did not have significant effect on the navigation processing.

The source system was fired at 7 m depth with 50 m shot interval, and the seismic reflection data were recorded by a streamer at 10 m depth, with 12.5 m channel interval (Table 4.2). The seismic data were sampled with 2 ms intervals and with a sample length of 20 bits, corresponding to a dynamic range of 120 dB (20 x 6 dB). The frequency band between 3 Hz and 180 Hz was chosen as low- and high-cut recording limits, respectively. The survey of the SVALEX was design to generate the largest constructive interference (Figure 4.2) between the primary reflection and ghost reflection by the array tuning for a single airgun with an airgun string and the source depth at 10 m. The geometry of the airgun configuration is shown in Figure 4.3, the far-field signature of the array is shown in Figure 4.4.A, whereas the amplitude spectrum of the source is presented in Figure 4.4.B.

ACQUISITION PARAMETERS	SPECIFICATION
Sailing Speed	4.5 knots
Number of Source	1-6
Number of Streamer	1
Streamer Length	3 km
Airgun Depth	7 m
GPS Antenna to centre of source	72 m
Streamer Depth	10 m
GPS Antenna to first active channel	150 m
Group Length	12.5 m
Shot-Point Interval	50 m
Sampling Interval	2 ms
Record Length	12 s
Low-cut Frequency	3 Hz and 18 dB/oct slope
High-cut Frequency	180 Hz and 72 dB/oct slope

Table 4.2 Acquisition parameters from SVALEX-2002 applied for Leg-1 and Leg-2, extracted from Mjelde (2003).

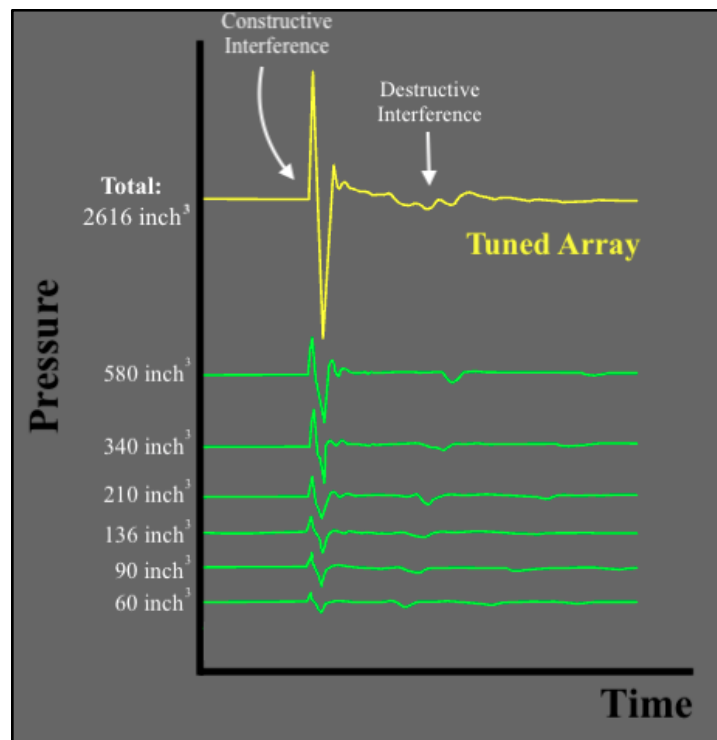


Figure 4.2 shows the tuned array (yellow) for 6 airguns (green). The constructive and deconstructive interference can be seen in the far-field source signature, modified from Mjelde (2011).

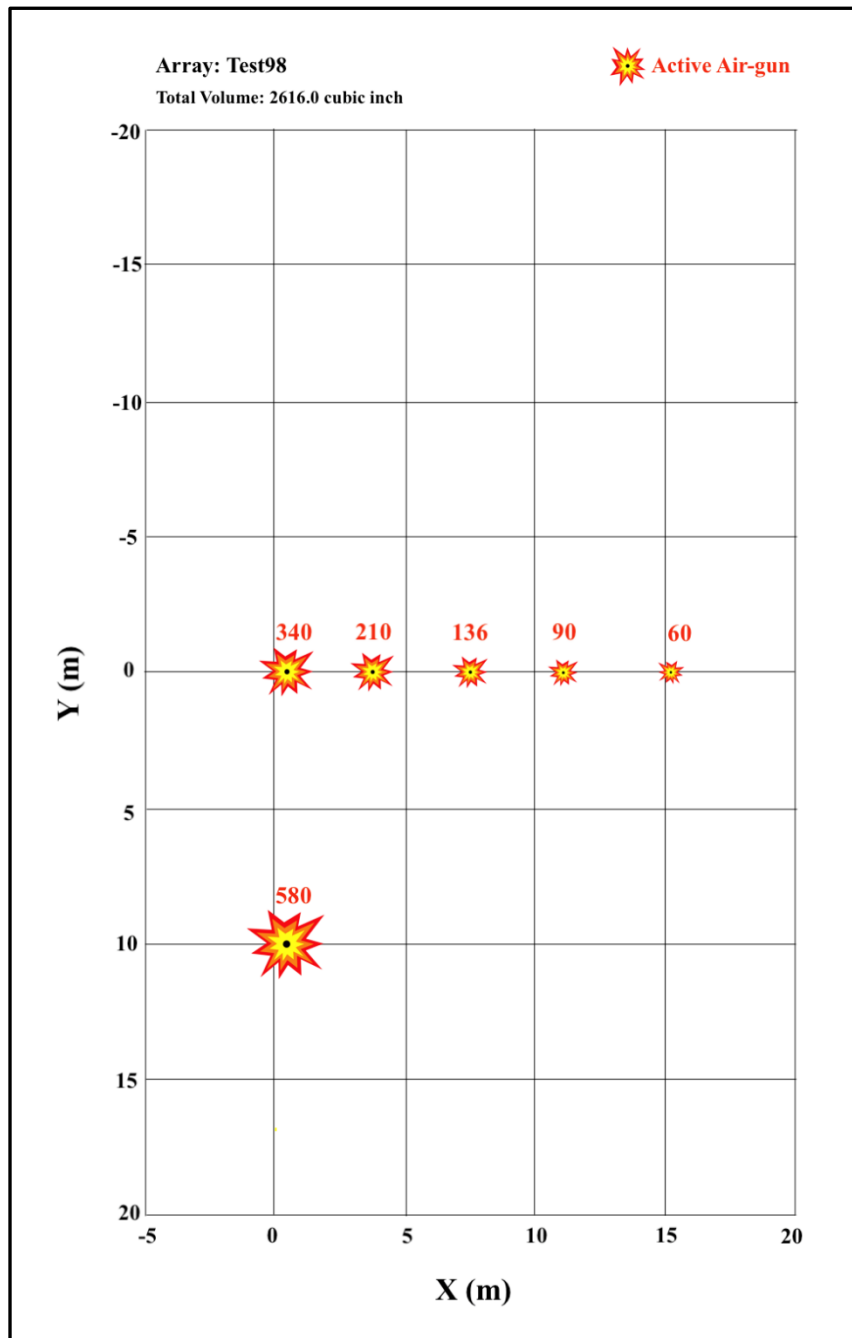
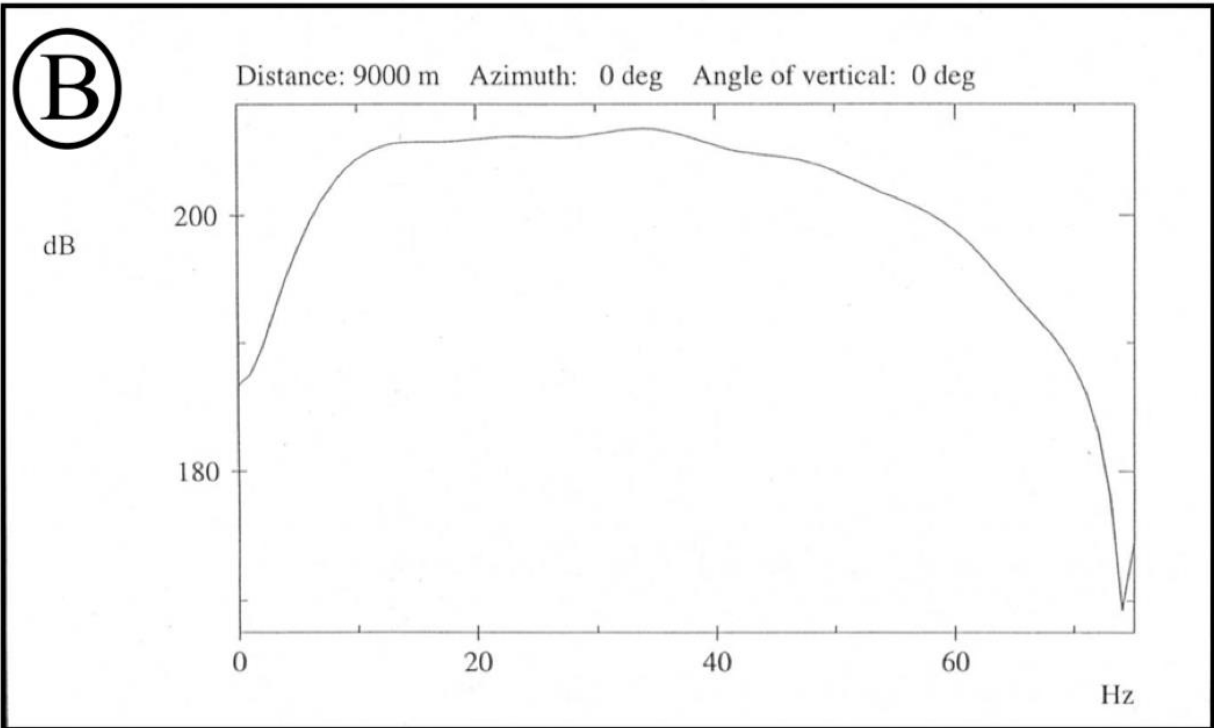
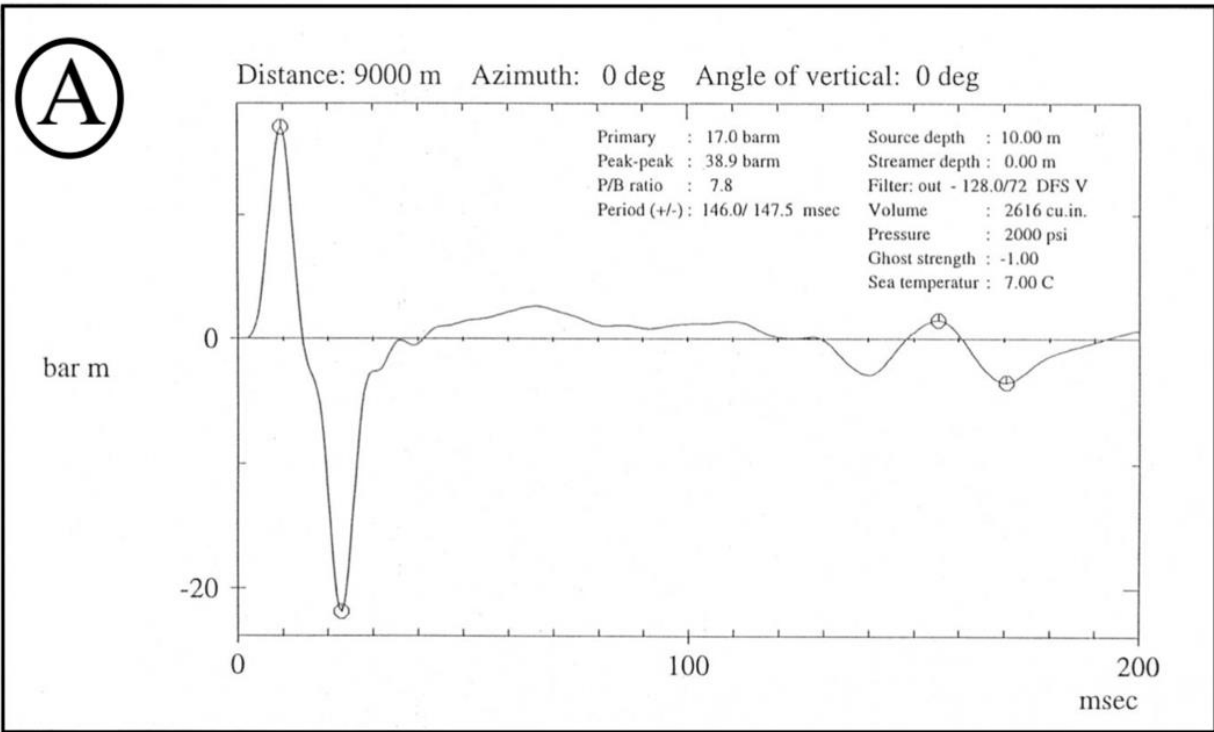


Figure 4.3 The schematic source geometry illustrates the array test for airgun configuration. Active airgun pressure units in cubic inch, modified from Mjelde (2003); redesigned in Inkscape.



1200,580 10m

Figure 4.4 The far-field signature of the array in the time domain (A), and the amplitude frequency spectrum (B), modified from Mjelde (2003).

## 4.2 SEISMIC DATA PROCESSING

The 72 m offset between the source and GPS antenna, which provided the UTM coordinates in zone 33X, had to be corrected to their true position by Matlab at GEO, UiB. The new dataset, called UIB, includes both original headers and corrected UTM and geographical coordinates (Mjelde, 2003).

The seismic data processing was done using the software package Geocluster 5.0 from CGGVeritas, released in 2008 (1.8.5). Geocluster includes various interactive applications and modules for analyzing and processing purposes run only on PC / Linux (CGGVeritas, 2008a).

Xjob is an interactive application tool to graphically construct processing workflows designed by the processing modules. The modules are placed in Xjobs to execute simple or complex processing sequences. The modules and their purposes are explained in their related processing sequences in the next chapters.

TeamView, released in 2010 (1.14.1), is a Java-based graphic application used for QC and analysing purposes on the displayed data sets such as shot and CDP gathers, single trace or stacked sections. It also operates basic mathematical functions to demonstrate amplitude and f-k spectrums, and to generate water bottom libraries.

ChronoVista is an interactive software in addition to the standard Geocluster distribution. The software package includes the GeoVel where the velocity picking is done in the time or the depth domain. The package also has different displaying options such as semblance spectrum, velocity fields, interval velocity, stacking velocity, CDP gathers before and after NMO, anisotropy fields, that all can be simultaneously displayed during the velocity analysis.

The XPS sub-system, which stand for eXtended Processing Support, manages, stores, and supply auxiliary data to the processing modules. The analyzed data are stored in a SQL database and can be viewed as spreadsheets in a related library, where they can be analyzed and modified. For

instance, picked water bottom library stores the information of trace attributes for the seafloor within TWT vs offset in a spreadsheet in the water bottom library. In case of modification on those picked points, it can be easily done in the XPS spreadsheet. XPS libraries are created by their ID and version names assigned in the processing modules in the Xjob applications.

A total of 5 different workflows are presented in Table 4.3, which produced either stacked or post stack time migrated sections. The main reason for trying different processing methods was to find out the best processing approach which enabling efficient attenuation of multiple noise, while increasing the amplitude of primary reflection events. Seismic line 8 was tested for all between those workflows and the 5th processing workflow provided the best S/N improvement, while removing the surface-related multiples. The chosen workflow is detailly presented with its processing sequences in Figure 4.5. These sequences have been applied to all seismic lines. The processing results shown in this chapter are from the seismic line 7 since this line has the outstanding S/N enhancement. In addition to the main results, the results from workflows 1-4 are presented in the appendix B.3.

Seismic Processing Workflows	Approaches for remedy of Multiple Noises	Input Dataset
1st Seismic Processing Workflow	• $f-k$ Filtering	Original CMP Gathers
	• Deconvolution	
2nd Seismic Processing Workflow	• $f-k$ Filtering	Interpolated CMP Gathers
	• Deconvolution	
3rd Seismic Processing Workflow	• Velocity Filtering in the $\tau-p$ domain	Interpolated CMP Gathers
	• Deconvolution in the $\tau-p$ domain	
4th Seismic Processing Workflow	• $f-k$ Filtering in the NMO-corrected CDP gathers	Interpolated CMP Gathers
5th Seismic Processing Workflow	• $f-k$ Filtering in the %70 NMO-corrected CDP gathers	Interpolated CMP Gathers
	• Multiple Extraction	
	• Adaptive Subtraction	

Table 4.3 shows the 5 different applied workflows and their main approaches within input datasets, the 5th one is the main workflow in this thesis.



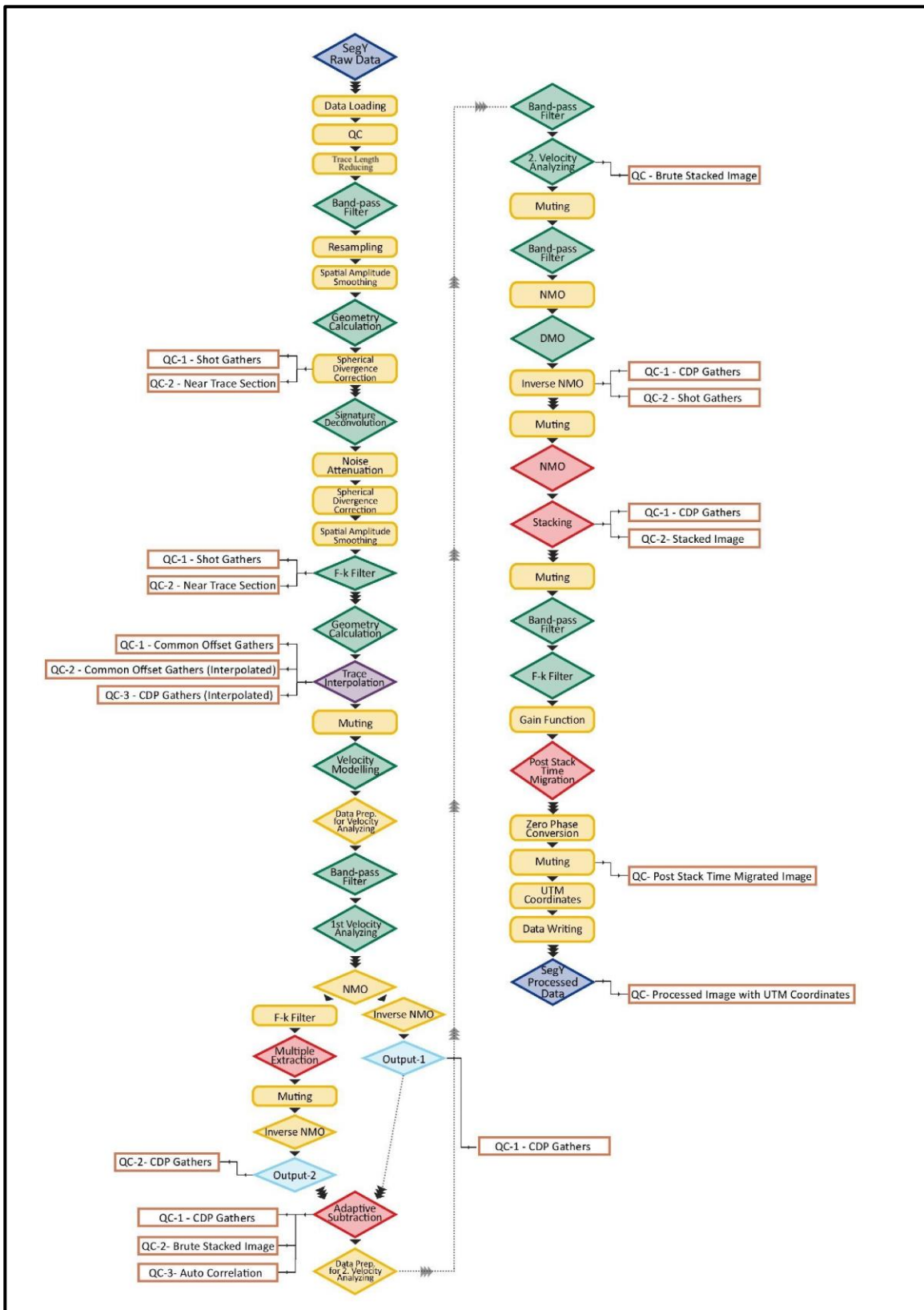


Figure 4.5 The schematic illustration of the 5th workflow of seismic data processing applied to the seismic lines 2, 6, 7, and 8, generated in Adobe Photoshop.

## 4.2.1 Pre-processing

The pre-processing was completed within two Xjob folders (Appendix A) prepared by several modules on Geocluster, which will be explained in the following sections. In the end of two Xjob folders, QC was done on the near-trace section to observe the advancements.

### 4.2.1.1 Data Loading and QC

The seg-y data format was loaded as input and read by the module SEGIN in the first Xjob window where it was reformatted to a new media that CGG Geolcluster used. Next, QC was done by the module QCTRL to check whether there is any missing shots and traces (channels) before moving forward to further processing steps. So, beginning of the processing of the data, QC was done on the near-trace image of the raw data (Figure 4.6).

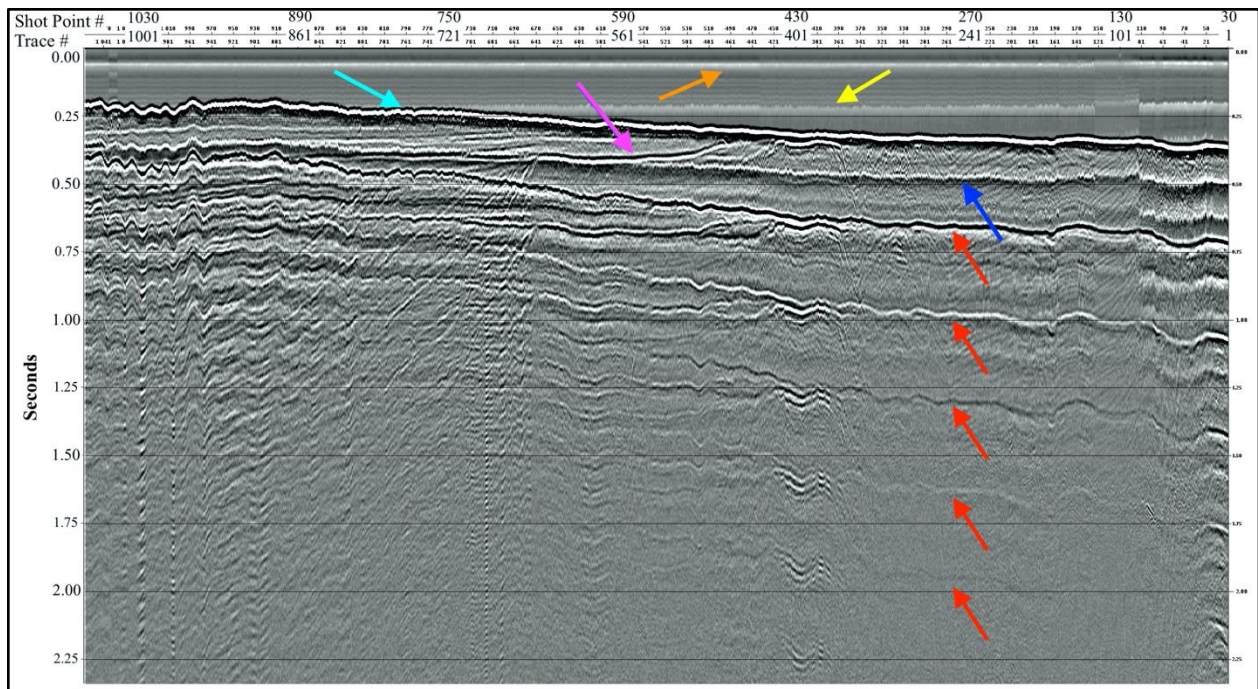


Figure 4.6 The near-trace section of the raw data in seconds (TWT). Seismic events are shown with various colored arrows on the section; the direct wave (orange), the bubble pulse of direct wave (yellow), seabed reflection (turquoise), subsurface reflection (pink), the bubble pulse reflected from seabed (blue) and surface-related multiples (red).

### 4.2.1.2 Trace Length Reducing

In the module HISTA, besides the main purpose of the module which is gun and streamer static correction by regional static correction, trace length modification can be also done (CGGVeritas, 2008b). The deeper parts of the seismic lines consisting of mainly noise and weaker signal were removed from the data by reducing the trace length from 12288 ms to 6144 ms (Figure 4.7). The data size reduction decreased the processing time of the next steps.

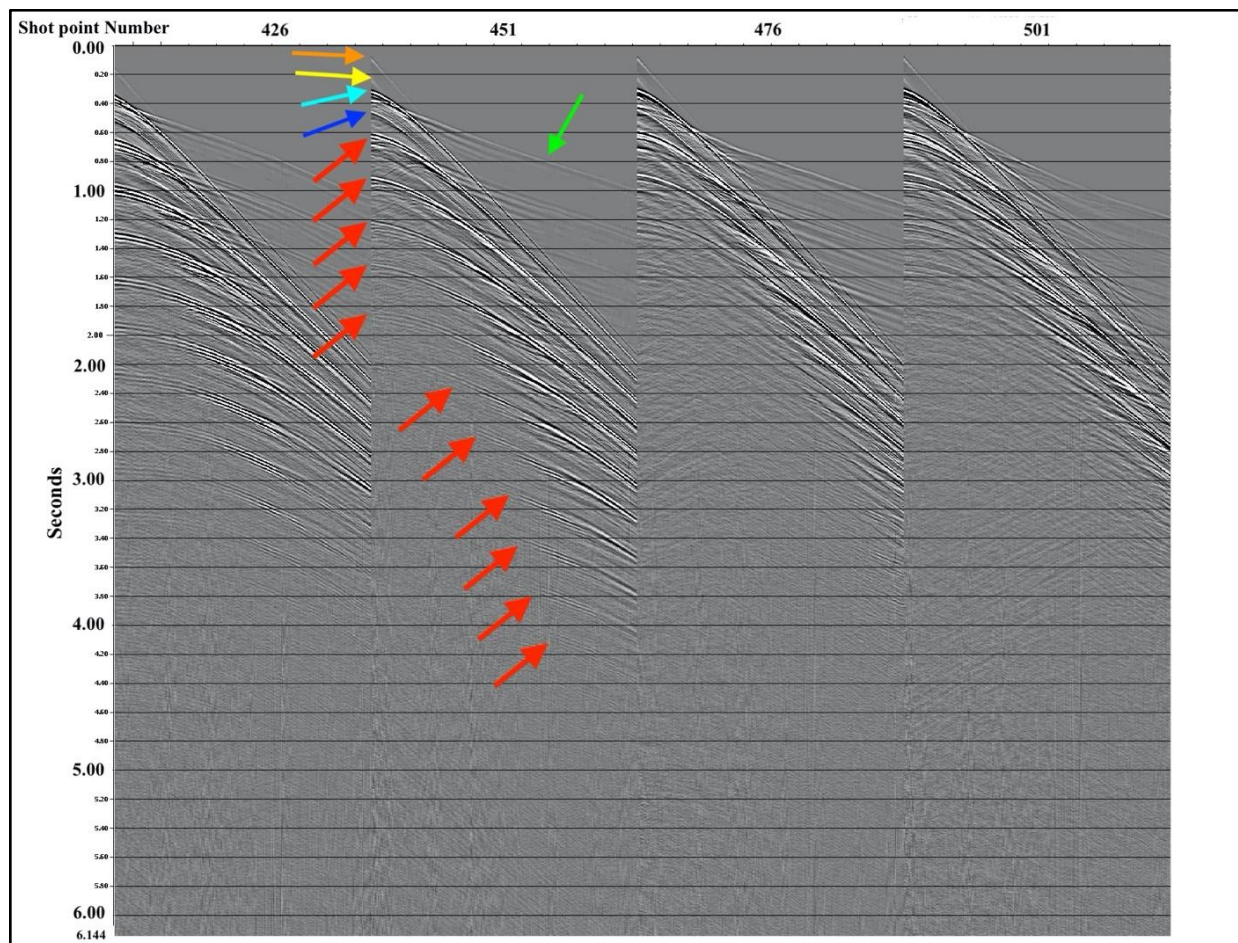


Figure 4.7 Shot gathers after the static correction with reduced trace length to 6144 ms (TWT). Seismic events are shown with various colored arrows on the shot gather 451; the direct wave (orange), the bubble pulse of direct wave (yellow), seabed reflection (turquoise), the bubble pulse reflected from seabed (blue), refracted wave along the seabed (green) and surface-related multiples (red).



### 4.2.1.3 Band-pass Filtering – Butterworth

The module FILTR was specified with a minimum-phase Butterworth filter operator to keep the minimum delay properties of the input dataset before signature deconvolution. The Butterworth filter was applied by defining low-cut ( $f_1$ ) and high-cut ( $f_2$ ) frequency values and two slopes  $S_1$  and  $S_2$  providing a transition for the band-pass filtering (CGGVeritas, 2008b). The operator length of filter ( $L$ ) was chosen 300 ms. The low-cut frequency was defined as 8 Hz with slope 24 dB/Oct to attenuate the swell noise (Figure 4.8). The high-cut frequency and its slope were determined as 90 Hz and 48 dB/Oct, respectively. Thus, high-frequency noise over 90 Hz from vessel were attenuated as well.

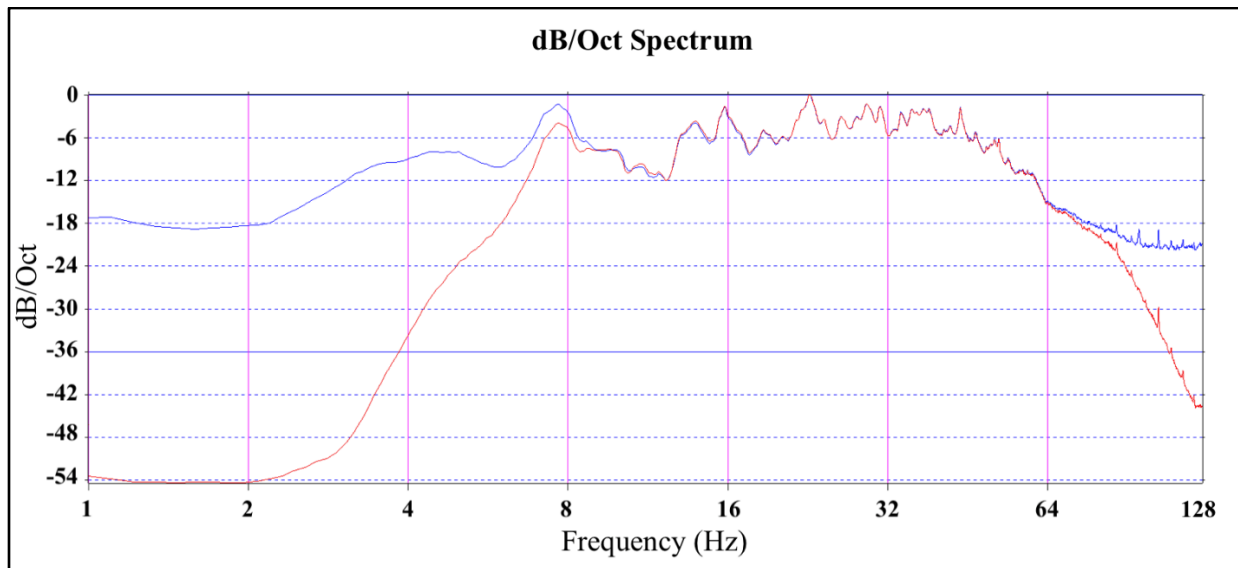


Figure 4.8 The results before (blue) and after Butterworth band-pass filtering (red) in dB/Oct Spectrum. The swell noise is suppressed below 8Hz. In addition, the peak about 7.5 Hz is due to the bubble pulse.

### 4.2.1.4 Resampling

The module RSAMP was used to digitized the recorded data by defining a new sampling interval and maximum frequency of the interpolation filter ( $F_{MAX}$ ), which is the highest frequency value to be preserved on output (CGGVeritas, 2008b).  $F_{MAX}$  was defined as 100 Hz, which is below the new Nyquist frequency after resampling. Because the Nyquist frequency was halved from 250 to 125 Hz, while sampling interval of the original data was increased from 2 ms to 4 ms.

#### 4.2.1.5 Spatial Amplitude Smoothing (with noise attenuation option)

Amplitude smoothing spatially was applied to attenuate the portions of a trace having noise bursts by the module SPASM. In this module, the parameters are dependent on user defined in the module, where number of input traces for comparison ( $NCa$ ) and length of the computation window ( $L$ ) for amplitude comparison. In addition, to activate the noise attenuation option, the amplitude threshold value ( $CTk$ ) and coefficient value for median amplitude at center ( $CMMp$ ) must also be determined, in addition to the mandatory parameters above. This method is based on a linear interpolation with coefficients between processing window centers (CGGVeritas, 2008b).  $CTk$  is operation of  $k$  times the value of median amplitude ( $CMM$ ). The amplitude at the center of the processing window is multiplied by

$$\frac{M}{m} \times p \quad (4.1)$$

where  $M$  is the median or average amplitude and  $m$  is the amplitude of the input trace, together ( $CMM$ ), and  $p$  is amplitude the coefficient value, which is defined as a real number varying in the range  $0.001 < p < 1.000$ .

For amplitude comparison and smoothing,  $NC$  was set as 11 and  $L$  was 500 as a default value.

For noise attenuation, the noise amplitude threshold value was set as 2.5, while the amplitude coefficient ( $p$ ) was set as 0.5 for multiplication by the average amplitude at the center of processing window.

#### 4.2.1.6 Geometry Calculation

The module MODET was used to modify the header definition and the geometry calculations for CDP gathers of the particular lines defined with the line number ( $W19$ ). The shot number ( $W2$ ) and the channel number ( $W17$ ) were extracted from seg-y headers as well. Therefore, offsets and number of the CDP gathers could be calculated from the information  $W2$  and  $W17$ . From the group interval ( $\Delta_R$ ) defined as 12.5 m which is divided by 2, the interval of CDP gathers was

calculated as 6.25 m, which is also their common-mid point. In addition to these computations for CDP gathers, the definition was completed with max fold calculation, which represents the maximum number of traces in CDP gathers by:

$$\begin{aligned} \text{Number of channels per streamer} &= \frac{\text{streamer length}}{\Delta_R} && (4.2) \\ &= \frac{3000}{12.5} \\ &= 240 \end{aligned}$$

and

$$\begin{aligned} \text{Max Fold} &= \frac{\text{number of channels} \times \Delta_R}{2 \times \Delta_S} && (4.3) \\ &= \frac{240 \times 12.5}{2 \times 50} \\ &= 30. \end{aligned}$$

#### 4.2.1.7 QC - 1 Spherical Divergence Correction

The gain function is computed by the module REFOR based on time raised to a power correction by amplitude multiplication compensating the geometrical spreading effect. The amplitude multiplication to the time of the sample ( $T$ ) in milliseconds was performed by multiplication coefficient  $(T/250)^n$  as the gain function, where  $n$  was set as 1. As a result of time raised to a power correction method, the amplitude of the late arrivals was increased, while the amplitude of the early arrivals was decreased. This step has been used only for QC purposes before displaying the sections in the TeamView. Thus, the data has not been impacted by the spherical divergence correction before implementation in the signature deconvolution in the next step.

#### 4.2.1.8 QC - 2 Near-Trace Section

Firstly, the module FANMO was applied to operate rapid NMO correction relying on only water interval velocity, 1480 ms since there had not been a velocity model library generated (from velocity analysis) yet. The module SELTR was used to pick out the near-offset trace (channel 1)

from each shot gather. The resulting near-trace section (Figure 4.9) for QC purposes at the end of the first Xjob before going through the next pre-processing sequences.

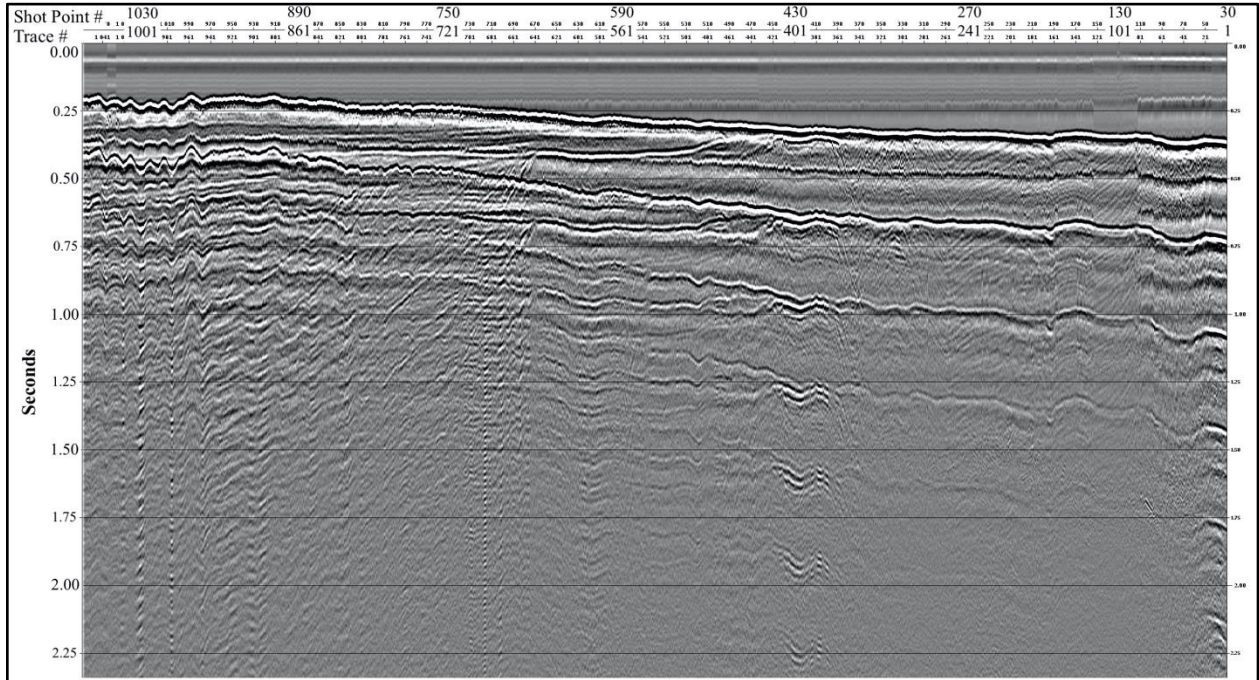


Figure 4.9 Near-Trace Section of the processed data after the first Xjob folder, including band-pass filtering, resampling, gain recovery by amplitude smoothing and spherical divergence correction.

#### 4.2.1.9 Signature Deconvolution

Signature deconvolution was applied by the module DESIG, computed by the desigature operator  $O_P(w)$  for arithmetic average of the amplitude spectrum in both the time and the frequency domain (CGGVeritas, 2008b). The program uses estimated values of roll-off slopes (dB/Oct) of low- and high-cut frequencies (Hz) of the source signal. Therefore, the minimum-phase of the output wavelet can be calculated by the desigature operator  $O_P(w)$ :

$$O_P(w) = \frac{A_T(w) \exp(iP_T(w))}{A_V(w) \exp(iP_V(w))} \quad (4.4)$$

where  $A_T(w)$  is the amplitude spectrum of the output wavelet;  $P_T(w)$  is the phase spectrum of the output wavelet;  $A_V(w)$  is the unmodified average amplitude spectrum with the addition of a white

noise parameter;  $P_V(w)$  is the minimum-phase spectrum computed from the modified amplitude spectrum (CGGVeritas, 2008b).

In the module, the operator length ( $LAR$ ) was determined as 350 ms and the low ( $FMIN$ ) & high ( $FMAX$ ) frequencies, as 8 and 90 Hz. The design window was set from 0 to 2500 ms. Thus, the input wavelet was reshaped a minimum-phase output wavelet. To do that, the high cut frequency ( $FMAX$ ) and high cut roll-off ( $SLPMX$ ) was set as same as minimum-phase anti-alias filter, which were 90 Hz and 48 dB/Oct respectively (Figure 4.10). Low cut roll-off parameter ( $SLPMN$ ) of the instrument was set as 24 dB/Oct. White-noise parameter ( $F$ ) was set 1010 as recommended value in CGG Veritas Release Notes. The effect of the signature deconvolution is presented in the QC results in Figure 4.12.

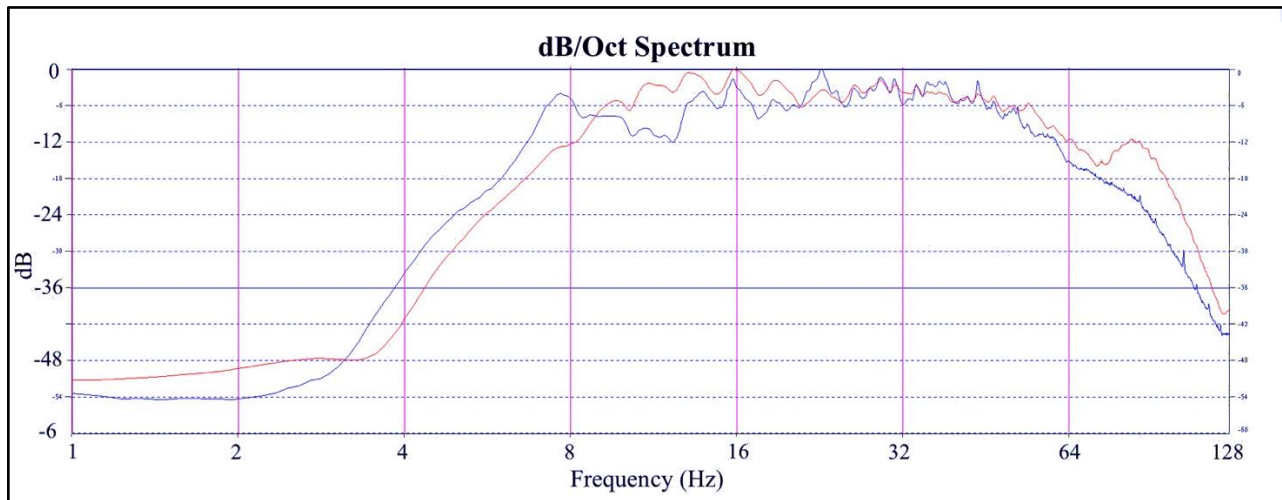


Figure 4.10 The results before (blue) and after signature deconvolution (red) in dB/Oct Spectrum. Even though the amplitude of the bubble pulses were suppressed at 8 Hz, random noise was boosted over 90 Hz.

#### 4.2.1.10 $f$ -x Projective Filtering

The module SPARN was used to attenuate incoherent noise after signature deconvolution and noise sources with a narrow frequency content, observed as spikes in the spectrum (Figure 4.10). The module computes  $f$ -x projective filtering instead of  $f$ -x predictive filtering (known as the  $f$ -x Decon). The projective filter is operated by computation of an auto-deconvolved prediction error filter ( $f$ ) in predictive deconvolution, to shorten the length of the input wavelet. The module was



used in the pre-processing workflow since it has been suggested to be applied before the muting step as it can cause noise in the muted zones (CGGVeritas, 2008b). The number of traces in the temporal elementary processing block was given as 50. Input traces were processed between the defined minimum and maximum frequency limits of impulsive noise as 7.5 and 50 Hz respectively. The length of the prediction error filter was defined as 11 (the value is the number of traces less than the number of input traces).

#### 4.2.1.11 Spherical Divergence Correction

The module REFOR for spherical divergence correction is suggested not to be applied before designature operation since noise after the process might be amplified due to a wrong estimation of the wavelet's roll-off parameters in the module DESIG (CGGVeritas, 2008b). However, spherical divergence correction had been already applied in the 1st Xjob folder was only for QC purposes that could not affect the dataset, where boosted traces appeared in that QC result. Therefore, spherical divergence correction by the module REFOR was applied after signature deconvolution not only to attenuate noise above the seabed but also to recover the amplitude of the late arrivals. So, the  $n$  value of the gain function  $(T/250)^n$  was determined as 1 to compute time raised to a power correction. Thus, the amplitudes of the late arrivals were recovered after 250 ms, while the amplitudes of the early arrivals were suppressed before 250 ms. Unfortunately, the amplitudes of the multiples were increased as well.

#### 4.2.1.12 Spatial Amplitude Smoothing

As a side effect of correcting for spherical divergence, amplitudes of seismic noise were strengthened. Spatial amplitude smoothing by use of the module SPASM in the 2nd Xjob folder was utilized to suppress that strong amplitude of noise. For amplitude comparison and smoothing, number of input traces ( $NC$ ) comparison was defined as 12 while the length of the computation window ( $L$ ) was set as 500. The noise attenuation option in this module was excluded as suggested as default in the Release Notes by CGG Veritas.

#### 4.2.1.13 $f$ - $k$ Filter

The module FKFIL was applied as a last step of the pre-processing step to filter undesired noise and seismic events such as the direct wave. The module requires the general parameters of the input traces which are trace number and interval, sampling interval, length of trace and maximum frequency going to be used in the velocity filtering in the  $f$ - $k$  domain. To define the apparent velocity limits, the shot gathers from the last processing result was used to transform the seismic traces from the  $t$ - $x$  domain to the  $f$ - $k$  domain by using of the Fourier transform. Then, the velocity boundaries were defined as -1750 and 1750 m/s in the  $f$ - $k$  spectrum to attenuate the energies in water column (Figure 4.11). The velocities higher than 1750 m/s in the positive panel of the wavenumber and the velocities lower than -1750 m/s in the negative panel of the wavenumber passed the filter, while the velocities below -1750 and above 1750 m/s were attenuated. For instance, the direct wave, whose velocity is approx. 1480 m/s, and streamer noise were eliminated from the data since their velocity is below 1750 m/s. Moreover, a wavenumber (spatial anti-aliasing) filter (*DECI*) was utilized in the module FKFIL applied as 2 in order to improve the interpolation for CMP gathers (in chapter 4.2.2).

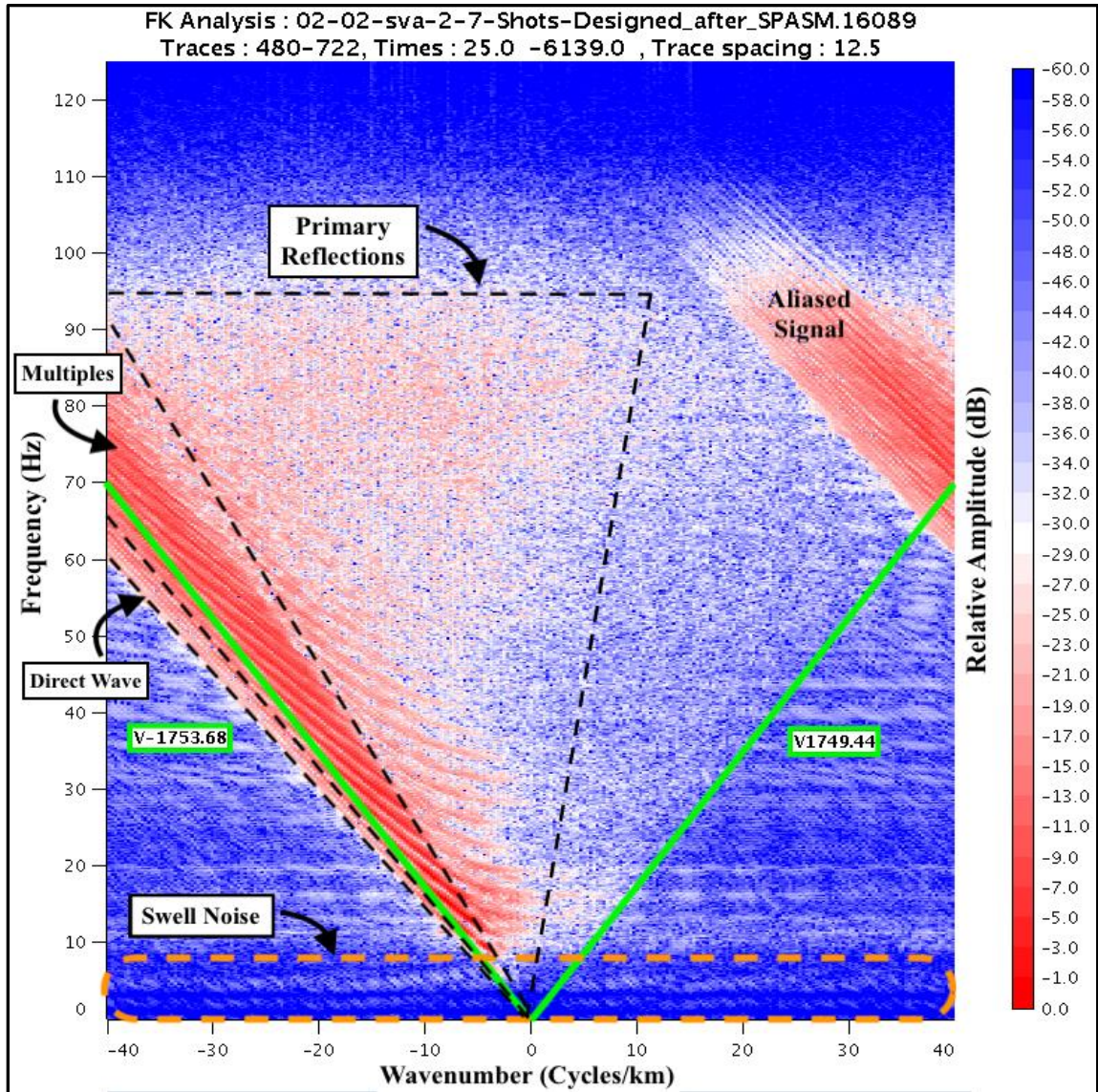


Figure 4.11 The  $f$ - $k$  Spectrum converted from shot gather # 101 to analyze the frequency (Hz), relative amplitude (dB) and apparent velocity (m/s) of the seismic traces. The velocity boundaries (green) were set as -1750 and 1750 m/s. Swell noise from the streamer are shown in the dashed polygon (orange). The primary reflections, the multiples, and the direct wave can be also distinguishable, as shown in the dashed polygons (black).

#### 4.2.1.14 QC - 3 Near-Trace Section

As result of the pre-processing, the direct wave, the bubble pulses, and the diffracted waves (mostly) were attenuated, while the low frequency component of the noise above the seabed reflection were amplified due to the side lobe of the  $f$ - $k$  filter shown in Figure 4.12. The side lobe would be removed by top muting before velocity modelling (4.2.3)



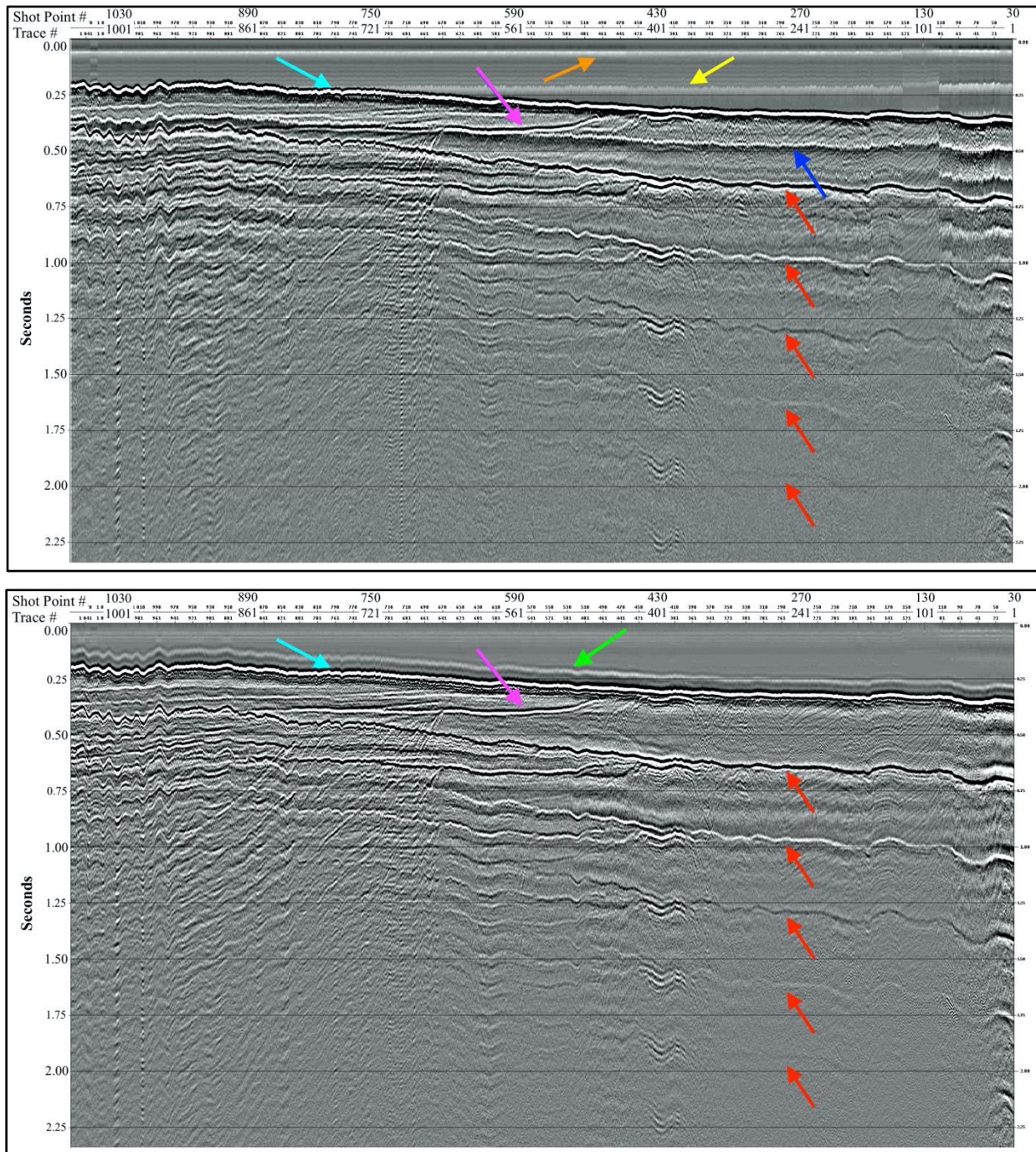


Figure 4.12 The comparison in near-trace sections for the raw data (top) and the preprocessed data (bottom). Seismic events are shown with various colored arrows; the direct wave (orange), the bubble pulse of the direct wave (yellow), seabed reflection (turquoise), subsurface reflection (pink), the bubble pulse reflected from the seabed (blue) and the surface-related multiples (red). As a result, the direct wave, bubble pulses and swell noise were attenuated, while side lobe of f-k filtering above seabed (green) were amplified.

### 4.2.1.15 Water Bottom Library

Water bottom library must be generated to be used in further processing sequences in CGG software. Therefore, seabed horizons were picked in the seismic lines on the TeamView, which saved the horizon information in water bottom libraries as CDP number versus time. As an example of water bottom library, seabed horizon picking for the seismic line 7 is shown in Figure 4.13.

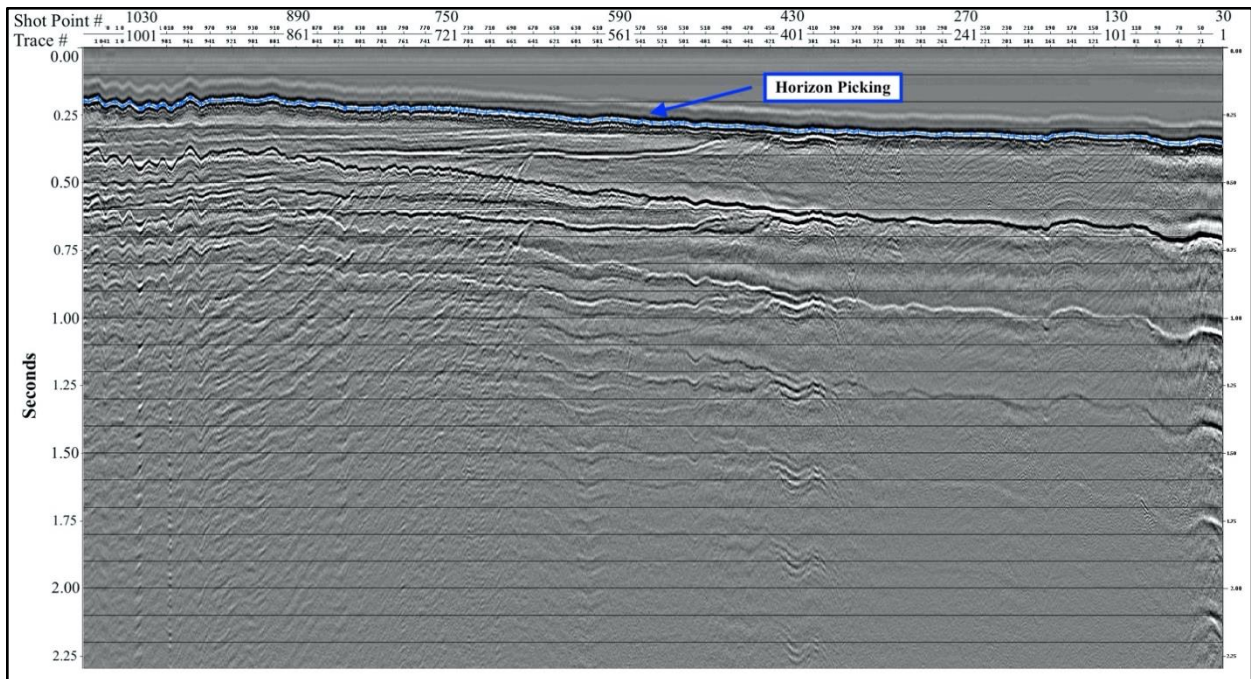


Figure 4.13 The near-trace section of the pre-processed dataset from the seismic line 7 demonstrates the extracted seabed horizon (blue line within the picked points) saved time vs distance in the water bottom library.

### 4.2.2 2D Spatial Trace Interpolation

In the Xjob processing folder, firstly, the module MODET was used to modify the header definition for number of the shots by multiplication of 4, which has increased the number of maximum fold from 30 to 120. Then next, the seismic traces in the CMP gathers were interpolated by the module INPOL. The module has generated the traces by regular interpolation option between two input traces. The output traces from regularly spaced CDPs issued by the processing the lag behind the input traces by

$$(NC-1)/2 \tag{4.5}$$

where NC is the number of traces in the model set as 7, which has generated 3 new model traces. Therefore, number of output traces per input trace (*INTERP*) was given as 4. After the last input trace, the post-processing loop is automatically issued number of times by

$$(INTERP \times (NC-1)/2) \tag{4.6}.$$

In addition, the module has also used the following information of the dip events for the interpolation (CGGVeritas, 2008b). The coefficient of adjustment of the dip selection threshold (*QZIX*) was 0.8. The calculation of the adjustment coefficients for each dip information was filtered out by a band-pass filtering within the defined limits: 8-16-40-60 Hz. The operator length of the band-pass filter (*L*) was set for 300 ms. The interpolated output traces were not filtered indeed but their amplitudes were synchronized by non-filtered input traces during the interpolation. Since the applied interpolation has been saved for each second CDP gathers, the CDP interval has increased from 6.25 m to 12.5 m. Therefore, the total number of traces saved in the CDP gathers has been doubled (Table 4.4). The similar geometry changes of other seismic lines after the interpolation can be found in the chapter A.2.2 as well as the near-trace section comparison of the line 7 for QC purpose (Figure A. 21).



Parameters of the Seismic Line 7	Specifications before the trace interpolation	Specifications after the trace interpolation
Minimum Shot Number	30	120
Maximum Shot Number	1087	4348
Number of Maximum Folds	30	120
Minimum Receiver Number	253	255
Maximum Receiver Number	9187	9187
Minimum CDP Number	500	501
Maximum CDP Number	9195	9195
Interval of the CDP Gathers	6.25 m	12.5 m
Number of the CDP Gathers	8695	4347
Total Number of the Traces in the Gathers	253920	507840

Table 4.4 The geometry parameters of the seismic line 7 before and after the interpolation.

### 4.2.3 Velocity Modelling

To have an estimated subsurface image of the research area, the interval velocities were converted to the RMS velocities to be used as velocity library in the velocity analysis preparation Xjob folder. To simply accomplished this processing sequence, the zero amplitude of the seismic traces were generated by the module DAGEN, within the defined range of the CDP gathers. The module MUTES was also utilized in the velocity modelling Xjob folder for external muting application above seabed, where the amplitudes of the first arrivals above seabed were zeroed out. To accomplished that, the water bottom library (in chapter 4.2.1.15) was used as well as the 2D deep water mute library (Table 4.5), which has been a user defined 2D muting function related to space variant. The mute function for marine seismic has been defined according to a water depth time ( $IQ$ ) (CGGVeritas, 2008b).

Water Depth (IQ Parameters) [ms]	Mute Time (M) [ms]	Mute Distance (X) [Offset Values]
0	0	0
0	1	100
3000	3000	0
3000	3000	100

Table 4.5 The 2D deep water mute library for water depth time (IQ) and the (M,X) pairs per mute functions, which is effective to mute above the seabed only. The length of the tapering was 40 ms applied to the starting of the mute function time.

The module MODET was utilized in the XJob folder 3 times in order to define the estimated velocities before and after muting operation. After the muting sequence and 3 times MODET application, the estimated interval velocities above and below the seabed were set as 1500 and 4500 m/s, respectively. In the module VI2VR, these estimated interval velocities were converted to the RMS velocities by

$$V_{RMS2} = \sqrt{\frac{(V_{INT}^2 \times (t_2 - t_1)) + (V_{RMS1}^2 \times t_1)}{t_2}} \quad (4.7)$$

where  $V_{RMS2}$  is the RMS velocity to calculate at the time  $t_2$ , which is the time of  $V_2$ .  $V_{RMS1}$  is RMS velocity at the time  $t_1$ , which is the time of  $V_{RMS1}$ .  $V_{INT}$  is interval velocity at the time  $t_2$ . Then, the velocity information from VI2VR was converted to the time sampled velocity traces in selected CDP gathers by the module TRVEL (CGGVeritas, 2008b). To generate volume of time sampled traces, the random times were set 80, 120, 180, 260, 360, 420, 500, 800, 1200, 1800, 2800, 4000 ms, respectively. Therefore, the generated velocity traces for the velocity analysis were saved in a velocity library (DBVI) including the information of selected random times within the selected CDP gathers. For the QC purposes, the model velocity was investigated virtually in the near-trace section (Figure 4.14).





Figure 4.14 The near-trace section of the modelled velocity ( $V_{RMS}$ ) image from the seismic line 7; ranging between 1500 - 4500 m/s.

#### 4.2.4 1st Velocity Analysis

The seismic traces in the CDP gathers were first prepared in a particular XJob folder to be used for velocity analysis in the time domain in the GeoVel package in the Chronovista software. In order to remove random noise, a band-pass filtering was applied to data by the module FILTR. The filtering limits were set with [5-10-87-105 Hz]. The operator length ( $L$ ) was given as 300 ms. The traces were computed and prepared for the velocity spectrums by the module VESPA using the generated velocity model as a reference. For the preparation, velocity library information was given from the velocity modelling library. The velocities, which have been displayed on the spectrum plot in GeoVel, were set between 1450 - 7000 m/s that are the typical velocities from Spitsbergen. The traces have been corrected by the  $n$  velocity function using the delta  $t$  coefficient, defined as 2.3, into a reference function. The  $n$  stack traces were generated as a percentage of the reference velocity ( $V_{INC}$ ) in steps of +/- 5% (CGGVeritas, 2008b). Number of analyzed function for lowest and highest values were given as -7 and +7, respectively. So, the minimum and maximum velocity functions were 65% and 135% of the reference velocity

function. Finally, the output CDP gathers from the preparation were sampled from the selected input CDP gathers with 2 km CDP interval (160\*12.5m), in order to display in the analysis software GeoVel. For instance, the input CDP gathers of the seismic line 7 were selected from #700 to #9160 with increment 160, which has displayed 53 CDP gathers in the velocity analyses of the seismic line 7. However, the analysis was performed for every displayed second CDP gather, a total of 27 CDP gathers, which yielded the CDP interval 4 km. The rest of the non-analyzed CDP gathers were interpolated to produce their  $V_{RMS}$ . In addition, the total number of displayed CDP gathers in the velocity analysis of the other seismic lines vary regarding to their latest acquisition geometry after the trace interpolation (A.2.2).

During the velocity picking, the simultaneous NMO corrected gathers, the shot gathers and the near-trace sections (Figure 4.15) were observed together for real-time QC purpose whether picked velocities were accurately chosen and flatten the primary reflections or not. Unfortunately, the hyperbolas of the primary reflections were almost masked by the surface-related multiples, which made the analysis very difficult. To avoid the multiples, the velocities were picked on the semblance (spectrum) plot by assuming that the velocities of primaries have been increasing downward below the surface. Therefore, the velocity analysis was not accurate for primary reflections and the multiples had to be suppressed by the adaptive subtraction method (explained in the chapter 4.2.5.4) to pick the more accurate velocities for the second velocity analysis (presented in the chapter 4.2.7). Once velocity picking is done, the obtained RMS velocities have been exported to a new velocity library as XPS to be used in the next processing sequences (CGGVeritas, 2008a).

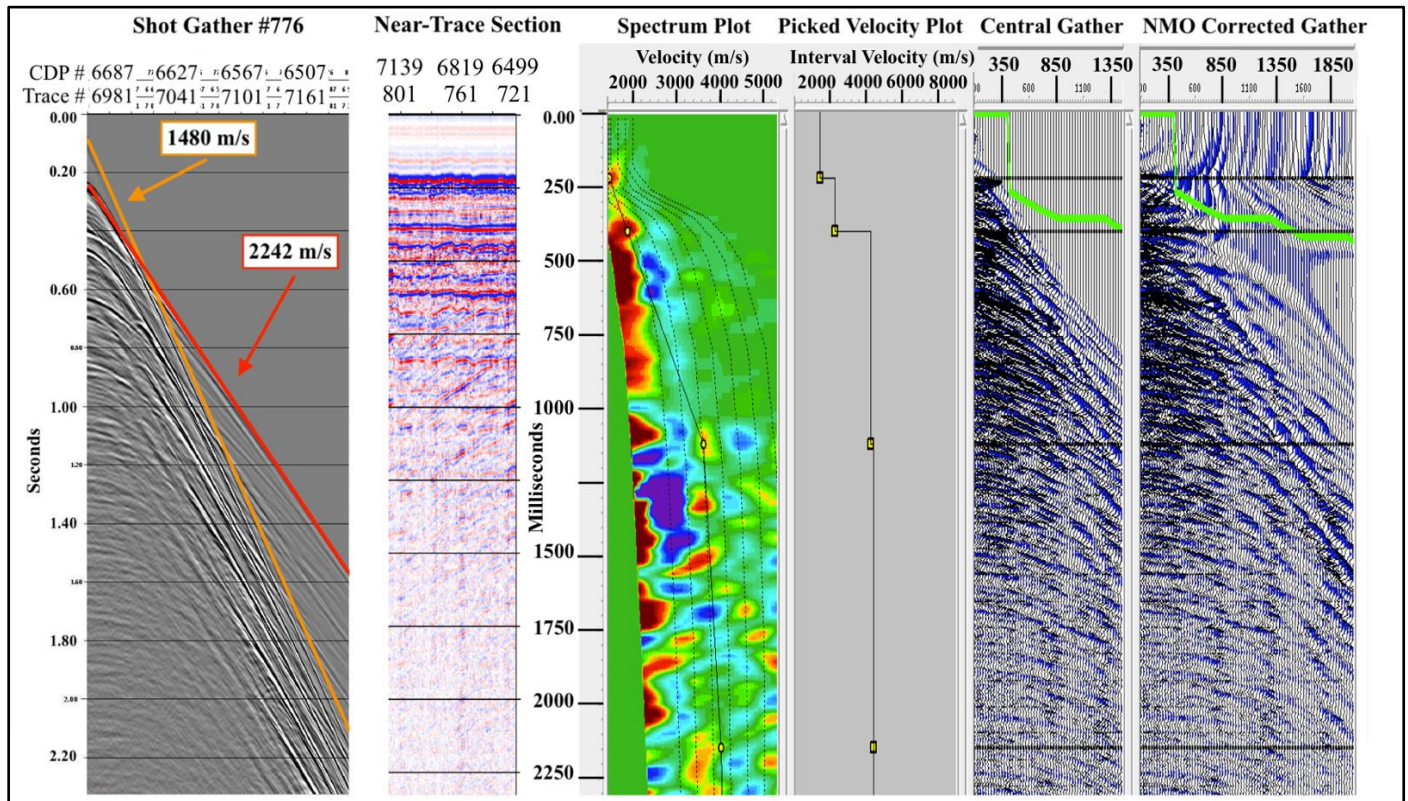


Figure 4.15 An example of the 1st velocity analysis performed on the spectrum plot by picking the velocities in the CDP gather #6625. The shot gather #776, providing the info for CDP #6625, was also used for the velocities of reflected (orange line) and refracted wave (red line). The interval velocities of the picked velocities can be seen as well as the real-time NMO correction. The green lines on the gathers define for the NMO stretch muting zone (above the line). The near-trace section after pre-processing were used not to pick surface-related multiples. However, the velocities could not be precisely picked between 400 and 1100 ms since the primary reflections were masked by the multiples below 600 ms.

Via the IsoVel package in the Chronovista software, the isovelocity contour map has been generated by RMS velocity for QC purpose to overcome velocity issues. The RMS velocities at the CDP #6625 in the model have been presented in the Figure 4.16. In general, the velocity model from RMS velocity has problematic velocity function due to the inaccurate picking velocities.

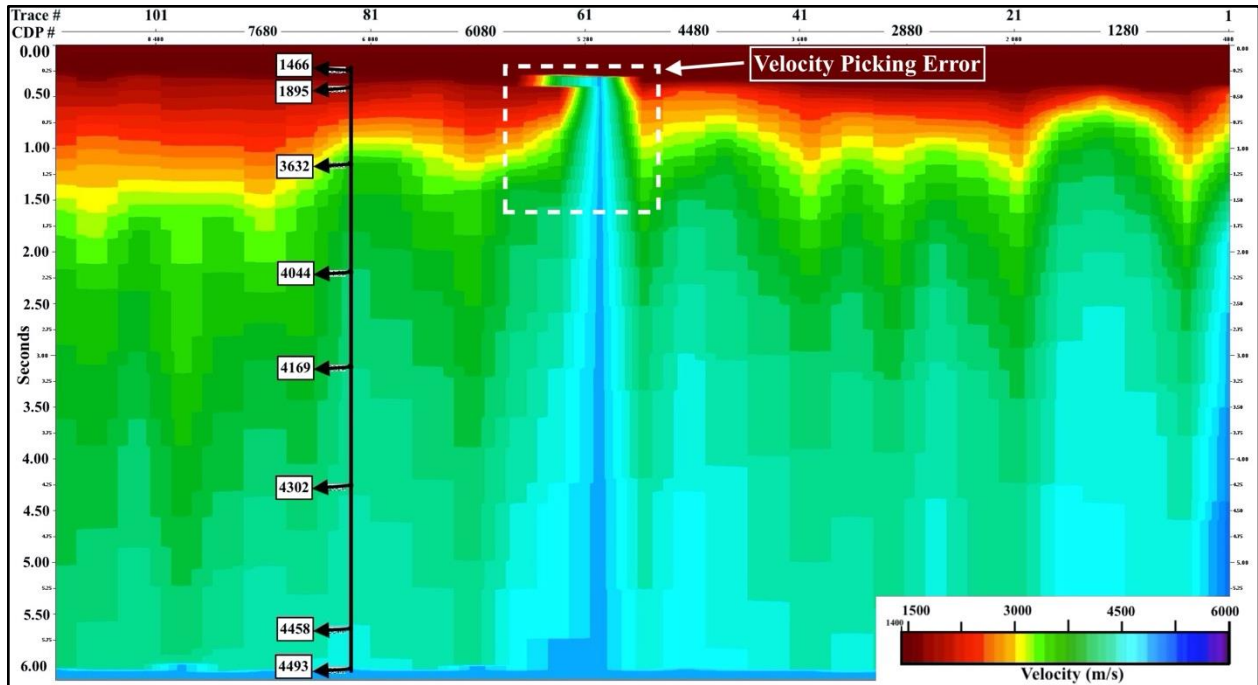


Figure 4.16 The isovelocity contour map illustrates the velocity field ( $V_{RMS}$ ) along the line 7 generated by the 1st velocity analysis. The RMS velocity values (m/s) from CDP #6625 are shown as an example of the RMS velocity range. This RMS velocity model includes problematic velocity functions for instance about CDP #5000 (the dashed polygon). The isovelocity contour map was derived using the velocity picks in the spectrum plots.

## 4.2.5 Multiple Extraction & Adaptive Subtraction

The surface-related multiples were suppressed by extracting the multiples and then adaptively subtracting them from the original data. To apply this approach, 2 sorts of datasets as inputs for the subtraction must be generated. These are the original dataset including both multiple and primary reflections and the 2nd dataset keeping only the surface-related multiple reflections. This approach was accomplished in 4 main steps, which will be explained in detail.

### 4.2.5.1 Step 1 - NMO Correction

In the beginning, the reflection hyperbolas of the multiples were kept bending downwards, while the reflection hyperbolas of the primaries were bent upwards from near- to far-offset by the forward NMO correction computed by 70% of the picked primary velocities (obtained in the 1st velocity analysis). The NMO correction was utilized in the Xjob folder with the module FANMO (forward). The results from different velocity percentages were also tested with 60%, 80% and



100% of the NMO velocities of the primaries through the subtraction approach (A.2.3). The best improvement for the subtraction was relying on the application with 70% (Figure 4.17).

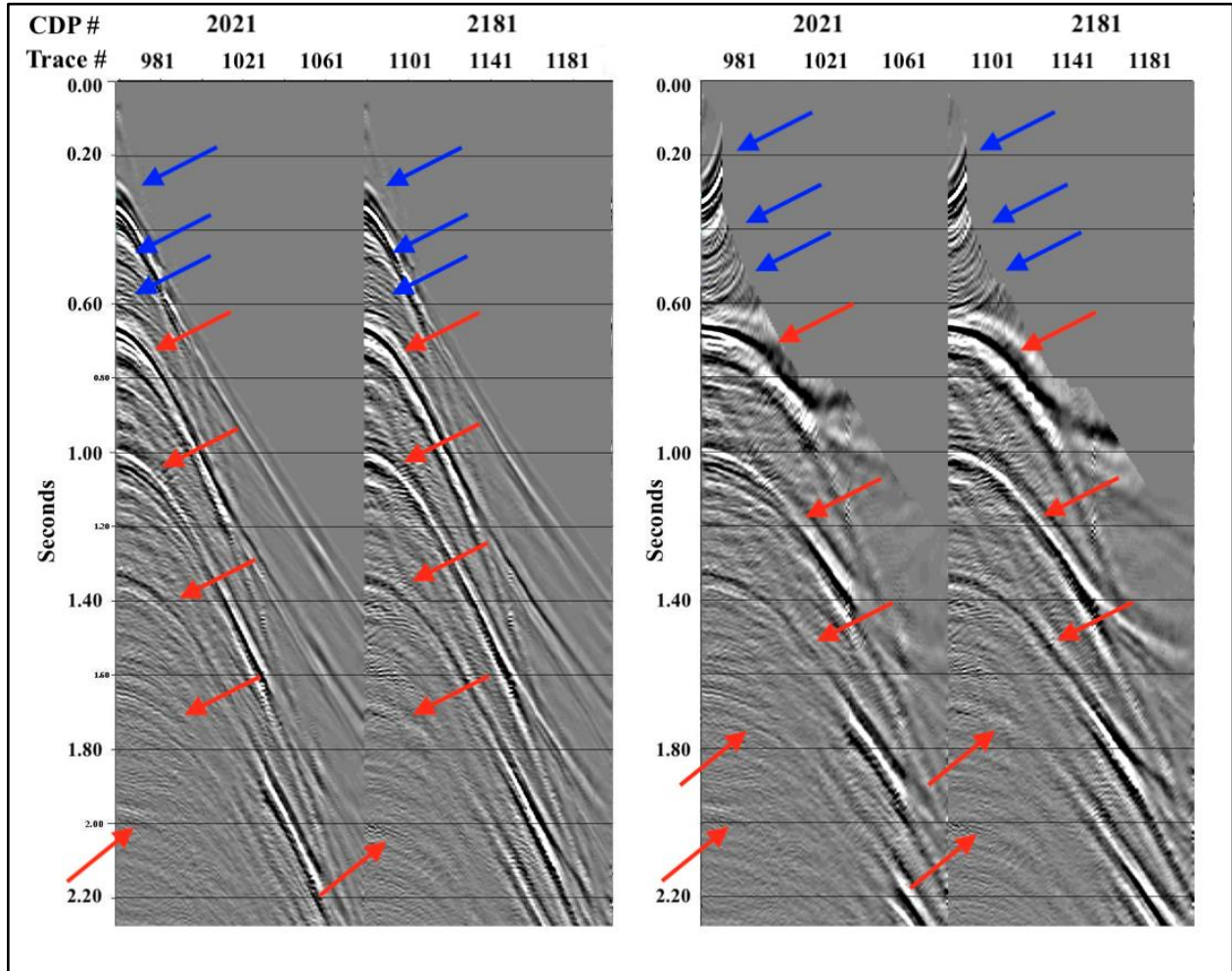


Figure 4.17 CDP gathers #2021 and #2181 were generated for QC purposes from interpolated data before (A) and after 70% NMO-corrected data (B), where hyperbola of the primary reflections (blue) bends upwards, while the multiples (red) bends downwards.

#### 4.2.5.2 Step 2 – Generating the 1st Dataset

The bent reflection hyperbolas of both primaries and multiples were returned to their original time by the inverse NMO correction using the module FANMO (inverse). The reason to apply the inverse NMO correction was to prevent the subtraction error due to the different NMO stretching, which may cause a mismatch between the two generated datasets. Thus, the 1st

modelled datasets as input1 for the subtraction was generated (Figure 4.18.A) by only applying the inverse NMO correction in order to keep both the primary and multiple reflections.

#### 4.2.5.3 Step 3 – Generating the 2nd Dataset: Multiple Modelling

To only keep the multiple reflections, the  $f$ - $k$  filter with the module FKFIL was used to eliminate the velocity of the primary events inside a filter polygon, while passing the velocity of the multiples by the module FKFIL. Therefore, the polygon boundaries were designed in the  $f$ - $k$  spectrum with -1750 and 150000 m/s as the band-pass filter for velocity. Then, the module HABIL was utilized to access the time of the seabed reflections in the water bottom library, where the picked seabed time vs CDP number were saved. Then, by the module MODET, these times of the seabed reflection were multiplied by 2 and subtracted by 100 ms. The calculated times of the seabed reflections were used in the module MUTES to mute the amplitudes above two times the seabed TWT. Because this part of the data does not contain any sea surface-related multiples and should, therefore, not be used in the adaptive subtraction. Finally, the inverse NMO correction bent the hyperbolas of the multiples downwards by use of the module FANMO (inverse). The 2nd modelled dataset was obtained consisting of mainly multiple reflections.

#### 4.2.5.4 Step 4 - Adaptive Subtraction:

The module LASUB for multichannel least-square adaptive subtraction was used in another Xjob folder that is a final step of the surface-related multiple attenuation approach that used two outputs generated from the multiple extraction Xjob folder. This subtraction was accomplished by a multi-model option as a two-step without iterative process (CGGVeritas, 2008b).

Firstly, the parameters of the adaptation operator were set as 100 ms for the length of the operator; 3 for the length of the operator in number of traces and 0.004 for pre-whitening factor. The computation of the operator was done by given

$$f_{min} = [d - (f_1 \star m_1) - (f_2 \star m_2)]^2 \quad (4.8)$$

where the asterisk stands for the convolution operation.  $d$  is the input dataset.  $m_1$  and  $m_2$  are the elements model data computed in spatial and temporal windows;  $f_1$  and  $f_2$  are the elements of 2D operator in the spatial and the temporal window, respectively.

In the final step of the two-step iterative process, this computed operator was applied to the model data by convolution in the spatial and temporal windows given by

$$m' = (f_1 \star m_1) + (f_2 \star m_2) \quad (4.9)$$

where  $m'$  is the adapted model data as input2 (Figure 4.18.B). Therefore, the energy of the modelled dataset was adapted to the recorded dataset  $d$ . Then, the resembled modelled dataset ( $m'$ ) as input2 was adaptively subtracted from the actual data ( $d$ ) as input1, which had the traces of both the multiples and primaries. The subtraction operation between these two datasets given by

$$d' = d - m' \quad (4.10)$$

where  $d'$  represents the adaptively subtracted data (Figure 4.18.C). As a result of multiple suppression, the reflection hyperbolas of the surface-related multiples were attenuated in the data. Thus, the velocity of the primary events could be more easily picked in the semblance spectrum window (Figure 4.20) in the second velocity analysis where the improvements are mentioned in the following chapter (4.2.6).

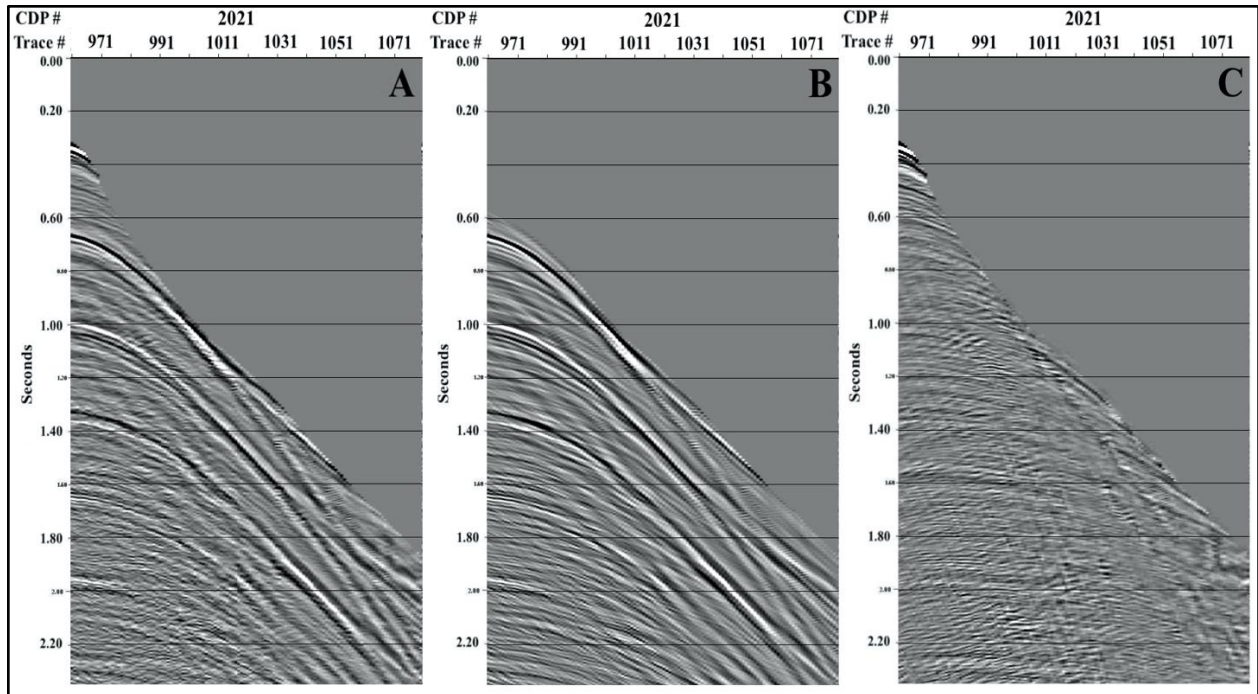


Figure 4.18 The figures show the impact of the adaptive subtraction method in the CDP gather #2021 from the actual input data (A) with hyperbolas of the primaries and the multiple reflections, extracted data (B) with hyperbolas of the surface-related multiples, adaptively subtracted data (C) with the attenuated multiples.

#### 4.2.6 QC Applications for Adaptive Subtraction Result

To have a quick look of the effectiveness of the adaptive subtraction, brute-stack images (A.2.3) were compared before and after the subtraction to investigate applied velocity percentages with the FANMO module as well. The results in brute-stack image (Figure A. 30) for 70% velocity were fascinating regarding to multiple removal comparing to alternative multiple elimination methods had been tried before (B.3). As a second QC, the CDP gathers #3781 from the seismic line 7 were displayed (Figure 4.19.A and Figure 4.19.B) in order to evaluate the multiple removals and increased amplitude of primary events in general. The multiples below approx. 600 ms were attenuated by the adaptive subtraction. Furthermore, the seismic traces in the CDP gathers from the subtraction as input were simply autocorrelated by the module CORRE for another QC. This computation was also applied to the traces before the subtraction method in order to observe the efficiency of the multiple removal in the autocorrelation sections (Figure 4.19.C and Figure 4.19.D). The comparisons in the autocorrelation sections have done for several CDP gathers as well.



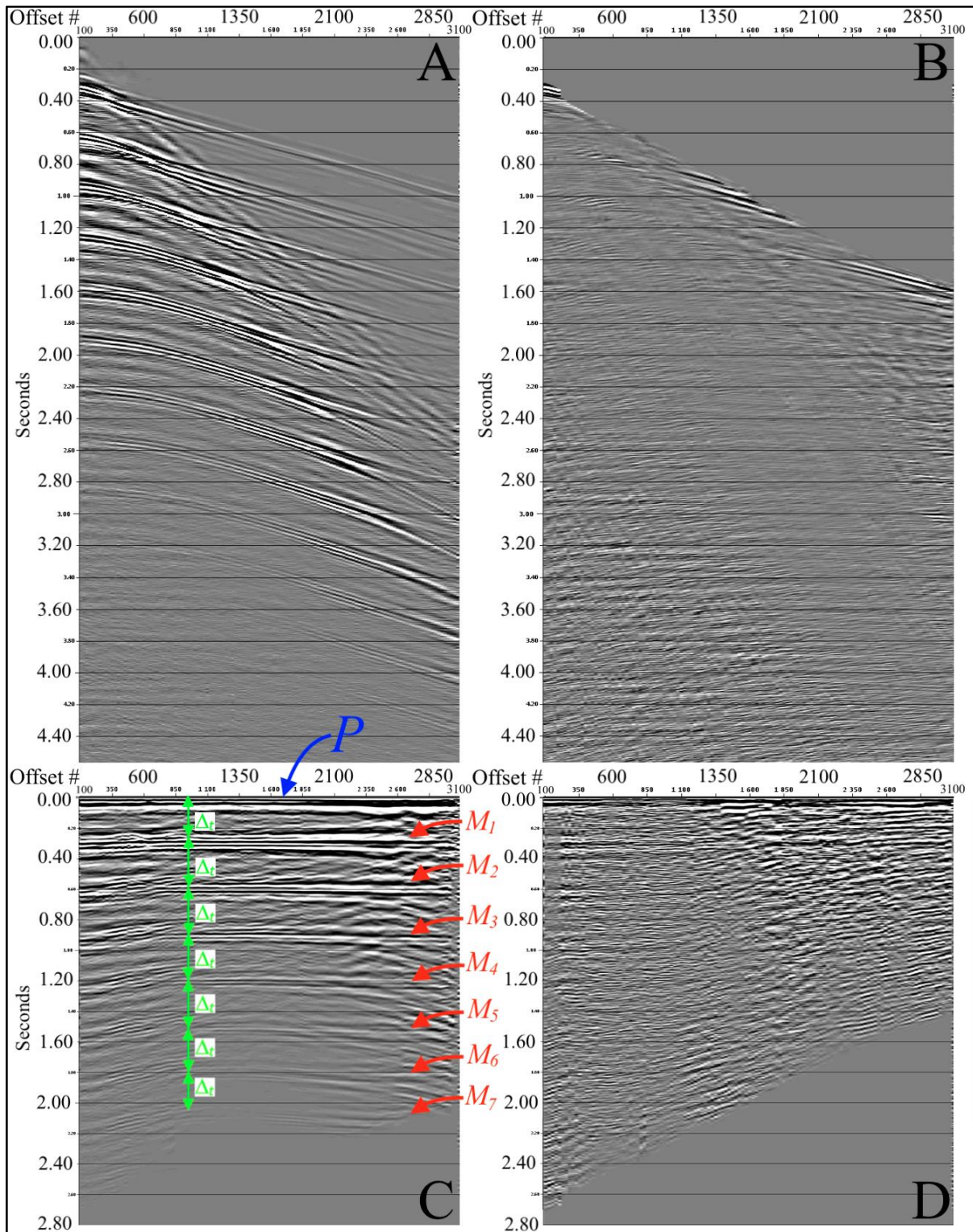


Figure 4.19 The CDP gathers #3781 before (A) and after (B) the adaptive subtraction with their corresponding autocorrelation sections (bottom). The primary reflection from the seabed (P), the surface-related multiples (M) and their recurrence interval ( $\Delta t$ ) as 0.3 s are shown in the autocorrelation section before the subtraction (C). The results after the subtraction have revealed that the multiples were attenuated below 0.6 s in the CDP gather (B); and below 0.3 s for every  $\Delta t$  in the autocorrelation section (D).

## 4.2.7 2nd Velocity Analysis

Thanks to the multiple suppression providing a higher S/N ratio from the adaptive subtraction method, the velocity analysis was done 2 more times for all seismic lines. Similarly, before the 1st velocity analysis, the output traces from the adaptive subtraction were prepared for the new velocity analysis by the module VESPA, which showed the CDP gather with the interval of 2 km. The second analysis was accomplished in every CDP gather, a total of 53 CDP gathers with interval of 2 km in seismic line, providing the better NMO corrections, especially at the dipping layers and graben structures. Thus, it was determined that velocity picking for all seismic lines after the adaptive subtraction should be done in every displayed CDP gather in the GeoVel during the 2nd velocity analysis. For instance, the 2nd velocity analysis performed in CDP #6625 was shown in Figure 4.20.

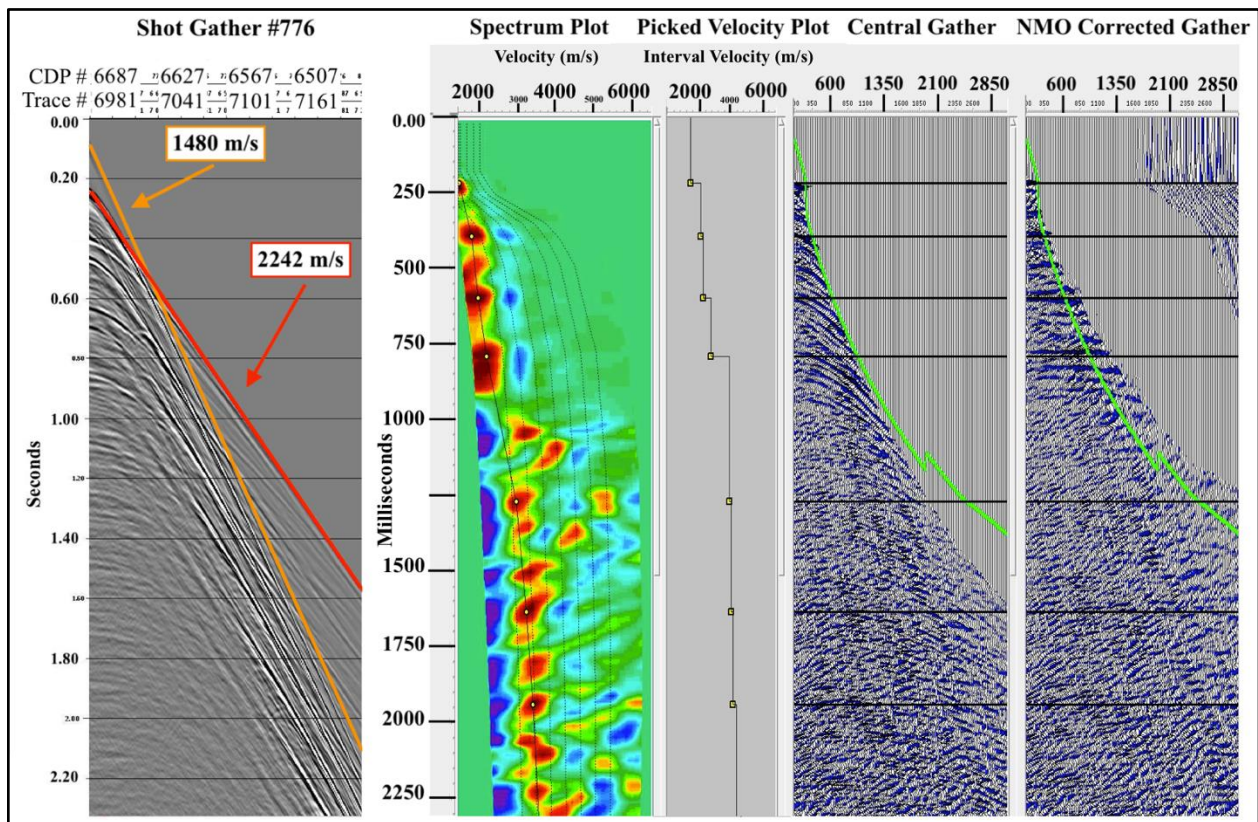


Figure 4.20 An example of the 2nd velocity analysis performed on the spectrum plot by picking the velocities in the CDP gather #6625. The shot gather #776, providing the info for CDP #6625, was also used for the velocities of the reflected (orange line) and the refracted wave (red line). The interval velocities of the picked velocities can be seen as well as the NMO correction. The green lines on the gathers define for the NMO stretch muting zone (above the line). Thanks to attenuated multiples below 600 ms, the velocities of the primaries could be picked easier than the 1st velocity picking, especially between 400 and 1100 ms.



Via the IsoVel package, the new isovelocity contour map has been generated by RMS velocity for QC purpose whether the issues were overcome or not. The RMS velocities at the CDP #6625 in the model have been presented in the Figure 4.21. In general, the new velocity model from RMS velocity has been a smoother version of the 1st velocity analysis. The latest velocity analyses result has been exported to XPS database to be used during the rest of the processing sequences.

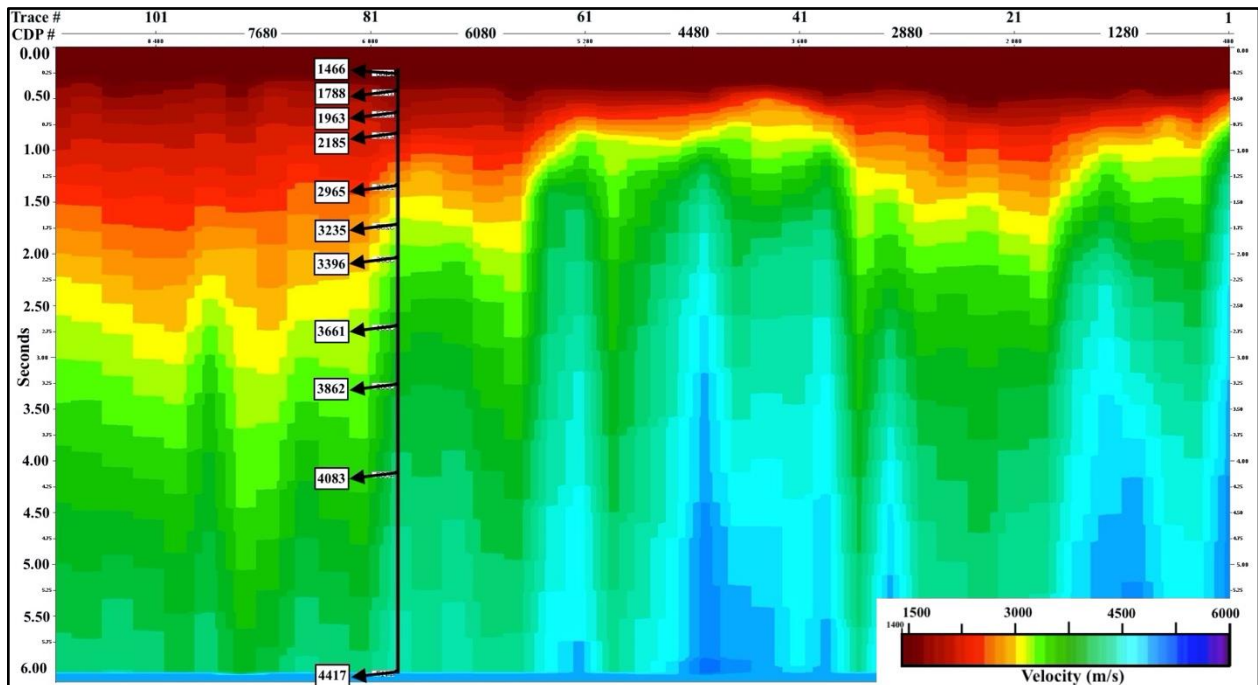


Figure 4.21 The isovelocity contour map illustrates the velocity field ( $V_{RMS}$ ) along the line 7 generated by the 2nd velocity analysis. The velocity values (m/s) from CDP #6625 are shown as an example of the RMS velocity range. Comparing the 1st velocity model ( $V_{RMS}$ ), this model has dealt with the picking issues in general and been smoother version. The isovelocity contour map was derived using the velocity picks in the spectrum plots.

#### 4.2.8 DMO Correction

The Xjob folder for DMO correction is utilized by several processing steps before the data has been DMO corrected. External muting the seismic traces based on the incidence angle approach by the module MUTAN, with the specific option of ray-bending approximation, was applied to the traces in the CMP gathers in order to eliminate the undesired effects, such as phase shift in wide-angle reflections, refracted waves and NMO stretching. The maximum muting angle was

set as 45° for seismic line 7, determined from the shallow areas on the near-trace section in the TeamView. Then, it was calculated from corresponding offsets to compute the traces within the velocity library (LIBRI VI), generated from the 2nd velocity analysis. The length of the smoothing angle for the ray-bending approximation was chosen as 120 ms. A band-pass filtering was applied to data by the module FILTR to attenuate the random noise. The filtering limits have been determined as [5-11.5-70-90 Hz] from the brute-stack image (A.2.3) generated for QC purposes after the adaptive subtraction. The operator length ( $L$ ) was given as 300 ms. Before applying the DMO correction, the traces were temporarily NMO corrected by the module FANMO. To overcome the conflicting dips issue, DMO correction was applied by the module KIDMO for the unstacked traces set for 2D mode. Hence, the wrong locations of the reflections were moved from source-receiver mid-point positions to their true zero-offset locations. Next, the DMO-corrected traces were inversely NMO corrected by another FANMO module.

#### 4.2.9 NMO Correction & Stacking

The distorted zone in the shallow part was muted by the module MUTAN, similarly in the DMO Xjob folder, in order to prevent the degradation impact from the DMO correction. This time, the maximum muting angle was set as 38° for seismic line 7, which was determined from DMO corrected CDP gathers. Then, the RMS velocities from the 2nd velocity analysis were used for the NMO correction by the module FANMO. Thus, the time shifts between the source and receivers of every single trace in the CMP gathers were moved out to their true zero-offset time before stacking. Finally, the NMO corrected traces in CMP gathers were totally stacked by the module STAPA. As a result of the NMO correction and the stacking, the resolution of the stacked images has significantly increased, as well as having considerably higher S/N ratio compared with the preprocessed data (Figure 4.22).

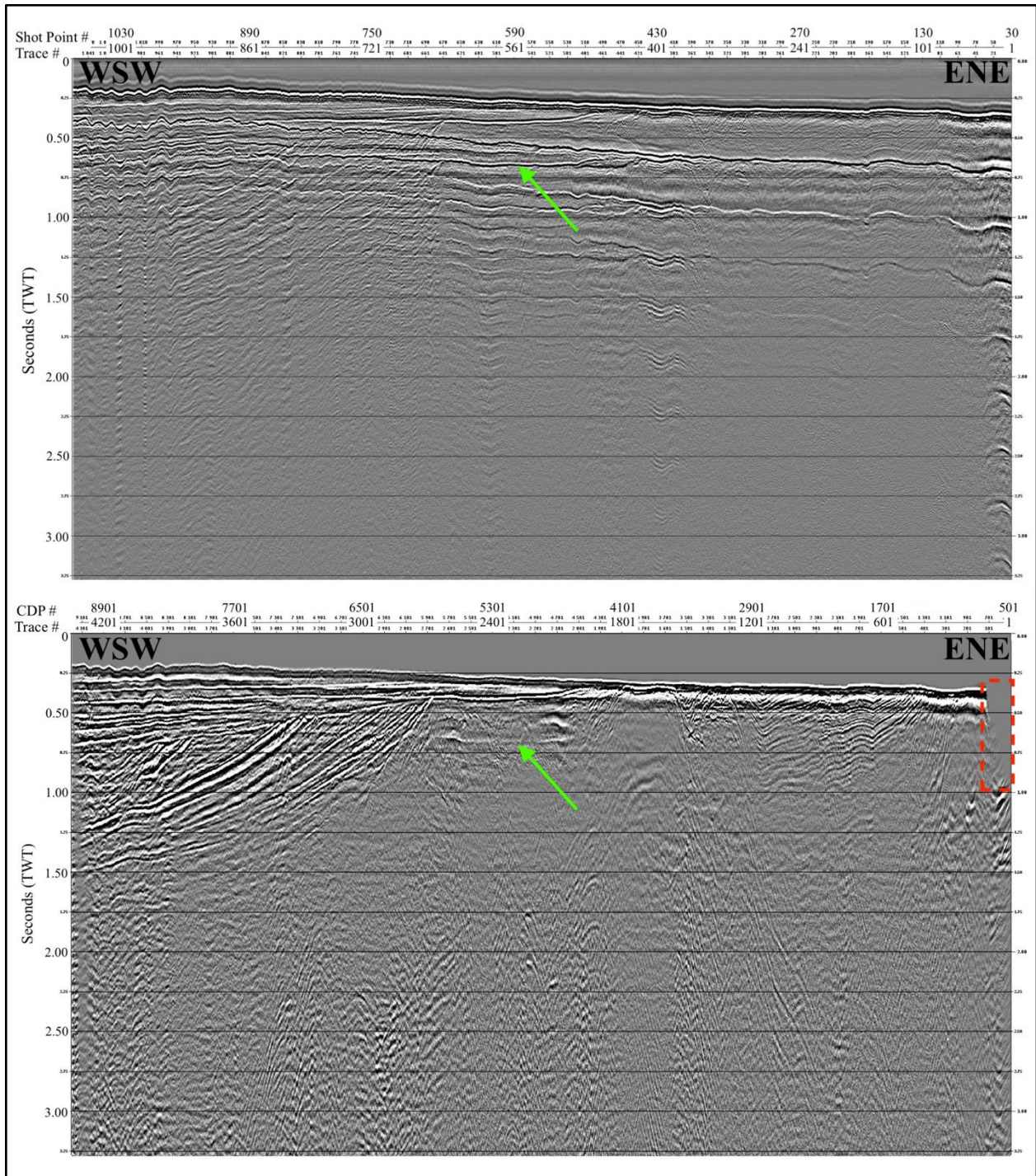


Figure 4.22 The comparison of the near-trace section after pre-processing (top) vs the stacked image (bottom) for QC purpose to find out the improvements in terms of the data quality and resolution thanks to completed processing steps. NMO stretch mute gap is shown in the red-dashed polygon. Green arrow shows the interbedded multiple which could not be completely attenuated by the adaptive subtraction.

#### 4.2.10 Post-Stack Processing Sequences Before the Migration

The Xjob folder for the post-stack time migration sequence consists of various modules to prepare the data for the seismic migration such as traces & header definitions, external muting, band-pass,  $f-k$  filtering, and amplitude scaling. At first, the module MNGTY was used to define whole stack section as one gather in order to apply  $f-k$  filtering to the stacked section. The headers were defined by the module MODET for the end of the front mute as 1 ms in order to reset the mute header word. The external muting before the migration was also applied by the module MUTES, where the amplitudes of the first arrivals above the seabed were zeroed out. The same water bottom library (chapter 4.2.1.15) and the 2D deep water mute library for water depth time ( $IQ$ ) and the ( $M,X$ ) pairs per mute functions were computed together in the module. The length of the tapering was 20 ms applied to the starting of the mute function time.

##### 4.2.10.1 Band-pass Filtering

A band-pass filtering was performed by the module FILTR, where the ideal filtering limits were determined as [5-15-45-80 Hz] among other tested limits, especially for the low frequencies. These different band-pass limits have been presented in Figure A. 37 showing the filtering impacts on low-frequency events, especially in the shallow part of the migrated section. The operator length of the band-pass filter ( $L$ ) was set to 300 ms.

##### 4.2.10.2 $f-k$ Filtering

The velocities of the diffractions have been measured mostly between 4500 and 6000 m/s in the TeamView. In some areas, the velocities have reached approx. 7000 m/s along the horst structure. To attenuate these high-velocity events, the FKFIL module designed as a four-velocity band-pass filter was applied to data before migration. The ideal limits among the tested ones were chosen as [-10000, -5500, 5000, 1000 m/s] for seismic line 7 where the steepest-dips were removed. In addition, the determined velocity limits have been varied for every seismic line. Significant results from the different  $f-k$  dips limits have been also shown in Figure A. 38.

### 4.2.10.3 Amplitude Scaling

The energy of the artificial effects from the stacking was reduced by the module SCALE before the migration. The spatial gain function with the value 0 was applied to the particular CDPs in order to taper the edges in both starting and ending of the section. Similarly, the bottom of the section was tapered to suppress the edge effects.

### 4.2.11 Post-Stack Time Migration

2D post-stack time migration was performed by the module FXMIG. The module algorithm is a special sort of implicit finite-difference migration solving the acoustic wave equation in the frequency-space ( $f$ - $x$ ) domain. The module was applied to zero-offset traces without the option (*LI*) since *LI* improves the steep-dips layer up to  $45^\circ$  in the module. Without this option, the module improves the steep-dip layer up to  $65^\circ$  (CGGVeritas, 2008b), which is the ideal approach for these structural apparent dips that have been calculated at about  $65^\circ$  in the stacked sections (Figure 4.22).

In order to solve the wave equation, the migration algorithm in the module has been operated on the pressure wavefield  $P(x,t,\tau)$  in two phases, where  $x$  is the depth point axis,  $t$  is the record time axis and  $\tau$  is the  $\tau$  time axis. The first phase was the implicit extrapolation of the frequency components of the wavefield in the time  $\tau$  by the successive iterations of the constant intervals (*TAU*). This phase is also called partial migration at the time  $\tau$ . The parameters of the partial migration for the *TSTART* and the *TSTOP* were defined as 0 and 6000, respectively. The program computes this 2D section at the  $i$ th iteration by

$$P(x,t,\tau=i.TAU) \tag{4.11}$$

where  $i$  was set as 12 ms due to the *TAU* value must be a multiple of sampling interval. User defined passband frequency components (Table 4.6) were used to form the extrapolation. Each extrapolation was done between the start time (*TSTART*) and the stop time (*TSTOP*) by



$$P(x,t,\tau=TSTART) \quad (4.12)$$

$$P(x,t,\tau=TSTOP) \quad (4.13).$$

In addition, the images of the subsurface  $R(x,\tau_i)$  were built between each extrapolation. These images were generated between the  $TSTART$  and the  $TSTOP$  by

$$R(x,\tau=TSTART) \quad (4.14)$$

$$R(x,\tau=TSTOP) \quad (4.15).$$

At the end of this partial migration process, the discrete sections were summed up to obtain the whole 2D section. Furthermore, the second phase was to generate the final migrated section by extracting the extrapolated data at time  $t = 0$  by

$$P(z,t,\tau) \quad (4.16)$$

$$P(z,t=0,\tau) \quad (4.17)$$

where  $z$  is the depths of the built subsurface images. During the partially migration, the time to the depth conversion was done by

$$z_n = (V_{INT} t_n)/2 \quad (4.18)$$

where  $V_{INT}$  used values from the velocity library of the 2nd velocity analysis. Moreover, the program also computed a time-variant bandpass filtering during the partial migration. As suggested in the CGGVeritas's Release Notes, these maximum frequencies were defined in decreasing order, while their corresponding time values were defined in increasing order, as shown in Table 4.6. The frequencies outside this passband, have not been migrated by the program algorithm.

Minumum Frequency (FMIN) [Hz]	Maximum Frequency (FMAX) [Hz]	Corresponding Time (TMAX) [ms]
5	100	250
5	90	600
5	80	1200

Table 4.6 shows the migrated frequencies of the passband and their corresponding times.

For seismic line 7, a total of 4347 traces ( $NT$ ), or CDPs, have been migrated to their true reflection points. The diffracted energy of the sections has been attenuated, while the structural dipping layers and lateral resolution has been improved.

A phase filter was applied to the data in order to convert the pulse shape of the migrated traces to zero-phase by the module PFILT. Before applying the phase filter, the computation of kurtosis ( $K$ ), also known as curvature for a group of input, was computed by the module. Therefore, the best result from the ideal phase filter could be provided by the kurtosis (CGGVeritas, 2008b), which is given as

$$k = \frac{\sum_{i=1}^N x_i^4}{(\sum_{i=1}^N x_i^2)^2} \quad (4.19)$$

where  $N$  is number of samples and  $x$  is the amplitude. Next, a user-defined filter forms the phase by the phase angle value ( $DANG$ ).  $DANG$  can be computed by either *the phase-rotation filters* ( $CO$ ) as user-defined, as constant angle values for all frequencies or *the p/f phase-filters* ( $PF$ ) given by

$$DANG = \frac{p}{f} \quad (4.20)$$

where  $p$  is a constant value and  $f$  is the frequency that should be approximately set at the center of the passband zone. However, the module was preferred to use by *the phase-rotation filters*

(CO) option, where the constant angle *DANG* was set as 25°. Hence, the traces were converted to zero-phase by the chosen filter with the kurtosis as a function of the angle.

Finally, an external muting was applied by the module MUTES in order to remove the noise above the seabed caused by the band-pass and the *f-k* filters, which were applied right before the migration. The muting parameters were set to remove all amplitudes above the seafloor. Hence, the migration sequence in the processing has been achieved.

#### 4.2.12 Seg-y Format Extracting

The last XJob folder was used to prepare the migrated data format (.cst) in the processing software CGGVeritas to convert a processed seg-y data format (.seggy) to be used in the Petrel software for seismic interpretation. To do that, the coordinate libraries (*LXY*) including x and y coordinates were accessed by the module HABIL, where x and y stand for easting and northing, respectively in the UTM-33zone. Next, the header of CDP, receiver and shot points were associated with these x and y coordinates by the module MODET. Then, the data became ready to be written as SegY format by the module SEGOU. First QC was done in the *cst* version of the seg-y data to observe in the TeamView whether the same x and y coordinates have been correctly engaged as same as the CDP, receiver and shot points. The final QC was done to compare the advancements between the near-trace image of the raw data and the fully processed migrated image from seismic line 7, as an example shown in Figure 4.23. All completely migrated seismic data can be seen in figures Figure 4.24 to Figure 4.27.

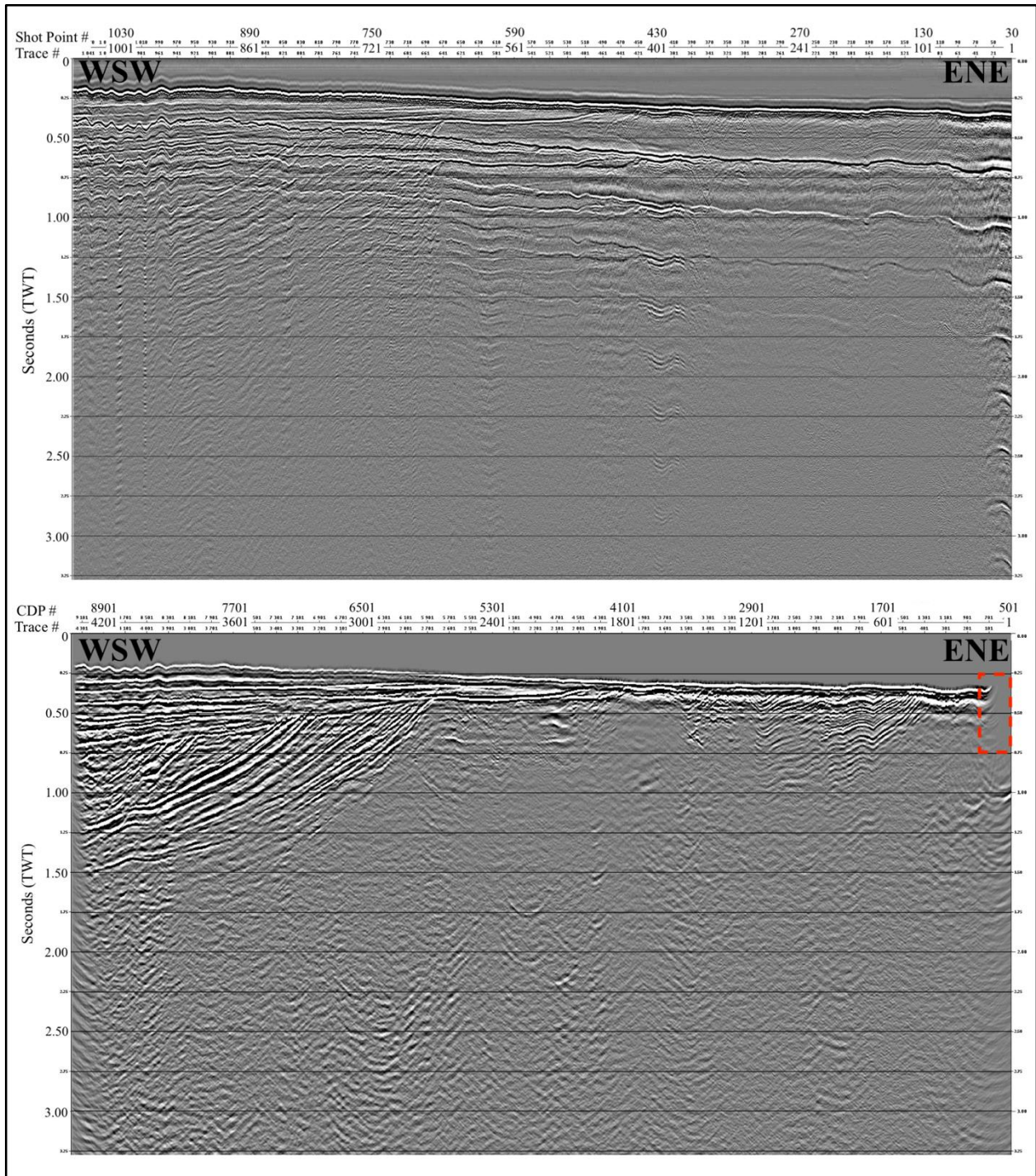


Figure 4.23 The comparison of the near-trace section of the raw data (top) vs the post-stack migrated image (bottom) for QC purpose to find out the improvements in terms of the data quality and resolution thanks to all processing steps. Swings are shown in the red-dashed polygon.



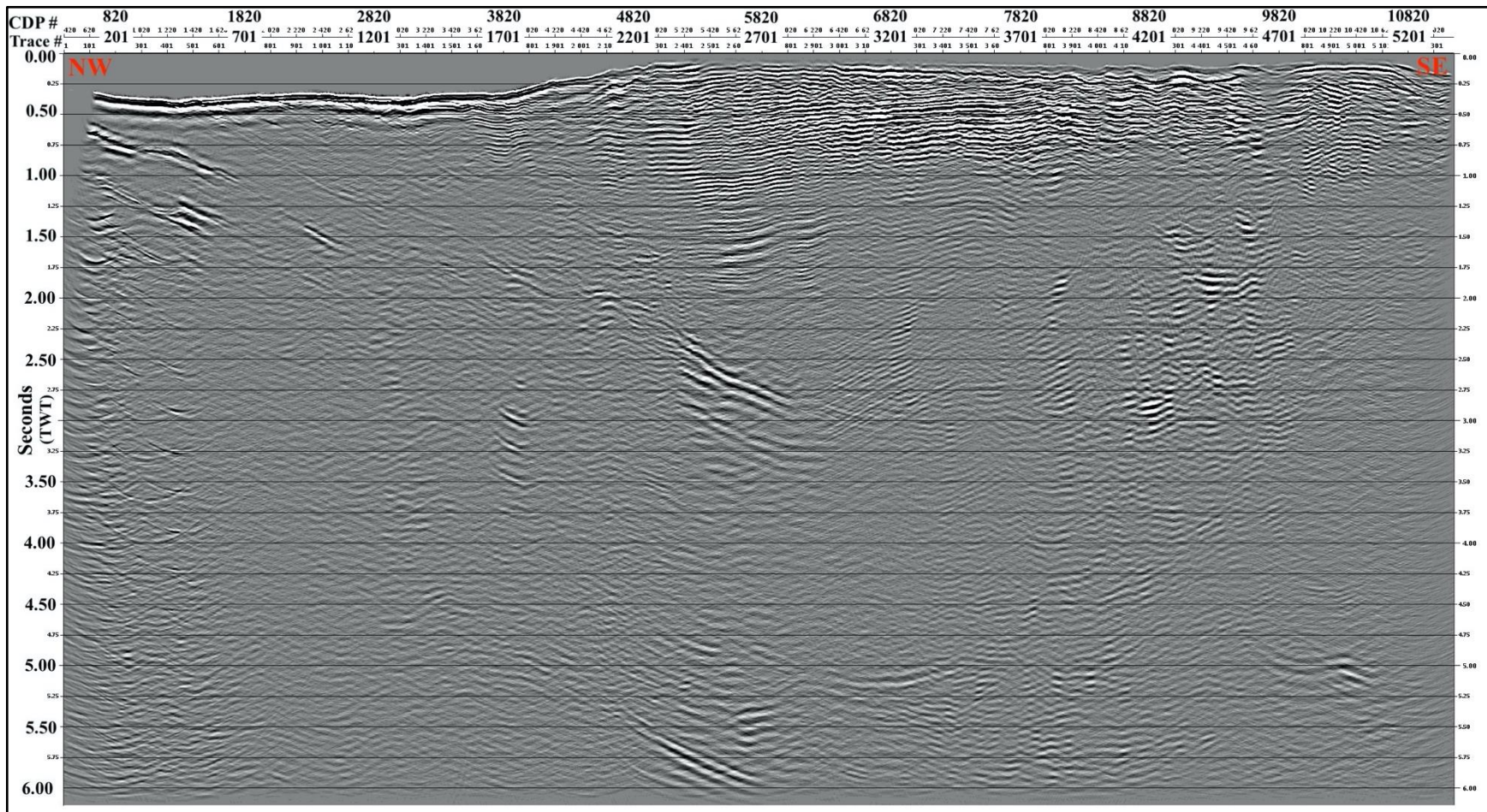


Figure 4.24 shows the seismic line 2 after post-stack time migration.



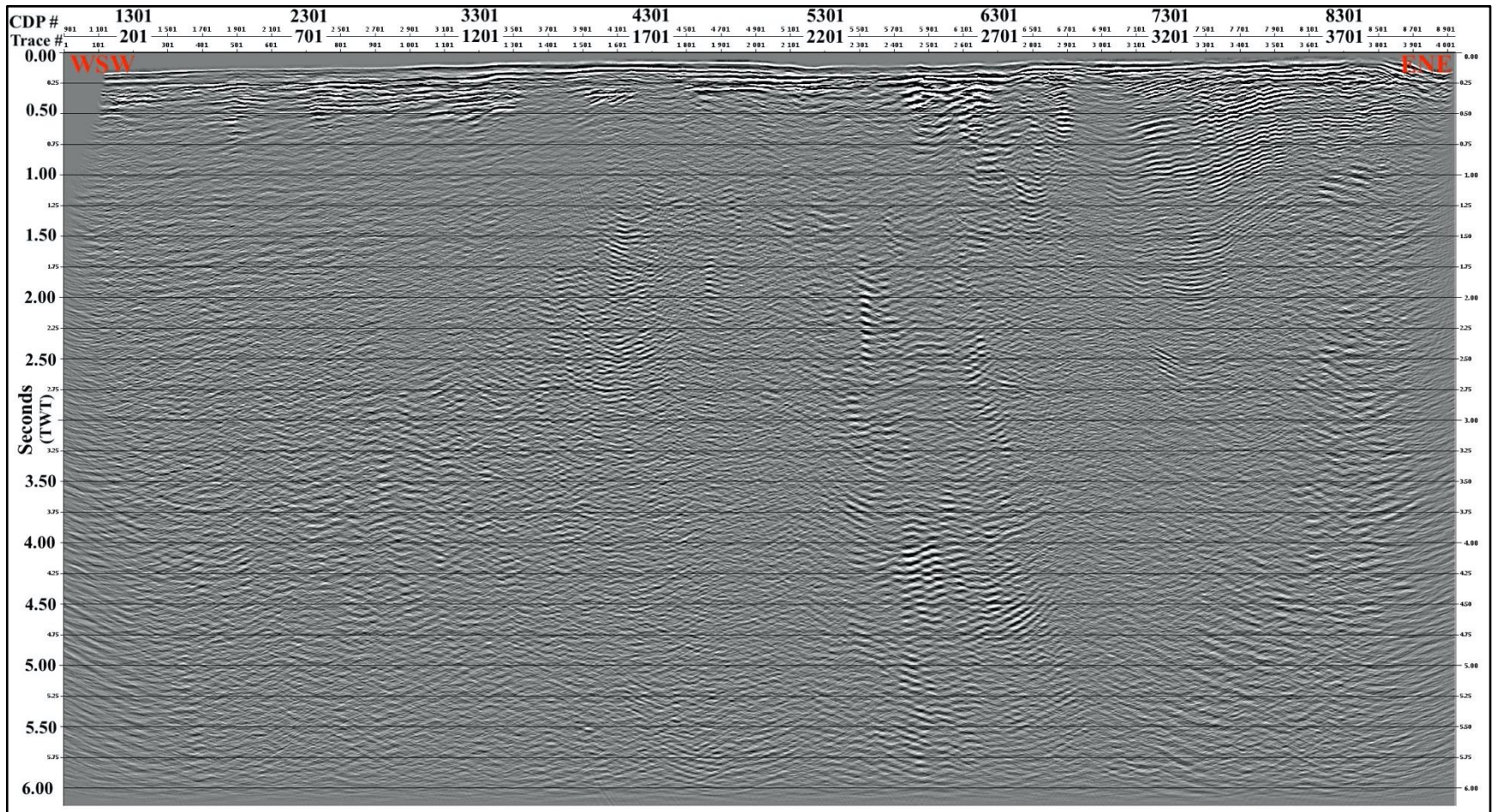


Figure 4.25 shows the seismic line 6 after post-stack time migration.



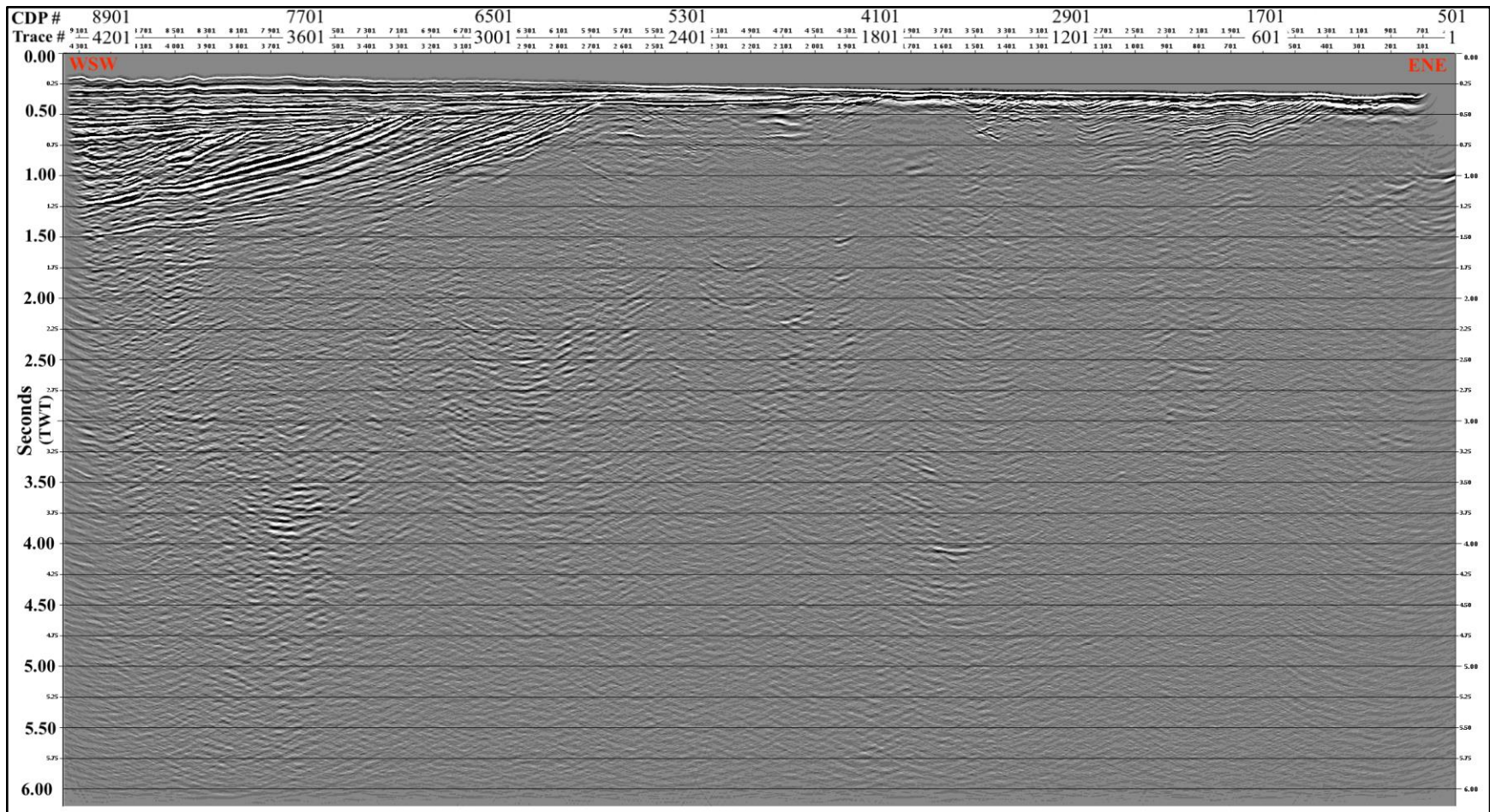


Figure 4.26 shows the seismic line 7 after post-stack time migration.



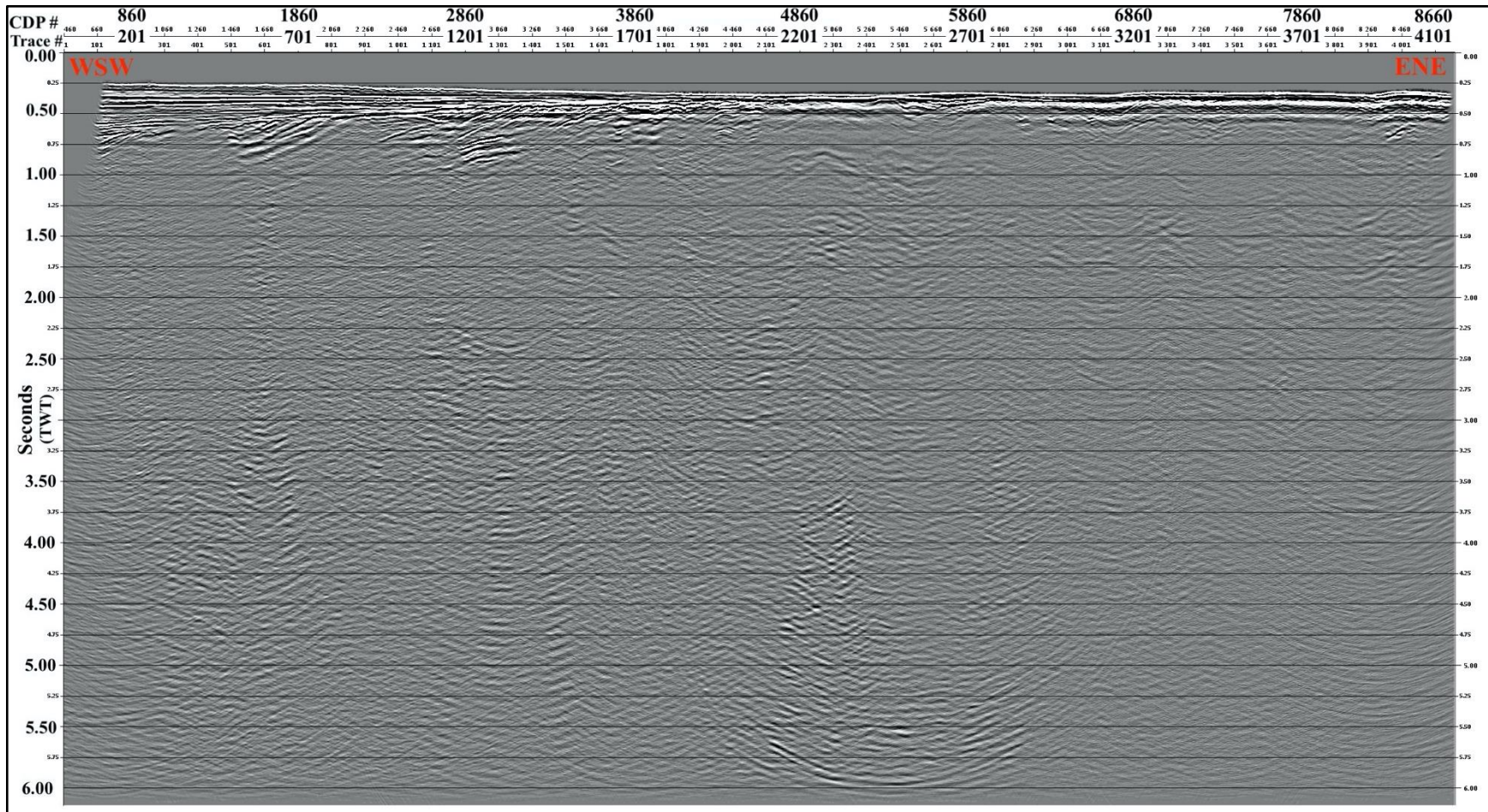


Figure 4.27 shows the seismic line 8 after post-stack time migration.

### 4.3 SEISMIC INTERPRETATION

The processed seismic datasets have been interpreted in order to analyze the stratigraphic units and deformation structures, which can reveal a possible structural model of the study area. The seismic interpretation has been done in Petrel software by Schlumberger (2020).

The 4 processed seismic lines were uploaded to Petrel as seg-y data format by setting the Coordinate Reference System (CRS), which is defined as ED50-UTM33. The stratigraphic units and faults were distinguished in the interpretation window. The horizons were picked by positive and negative polarities indicating the changes in acoustic impedance defined as peaks and troughs displayed by red and blue colors, respectively. During the horizon interpretation, 2 main modes were used: autotracking and manual. Autotracking mode was preferred for the continuous reflectors, while the manual mode was used for discontinuous, truncated and onlapping reflectors. Surface maps were then generated from the interpreted seismic horizons. To calculate the volume of the units, the surface maps were used to obtain thickness maps displaying the variation of the units in the 2D window. The surface maps and fault structures have been displayed together to correlate all outcomes in both 2D and 3D windows.

The seismic interpretation has been combined, correlated, and compared with several studies from western Svalbard with the aim of identifying the main structures and describing their tectonic development in the research area. The mainly used articles are from Blinova et al. (2009, 2013) and Dallmann (2015), while the other sources can be found below:

- Blinova, M., Thorsen, R., Mjelde, R., & Faleide, J. I. (2009): *Structure and evolution of the Bellsund Graben between Forlandsundet and Bellsund (Spitsbergen) based on marine seismic data*. Describes multichannel seismic reflection data from Isfjorden, Van Mijenfjorden and analyses the tectonic events, deformation structures and stratigraphic units of the West Spitsbergen continental margin.

- Blinova et al. (2013): *Analysis of structural trends of sub-sea-floor strata in the Isfjorden area of the West Spitsbergen Fold-and-Thrust Belt based on multichannel seismic data*. Describes multichannel seismic reflection data from Isfjorden, analysing the fold-and-thrust structures and stratigraphic units in the central part of the West Spitsbergen.
- Dallmann, W. K. (2015): *Geoscience Atlas of Svalbard*. Describes the evolution of Svalbard and West Spitsbergen area, explains the tectonic events and deformation structures in Svalbard as well as the essential information of the bedrock geology and stratigraphy of the area.
- Ågesen, L (2021): *Processing and interpretation of reflection seismic data from Isfjorden, Svalbard*. Describes reflection seismic data from Isfjorden, analyzing the deformation structures and stratigraphic units in the area (Master of Science Thesis, Department of Earth Science, University of Bergen).

During the interpretation of the Cenozoic sediment wedge, the unit has been subdivided into two main units by the unconformity layer (URU), as described by Blinova et al. (2009). The uppermost unit is a younger Cenozoic wedge consisting of subparallel horizons to the seabed and having strong amplitude. The underlying unit includes countless westward dipping sedimentary units. Neither these units nor sublayers have been previously given any specific name by other researchers. In this study, these dipping layers will be called the HFZ westward dipping layers 1-5.

Regarding the interpretation results by Blinova et al. (2009), although there was no clear indication that Paleozoic and Mesozoic sedimentary units may exist between the CSW and the underlying basement due to the multiples in the seismic images, it was still possible that Paleozoic or Mesozoic sedimentary rocks existed in the study area. In addition, Devonian sedimentary units in graben structures of inner Isfjorden have been characterized by Blinova et al. (2013). The seismic character of Devonian sediments has been described as chaotic and

discontinuous or with short reflectivity intervals, and the amplitude was scattered and relatively weak compared to the basement. Therefore, the potential unit overlying Hekla Hoek was interpreted as Old Red sediments, without certain evidence indicating its geological period either from Devonian or Early Carboniferous. This unit has been named Devonian during the seismic interpretation of this thesis, since these Old Red sediments were the erosional product of the post-Caledonian orogeny in Devonian (Dallmann, 2015).

Hekla Hoek basement rocks were characterized as deformed and faulted by Blinova et al. (2013). The reflection character of the basement was described as a chaotic and discontinuous short reflectivity pattern having low amplitude.

#### 4.3.1 Horizon and Fault Interpretation

Reflection layers and fault indications have been interpreted in order to analyze the formation structures and the stratigraphic units in the study area. Thanks to the high S/N ratio and better data quality, 9 seismic horizons in total have been distinguished only in seismic line 7. 4 of them are the main horizons; Seabed, URU, top Devonian and top Hecla Hoek, which have been interpreted in all seismic lines as well. The rest of them are unknown westward dipping layers in CSW overlying relatively flat unconformities, named the HFZ westward dipping layers 1-5. Only the HFZ westward dipping layers 4 and 5 were barely interpreted in seismic lines 6 and 8. The HFZ dipping layer 3 was inaccurately interpreted as an assumption.

Due to the high resolution and better continuity of the horizons, the interpretation was completed in seismic lines 2 and 7 first. Then, generated composite lines were used to correlate the horizons at their intersected points among the lines. The 3D window feature of the Petrel has also been used to observe any mismatching at the intersections. Therefore, horizon interpretation was succeeded with high accuracy, especially for the Seabed and URU. The uncertainties of the top Devonian and top Hecla Hoek horizons will be mentioned in the discussion part.

During the horizon interpretation, the positive and negative polarities of the signal at reflection layers were picked from both peaks and troughs, respectively regarding their reflection characters (Table 4.7). Thanks to medium to high amplitude and mainly continuous reflectors, the Seabed and URU horizons have been mostly interpreted by the 2D autotracking mode. Due to the top muting steps to remove the noise above the seabed during the seismic data processing, the amplitude of the seabed horizon has been weakened. Due to the truncation impact, some discontinuous reflectors at the angular unconformity horizon URU have been completed by manual interpretation mode as well. The westward dipping layers underlying the URU horizon have been identified by both the 2D auto-tracking and manual settings. The unconformity layer Top Devonian has been characterized only in BG by manual interpretation. From the south to north direction in seismic line 2, onlapping strata to Devonian sedimentary strata have been observed. The interpretation of top Hecla Hoek has been mostly manually interpreted by connecting the strong amplitude reflectors interpreted by 2D autotracking.



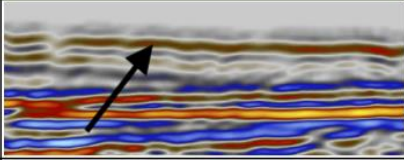
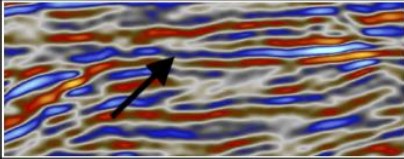
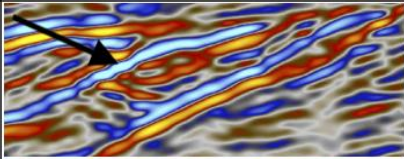
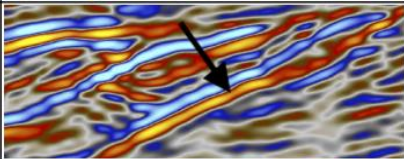
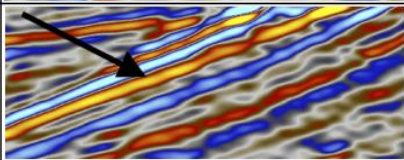
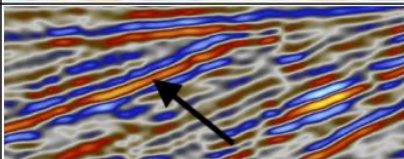
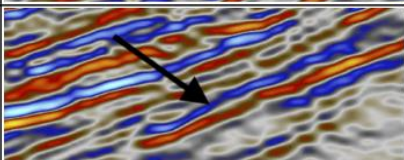
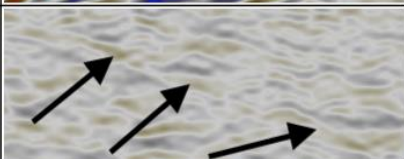
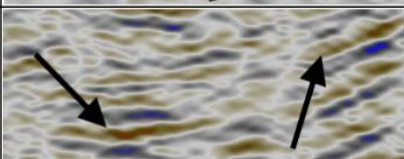
Seismic Horizons	Polarity	Reflection Character	Seismic Signature
<b>Seabed</b>	Positive (Peaks)	-Medium to High Amplitude, -Mostly Strong Continuous Reflectors	
<b>URU</b>	Negative (Troughs)	-Medium to High Amplitude, -Continuous to Discontinuous Reflectors	
<b>HFZ Westward Dipping Layer 1</b>	Negative (Troughs)	-Very Strong Amplitude -Continuous to Discontinuous Reflectors	
<b>HFZ Westward Dipping Layer 2</b>	Positive (Peaks)	-High Amplitude, -Continuous to Discontinuous Reflectors	
<b>HFZ Westward Dipping Layer 3</b>	Positive (Peaks)	-Very Strong Amplitude, -Mostly Strong Continuous Reflectors	
<b>HFZ Westward Dipping Layer 4</b>	Positive (Peaks)	-Low to High Amplitude, -Continuous to Discontinuous Reflectors	
<b>HFZ Westward Dipping Layer 5</b>	Negative (Troughs)	-Low to Medium Amplitude, -Continuous to Discontinuous Reflectors	
<b>Top Devonian</b>	Positive (Peaks)	-Weak Amplitude, -Mostly Discontinuous Reflectors	
<b>Hecla Hoek</b>	Positive (Peaks)	-Low Amplitude, -Continuous to Discontinuous Reflectors	

Table 4.7 The table shows the reflection character and seismic signature of seismic line 7 and picked polarities as peaks or troughs during the horizon interpretation.



During the interpretation of top Devonian and top Hecla Hoek horizons, the apparent major and minor down-faulted blocks in the HFZ and BG were also interpreted at the same time. The slight tilts, the shift of the similar and parallel continuous horizons, the undulated horizons and the instant transparency of the amplitudes were very helpful to interpret these faults in the HFZ and BG locations. At chaotic reflectivity patterns and suspicious areas, stacked images of the seismic lines were visited to identify the edge of the fault blocks roughly by the related diffractions. The horizons and faults interpreted for all seismic profiles can be seen in figures Figure 4.28 - Figure 4.31.

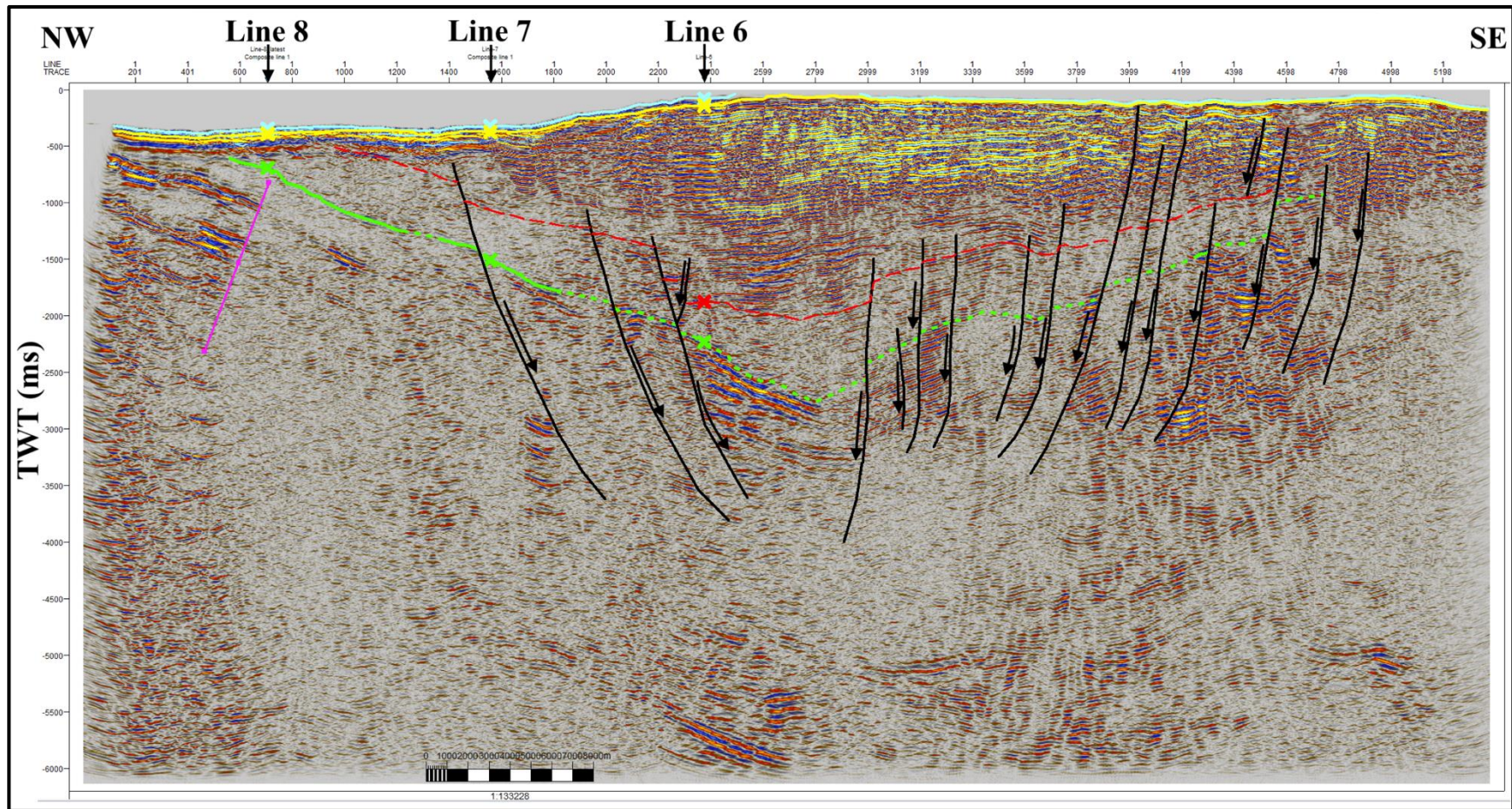


Figure 4.28 Horizon and fault interpreted image from seismic line 2. The interpreted horizons: Seabed (turquoise blue), URU (yellow), top Devonian (dashed red line), and top Hecla Hoek (green dashed & straight lines). The black lines and arrows present the faults and their motions. The symbol X indicates the horizons at their intersecting points with other seismic lines. The strike-slip fault off Isfjorden is indicated as pink line.



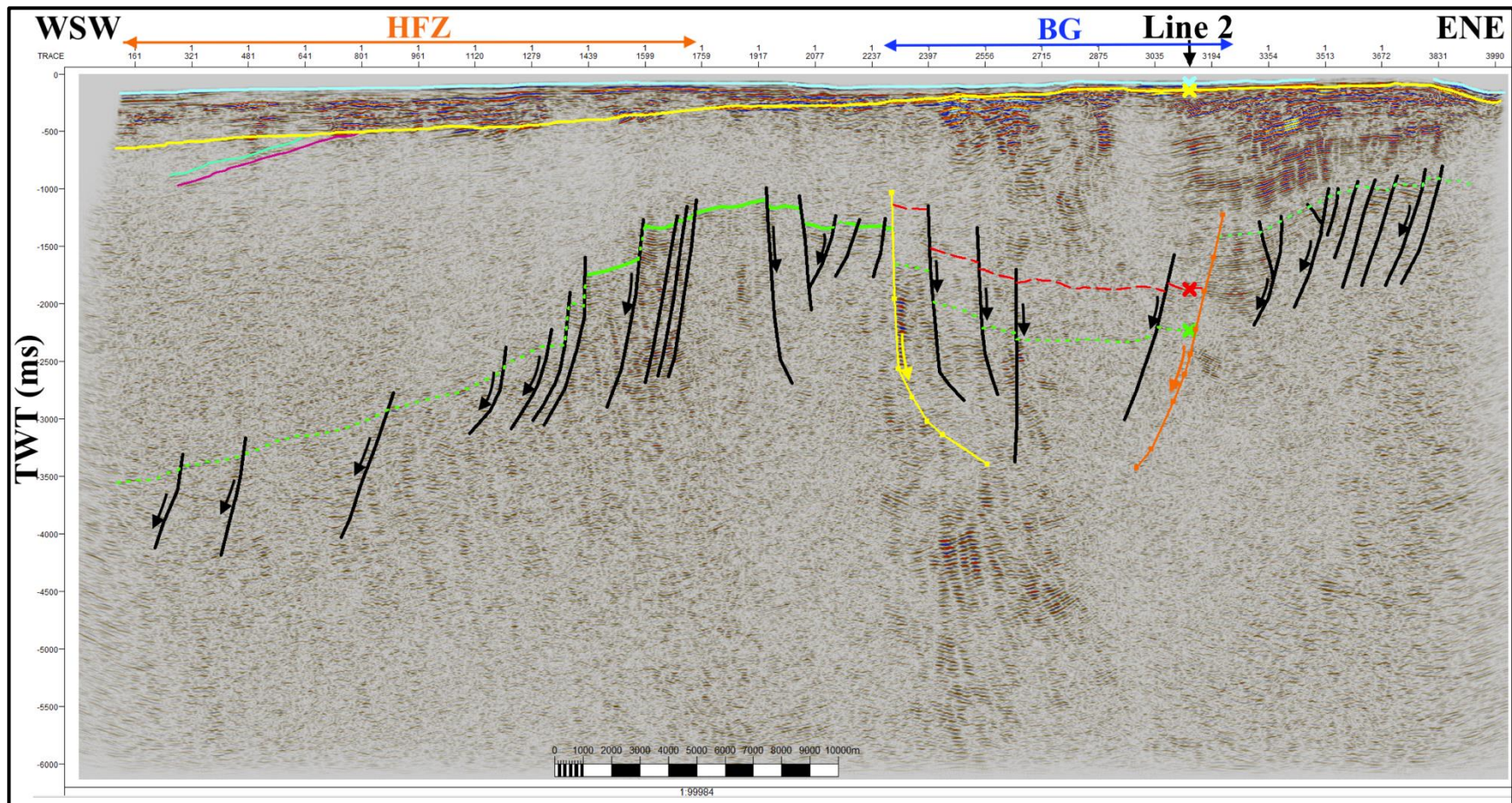


Figure 4.29 Horizon and fault interpreted image from seismic line 6. The interpreted horizons: Seabed (turquoise blue), URU (yellow), HFZ dipping layers 4-5 (turquoise green and purplish red lines, respectively), top Devonian (dashed red line), and top Hecla Hoek (green dashed & straight lines). The black lines and arrows present the faults and their motions. The eastward dipping major fault (yellow) at the western boarder of the basin. The westward dipping major fault (orange) at the eastern boarder of the basin. The symbol X indicates the horizons at their intersecting points with seismic line 2. HFZ: The Hornsund Fault Zone; BG: The Bellsund Graben.



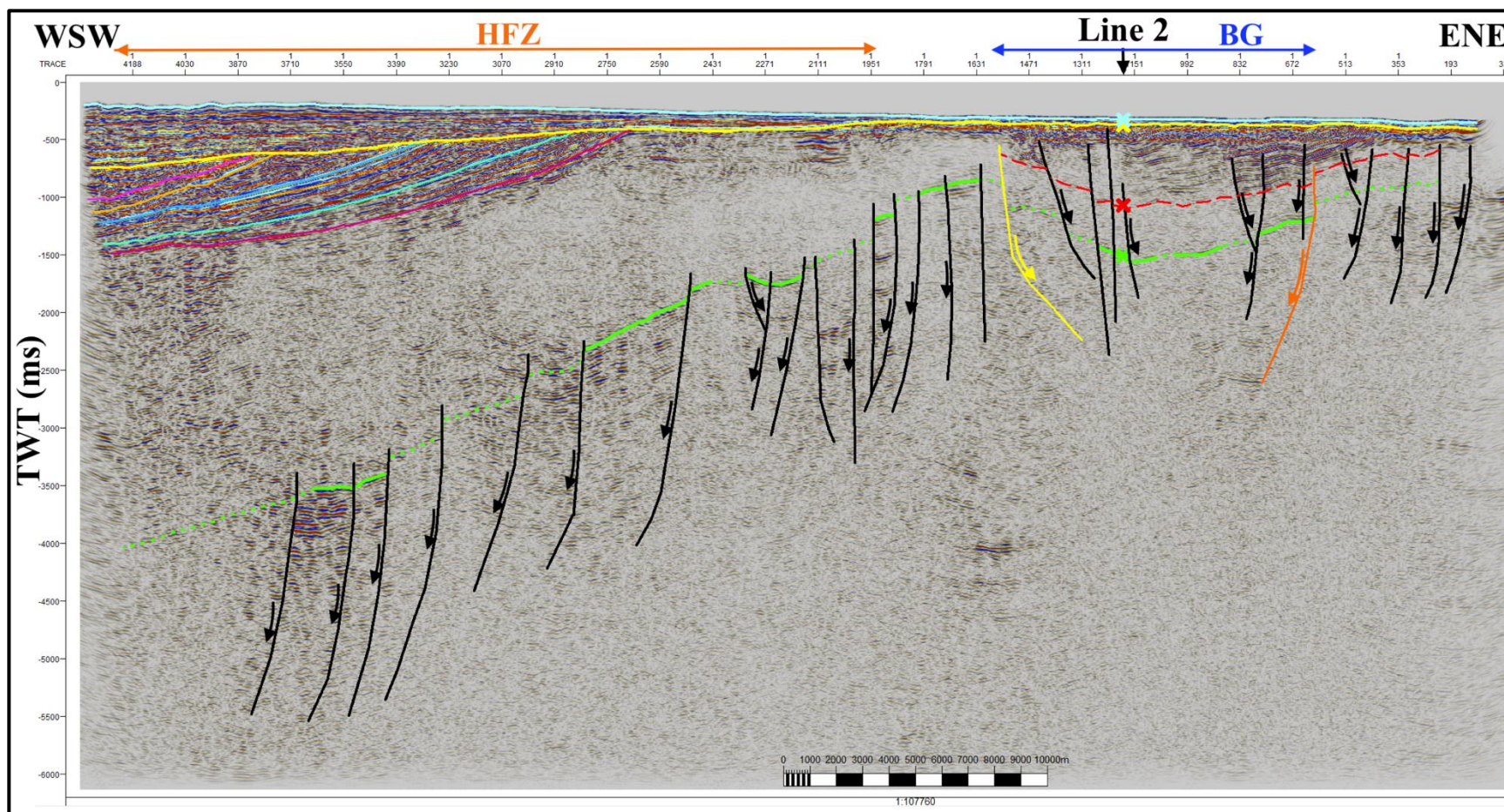


Figure 4.30 Horizon and fault interpreted image from seismic line 7. The interpreted horizons: Seabed (turquoise blue), URU (yellow), the HFZ dipping layers 1-5 (pink, orange, blue, turquoise green and purplish red lines, respectively), top Devonian (dashed red line), and top Hecla Hoek (green dashed & straight lines). The black lines and arrows present the faults and their motions. The eastward dipping major fault (yellow) at the western boarder of the basin. The westward dipping major fault (orange) at the eastern boarder of the basin. The symbol X indicates the horizons at their intersecting points with seismic line 2. HFZ: The Hornsund Fault Zone; BG: The Bellsund Graben.



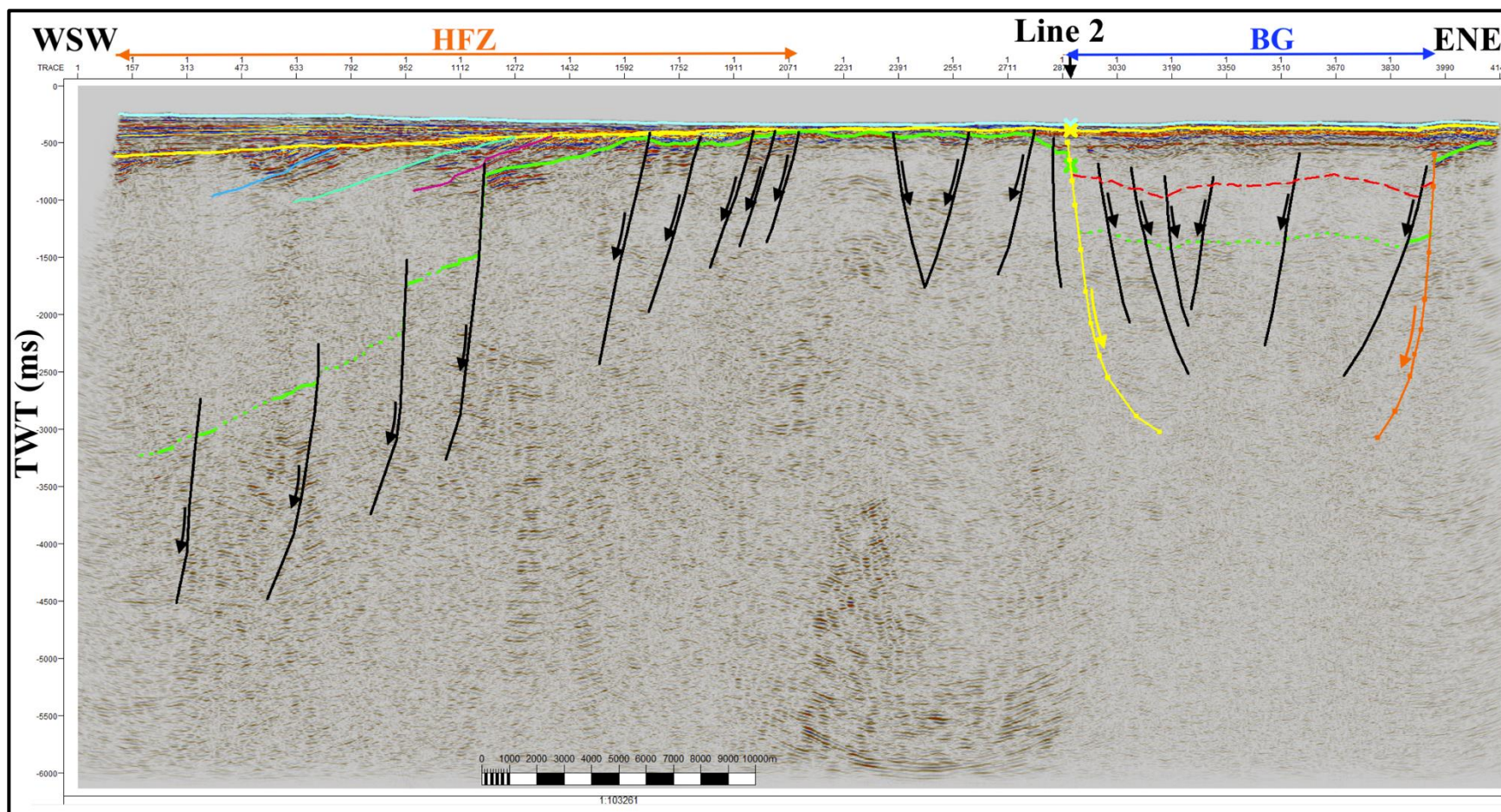


Figure 4.31 Horizon and fault interpreted image from seismic line 8. The interpreted horizons: Seabed (turquoise blue), URU (yellow), the HFZ dipping layers 3-5 (blue, turquoise green and purplish red lines, respectively), top Devonian (dashed red line), and top Hecla Hoek (green dashed & straight lines). The black lines and arrows present the faults and their motions. The eastward dipping major fault (yellow) at the western boarder of the basin. The westward dipping major fault (orange) at the eastern boarder of the basin. The symbol X indicates the horizons at their intersecting points with seismic line 2. HFZ: The Hornsund Fault Zone; BG: The Bellsund Graben.

### 4.3.2 Surface Maps

The surface or horizon maps (isopach) were generated from the interpreted horizons in 4 seismic profiles to be able to observe horizon elevations, analyze stratigraphic units and characterize the deformation structures at the next step. Every surface map was generated by using the polygon boundaries to minimize the uncertainties caused by the extrapolation. The surface maps have been demonstrated both in 2D and 3D windows in Petrel.

#### 4.3.2.1 Seabed

The surface map of the seabed (Figure 4.32) shows the elevation of the bathymetry in TWT varying between 21 and 392 ms in the study area. The bathymetry is getting deeper northward

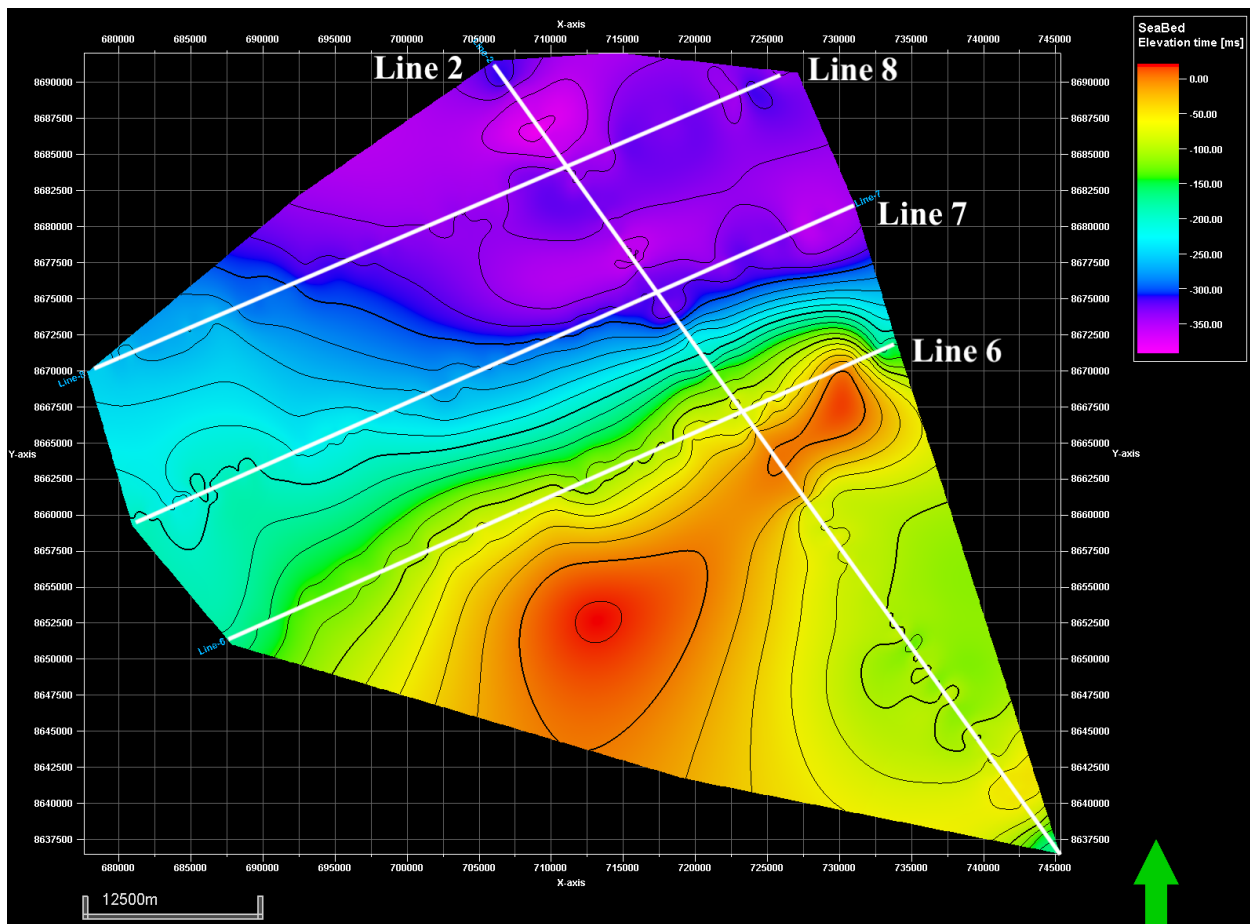


Figure 4.32 Surface map of seabed with isochrons in TWT (ms) and all seismic lines (white straight lines), displayed in 2D window.



when the study area is getting closer to Isfjorden. The sharp bathymetry change is likely the result of ice retreatments during the last deglaciations. There are uninterpreted reflectors in a small portion of seismic lines 2 and 6, but automatically extrapolated by generating the surface map, represented by red color for approximately 0 elevation. 0 elevation for the water column is not possible in marine seismic and the shallowest point has been measured at 21 ms. in seismic line 2. The reason for this uncertainty will be presented in the discussion chapter (Figure 5.3).

#### 4.3.2.2 Upper Regional Unconformity

The Upper Regional Unconformity horizon was interpreted as one of the major unconformity layers in the study area, truncating the underlying westward dipping layers in the HFZ. The surface map of URU (Figure 4.33) shows that the elevation in TWT varies from 46 to 760 ms.

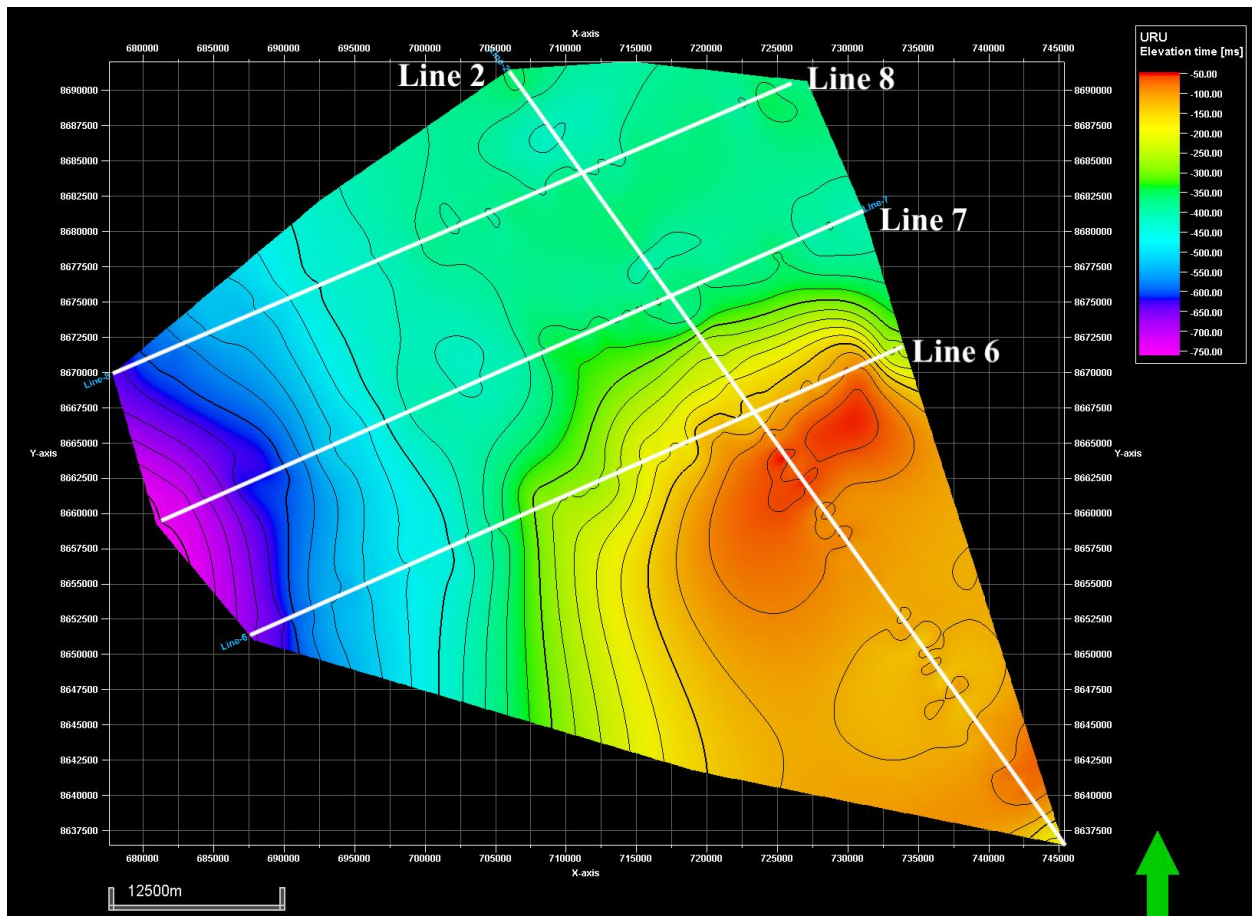


Figure 4.33 Surface map of URU with isochrons in TWT (ms) and all seismic lines (white straight lines), displayed in 2D window.

### 4.3.2.3 The HFZ Westward Dipping Layer 5

The HFZ westward dipping layer 5 is the only generated surface map among all of the interpreted HFZ westward dipping layers, since it would be the bottom surface to measure the thickness of Unit 2. It has the second most continuous reflector after the dipping layer 4 and has higher amplitude than other westward dipping layers in seismic lines 6, 7 and 8. A surface map was generated (Figure 4.34) relying on the elevation values in seismic line 7, extrapolated through the lines 6 and 8, since the depth of the interpreted dipping layers has been shallower compared to seismic line 7 due to the discontinuity. The surface map of the HFZ westward dipping layer 5 shows that the elevation in TWT is varying from 410 to 1608 ms.

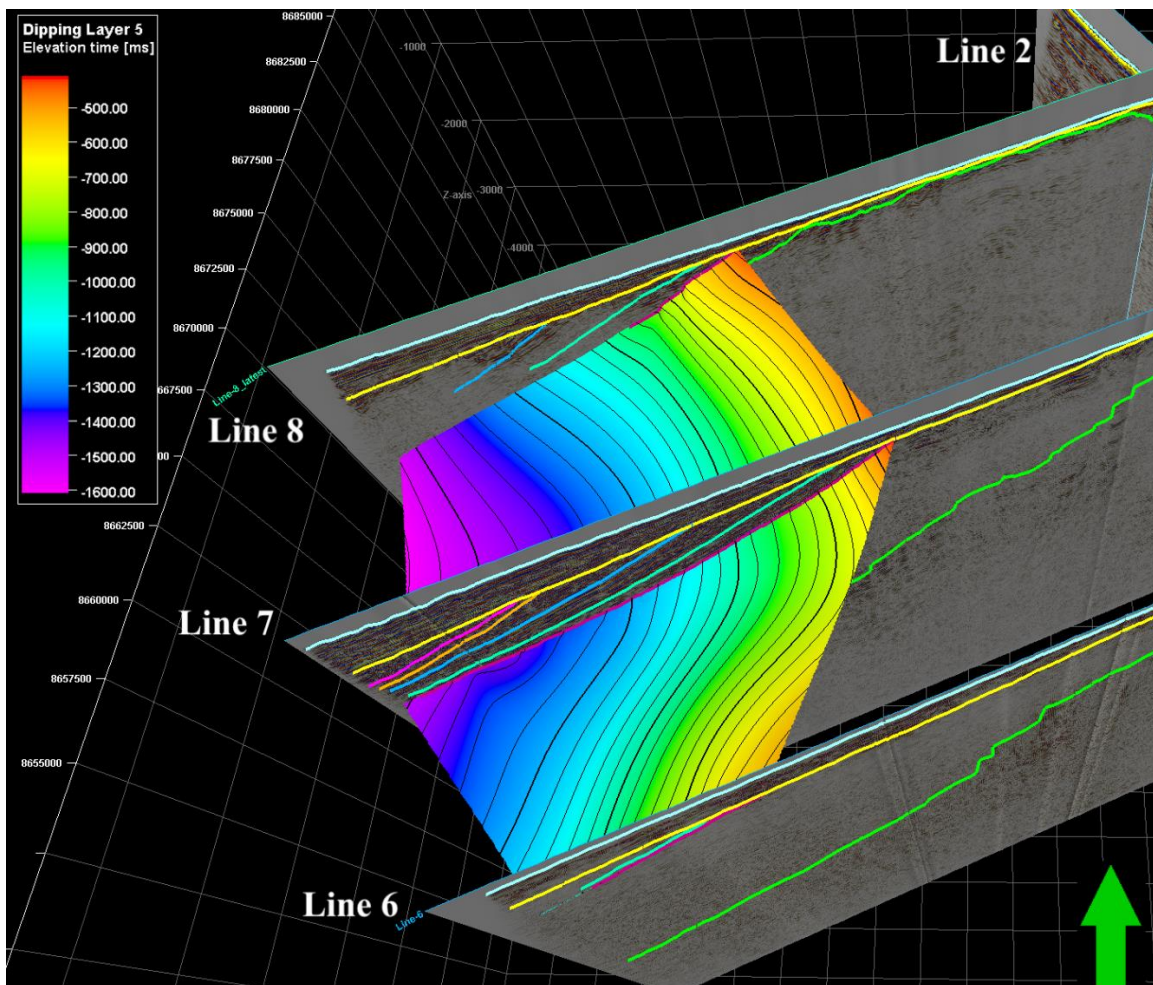


Figure 4.34 Surface map of the HFZ westward dipping layer 5 with isochrons in TWT (ms) and all seismic lines are displayed in 3D window. The interpreted horizons can be seen: Seabed (turquoise blue), URU (yellow), HFZ dipping layers 1-5 (pink, orange, blue, turquoise green and purplish red lines, respectively) and top Hecla Hoek (green line).

#### 4.3.2.4 Top Devonian

Although the top Devonian seismic horizon could be interpreted both inside and outside of the basin structure in all seismic lines, the surface map has been limited by the designed polygon only inside the basin structure. The aim was to use that polygon to measure only the thickness of the Devonian Old Red sediments accumulated inside the basin. The generated surface map of the Top Devonian (Figure 4.35) shows that the elevation in TWT varying from 480 to 1939 ms.

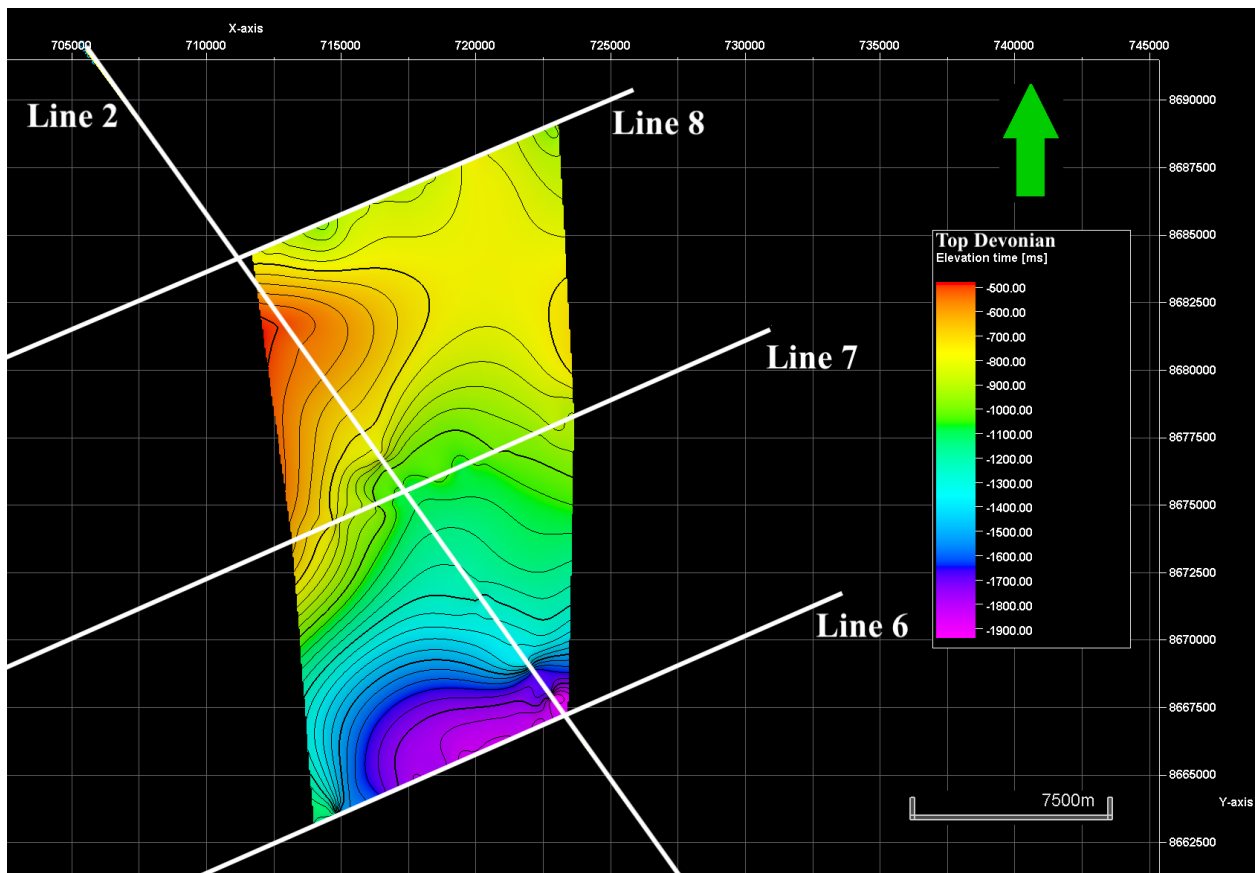


Figure 4.35 Surface map of top Devonian with isochrons in TWT (ms) and all seismic lines (white straight lines), displayed in 2D window.

#### 4.3.2.5 Top Hecla Hoek

The deepest surface analyzed is the top Hecla Hoek, as it is the basement of the study area. Due to the discontinuous reflectors, most of the horizon was interpreted as a prediction. Therefore, the generated surface map (Figure 4.36) has some uncertainties over the horst structure

between the HFZ and GB areas regarding the instant elevation changes. The surface map shows that the elevation in TWT is varying from 320 to 4033 ms. Relying on the gradual increasing elevation from south to north in the map, the Hecla Hoek basement might have been affected by uplifting during the Permian-Triassic transition (Blinova et al., 2013).

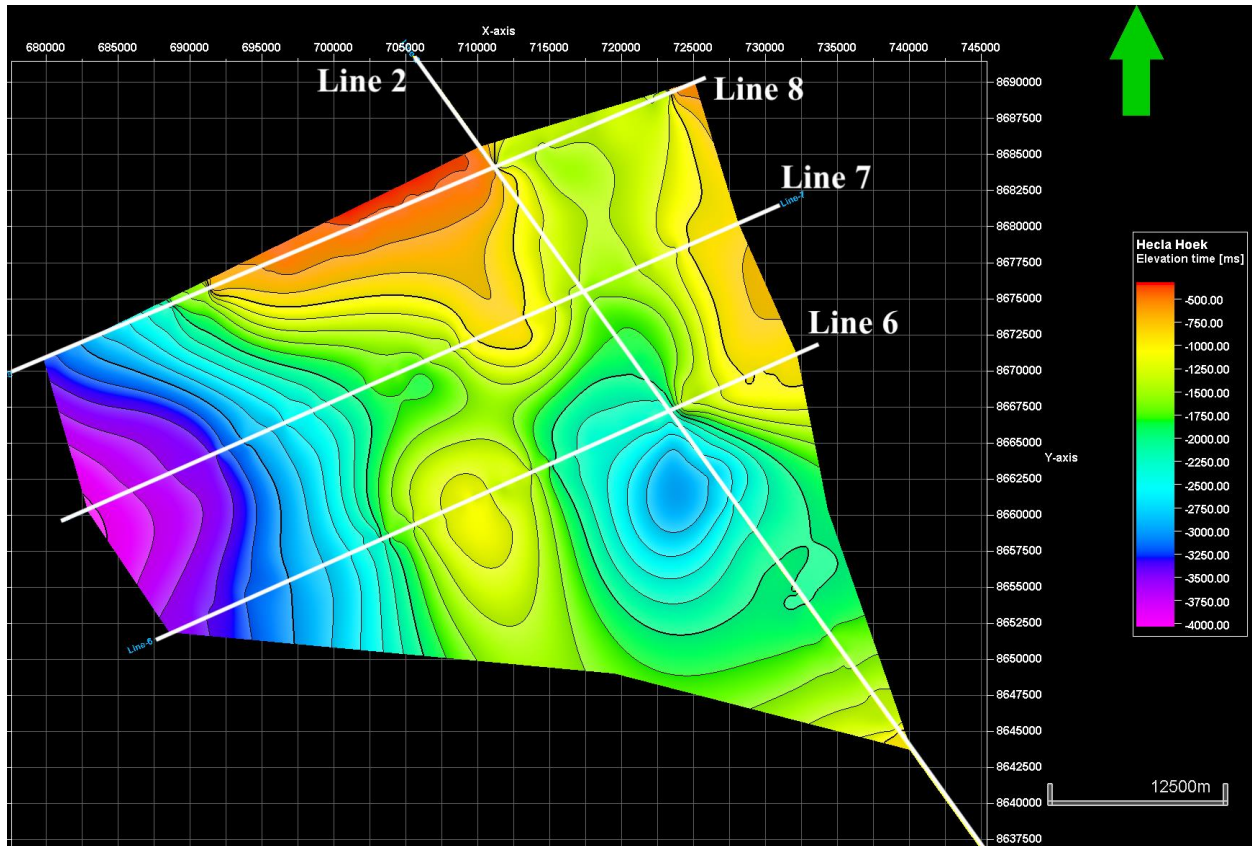


Figure 4.36 Surface map of Hecla Hoek with isochrons in TWT (ms) and all seismic lines (white straight lines), displayed in 2D window.

### 4.3.3 Stratigraphic Units

The study area has been separated into 5 main seismic units. Only units 1 and 5 cover the whole study area, while other units are limited to in particular areas. In order to observe the volume of the stratigraphic units, the thickness maps were generated between their associated surface maps limiting the units at the top and bottom. The Cenozoic sediments are divided into two units by the unconformity horizon URU, where the Unit 1 representing the younger CSW is limited between the seabed and URU. The Unit 2, including the older CSW, is limited between URU to



the HFZ westward dipping layer 5. There is no obtained thickness map for Unit 3 as it does not have absolute top and bottom horizons to measure the thickness. The thickness of Unit 4 consists of Devonian Old Red sediments measured between the top Devonian and top Hecla Hoek horizons. All thickness maps have been analyzed to reveal the history of the sediment accumulations in the study area impacted by deformation structures, erosion, uplifting and glaciations.

#### 4.3.3.1 Unit 1: From Seabed to URU

Unit 1 is filled with Quaternary sediments. The seismic character of the Unit 1 can be described as subparallel continuous reflectors having medium to high amplitude in general. The reflectors in Unit 1 have indicated that the accumulation of the sedimentary layers was conformably. The thickness of the unit 1 from the seabed to URU horizons (Figure 4.37) varies from 6 to 567 ms., which makes it the thinnest unit in this study.

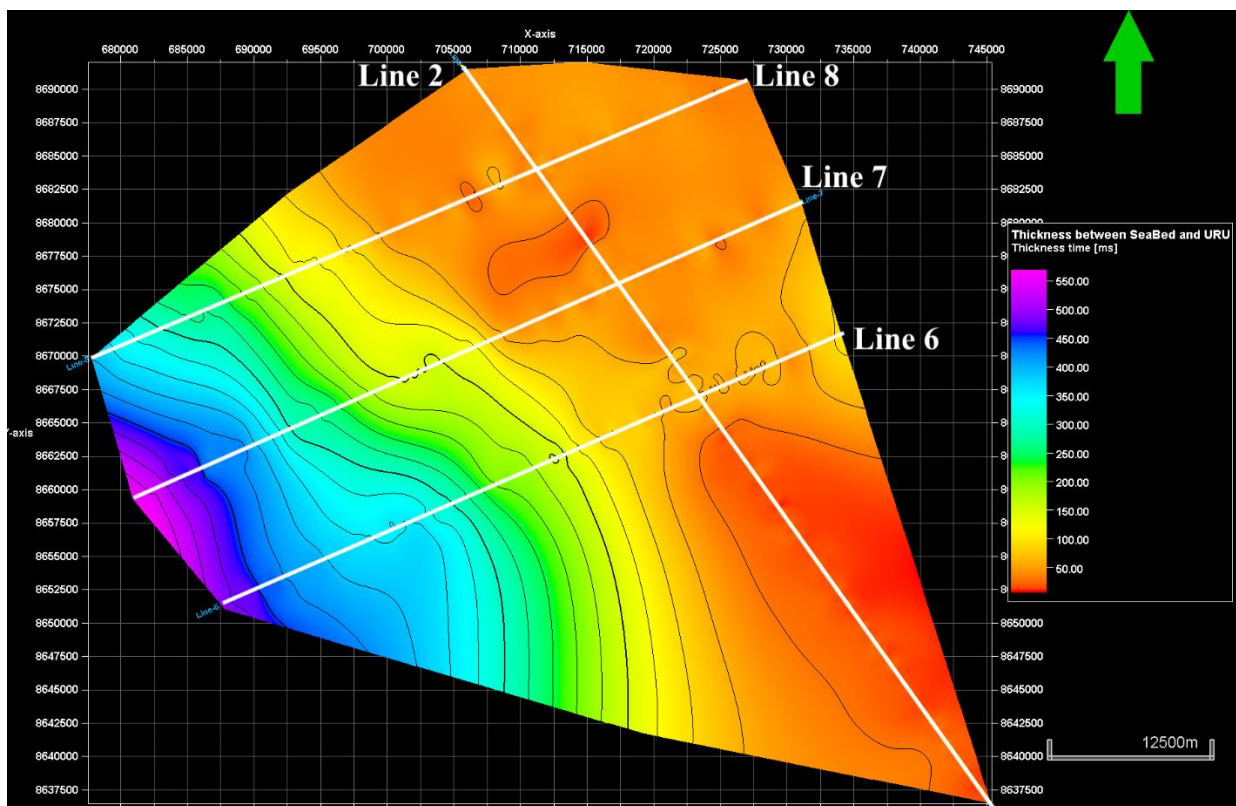


Figure 4.37 The thickness map of Unit 1 from seabed to URU horizons with isochrons in TWT (ms) and all seismic lines (white straight lines), displayed in 2D window.

#### 4.3.3.2 Unit 2: From URU to The HFZ Westward Dipping Layer 5

Unit 2 consists of the older Cenozoic sedimentary sequence truncated by URU. Like for previous studies, the most continuous westward dipping layers have been observed in WSW-ENE oriented seismic lines. Especially in seismic line 7, the amplitudes of these dipping reflectors were strong, making it possible to define a surface map for the HFZ westward dipping layer 5 to limit the bottom of the Unit 2. The thickness of Unit 2 from URU to the HFZ westward dipping layer 5 horizons (Figure 4.38) varies from 0 to 950 ms. The zero values indicate the truncated areas of the Unit 2 by URU. Unit 2 gets thicker seaward from east to west.

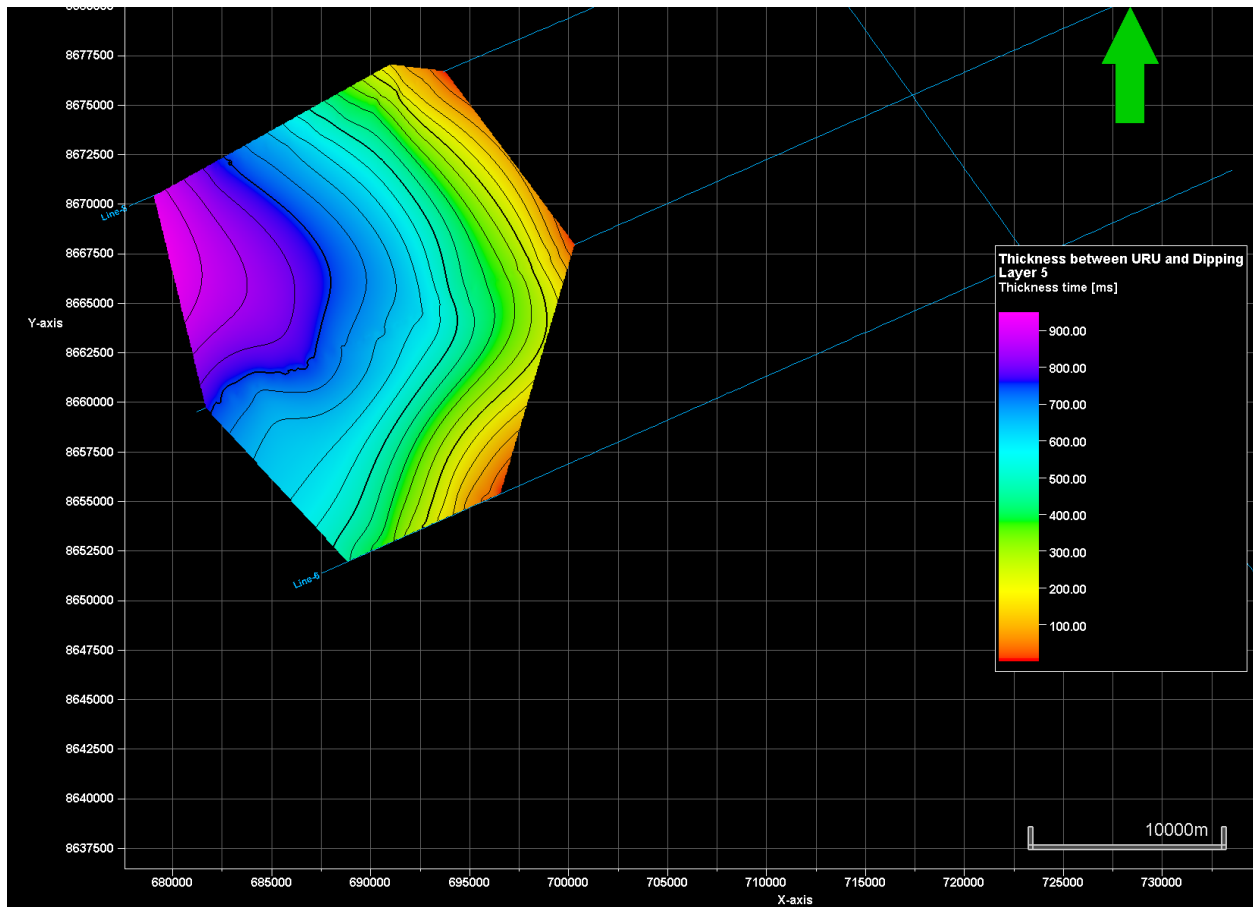


Figure 4.38 The thickness map of Unit 2 from URU to the HFZ westward dipping layer 5 horizons with isochrons in TWT (ms) and all seismic lines (white straight lines), displayed in 2D window.



#### 4.3.3.3 Unit 3: From The HFZ Westward Dipping Layer 5 & URU to Top Hecla Hoek

From the west to the east direction in the HFZ area, the upper boundary of Unit 3 represents the combination of the HFZ westward dipping layer 5 and URU horizons, while the bottom boundary is the top Hecla Hoek horizon (Figure 4.39). The reflector characters in this unit for lines 6 and 8 are not as clear as for line 7. Because of the uncertainties in those two lines, a thickness map could not be generated for this unit. The age of the sediments filled in this unit can be considered younger than the underlying basement rock but older than the overlying Cenozoic sediment wedge. Blinova et al. (2009) inferred that Mesozoic and Paleozoic sedimentary strata could possibly exist between CSW and basement. The thickness of unit 3 approximately varies from about 500 to 4000 ms, which makes it the thickest unit in this study area. It is clearly seen (Figure 4.39) that the Units 2, 3 and 5 in the HFZ area have been uplifted by the compressional forces in the pre-latest Paleocene and then the units 2 and 3 were truncated by URU.

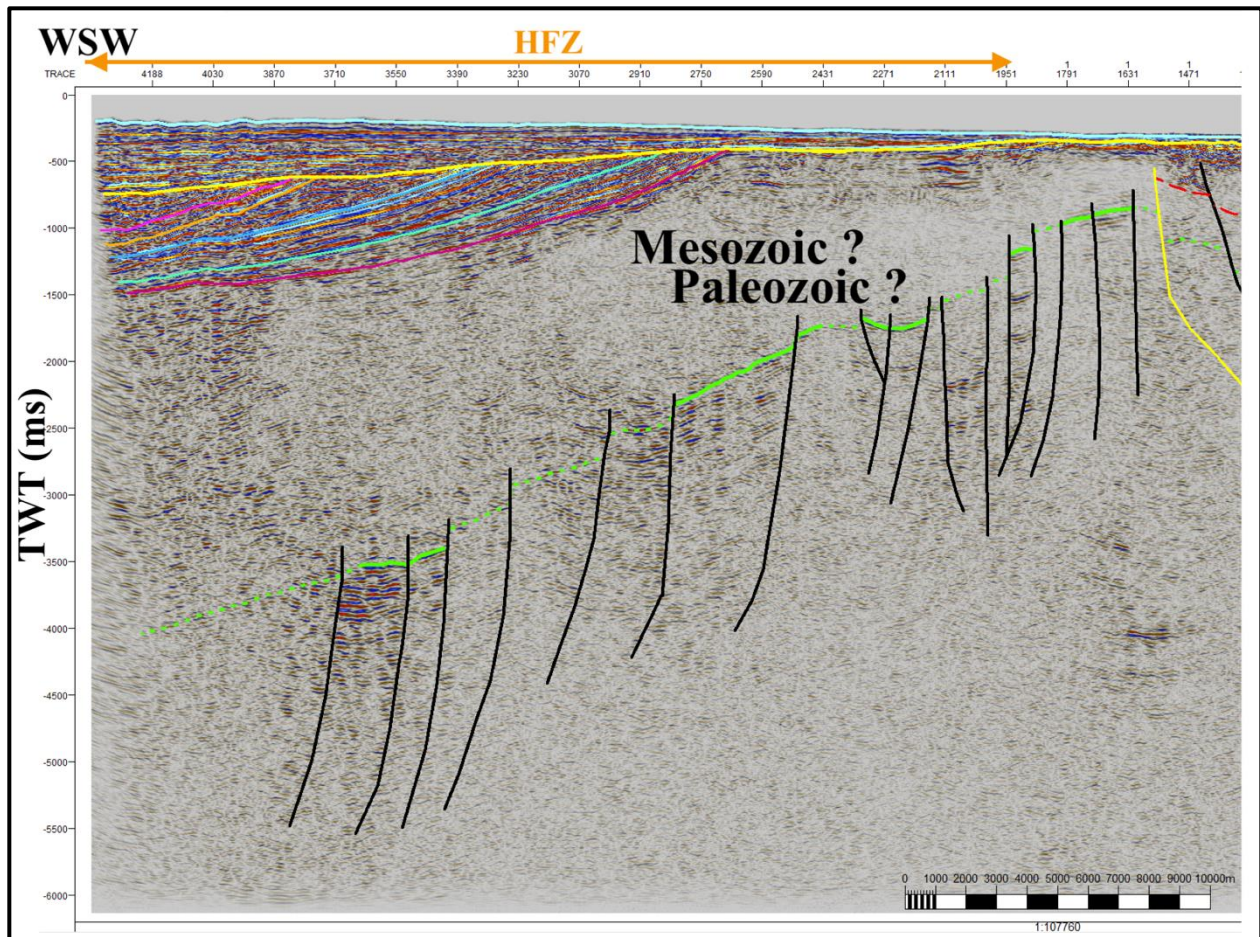


Figure 4.39 Unit 3 without a certain age for sediment fill; Mesozoic (?) or Paleozoic (?) from horizon and fault interpreted seismic line 7. The interpreted horizons: Seabed (turquoise blue), URU (yellow), the HFZ dipping layers 1-5 (pink, orange, blue, turquoise green and purplish red lines, respectively), top Devonian (dashed red line), and top Hecla Hoek (green dashed & straight lines). The black lines present the faults. The eastward dipping major fault (yellow) at the western boarder of the basin. HFZ: The Hornsund Fault Zone.

#### 4.3.3.4 Unit 4: From Top Devonian to Top Hecla Hoek

Unit 4 identifies the Devonian Old Red sediments accumulated in the basin structure, and represents the most chaotic unit among all characterized units. The generated thickness map (Figure 4.40) shows the volume of the deposited Old Red sandstones in the basin. The thickness of the unit 4 from top Devonian to top Hecla Hoek in the basin varies from 26 to 688 ms. The apparent thinning of the unit following the trend of line 7 may be an artifact due to the uncertainty in the interpretation.

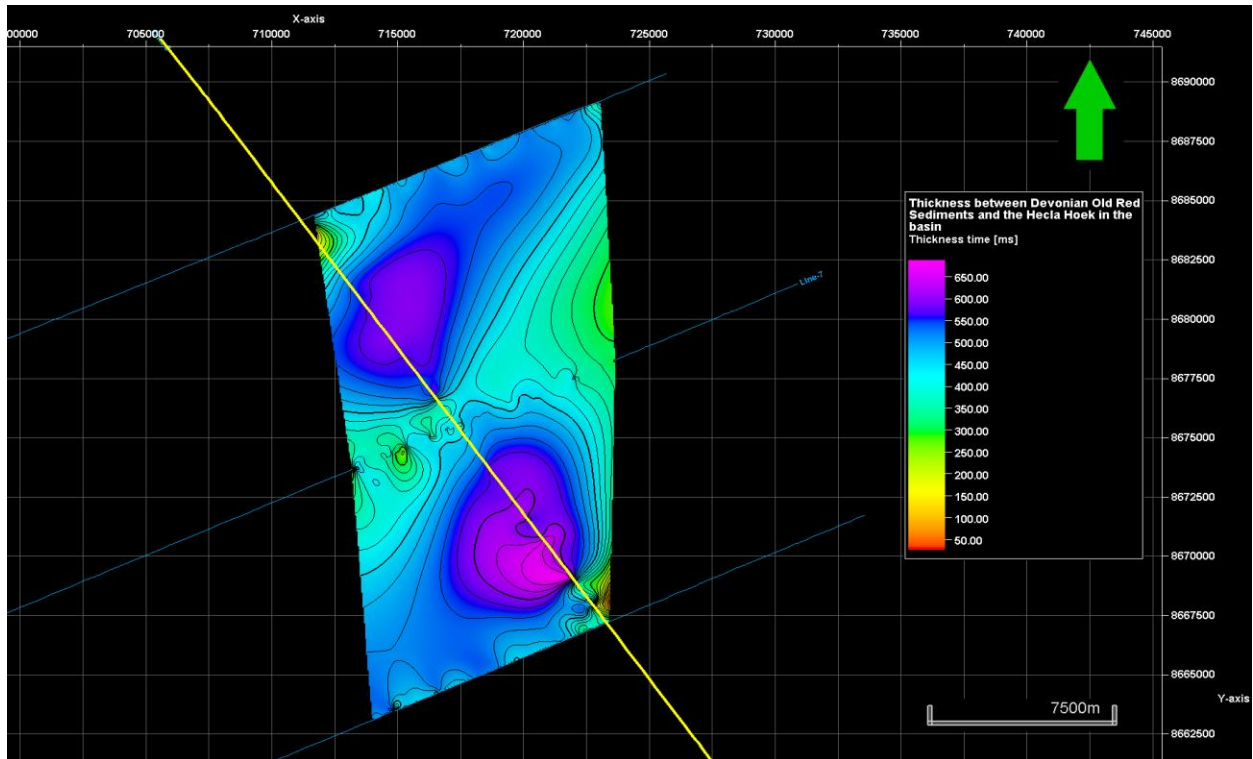


Figure 4.40 The thickness map of Unit 4 from top Devonian to top Hecla Hoek horizons in the N-S trending basin. Horizons with isochrons in TWT (ms) and all seismic lines (white straight lines) are displayed in 2D window.

#### 4.3.3.5 Unit 5: Hecla Hoek

Unit 5 is the pre-Caledonian basement rock of the study area. This unit is filled with magmatic and metamorphic rocks. The unit can be characterized as mostly chaotic, but some of the continuous reflectors have high amplitudes, indicating high impedance contrast between the basement rocks and the overlying Devonian Old Red sediments. The discontinuity of reflectors in this unit have been interpreted as normal faults, both in the HFZ and in the graben structure.



## 5 DISCUSSIONS

In this chapter, advantages and the effectiveness of the methods applied will be highlighted, some drawbacks and uncertainties will be discussed. There are also significant points of the solutions that shows how to overcome practically some challenges during the data processing and the seismic interpretation. The figures from the QC tests and the comparisons of different results and advancements are shown in both this chapter and appendixes in order to compare alternative methods and optimize the procedures.

### 5.1 SEISMIC DATA ACQUISITION

Reflectivity loss has been observed during the data processing and interpretation in some parts of seismic profiles at the shallow seabed depth and the basement in this study. Acquisition surveys and applications should take into consideration to redesign for future studies in the same study location for different imaging purposes, which will also provide easiness to process the raw data. For instance, the raw data with a wider or narrower frequency content requires different processing sequences since the depths of the source and streamer array have a direct impact on the frequency band, which is also related to the determination of cut-off frequency limits in the band-pass filtering according to Dondurur (2018). However, the survey design of leg-2 used in this study was also limited to freely arraying the source and the streamer deeper in the sea due to the shallow seabed which could be a risk for the instruments during the seismic operation. This may have been the main reason for the reflectivity loss in some areas.

### 5.2 SEISMIC DATA PROCESSING

To begin with, there are important impacts of the pre-processing sequences on the seismic data. The resampling did not only prevent the data from aliasing by use of a defined sampling interval, but also provided a precise dynamic range of the digitalized signal as 4 ms from the recorded one (2 ms). Reducing the trace length from 12288 to 6144 ms has provided faster processing speed in general thanks to the halved size of datasets. Spherical divergence correction applied after the

signature deconvolution has preserved the amplitude variations obviously both in early and late arrivals in the data by the set gain function parameters, for instance, 250 ms determined for seismic line 7. It was determined for each seismic line individually to obtain the most matching values.

The limits of the band-pass filter used in pre-processing accomplished to remove swell noise. Most QC tests have also shown that the vertical resolution has decreased due to the narrow-designed bandpass filter limits. Thus, the filter limits were set carefully for each seismic line by designing them in their amplitude spectrum, like the one from seismic line 7 (Figure 4.8).

The undesired noise and direct waves in the seismic lines were dealt with by  $f-k$  filtering during the pre-processing. However, an artificial reflection layer appeared above the seabed (Figure 4.12) at the end of the pre-processing. This layer, called as side lobe, was caused by the  $f-k$  filtering, which is similar to the side lobes caused by a zero-phase band-pass filter. Since the side lobe of a zero-phase wavelets can boost its low frequency (Zhou, 2014), all seismic lines had this issue above the seabed after the pre-processing (Appendix A.2.1), where the low frequency is in SVALEX data. However, they were removed easily by top muting from the data.

During the seismic data processing, the top muting was applied to datasets after several sequences, which was naturally effective to remove the noise above the seabed. However, in the shallowest areas, the seabed has lost the reflection continuity, since at some parts the amplitude literally zero-outed. For instance, in seismic line 2, the seabed reflection between CDPs #5320 and #7000 was removed from the migrated data (Figure 4.24) compared with the preprocessed image (Figure A. 17).

As a single trace section (common-offset section) has a very low S/N ratio and resolution, applying a brute-stack operation for QC purposes is very beneficial to compare the results after main seismic processing applications, such as band-pass filtering, deconvolution,  $f-k$  filtering and subtraction (Dondurur, 2018). Therefore, the comparison of the different parameters has been



beneficial to define the ideal parameters for a particular processing level. Eventually, it saved a lot of time to have rough stacked sections instead of employing further steps and waiting for their running time which makes the QC tests on the brute-stacked images very crucial due to the rapidity. However, according to Yilmaz (2001), the NMO correction can cause misalignments that blurred and degraded the brute-stack sections, since their corrections were not done by accurately picking the velocities from the analysis but those used from velocity modelling. Therefore, the brute-stack sections before the velocity analysis have not been very reliable due to their inaccurate NMO corrections roughly done by the velocity models, which were used as the references to prepare the semblance plots in the 1st velocity analyses in all seismic profiles.

The velocity models may have some uncertainties, particularly in the shallower areas, since the seabed horizons were manually picked on the near-trace sections in order to generate water bottom libraries of individual seismic lines used during the seismic processing. One of the main reasons for these uncertainties is that during the seabed horizon picking on the near-trace sections, the TeamView software has a limited number of picked points on horizons, which prevents the user to pick the point at short intervals. Therefore, the picked points were not so close to each other. For instance, the undulated surface between shot points #980 and #1087 in seismic line 7 (Figure 4.13), may have been uncertainly generated by the interpolation between only the picked points, used in next processing steps as a reference (water bottom library). Nonetheless, this was not a major problem for the data processing since the velocity analyses have been precisely done several times for each seismic line in order to have the most accurate picked velocity libraries. However, the NMO and the DMO corrections and migration should be taken into consideration concerning similar uncertainties caused by the manually picked seabed horizon.

Since velocity analysis is one of the most significant processing sequences, the previous steps should be done precisely to remove the noise and the multiples from the data. Then, a reasonable velocity model can be obtained by picking the correct velocities at their associated arrival time (TWT) in clearly displayed semblance (spectrum) plots. The major challenge during the seismic

processing in this research was to have noise- and multiple-free CDPs used in the velocity analysis. Because the SVALEX data were especially mostly impacted by the scattered waves and the surface-related multiples in general, and amplitudes of these undesired artifacts were strong in the semblance plots.

The surface-related multiples made the semblance plots very complicated to pick for the primary velocities, especially difficult to pick up these velocities interfered by the first-, second- and third-order multiples in the plots, during the 1st velocity analysis. For instance, since the reflection hyperbolas have interfered with the hyperbolas of the multiples, the velocities of primaries were masked in the semblance plots and any velocities could not be picked up mostly between approximately 450 and 1100 ms in all seismic lines (Figure 4.15). The near-trace section from the pre-processing had to be used not to pick the multiples accidentally. This was very supportive during the analysis. However, often velocity picking had to be skipped since there was no energy from the primary events. Hence, the 1st velocity analysis did not provided an accurate velocity model (Figure 4.16), since the improper velocity function could not flatten the hyperbolas during the real-time NMO (Figure 5.1).

In addition, curvatures of the reflection hyperbolas from the steep-dip layers might have been distorted due to the diffraction events from these steep-dip layers, yielding their energies and arrival times incorrect from these areas in the semblance plots. Therefore, the 1st velocity analysis did not provided a perfect moveout to flatten these hyperbolas during the NMO correction as well. Even though these layers exist especially in the western part of the seismic lines, their degraded amplitudes cannot be seen in the semblance plots, which makes it difficult to pick their velocities. Furthermore, the semblance plots in the 1st velocity analysis might have been also impacted by other factors such as the signal frequency, the streamer length used during the acquisition, the S/N ratio of the data, the velocity model as reference and the sampling rate used at the preparation step for the analysis where the semblance plots were calculated and generated.

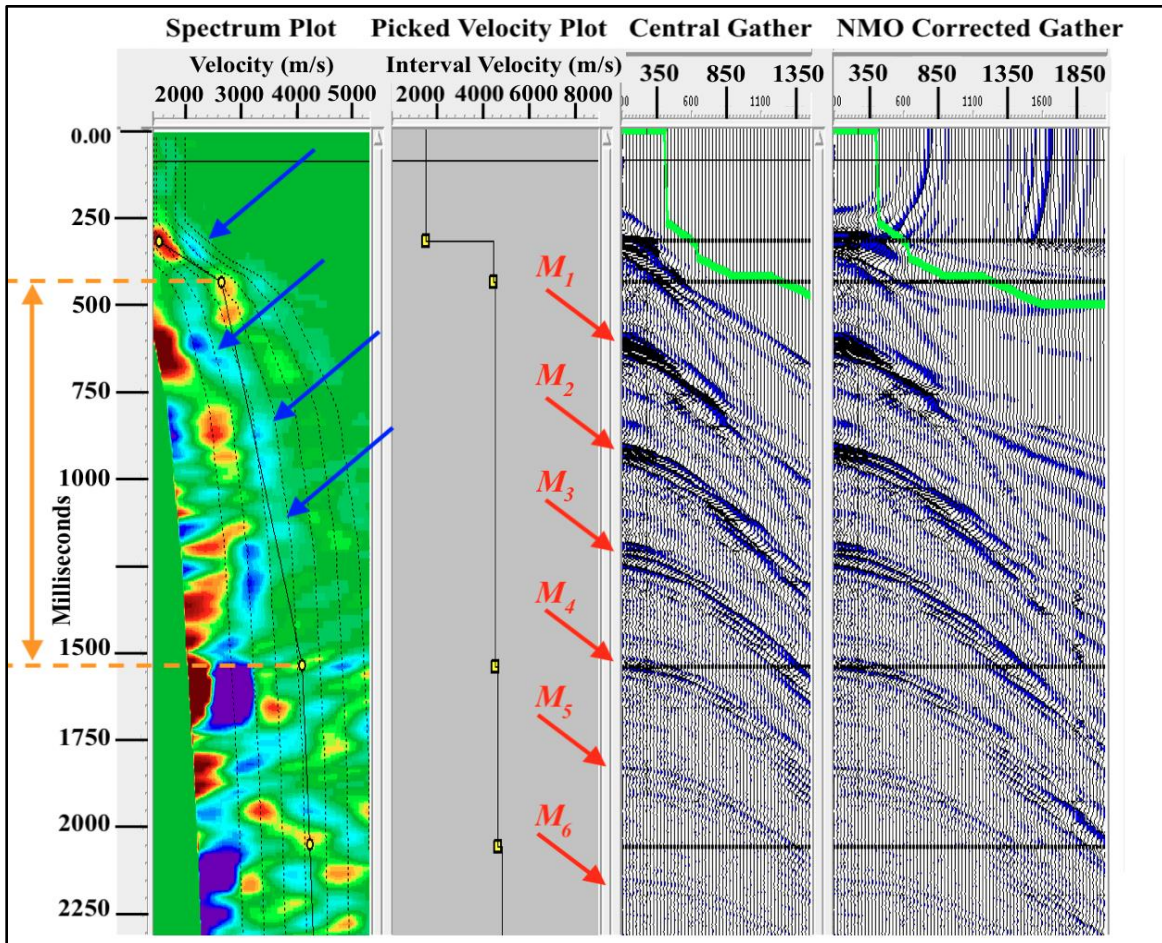


Figure 5.1 An example of the 1st velocity analysis performed on the spectrum plot by picking the velocities in the 120-fold CDP gather #4065. In this CDP, velocity picking between 425 and 1550 ms (orange arrow) is prevented by the multiple enclosures ( $M$ ). Since the primary reflections were masked in this multiple enclosure area, the velocity function is ineffective to flatten the hyperbola curves as seen in the real-time NMO corrected gather. The green lines on the gathers define for the NMO stretch muting zone (above the line). The random noise in the spectrum plot is showed by blue arrows whose amplitudes are reduced by the increased fold number.

It is highly recommended by Dondurur (2018) that the noise attenuation should be done by various processing steps to have an accurate velocity analysis as the semblance calculation can be influenced by the random noise. During the pre-processing in this study (chapter 4.2.1), the noise influencing the data has been attempted to be suppressed as much as possible by several processing sequences. However, the semblance plot was still affected used in the 1st analysis by random noise after these processing steps. According to Yilmaz (2001), a higher fold number in CMP gathers provides more traces in the semblance calculation, and the quality of the semblance

becomes higher. Therefore, the fold numbers in CMP gathers were increased from 30 to 120 thanks to the trace interpolation before the 1st velocity analysis. The comparison of the velocity analyses with 30-fold CDPs and 120-fold CDPs revealed that the amplitude of the random noise was reduced in the semblance plot with the 120-fold CDPs (Figure 5.1). Moreover, amplitude degradation of the primary reflections in the semblance plot by unwanted noise was slightly prevented thanks to the 120-fold CDPs.

Besides the most dominant noise, especially the surface-related multiples, another dominant noise has been the diffracted waves repeatedly reflected from the hard seafloor or the upper subsurface units, especially in shallow waters of the study area. For instance, the horst structure in seismic line 8, appearing in CDPs # 4061 - 6061, caused these diffracted waves travelling with very higher velocities (4000 - 6500 m/s) compared to the velocity of the diffracted waves in any other CDPs. The amplitudes of these linear events have dominated the amplitude of the primary reflections, which have been mostly in the same frequency band of the primary reflections in the far-offsets that appeared both in shot and CDP gathers. The 1st and 2nd workflows have been designed to attenuate the diffractions by the  $f-k$  and band-pass filtering and to attenuate the multiples by the predictive deconvolution. In the 3rd workflow, the linear events have been attempted to suppress in the  $\tau-p$  domain. Therefore, the multiples were also aimed to be attenuated by the predictive deconvolution in the  $\tau-p$  domain. The 4th workflow has been designed mainly to eliminate the multiples by  $f-k$  filtering applied to the NMO over-corrected CDP gathers.

The results from the predictive deconvolution applied to the original CMP gathers have revealed that only the multiples intersecting with the westward dipping layers (downwards from 0.75s) in the western part of the seismic line 8 were suppressed, while the amplitude of the primary reflections upwards from 0.75 s were weakened, especially in the shallower parts. The deconvolution could not be attenuated multiples at all from the center to the eastern end of the profile (CDPs #4060 - 8779). Therefore, instead of the deconvolution method, new multiple elimination methods were considered, which have been the deconvolution in the  $\tau-p$  domain and

the  $f-k$  filtering applied to the NMO over-corrected CMP gathers. To increase the efficiency of the newly designed multiple elimination methods, the truncation impacts from the  $f-k$  filtering and the  $\tau-p$  transforms have been aimed to be prevented thanks to the trace interpolation.

The trace interpolation was applied to the common-offset gathers not shot gathers to increase the number of traces, but saved in every second of CDP gathers that increased. The CDP intervals have been increased from 6.25m to 12.5m, while the number of the CDP gathers was halved from 8695 to 4347. Therefore, the total number of the traces in the gathers has become 507840 instead of 1015680 as it was supposed to be after the interpolation (Table 4.4). Even though the interpolation has increased the number of traces in CMP gathers, it has not reduced the spatial aliasing and has not recovered the frequencies lost from the sampling. However, the reduction of spatial aliasing is as a consequence of the  $f-k$  filtering applied before the trace interpolation. Overall, the interpolation has several benefits for the processing, such as preventing the sharp truncation effect and enhancing the horizontal resolution thanks to the increased number of shots and the maximum fold number of the CMPs multiplied by 4.

After the trace interpolation, the 1st processing workflow was repeated with the interpolated CMP gathers, so-called the 2nd processing workflow, to compare the deconvolution and other seismic step results from the original (Appendix B.3.1) and interpolated CMP gathers (Appendix B.3.2). The surface-related multiples were suppressed more in the deeper parts, while the primary reflections were preserved with higher S/N ratio. Since the 2nd processing workflow has been completed with better results, it was determined to proceed to apply the next multiple elimination methods to the interpolated CMP gathers in the 3rd and 4th workflows.

The deconvolution in the  $\tau-p$  domain has been performed in the 3rd workflow. In the beginning, results from the deconvolution (Appendix B.3.3) were promising regarding the S/N ratio in the westward dipping layers and the shallower parts of the stack and migration sections. However, it has not been that much successful particularly in removing the 1st and 2nd order surface-related multiples due to the refracted waves travelling in the subsurface sediment units with the

high velocities varying from 4500 to 6000 m/s. These high velocities have been tried to mute in CGG Geocluster by the user-defined velocity muting polygon in the TeamView. Manually picking every individual point, and shaping the muting zone, in all displayed  $\tau$ - $p$  gathers in the TeamView has been one of the most challenging approaches among all processing steps in this thesis. Because the TeamView had crashed and did not give any response during the velocity picking in the gathers. Once it had occurred, all picking completed gathers were lost, and this picking had to be repeated in the gathers over again. As it has costed too much time and lost its efficiency to be applied on both TeamView and CGG Geocluster, this workflow had to be cancelled to proceed.

According to Dondurur (2018), deconvolution is almost ineffective on the multiples with a period larger than approximately 200 ms, while it is particularly efficient on short-period multiples. The reason behind this has been explained by the periodicity of the multiples varying with the increasing offset due to the normal moveout of the reflection hyperbolas. As the period of the surface-related multiples are 300 - 350 ms observed in the 4 seismic profiles of this study, trying to improve multiple attenuation by the deconvolution has been switched to alternative elimination methods. The next multiple approaches that have been implemented in the 4th workflow is the  $f$ - $k$  filtering applying to the over-corrected CMP gathers (interpolated). The results have revealed (Appendix B.3.4) that the multiples were barely removed for instance in the westward dipping layers, but the surface-related multiples have been interfered with interbed multiples downwards the horst structure. The stacking and migrating results have also shown that the S/N ratios in the sections have dramatically increased.

Eventually, all four previously attempted attenuations of the surface-related multiples have not been succeeded as its targeted but the approach by multiple extraction & the adaptive subtraction in the main processing workflow. There has been a very significant point in this approach that the 1st input datasets were implement by the same forward and inverse NMO corrections as used for the 2nd input datasets multiple extracted ones. Therefore, the 2 sets of CDP gathers have the same changes such as NMO stretching in order to avoid the sudden



amplitude amplification of the reflections and noise during the adaptive subtraction. These modelled 2 set of CDPs gather has been computed by the 70% of the velocity functions in the NMO correction as part of the approach to bend up-and downwards the hyperbolas of primaries and multiples.

To find out the pros and cons of this approach, 4 different velocity percentages for 100%, 80%, 70% and 60%, has been compared each other (Appendix A.2.3). The comparison has shown that even though this multiple attenuation approach has been accomplished better than other performed multiple elimination methods during this thesis project, there has been always data loss, which could not be prevented with the tested velocity percentages. Absolutely, computing the slower velocities to generate 2 datasets and adaptively subtracting each other has been a trade-off between receiving almost multiple-free data and primary reflections preserved data. Overall, the data lost has been obvious in seismic lines 6 and 8, especially crucial for the line 8, which is the main disadvantage. Contrarily, there has not been any significant data loss observed in seismic lines 2 and 7.

The westward dipping layers of the CSW unit has been drastically lost the reflection continuity of these layers in seismic profiles 6 and 8. It can be considered that their amplitudes might have been already weak in these seismic lines once they had been acquired. So, during the multiple elimination, these weak energies of primaries may have been wiped out together with the multiples. There might be a few factors why their amplitudes were acquired too low. On the one hand, the seismic energy may have been already lost before arriving at the deeper part of these layers due to several destructions of the signal quality, which are the diffractions from truncated sublayers and suddenly terminated sublayers; the scatterings at the possible pockmarks and the undulated surfaces such as some part of the seabed and the unconformity layers like URU in the study area described by Blinova (2009). On the other hand, the amplitude of the signal might have been reduced by the directivity effect which is described by Dondurur (2018) that as the incidence angle of the reflection signal increases, each hydrophone receives the signal with a certain time delay depending on the frequency of the signal, channel number and group length.

Nevertheless, acquiring the reflection seismic data with different techniques in the same location may overcome the signal quality and the directivity in the streamer group.

Even though the multiple extraction & adaptive subtraction determined velocity percentage of 70% has provided the best remedy for the surface-related multiples, amplitudes of the interbed multiples were amplified in some areas, especially in seismic lines 7 (Figure A. 30) and 8 (Figure A. 26). However, amplitudes of the interbed multiples have been suppressed in the migration sections compared to their brute-stack sections from the adaptive subtraction applied with 70% velocity. The strongest suppression has been mostly accomplished during the 2nd velocity analysis performed in every displayed CDP gathers in the Teamview. Moreover, the  $f-k$  and band-pass filters applied to the datasets just before the migration (chapter 4.2.10) have attenuated the amplitudes of the interbed multiples.

Thanks to the adaptive subtraction method, the CMP gathers have become almost multiple-free leading to a better semblance calculation. When the 1st velocity analysis (Figure 4.15) is compared to the 2nd analysis, it is clearly seen in the semblance of the 2nd analysis that primary reflections appeared between 400 and 1100 ms (Figure 4.20), which could be picked easier than the 1st analysis. During the 2nd velocity analysis, the brute-stack sections after adaptive subtraction (as an example, Figure A. 30) were also used sometimes to support picking the velocities carefully around the dipping layers in order not to miss them. Thus, the velocity function has been obtained more accurately, which also improved the efficiency of the DMO and the NMO corrections and the migration. Comparison of isopach maps and brute-stack sections after 1st and 2nd velocity analyses has revealed the importance of the 2nd velocity analysis performed in the multiple attenuated CDPs.

After the complete data processing, the migrated images were uploaded into the Petrel for interpretation. Unfortunately, an intersection problem occurred between seismic lines 6 and 2 in the Petrel (Figure 5.2.A). The possible reasons for this problem were checked in detail through all applied individual processing steps and even the engaged UTM coordinates on the migrated

sections. Once the error was discovered due to the extrapolation issue between the high CDP interval, where the velocities were only picked in the semblance plots from these CDPs with 4 km interval during the second velocity analysis in the GeoVel. The extrapolation between 4 km CDPs led to an error in obtaining an accurate velocity function for seismic line 6, especially at the intersection point with line 2. Because the velocity picking in the intersecting CDPs in these two lines had not been analyzed by coincidence. Briefly, the NMO correction in seismic line 6 had failed to move the traces to their true zero-offset times by the inaccurate velocity function, due to the wrong extrapolation for the 4 km CDP interval. The second velocity analysis was thus repeated in both lines 6 and 2 by reducing the CDP intervals from 4 to 2 km to pick the velocities in every displayed CDP gather (semblance plot) in the GeoVel. For example, in seismic line 6, the velocities picked CDPs were increased from 24 to 49 CDPs. That has provided improvement at the intersection point. Thus, the TWT matching issues between the two lines in the shallow part were overcome (Figure 5.2.B).

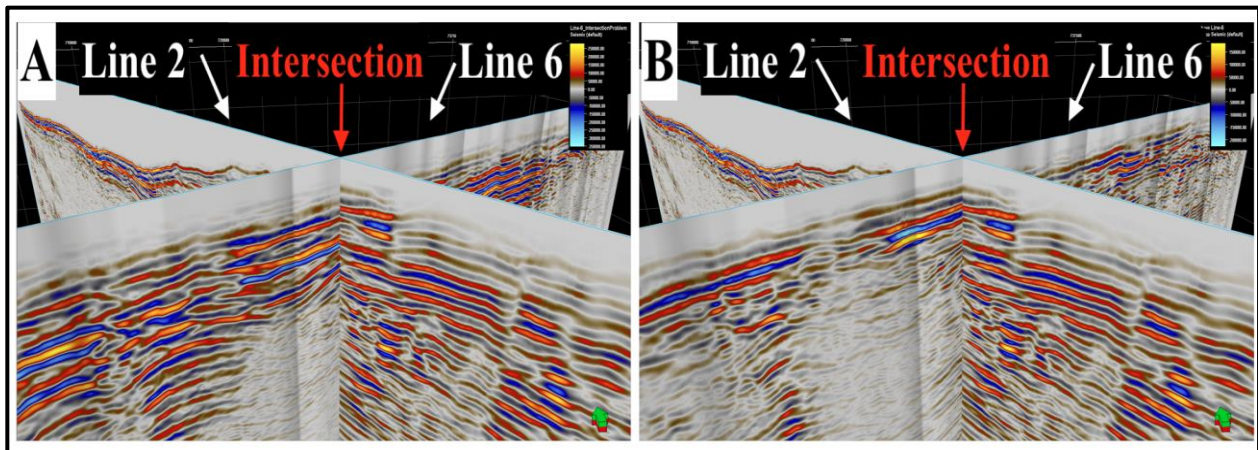


Figure 5.2 shows the mismatch (A) at the intersection of seismic lines 6 and 2 and the fixed error at the intersections (B) by repeated 2nd velocity analysis in every semblance plot displayed in GeoVel.

Another benefit of performing a velocity analysis in every semblance plot is to enable us to suppress the amplitude of the interbed multiples so that the adaptive subtraction could not eliminate them. For instance, 2nd velocity analyses done in every displayed CDP gather in GeoVel (totaling 50) has dealt with suppressing the amplitude of the interbed multiples in seismic line 8 (Figure A. 32.B), compared to the analyses done with every displayed second CDP gather before,

totaling 25 (Figure A. 32.A). Therefore, it was decided to repeat the 2nd velocity analysis in all seismic lines with the shortest CDP interval, which was reduced from 4 to 2 km. Once the repeated velocity analysis increased the accuracy of the velocity functions providing higher quality in the sections, the rest of the processing steps in all seismic lines were also applied again. Then, all seismic lines become more reliable without any intersection problems in Petrel, as well as higher S/N ratio thanks to the suppressed interbed multiples. However, both repeating the velocity analyses in every displayed CDP gather and processing steps falls beyond the scope of implied this thesis project.

After the DMO correction, the CDP gathers and brute-stack sections have been investigated before and after the implementation, which shows that the steep coherent noise has been suppressed as well as the dipping layers and oblique fault planes have been much identical. In the brute-stack sections, steep-coherent noise diffracted from the truncated and eroded layers in some shallow areas has been attenuated. The results from NMO-corrected of stacked the data have shown that all curvature of the primary events were flattened besides some problematic CDPs due to inaccurate velocity functions by the velocity picking errors, especially during the 1st velocity analysis. As an example, this error has been illustrated in the iso-velocity contour map for seismic line 7 (Figure 4.16). In addition, similar but minor flattening issues have been observed in the shallow part of the brute-stack section from line 7 (Figure A. 30), particularly in the sediment packages. These picking issues were overcome during the 2nd and 3 velocity analyses where the velocity picking had been done precisely with the shortest CDP interval. Even though the 2nd analysis was similarly completed with the denser CDP interval, seismic lines 6 (Figure A. 34) and 8 (Figure A. 36) have lost their primary events of the steep-dipping layers in the western side of the sections. This can be another challenge apart from the velocity functions used in the NMO correction for SVALEX data, where the western side consists of steep-dip layers and the westward dipping layers in the CSW. This fact is underlined by Dondurur (2018), who states that steep-dip and complex seafloor morphology cannot be flattened by NMO aside from the velocity function issue.

The enhancements of the S/N ratio in stacked sections from 4 seismic lines are quite appropriate in general, thanks to the accurate velocity field from the second analysis used in the stacking where all primary reflections are apparently flattened. It must be kept in mind that there is also a remarkable contribution to increasing the S/N ratio from the interpolated traces yielding the fold number 120 as well. The quality and S/N ratio of the stacked images can also be influenced by the NMO stretch mute percentage. In the case of a higher muting percentage, the quality of stacked data is reduced, due to the fact that the weakened amplitudes of low frequencies from far-offsets are initiated with stacked data, yielding a narrower NMO stretch mute gap. Contrarily, when this percentage is too low, there is no contribution from the far-offsets to increase the S/N ratio, which causes a larger NMO stretch mute gap. As a result of the muting, one way or another, NMO stretch mute gaps occur at the start-of-line (beginning of the seismic acquisition) in the stacked sections, where these gap zones are inversely proportional to the muting percentage (Dondurur, 2018). Therefore, the NMO stretch mute percentage (*SMU*) was tested in the FANMO module for 70%, 100% and 130% in the NMO corrected CDP gathers. The 100% stretch mute percentage provided the ideal S/N ratio in the stacked image as well as the muted zone to remove the stretching effect precisely. The NMO stretch mute gaps caused by the 100% stretch mute percentage were not so huge and removed the stretching effect successfully from all seismic lines. For instance, it is presented in the red-dashed polygon in seismic line 7 (Figure 4.22), where the gap occurred between 0.3 and 0.9 seconds along with 200 CDPs. In order not to decrease the quality of stacking with unnecessarily low or high mute percentages, the NMO stretch mute percentage should be chosen very carefully before applying the NMO correction. Most of the artificial dipping layers in the stacked sections are the diffractions from the edge of the fault blocks which are also strong indications that the research area consists of numerous fault blocks. Thus, the stacked sections were used to identify especially the faults during the seismic interpretation.

The gain recovery was applied, by the REFOR module, to the CMP stacked data in order to find out the best parameter for seismic profile 8 among the different multiplication coefficient ( $n$ ) values such as -1.0, -1.5, and -2.0. Although the positive values varying +1.0 to +2.0 applied

normally to correct the geometrical spreading effect, the purpose of applying negative values was to amplify the early arrivals in the seismic data, such as the seabed reflections. The comparison of these different  $n$  values has been observed both in the stacked sections and in further migration results. They have shown that the value  $n = -2.0$  mostly attenuated the high-amplitude spike noise amplifying the smiling effect, especially from 1.5 to 6 seconds in the part of both the stacked sections and the migrated images. Moreover, the potential useful signal in the deeper part of the seismic sections became weaker. The noise was boosted between 1 and 3 seconds (TWT). These tests have also revealed noise was amplified both above and below the seabed reflection, which also reduced the frequency of the seabed due to the altered waveshape by gain recovery. Therefore, applying the gain recovery to the stacked and migrated data has been a trade-off and omitted in the last processing sequences.

There have been significant processing steps applied to stacked data before the migration, which are  $f-k$  and band-pass filters and amplitude scaling. The results from different band-pass filtering limits have been compared to find out the best efficiency on low-frequency events in the shallower part of the migrated sections. The results have revealed the effectiveness of implementing  $f-k$  filtering in the stacked data to remove the dipping diffractions in all seismic sections. The steeply-dipping diffraction events left after the  $f-k$  filtering have been achieved to collapse by the FD with the omega-x algorithm. Hence,  $f-k$  filtering and the migration algorithm together have had the maximum improvement in the seismic images regarding the total removal of the dipping events at the end of the data processing. Migration has advanced the clarity of the subsurface images, especially for the steep-dip layers up to  $65^\circ$  thanks to moving them to their true locations.

However, smiling effects in the images have drawn the attention easily, which might have been due to the high amplitude spike noise, side-sweep diffractions and overmigrated data due to either downward continuation of the receivers or possible higher velocity function analyzed in the 2nd velocity analysis. Dondurur (2018) has emphasized the smiling effects can be handled by suppressing the spike noise and performing a new velocity analysis in case of higher velocity



function is used by the migration algorithm. However, since the side-sweep noise comes from the out-of-the 2D plane (3D), 2D migration cannot eliminate them completely. In order to prevent smiling effects in the seismic images, high-amp spike noise might have been tried to identify and remove from the data before the migration, which was not possible due to the stacked sections without a sufficient S/N ratio.

There have been also swings noise observed at the beginning of migrated images caused by the NMO stretch mute gaps of the stacked data. The simple explanation for why they have appeared is that they were not muted automatically by the same NMO-stretch muting in the migration module. To avoid the swings, a surgical muting should have been applied to the migrated data together with the final top muting, which has removed the noise above the seabed.

### 5.3 SEISMIC INTERPRETATION

The general difficulties, uncertainties and beneficial methods during the interpretation in Petrel has been summarized in this chapter. The main deformation structures identified in the research area are The Hornsund Fault Zone, Horst Structure and Devonian Graben (in the previous studies described as the Bellsund Graben). These results were compared with previous interpretation results and speculations from the published articles by Blinova et al. (2009 and 2013) and some important findings facts in the West Spitsbergen area emphasized by Dallmann (2015). Major similarities and differences will be discussed in this chapter as well.

The auto-tracking mode used in Petrel during the horizon interpretation of Seabed and URU was very adventurous in terms of receiving rapid results. However, some discontinuous, undulated and truncated reflectors had to be edited by manual interpretation mode in order to obtain more natural geological structures in the study area. The interpretation of the HFZ westward dipping layers in the western part of the seismic line 7 was mostly completed with high accuracy regarding the strongest reflector continuities. The surface map of the HFZ westward dipping layer 5 (Figure 4.34) was automatically extrapolated by Petrel from seismic lines 7 to 6 and to 8 from x to 1600 ms in the determined polygon. The extrapolated layers in the lines 6 and 8 vary 1000 –

1200 ms and 900 - 1600 ms, respectively. Therefore, the uncertainty of this surface map is increasing from the central part to the polygon border.

The interpretation of top Hecla Hoek was challenging due to the discontinuity of the reflections in the seismic images leading to uncertainties for Hecla Hoek, especially for seismic lines 6 and 8 having very low S/N ratio. Therefore, the surface map generated from the Hecla Hoek horizon does not have high accuracy. Determining the ideal top Hecla Hoek and top Devonian horizons has required the development of several alternatives and efforts to choose the most realistic one matching the evolution of the Spitsbergen area distinguished in various studies. These alternative horizon interpretations for top Hecla Hoek can be seen in APPENDIX C. Hecla Hoek has been interpreted as going deeper down westward in the HFZ than the results by Blinova et al. (2009), which is approximately 1000 ms (TWT). That could be related attenuated multiples and noise provided us to have different seismic signature in that deeper parts to interpret the reflectors as Hecla Hoek.

It was easier to interpret the major faults in the Hornsund Fault Zone and the Bellsund Graben along the seismic lines 2 and 7 than in the lines 6 and 8 due to their very low signal quality in the deeper parts. In addition to the fault interpretation guided by horizon shifting, the diffractions in the stacked sections were also used to approximately locate the edge of the faults in the suspicious areas. Thereby, the accuracy of the fault interpretation has been increased. Chasing the amplitude scatterings, looking almost colorless peaks and troughs, along the potential fault blocks was also supportive, especially at the chaotic reflectors. In all seismic lines, the interpreted fault blocks were only regional down-faulted blocks mostly in the HFZ and graben structure. In the interpreted seismic lines, minor faults have also been observed but not initiated in the results due to their uncertainties. There have also been some indications of possible strike-slip faults in some areas, in the horst structure and the west of the graben structure for instance. However, they have not been mentioned and defined in the results due to a lack of evidence from the previous studies. However, only one W-E trending strike-slip fault (Figure 4.28) could be

identified in seismic line 2 thanks to the interpretation results detailedly explained by Blinova et al. (2009).

The most obvious uncertainty of surface maps has been observed from the seabed. The extrapolating to generate a surface map between line 2 and the southernmost line 6 created an uncertain elevation of about 0 s (TWT). There could be a few reasons behind that. Due to the discontinuous seabed reflectors in seismic data, there are uninterpreted seabed horizons in seismic lines 2 and 6 presented in Figure 5.3.C and A, respectively. Thus, the extrapolation would have been done by chasing the same trend of the seabed interpretation in these lines, which are getting shallower. Therefore, the generated surface map has ended at 0 elevation value in seismic lines 2 and 6 (Figure 5.3.D and B, respectively).

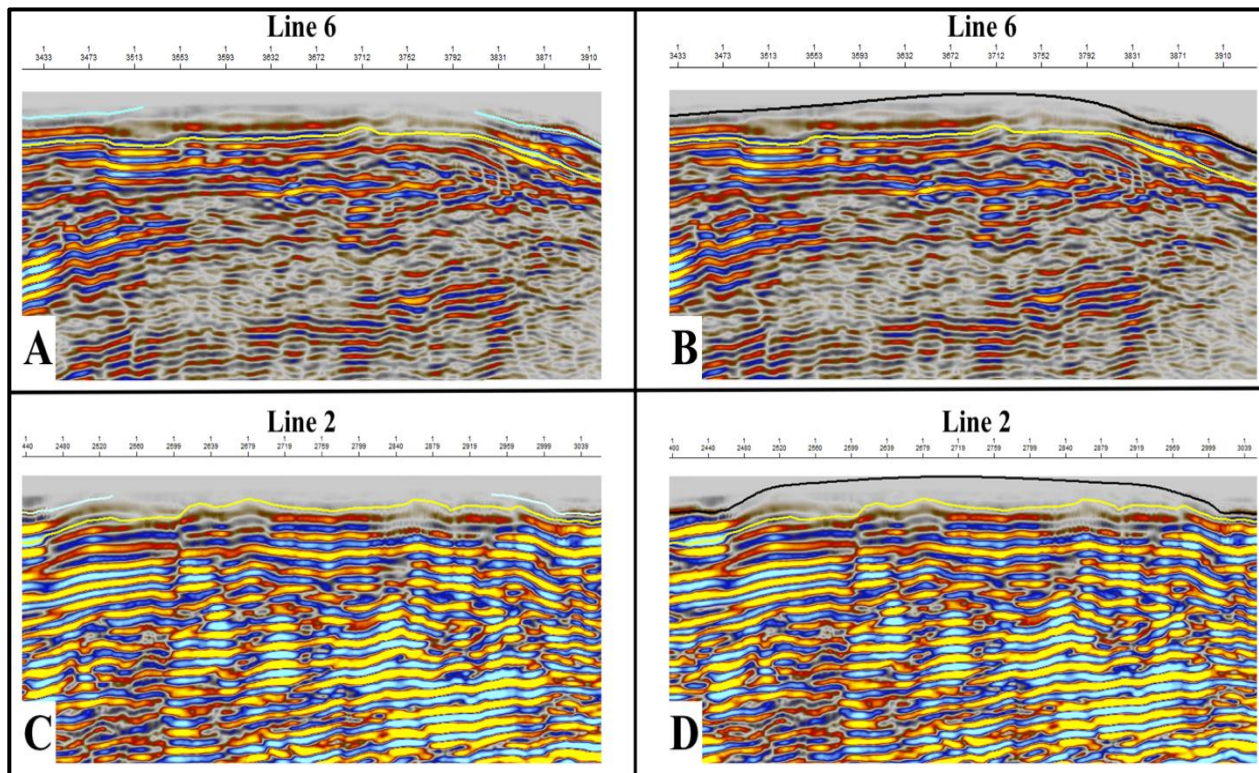


Figure 5.3 Interpreted seabed horizons in seismic line 2 (C) and 6 (A) and the extrapolated surface map displayed in the seismic line 2 (D) and 6 (B).

As there are no well logs and more evidence collected around the study area, some of the interpreted units may have uncertainties, especially Unit 3. The other units have been characterized and correlated with similar research in the same study area. For example, the exact age of Unit 1 is unknown, but it is described as a Cenozoic sediment wedge together with Unit 2 by Blinova et al. (2009). In our study, Unit 1 is roughly described as it is younger Cenozoic sedimentary strata than the underlying CSW. The unconformity horizon URU is well defined during the interpretation, which is a strong indicator of the glacial erosions truncating the westward dipping strata (Blinova et al., 2009; Dallmann, 2015). Since Unit 1 might have been accumulated from the last deglaciations to the present, it might be specifically differentiated as Quaternary sediment wedge. These glacial sediments might have been transported by meltwater, glacial transport or within a subglacial layer of deformation (Faleide et al., 1996).

The reasons why Unit 1 is thinner than Unit 2 and these units become thicker seawards can be associated with the thinning of the continental shelf of West Spitsbergen due to the seafloor spreading (Blinova et al., 2009). Regarding the interpretation results of this thesis, there is a solid agreement with Blinova et al. (2009) that these Cenozoic sediment strata in the HFZ becomes thicker and broader seaward because the outer part of West Spitsbergen was affected by the increased crustal thinning leading to break-up and accretion of oceanic crust.

The reflection character of Unit 3 is very chaotic having very weak amplitudes that might be associated with partly overlying unconsolidated sediments in the late Cenozoic and underlying consolidated sedimentary strata in Mesozoic and/or Paleozoic. Therefore, there is an agreement with Faleide et al. (1996) that the outer shelf of western Svalbard could have been affected by the rapid uplifting of overlying unconsolidated sediment strata. The seismic character of Unit 3 could not be correlated among seismic lines 6,7 and 8. Because lines 6 and 8 still included noise and possible side-sweep reflections shadowing the sediments in this unit. Nevertheless, the first three stratigraphic units in this thesis have been analyzed by differentiating them in terms of accumulation in different periods. So, there is little agreement with Blinova et al. (2009), who interpreted these units as a completely Cenozoic Sediment Wedge. Stratigraphic results of this

thesis, especially from seismic line 7 (Figure 4.39), reveals the potential division of sediment groups into unit 1, 2 and 3 in the HFZ area, indicating the different geological periods in terms of their various reflector characters. From that figure, it has been also correlated with Blinova et al. (2009) that how the units 2,3 and 5 were uplifted by the compressional forces in in the pre-latest Paleocene and truncated by URU later.

Because of the chaotic and discontinuous weak reflectors, Unit 4 is the most uncertain unit among all interpreted units in this study. The reflector layers have been interpreted in the basin and southeastern part of the area as well. A similar seismic signature for Devonian Old Red sediments could not be identified in the Hornsund Fault Zone. This is the main reason why the surface and thickness maps of Unit 4 were generated only in the graben structure. On the one hand, since there is also no solid correlation between the study in the same area by Blinova et al. (2009) and this thesis research about Devonian Old Red sediments, the existence of unit 4 relies on assumptions, thanks to its unique reflection character.

On the other hand, the similar reflector character and polarity changes of the Old Red sedimentary fill of the graben structure in this study have also been observed as scattered and discontinuous in the Devonian Graben in inner Isfjorden by Blinova et al. (2013). It has been given an example from a 1988 survey by Equinor (formerly Statoil) that the seismic reflectivity of Devonian sedimentary strata was characterized as scattered and weak amplitude signal. It has also been highlighted that strong short reflectors within the seismic signature of Devonian sediments may be associated with the dolerite sill intrusions (Blinova et al., 2013). Furthermore, it has been also mentioned by Blinova et al. (2009) that Paleozoic and Mesozoic sedimentary strata may possibly be present underlying the Cenozoic sedimentary wedge to the crystalline basement in the location of this thesis research.

Therefore, the possible existence of filling Devonian Old Red sediments overlying Hecla Hoek in the basin can be associated with other discoveries of this thesis, in order to reveal an alternative development history of this graben structure. One of the different outcomes observed during the

interpretation is the graben structure in the Bellsund area. The basin might be impacted by N-S extending major faults along the basin (Figure 5.4), and can be correlated with N-S trending fault-bounded rift basins as a result of the collapsed Caledonian orogeny described by Dallmann (2015). Eventually, this new finding of the N-S trending basin is not consistent with the identified NW-SE oriented Bellsund Graben by Blinova et al. (2009).

The top Hecla Hoek surface has been investigated in 3D display in Petrel (Figure 5.5) to correlate new findings and similarities of the Hornsund Fault Zone and Devonian Graben (?), initiated in Devonian but also reactivated later probably containing the Cenozoic, Mesozoic and/or Paleozoic sedimentary rocks. The map also revealed a horst structure between the eastern border of the HFZ and the western border of the graben.

### **The Hornsund Fault Zone**

The interpretation results from the Hornsund Fault Zone are consistent with the development of the HFZ distinguished by Blinova et al. (2009) as a reactivation of the old compressional and strike-slip structures (detail explained in chapter 2.2.1) in Cenozoic. Because of these deformation structures, and later Cenozoic extension, the Hornsund Fault Zone comprises several obliquely westward tilted down-faulted blocks from the western boundary with the horst structure, which have been clearly observed during the horizon and fault interpretation, seen in the 3D surface map of Hecla Hoek (Figure 5.5) as well. The 3D map has also revealed the trend of the HFZ of this thesis result to be the same NNW-SSE as the same trend described for HFZ by Blinova et al. (2009).

### **The Horst Structure**

The horst structure which is located between the eastern part of HFZ and the western part of the graben structure is shallowing from south to north (Figure 5.5), which corresponds to the description for the horst structure by Blinova et al. (2009). However, there is a slight difference, as the horst structure becomes narrower from north to south in this study.



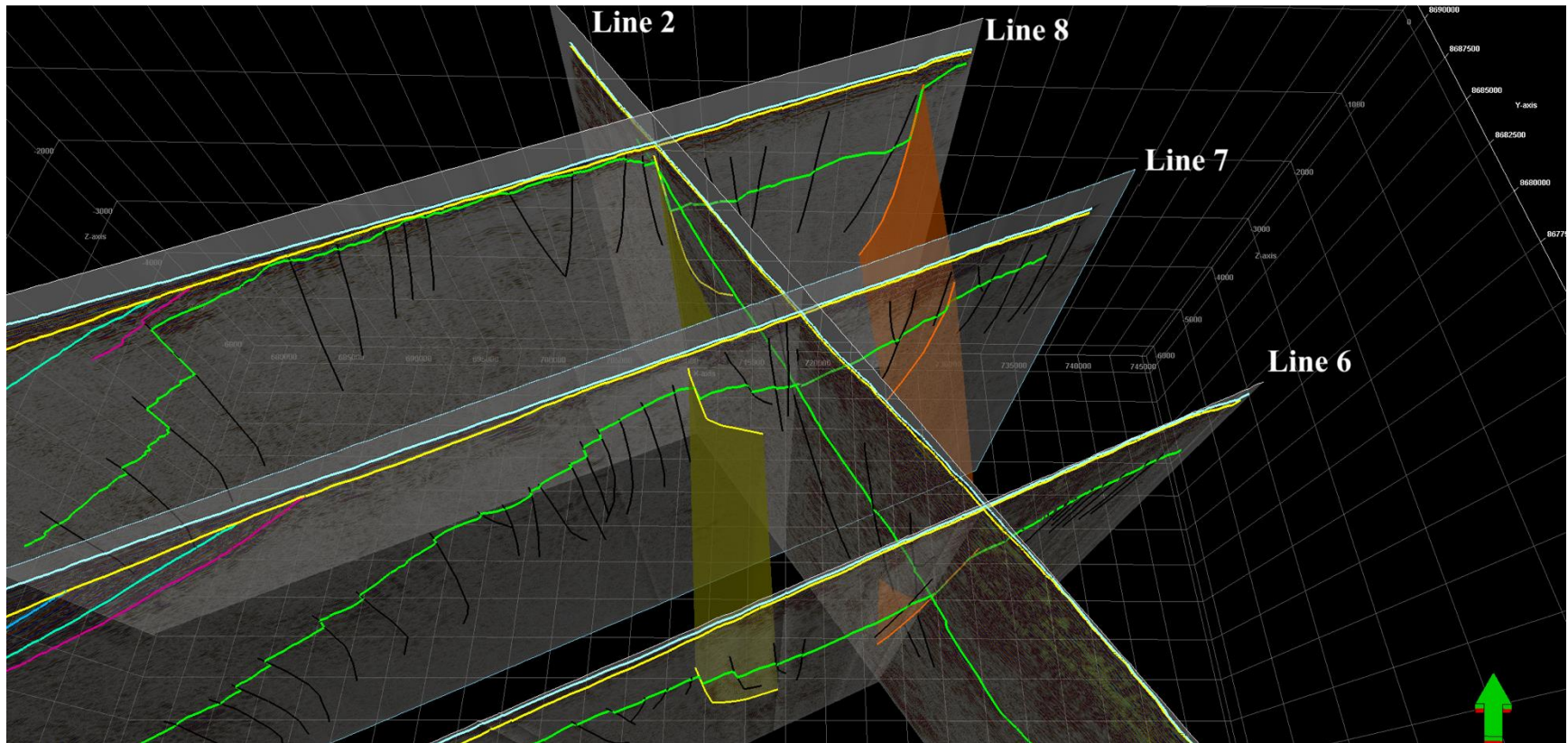


Figure 5.4 The 3D display of the N-S trending fault-bounded rift basin. The eastward dipping major fault (yellow) at the western boarder of the basin. The westward dipping major fault (orange) at the eastern boarder of the basin. The black lines indicate the normal down-faulting blocks in the study area. The faults in HFZ trending NNW-SSE. The interpreted horizons in all seismic lines; Seabed (turquoise blue), URU (yellow), the HFZ dipping layers 3-5 (blue, turquoise green and purplish red lines, respectively), and top Hecla Hoek (green).

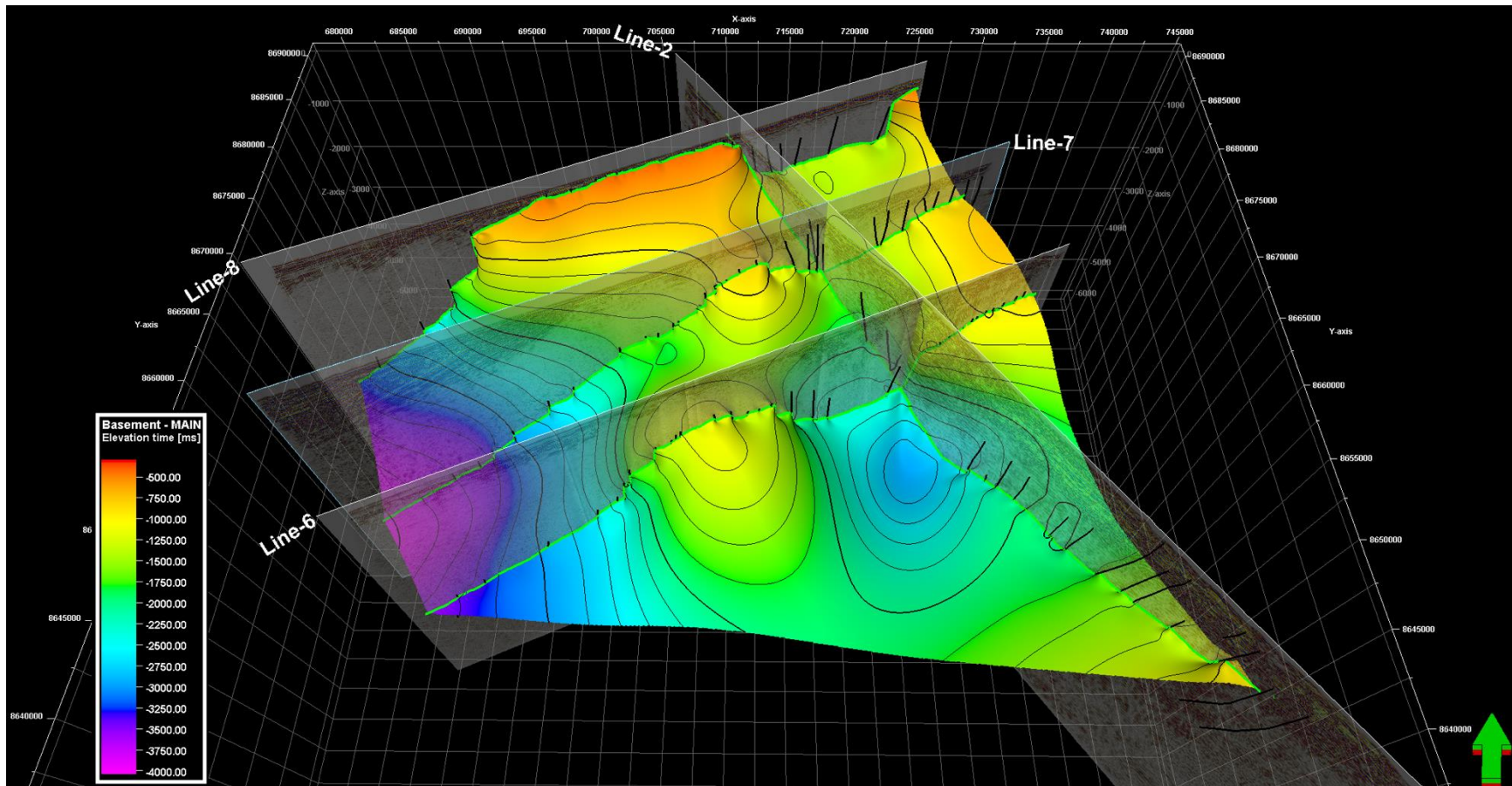


Figure 5.5 3D surface map of top Hecla Hoek with isochrons in TWT (ms) and all seismic lines with the faults are displayed. The map reveals that the N-S trending graben structure has been uplifted northwards. The Hornsund Fault Zone consisting of downfault blocks is trending NNW-SSE. The N-S trending horst structure between the HFZ and graben structure might have inconsistency between seismic lines 7 and 8.

## The Devonian Graben

Therefore, a model associated with these new outcomes above might have an alternative tectonic history for the Bellsund Graben, which could be related to the N-S trending Devonian graben structure in inner Isfjorden observed by Blinova et al. (2013). The new model of graben structure can be outlined below:

1. Late Proterozoic – Early Silurian: Hecla Hoek Basement developed consisting of metamorphic and magmatic rocks (Blinova et al., 2013; Blinova et al., 2009).
2. Early Ordovician – Early Devonian: Caledonian mountain range was developed during the collision between Laurentia and Baltica continents (Dallmann, 2015).
3. Devonian: Extensional regime causing collapse of the Caledonian mountain range in Spitsbergen and formation of the N-S trending fault-bounded rift basin, the so-called Devonian graben (Blinova et al., 2013; Dallmann, 2015).
  - a. During and after the basin collapse, the Old Red sediments were eroded and accumulated up to 8000 m in thickness until Early Carboniferous and rested unconformably over the crystalline basement (Blinova et al., 2013; Blinova et al., 2009; Dallmann, 2015).
  - b. The Old Red sediments may have been preserved in the down-faulted basin in the research area of this thesis, which may be a continuation of Devonian grabens of northern Spitsbergen and inner Isfjorden (Blinova et al., 2013; Dallmann, 2015). In this basin, younger rock formations overlying Devonian Old Red sediments might be present, but there are no strong indications in the seismic images to discuss.
4. Cenozoic: The basin may have been reactivated.
  - a. Early Oligocene: The basin might have been reactivated by oblique extension during the subsequent regional transtension along western Spitsbergen, which is associated with seafloor spreading between Greenland and Svalbard (Blinova et al., 2009). The oblique extension was the possible reason for the normal faulting, where the down-faulting blocks were observed in the Hornsund Fault Zone.
  - b. Oligocene: After the final graben development, thinning of the continental shelf of the western Svalbard margin may have taken place by the extension (Blinova et al.,

- 2009). That might have resulted in the accumulation of the thick CSW over the Devonian and younger strata in the N-S trending basin.
- c. Neogene - Present: Younger CSW (Quaternary successions of glaciomarine) accumulated during the at least 16 major glacier advances offshore to the west and north of Svalbard since the onset of Pleistocene (Dallmann, 2015).

## 6 CONCLUSIONS

### 6.1 SEISMIC DATA PROCESSING

A total of four 2D multichannel seismic reflection profiles acquired off Isfjorden have been processed. 5 different workflows of seismic data processing have been performed in seismic line 8 in order to find out the best remedies, especially for the surface-related multiples with long periods due to the very hard and shallow seafloor. Once the most ideal workflow has been determined, it has been implemented on all seismic lines.

- The main processing workflow consists of pre-processing, top muting, trace interpolation, 1st velocity analysis, multiple extraction & adaptive subtraction, 2nd velocity analysis, DMO and NMO corrections, stacking, top muting, band-pass filtering,  $f-k$  filtering, amplitude scaling, post-stack time migration, final-top muting.
- Since velocity analysis is one of the most significant processing sequences in seismic data processing, pre-processing steps have been done precisely to obtain a high S/N ratio by suppressing the undesired noise and removing the artificial effects. The  $f-k$  and band-pass filter and the signature deconvolution were the major contributors during the pre-processing sequence.
- The trace interpolation has not only enhanced the S/N ratio, but also increased the efficiency of the processing sequences and become an augmentation for the semblance plots in the velocity analyses thanks to the increased 120-fold CMP gathers.
- Due to the scattered waves and the surface-related multiples, amplitudes of the primary reflections were degraded and masked, making it almost impossible to pick velocities below 500 ms in the semblance plots. Thus, the 1st velocity analysis has not provided an accurate velocity model.

- The 2nd velocity analysis has been performed in the almost multiple-free CDPs generated by the multiple extraction and adaptive subtraction method, in order to flatten the hyperbolas of the primary reflections that could not be accomplished by the NMO correction after the 1st velocity analysis.
- The certainty of the new velocity model from the 2nd analysis has been increased by more picked velocities of the primary reflections that were mostly masked by the surface-related multiples before.
- It has also been experienced that when the velocity analysis was performed with the shorter CDP interval, the velocity functions provided higher accuracy, which is crucial for both the NMO correction and the migration algorithm.
- Although the multiple extraction & adaptive subtraction approach has accomplished removal of the surface-related multiples from all seismic profiles, the amplitude of most of the westward dipping layers has been lost after a certain arrival time (TWT) in seismic lines 6 and 8, especially in the western side of the sections.
- After the subtraction, interbed multiples have been also appeared in some parts of the seismic lines 7 and 8, whose amplitudes were slightly attenuated by the 2nd velocity analysis, as well as the  $f$ - $k$  and band-pass filter applied to the stacked data.
- All in all, the multiple extraction & adaptive subtraction method has provided the best multiple-free data among all multiple attenuation approaches performed in five workflows. However, the method is a trade-off between data loss and removal of the multiples. Therefore, alternative methods should be taken into consideration for different processing goals.



- Each seismic trace has been moved to its true zero-offset location by the DMO correction. Thus, some steep, coherent noise from the truncated sub-dipping layers in the study area and fault planes has become more obvious.
- Thanks to the accurate velocity functions used by the NMO correction, hyperbolas of the primary reflections have been perfectly flattened by moving the traces to their true zero-offset times in the CMP gathers.
- Owing to the stacking of the NMO-corrected CMPs, the data quality of the stacked sections has been dramatically enhanced, thanks to the improved S/N ratio compared to the pre-processed seismic profiles.
- The FD with the omega-x algorithm has worked well to improve both the structural image of the dipping layers and the lateral resolution, while not being affected by lateral nor vertical velocity variations.
- The migration results have been exposed by smiling effects which might have been caused by high amplitude spike noise, side-sweep diffractions or overmigrated data, due to possible too high velocity functions.
- High amplitude spike noise may have been investigated and tried removed from the stacked sections, in order to prevent smiling effects on the migrated images and to keep the largest S/N ratio.

Consequently, multiple extraction & adaptive subtraction can be considered a promising technique for this type of data, in spite of all geologic complexities and acquisition limitations. Yet, the alternative multiple elimination methods and migration algorithm can be taken into consideration for future processing of 2D multichannel reflection seismic data in the same research area, in order to deal with the surface-related multiples and challenging steep-dip

events, while obtaining the subsurface images with minimum data loss and smiling effects, and maximum data quality.

## 6.2 SEISMIC INTERPRETATION

The seismic interpretation has been completed with nine interpreted seismic horizons and five distinguished stratigraphic units along four seismic profiles, supported by five surface and three thickness maps. The surface and thickness maps for the units have been used frequently to provide detailed observations by demonstrating the results in 2D and 3D. Stratigraphic units have been differentiated precisely to find out their accumulation histories. Hence, the Hornsund Fault Zone, a horst, and a graben structure have been identified and compared to the previous research in West Spitsbergen. Almost all results have been consistent with earlier studies, with exception of an alternative development history of the graben structure in light of possible discoveries of Devonian Old Red sediments and a N-S trending fault-bounded rift basin.

- Numerous eastward and westward-dipping major faults have been interpreted in all seismic lines. W-E trending strike-slip fault has been identified only in the northern part of seismic line 2, which is consistent with the previous research in the same study area.
- The stratigraphic units overlying the basement in the HFZ divided into three units is slightly different from previous studies due to the reflection patterns disclosing the presence of an additional unit underlying the first two units, the Cenozoic sediment wedge. Therefore, unit 3 might be Mesozoic or Paleozoic consolidated sedimentary rocks and younger partly unconsolidated Cenozoic sediments.
- The first two stratigraphic units have been expressed as the overlying Quaternary subparallel sediment strata and the older westward dipping Cenozoic sedimentary wedge, which have been separated by the unconformity URU.

- It has been found that Cenozoic sediments accumulated offshore by thinning of the continental shelf of West Spitsbergen due to the continental extension from the latest Paleocene to Oligocene. The accumulation of younger sediments has taken the place due to the repeated ice ages in Quaternary to the present.
- Unit 5 has been explained as the oldest basement rock in Svalbard, which is Hecla Hoek. It has been interpreted that units 2, 3 and 5 in HFZ represent uplifted sediments related to the compressional regime in late Paleocene. Then units 2 and 3 were glacially eroded during repeated glaciations-deglaciations.
- The top Hecla Hoek has been defined as a deformed basement horizon by normal faults striking NNW to SSE in HFZ and N-S in the graben structure. Interpretation of Hecla Hoek has been significant to provide better understanding, especially concerning the development of the HFZ and graben structure.
- The Hornsund Fault Zone has been interpreted in accordance with the previous studies, suggesting that the area was reactivated by compressional forces in early Cenozoic. This was followed by continental extension deforming the basement and shallower sedimentary strata. As a result, numerous obliquely down-faulted blocks with dipping towards west-southwest, are found in the HFZ.
- An NNW-SSE trending horst structure has been described within the top Hecla Hoek, shallowing from south to north along West Spitsbergen. The horst structure is located between the western border of the graben structure and the eastern border of the HFZ.
- A N-S trending fault-bounded rift basin partly filled in with Devonian Old Red sediments has been interpreted in the Bellsund area. The basin may have emerged from the collapse of the Caledonian mountain range. The Devonian Old Red sediments might have accumulated in the basin as the erosional product of the collapsing Caledonian mountain range.

- The Bellsund Graben, named from an earlier study, has been reinterpreted as a potential Devonian Graben including down-faulted blocks inside the basin. This is one of the main new outcomes from this thesis.

All distinguished and characterized geological results rely on the quality of the 2D multichannel seismic reflection data, which has limitations to image the very complex geology in the study area. Nevertheless, the utmost efforts have been put to interpret the seismic data by correlating the evolution history of the structures from earlier studies. Thanks to the enhancement of the S/N ratio provided by the processing, the new outcomes have strengthened the possibilities of an alternative history of the development. Consequently, these findings might be encouraging for future studies using different sorts of acquisition techniques, seismic processing workflows and interpretation methods, in order to explore more of Svalbard's geology.

## REFERENCES

- AlAli, A., & Anifowose, F. (2022, 2022/01/01). Seismic velocity modeling in the digital transformation era: a review of the role of machine learning. *Journal of Petroleum Exploration and Production Technology*, 12(1), 21-34. <https://doi.org/10.1007/s13202-021-01304-0>
- Blinova, M., Faleide, J. I., Gabrielsen, R. H., & Mjelde, R. (2013). Analysis of structural trends of sub-sea-floor strata in the Isfjorden area of the West Spitsbergen Fold-and-Thrust Belt based on multichannel seismic data. *Journal of the Geological Society*, 170(4), 657-668.
- Blinova, M., Thorsen, R., Mjelde, R., & Faleide, J. I. (2009). Structure and evolution of the Bellsund Graben between Forlandsundet and Bellsund (Spitsbergen) based on marine seismic data. *Seismic study along the west Spitsbergen continental margin and adjacent area of the West Spitsbergen Fold and Thrust Belt (Isfjorden)*.
- CGGVeritas. (2008a). Geocluster User's Guide.
- CGGVeritas. (2008b). Release Notes.
- Dallmann, W. K. (1999). Lithostratigraphic lexicon of Svalbard: review and recommendations for nomenclature use: Upper Palaeozoic to Quaternary bedrock.
- Dallmann, W. K. (2015). Geoscience Atlas of Svalbard.
- Dondurur, D. (2018). *Acquisition and Processing of Marine Seismic Data*. Elsevier Science. <https://books.google.no/books?id=pyk0DwAAQBAJ>
- Dragoset, W. H., & Jeričević, Ž. (1998). Some remarks on surface multiple attenuation. *Geophysics*, 63(2), 772-789.
- Faleide, J. I., Solheim, A., Fiedler, A., Hjelstuen, B. O., Andersen, E. S., & Vanneste, K. (1996). Late Cenozoic evolution of the western Barents Sea-Svalbard continental margin. *Global and Planetary Change*, 12(1-4), 53-74.
- Gadallah, M. R., & Fisher, R. (2009). *Exploration Geophysics*. Springer Science & Business Media. <https://doi.org/10.1007/978-3-540-85160-8>
- Herron, D. A. (2011). *First Steps In Seismic Interpretation*. Society of Exploration Geophysicists.
- Hübscher, C., & Gohl, K. (2013). Reflection/Refraction Seismology. In J. Harff, M. Meschede, S. Petersen, & J. Thiede (Eds.), *Encyclopedia of Marine Geosciences* (pp. 1-15). Springer Netherlands. [https://doi.org/10.1007/978-94-007-6644-0\\_128-1](https://doi.org/10.1007/978-94-007-6644-0_128-1)

- Kanasewich, E. R. (1981). *Time Sequence Analysis in Geophysics*. University of Alberta.
- Kearey, P., Brooks, M., & Hill, I. (2002). *An Introduction to Geophysical Exploration* (3 ed., Vol. 4). John Wiley & Sons.
- Landrø, M., & Amundsen, L. (2018). *Introduction to Exploration Geophysics with Recent Advances*. Bivrost.
- Liner, C. L. (2016). *Elements of 3D Seismology*. Society of Exploration Geophysicists.
- Mitchum Jr, R., Vail, P. R., & Thompson III, S. (1977). Seismic stratigraphy and global changes of sea level: Part 2. The depositional sequence as a basic unit for stratigraphic analysis: Section 2. Application of seismic reflection configuration to stratigraphic interpretation.
- Mjelde, R. (2003). *SVALEX 2002: MCS survey Isfjorden and shelf by use of Håkon Mosby*.
- Mjelde, R. (2011). *Seismic Acquisition: Geophysical Principles* <http://buster.geo.uib.no/emodules/modules/Seismic%20acquisition%20principles/index.html>
- Sheriff, R. E. (2002). *Encyclopedic Dictionary of Applied Geophysics* (4th ed.). Society of Exploration Geophysicists. <https://doi.org/http://dx.doi.org/10.1190/1.9781560802969>
- Sheriff, R. E., & Geldart, L. P. (1995). *Exploration Seismology*. Cambridge university press.
- Verschuur, D. J. (2013). *Seismic Multiple Removal Techniques: Past, Present and Future*. EAGE Publications Houten, The Netherlands.
- Verschuur, D. J., & Berkhout, A. J. (1997). Estimation of multiple scattering by iterative inversion; Part II, Practical aspects and examples. *Geophysics*, 62, 1596-1611.
- Yilmaz, O. (2001). *Seismic Data Analysis: Processing, Inversion, and Interpretation of Seismic Data* (Vol. 1). Society of Exploration Geophysicists. <https://books.google.no/books?id=ZDJNAQAAIAAJ>
- Zhou, H. W. (2014). *Practical Seismic Data Analysis*. Cambridge University Press. <https://books.google.no/books?id=rRliAgAAQBAJ>



## FIGURE REFERENCE

Figure 1.1. Google Earth Pro, 2022 (Version7.3.4). Google Inc. Exported online version: (9 September 2022).

Figure 2.1. Svalbardkartet, 2022. Norwegian Polar Institute. Accessed online:  
<<https://geokart.npolar.no/Html5Viewer/index.html?viewer=Svalbardkartet>> (22 June 2022).



# APPENDIX A

## A.1. MAIN PROCESSING WORKFLOW

The different processing sequences applied during the main processing workflow (the 5th one in the Table 4.3) has been presented by their screen-captures of the Xjob folders from the CGG Geocluster. The only different XJob folders are from the different multiple elimination approaches.

### A.1.1 Reformat Xjob Folder

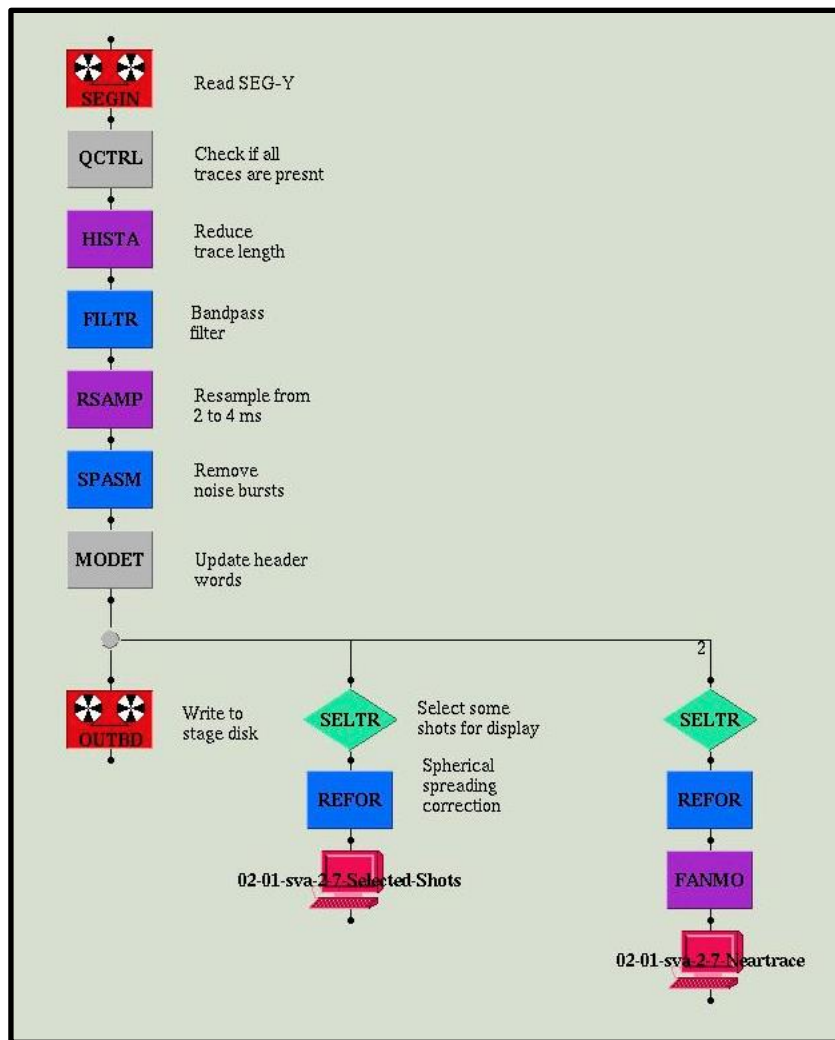


Figure A. 1 Reformat Xjob Folder as 1st part of the pre-processing sequence, extracted from CGG Geocluster.

## A.1.2 Design Xjob Folder

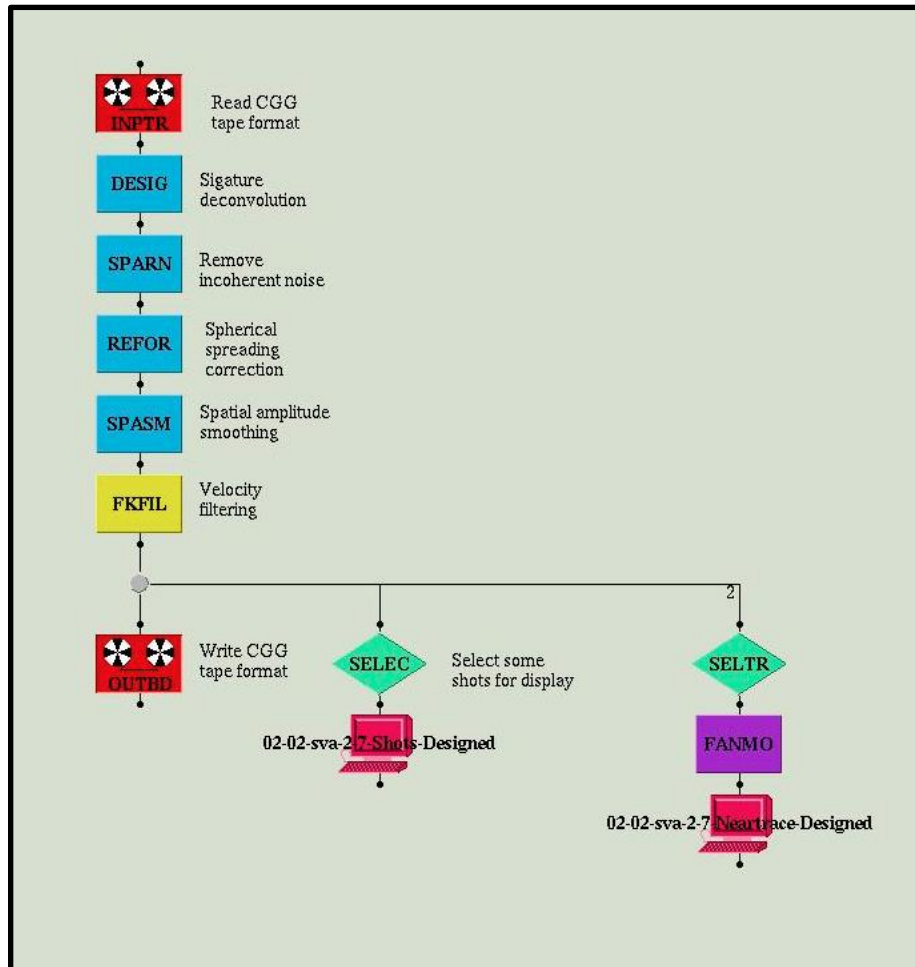


Figure A. 2 Design Xjob Folder as 2nd part of the pre-processing sequence, extracted from CGG Geocluster.

### A.1.3 Interpolation Xjob Folder

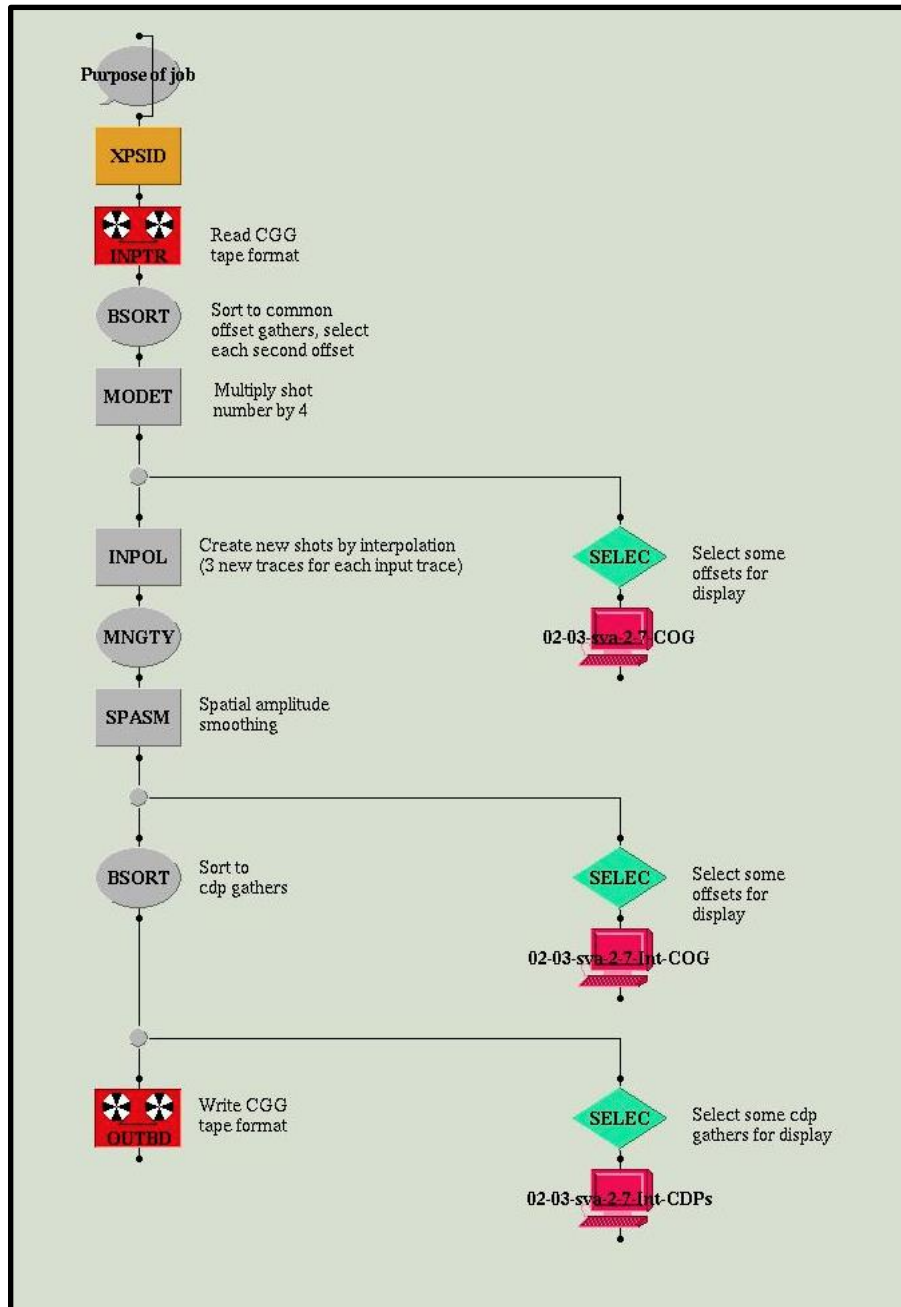


Figure A. 3 Interpolation Xjob Folder, extracted from CGG Geocluster.

### A.1.4 Velocity Modeling Xjob Folder

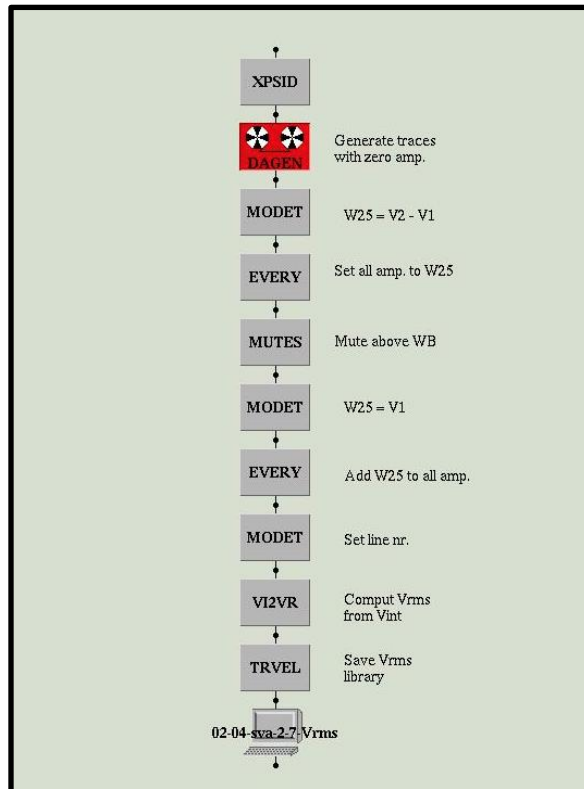


Figure A. 4 Velocity Modeling Xjob Folder, extracted from CGG Geocluster.

### A.1.5 Preparation for the 1st Velocity Analysis Xjob Folder

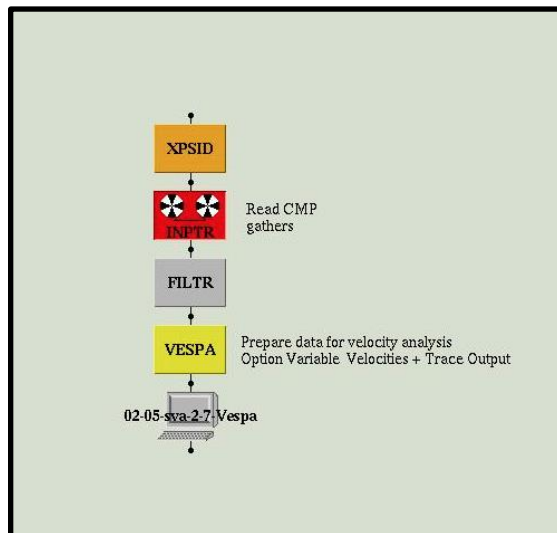


Figure A. 5 Preparation for the 1st Velocity Analysis Xjob Folder, extracted from CGG Geocluster.



## A.1.6 Multiple Extraction Xjob Folder

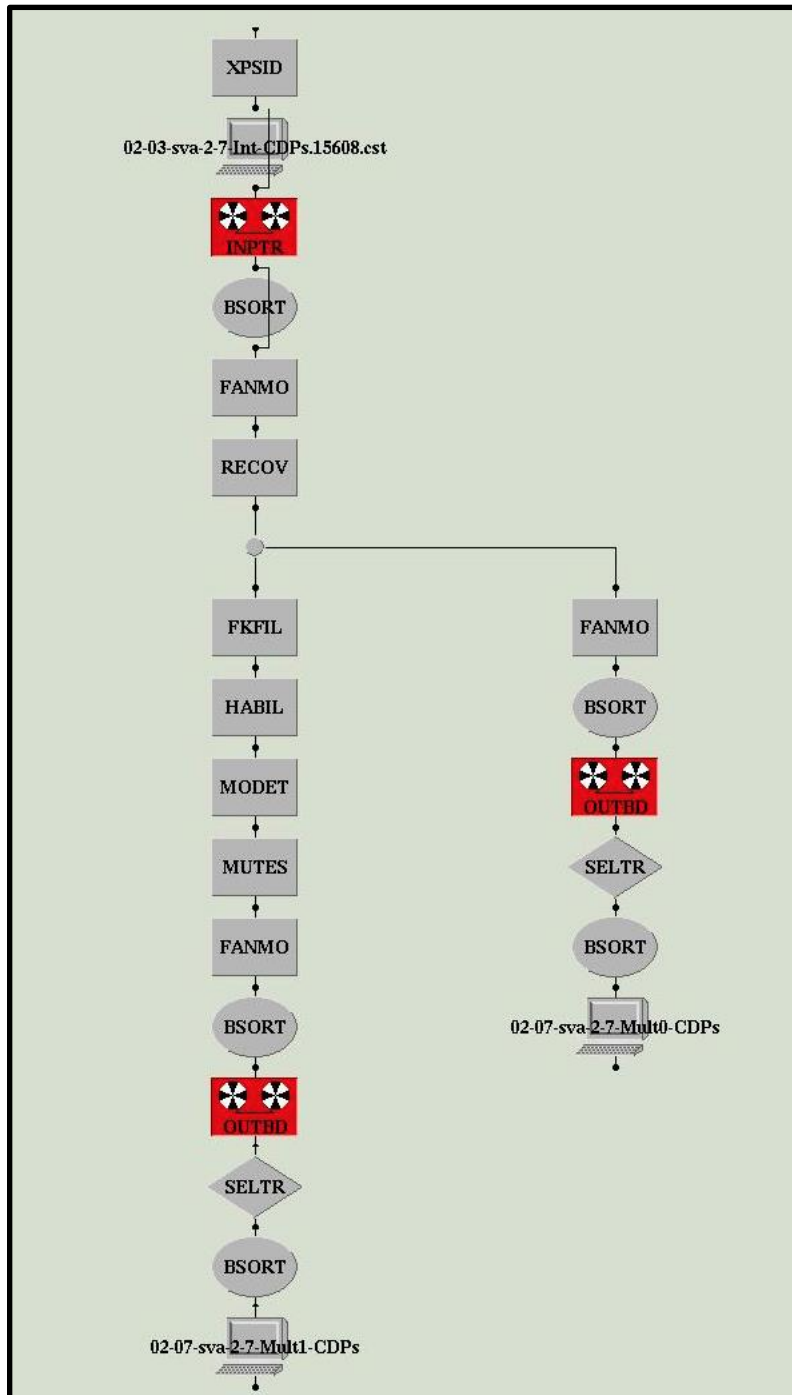


Figure A. 6 Multiple Extraction Xjob Folder, extracted from CGG Geocluster.

### A.1.7 Adaptive Subtraction Xjob Folder

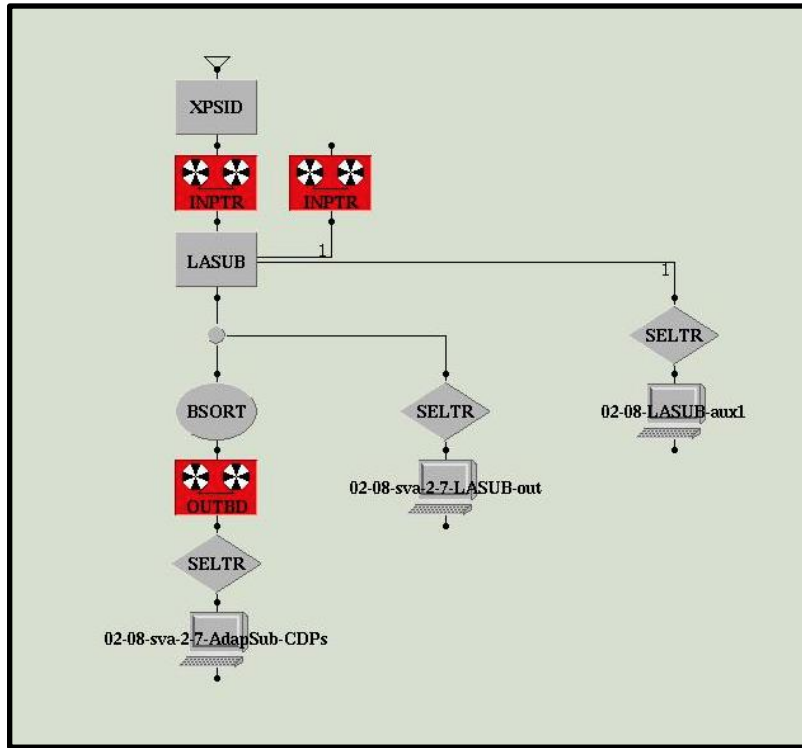


Figure A. 7 Adaptive Subtraction Xjob Folder, extracted from CGG Geocluster.

### A.1.8 1st QC - Brute-stack Section for Adaptive Subtraction Xjob Folder

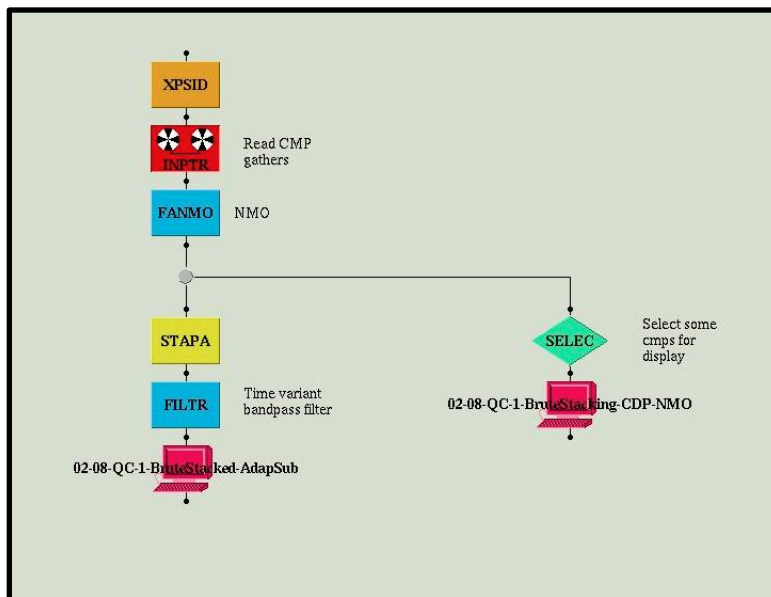


Figure A. 8 1st QC - Brute-stack Section for Adaptive Subtraction Xjob Folder, extracted from CGG Geocluster.

### A.1.9 2nd QC - Autocorrelation for Adaptive Subtraction Xjob Folder

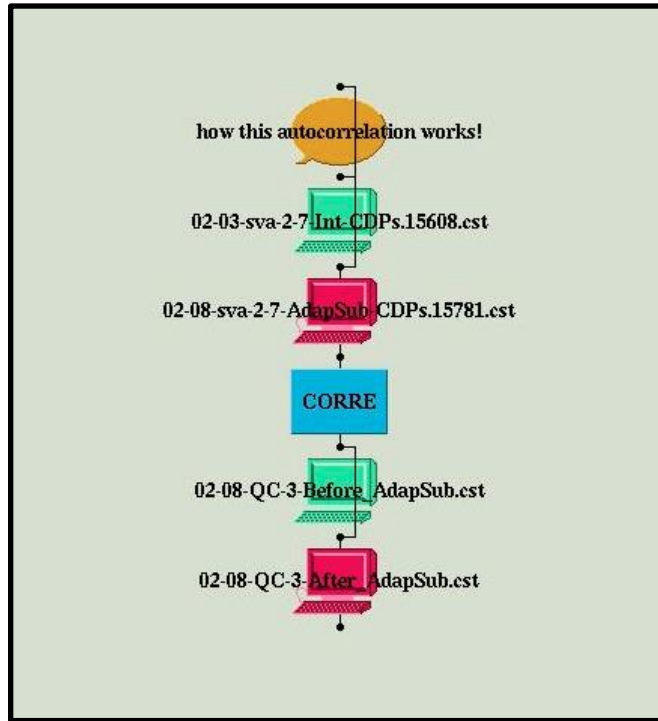


Figure A. 9 2nd QC - Autocorrelation for Adaptive Subtraction Xjob Folder, extracted from CGG Geocluster.

### A.1.10 Preparation for the 2nd Velocity Analysis Xjob Folder

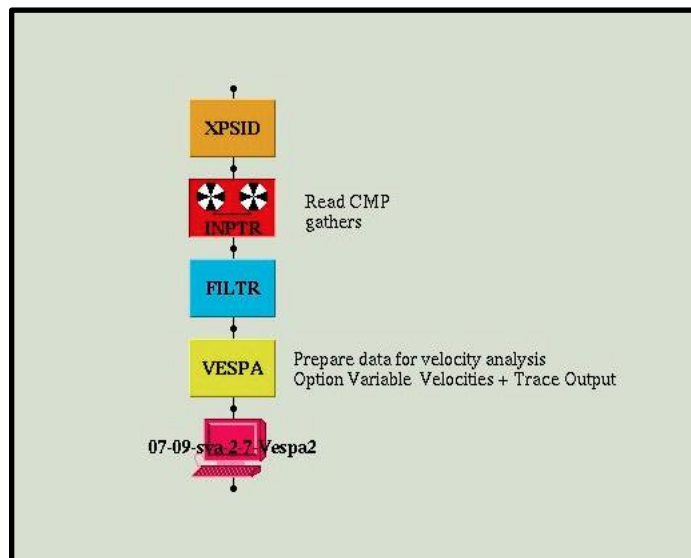


Figure A. 10 Preparation for the 2nd Velocity Analysis Xjob Folder, extracted from CGG Geocluster.

### A.1.11 QC - Brute-stack Section after the 2nd Velocity Analysis Xjob Folder

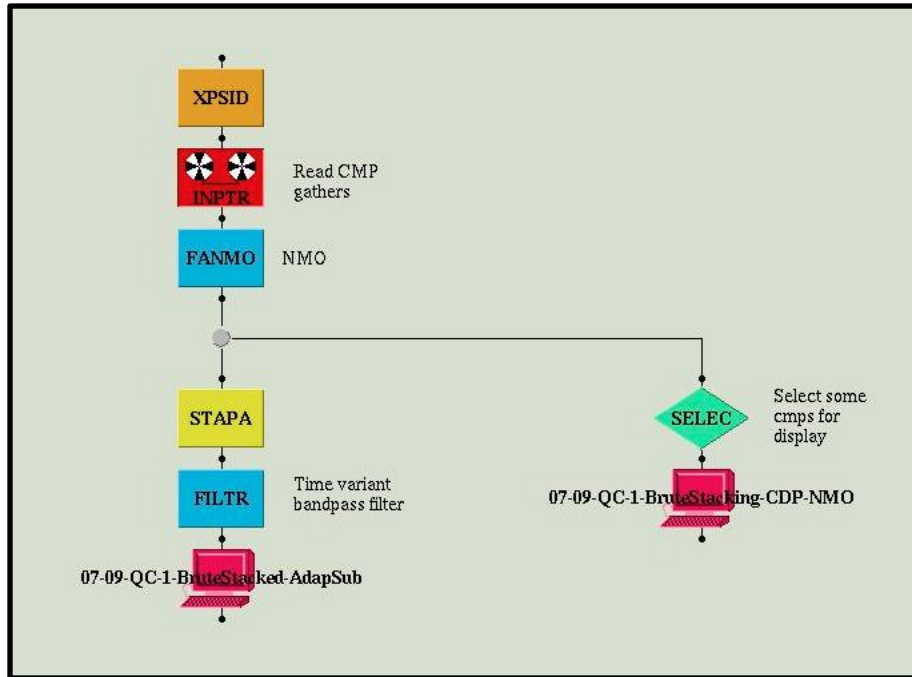


Figure A. 11 QC - Brute-stack Section after the 2nd Velocity Analysis Xjob Folder, extracted from CGG Geocluster.

### A.1.12 QC - Band-Pass Filtering for DMO Correction Xjob Folder

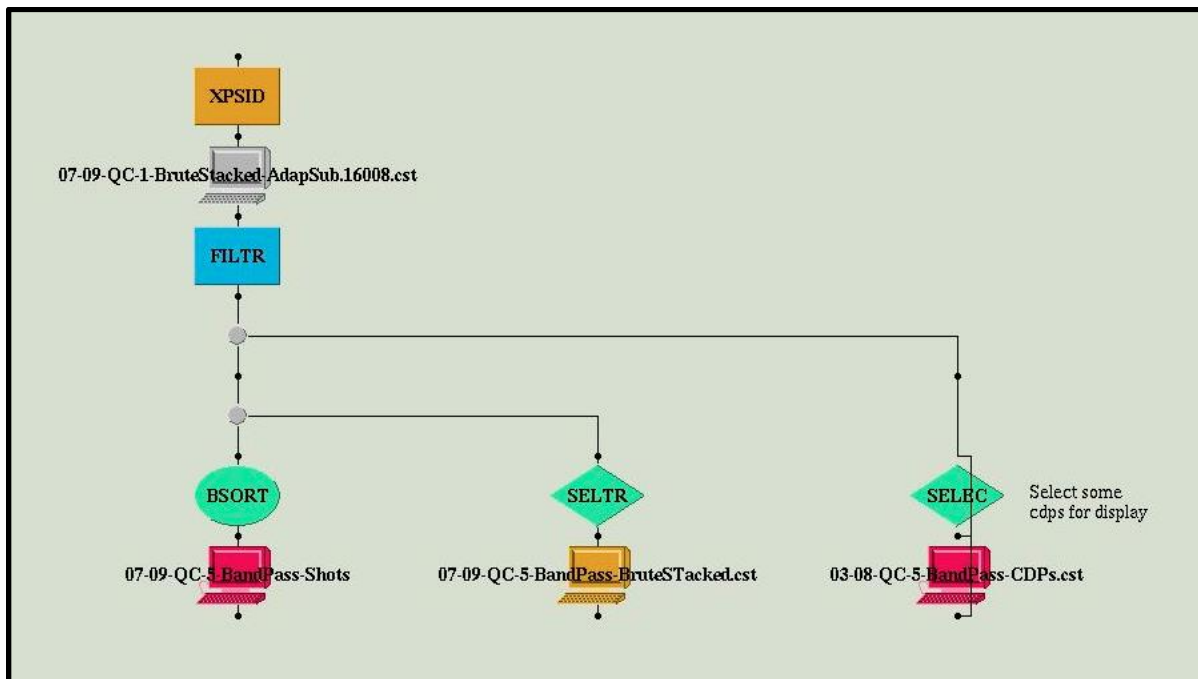


Figure A. 12 QC - Band-Pass Filtering for DMO Correction Xjob Folder, extracted from CGG Geocluster.

### A.1.13 DMO Correction Xjob Folder

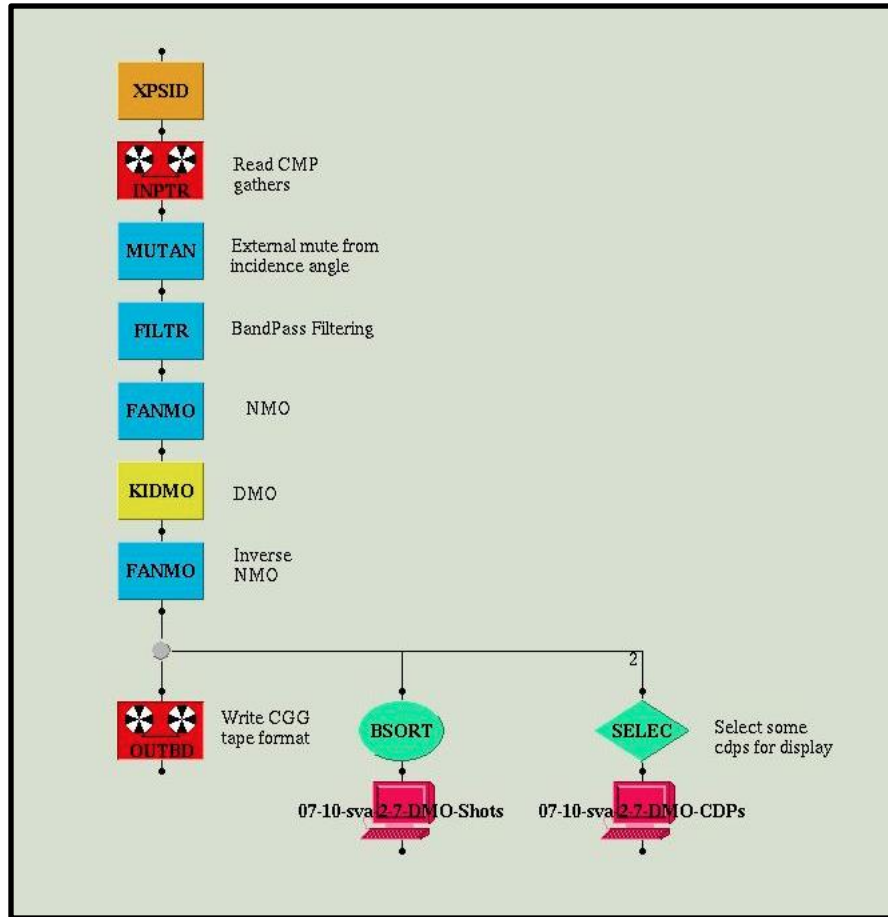


Figure A. 13 DMO Correction Xjob Folder, extracted from CGG Geocluster.

### A.1.14 NMO Correction and Stacking Xjob Folder

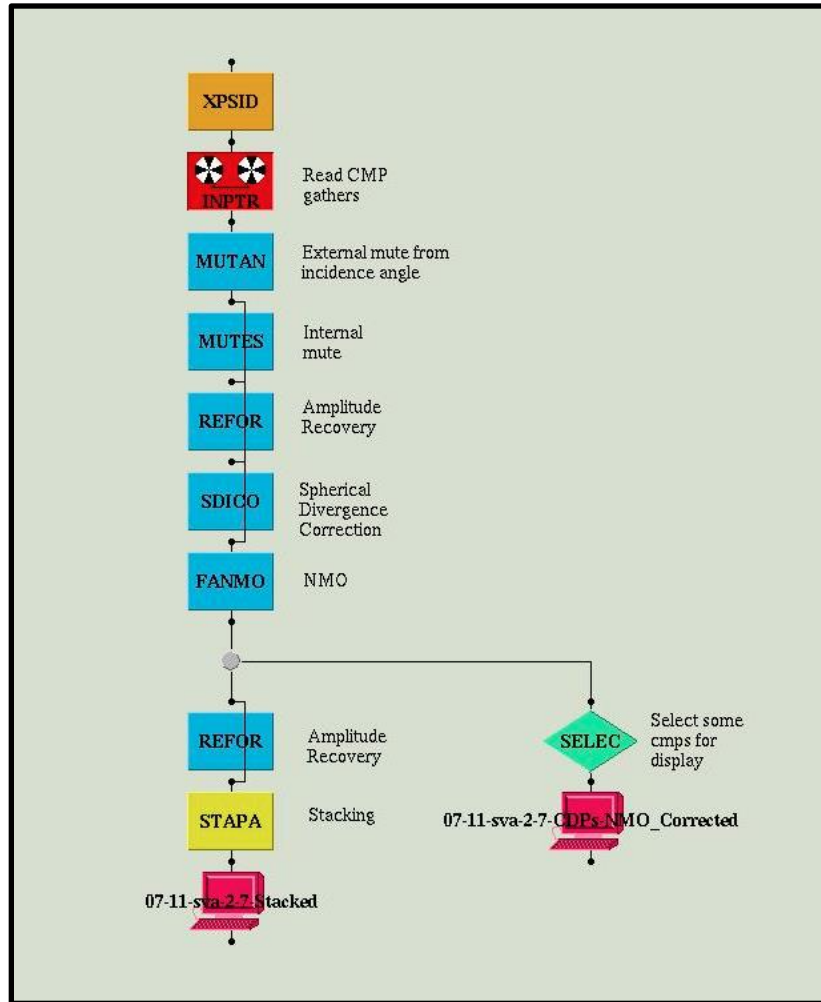


Figure A. 14 NMO Correction and Stacking Xjob Folder extracted from CGG Geocluster.



### A.1.15 Post-stack Time Migration Xjob Folder

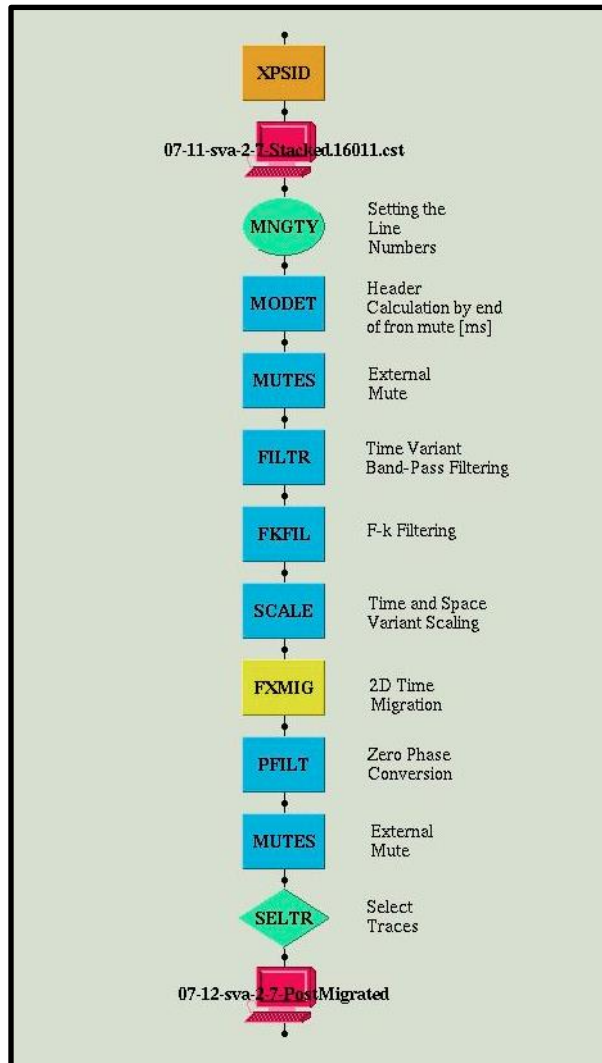


Figure A. 15 Post-stack Time Migration Xjob Folder, extracted from CGG Geocluster.

## A.1.16 Seg-y Output Xjob Folder

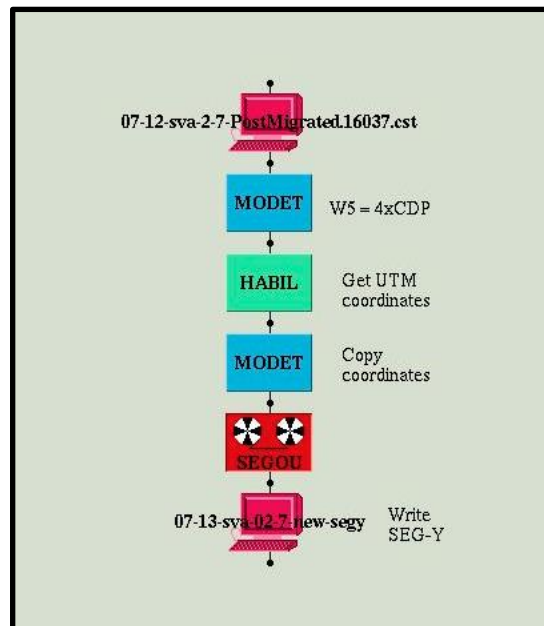


Figure A. 16 Seg-y Output Xjob Folder, extracted from CGG Geocluster.

## A.2. ADDITIONAL RESULTS FROM THE MAIN PROCESSING WORKFLOW

### A.2.1 Pre-processing Results

Pre-processing results of all seismic can be found in the following near-trace sections.

### A.2.1.1 Seismic Line 2

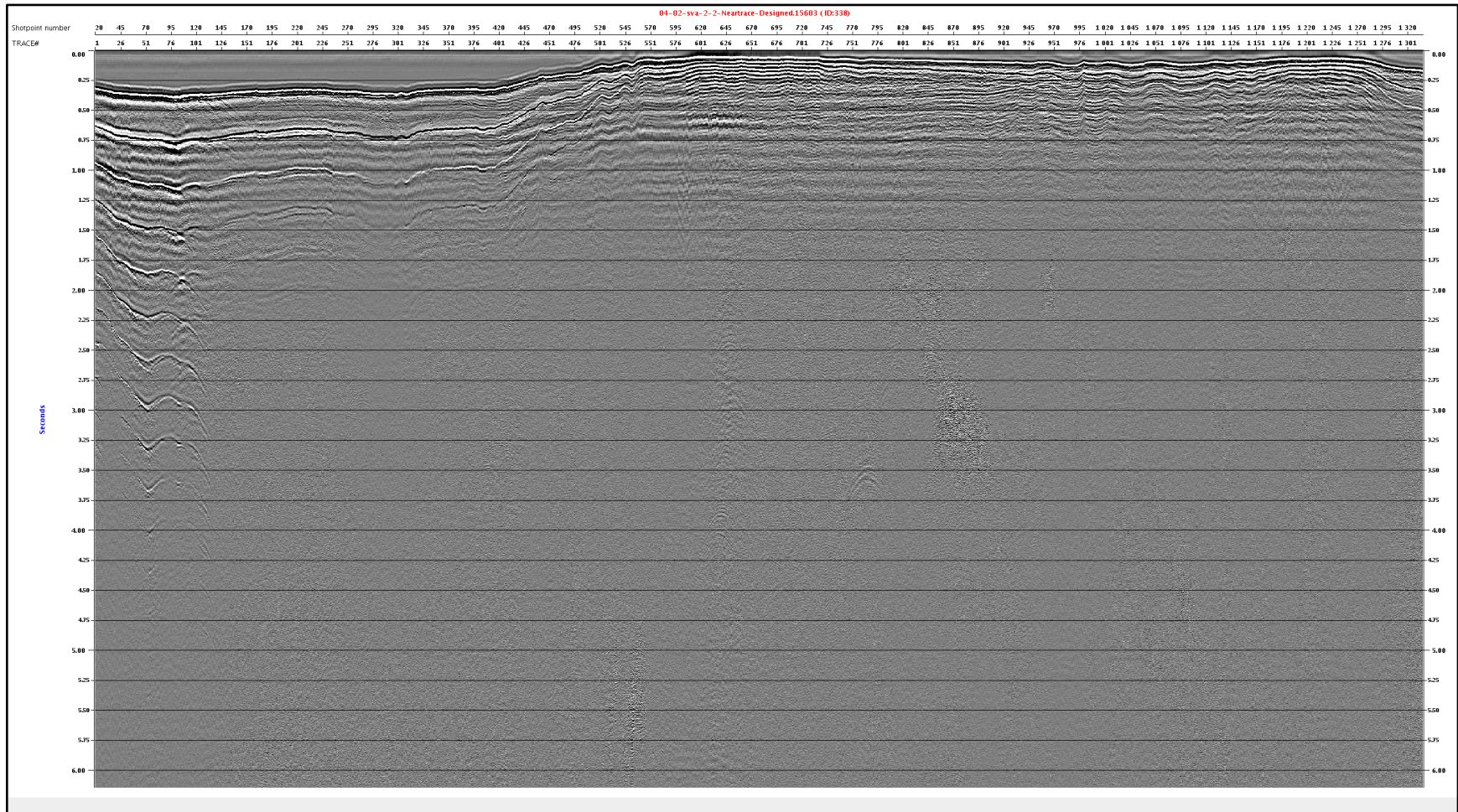


Figure A. 17 shows the near-trace section of seismic line 2.



### A.2.1.2 Seismic Line 6

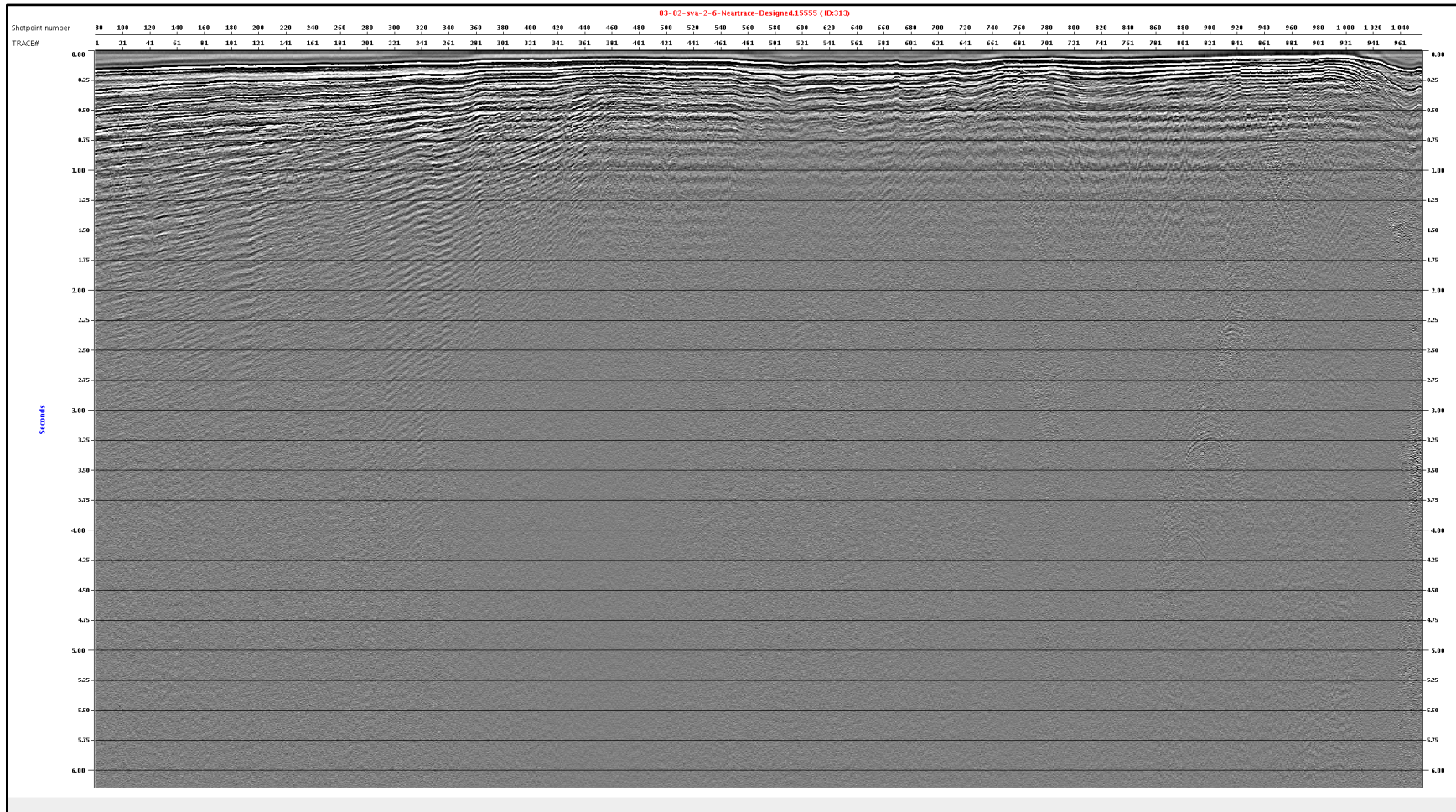


Figure A. 18 shows the near-trace section of seismic line 6.



### A.2.1.4 Seismic Line 7

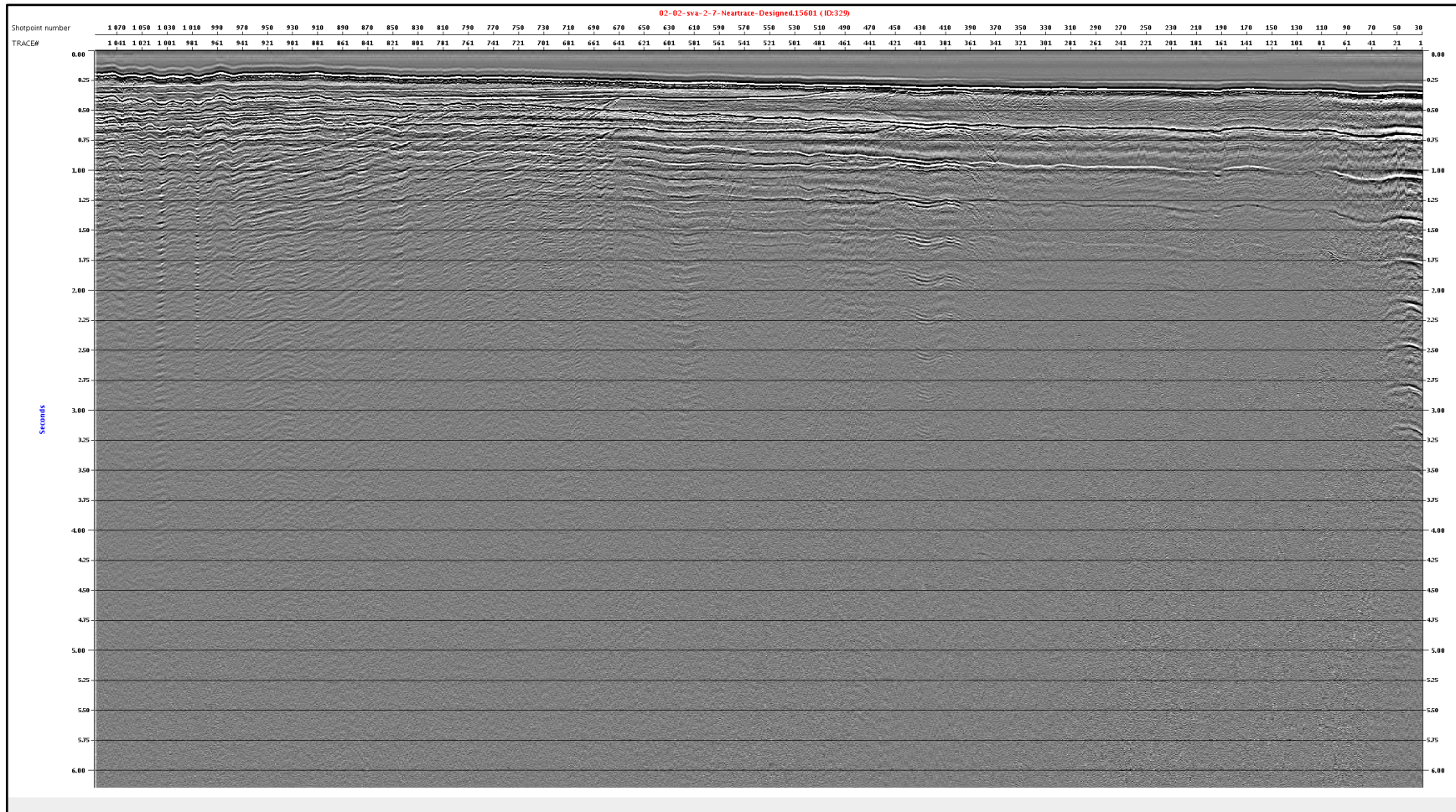


Figure A. 19 shows the near-trace section of seismic line 7.



### A.2.1.4 Seismic Line 8

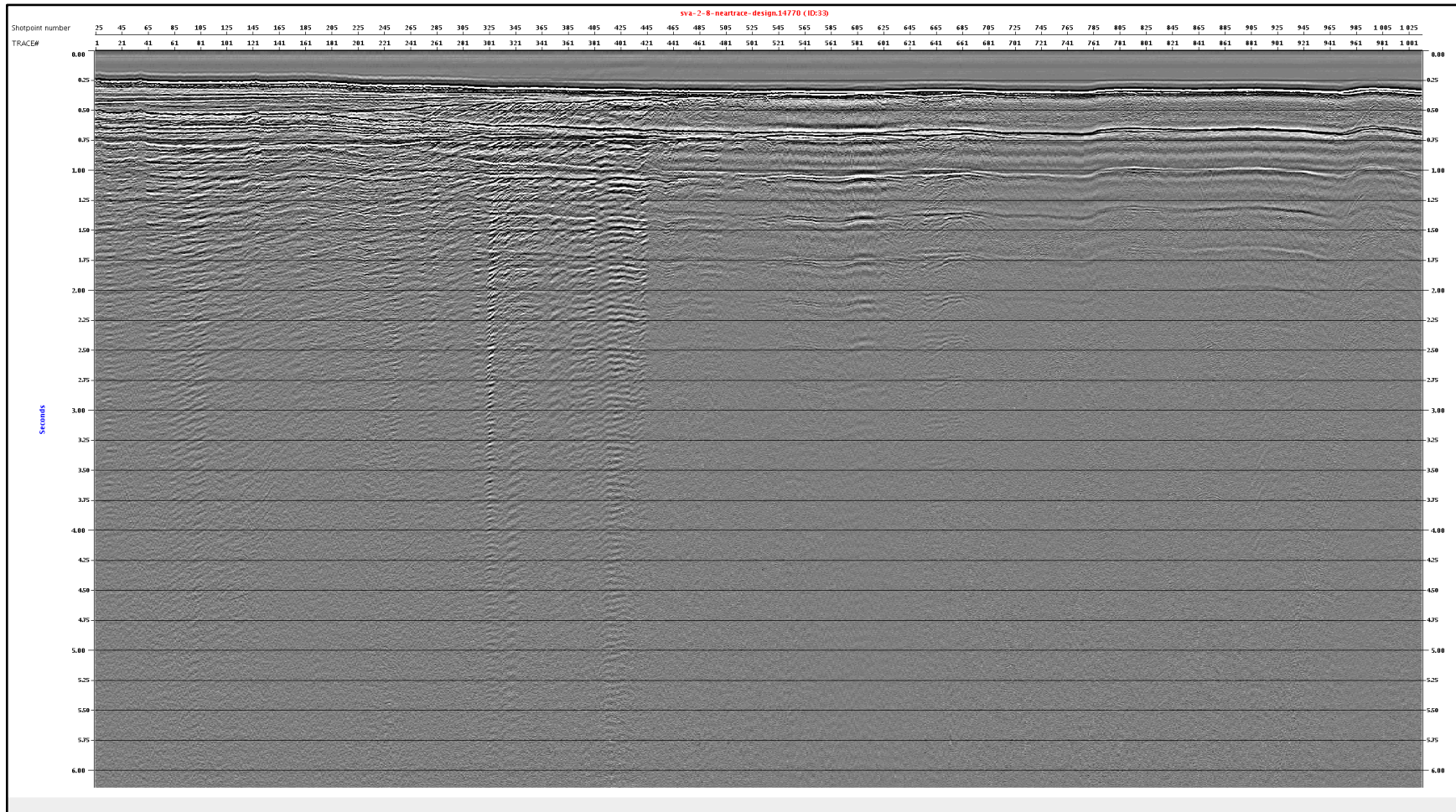


Figure A. 20 shows the near-trace section of seismic line 8.



## A.2.2 The Trace Interpolation Results

The geometry changes of seismic lines 2, 6 and 8 after the interpolation.

### A.2.2.1 Seismic Line 2

Parameters of the Seismic Line 2	Specifications before the trace interpolation	Specifications after the trace interpolation
Minimum Shot Number	20	80
Maximum Shot Number	1335	5340
Number of Maximum Folds	30	120
Minimum Receiver Number	173	175
Maximum Receiver Number	11171	11171
Minimum CDP Number	420	421
Maximum CDP Number	11179	11179
Interval of the CDP Gathers	6.25 m	12.5 m
Number of the CDP Gathers	10759	5380
Total Number of the Traces in the Gathers	315840	631320

Table A. 1 The geometry parameters of seismic line 2 before and after the interpolation.

### A.2.2.2 Seismic Line 6

Parameters of the Seismic Line 6	Specifications before the trace interpolation	Specifications after the trace interpolation
Minimum Shot Number	80	320
Maximum Shot Number	1056	4224
Number of Maximum Folds	30	120
Minimum Receiver Number	653	655
Maximum Receiver Number	8939	8939
Minimum CDP Number	900	901
Maximum CDP Number	8947	8947
Interval of the CDP Gathers	6.25 m	12.5 m
Number of the CDP Gathers	8048	4024
Total Number of the Traces in the Gathers	234480	468600

Table A. 2 The geometry parameters of seismic line 6 before and after the interpolation.

### A.2.2.3 Seismic Line 8

Parameters of the Seismic Line 8	Specifications before the trace interpolation	Specifications after the trace interpolation
Minimum Shot Number	25	100
Maximum Shot Number	1035	4140
Number of Maximum Folds	30	120
Minimum Receiver Number	213	215
Maximum Receiver Number	8771	8771
Minimum CDP Number	460	461
Maximum CDP Number	8779	8779
Interval of the CDP Gathers	6.25 m	12.5 m
Number of the CDP Gathers	8320	4160
Total Number of the Traces in the Gathers	242640	484920

*Table A.3 The geometry parameters of seismic line 8 before and after the interpolation.*

QC has been applied in the seismic lines. The purpose of this QC is to observe whether the interpolation has properly worked and whether any useful information has been lost. As an example, the comparison of near-trace sections from seismic line 7 is shown in the Figure A. 21.

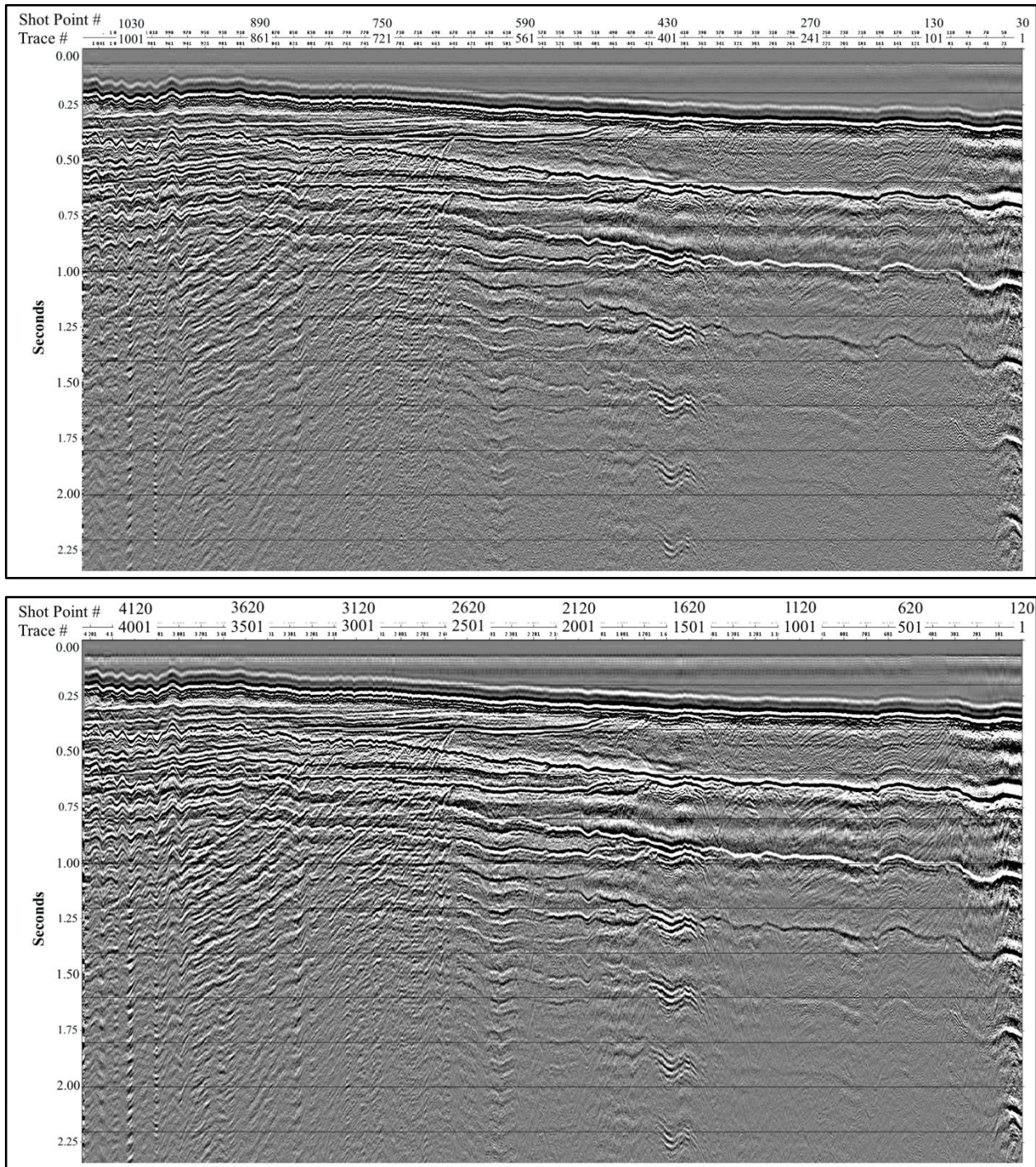


Figure A. 21 The sections from the common-offset gather #100. The comparison between the interpolation (top) and after the interpolation (bottom) shows enhancement of the S/N thanks to the increased max fold number from 30 to 120. The multiplied shot numbers by 4 can also be seen in the interpolated near-trace section.

### A.2.3 Adaptive Subtraction Results

There are different results provided by the different velocity percentages applied during the adaptive subtraction method in order to find out the ideal velocity percentage. The applied velocities are 100%, 80%, 70% and 60% to seismic line 8 presented in this chapter.



### A.2.3.1 Adaptive Subtraction Results with 100% Velocity from seismic line 8

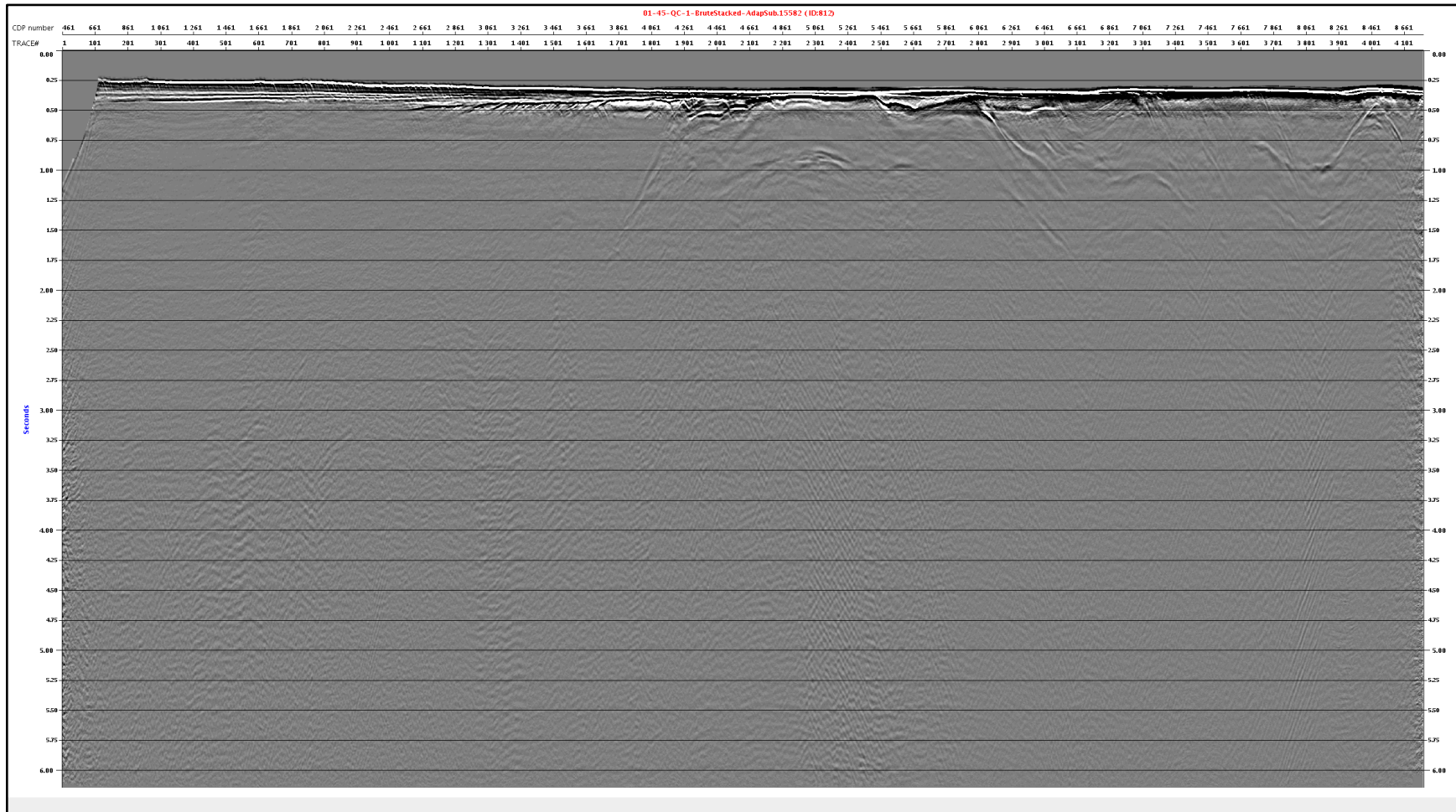


Figure A. 22 Brute-stack section after the subtraction with the applied velocity percentage 100%.

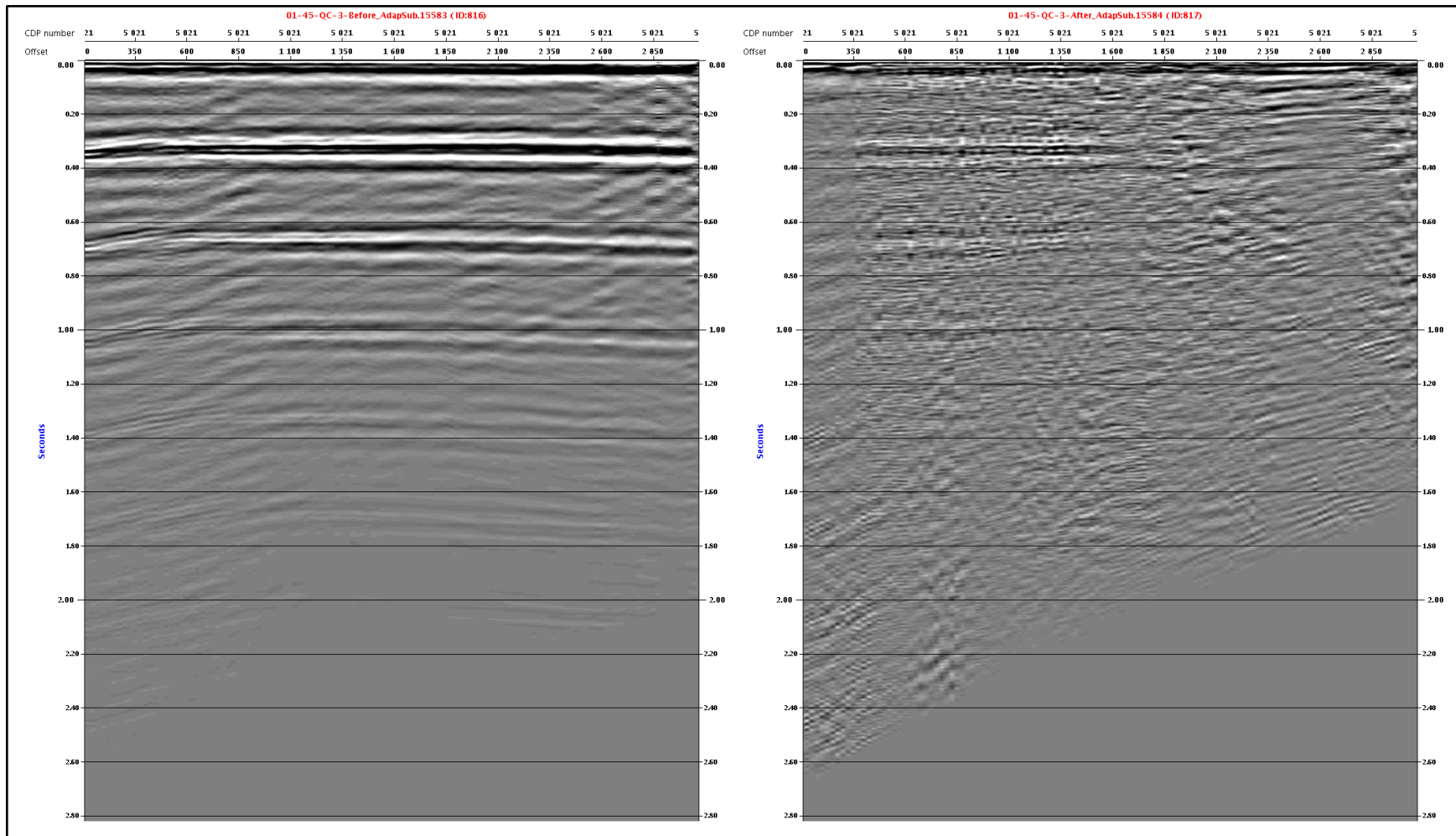


Figure A. 23 Autocorrelation section from the CDP #5021 before (left) and after the subtraction with the applied velocity percentage 100% (right).



### A.2.3.2 Adaptive Subtraction Results with 80% Velocity from seismic line 8

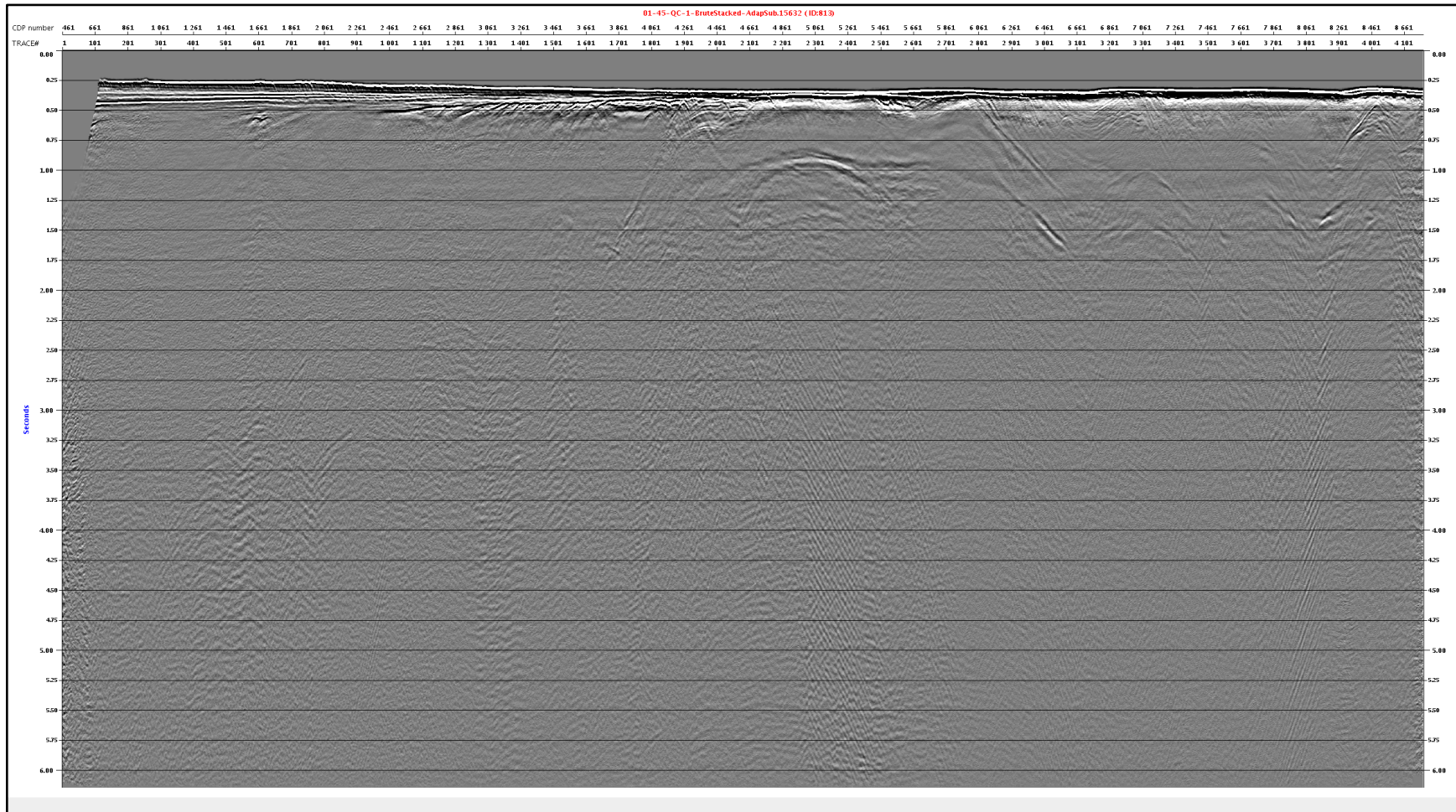


Figure A. 24 Brute-stack section after the subtraction with the applied velocity percentage 80%.

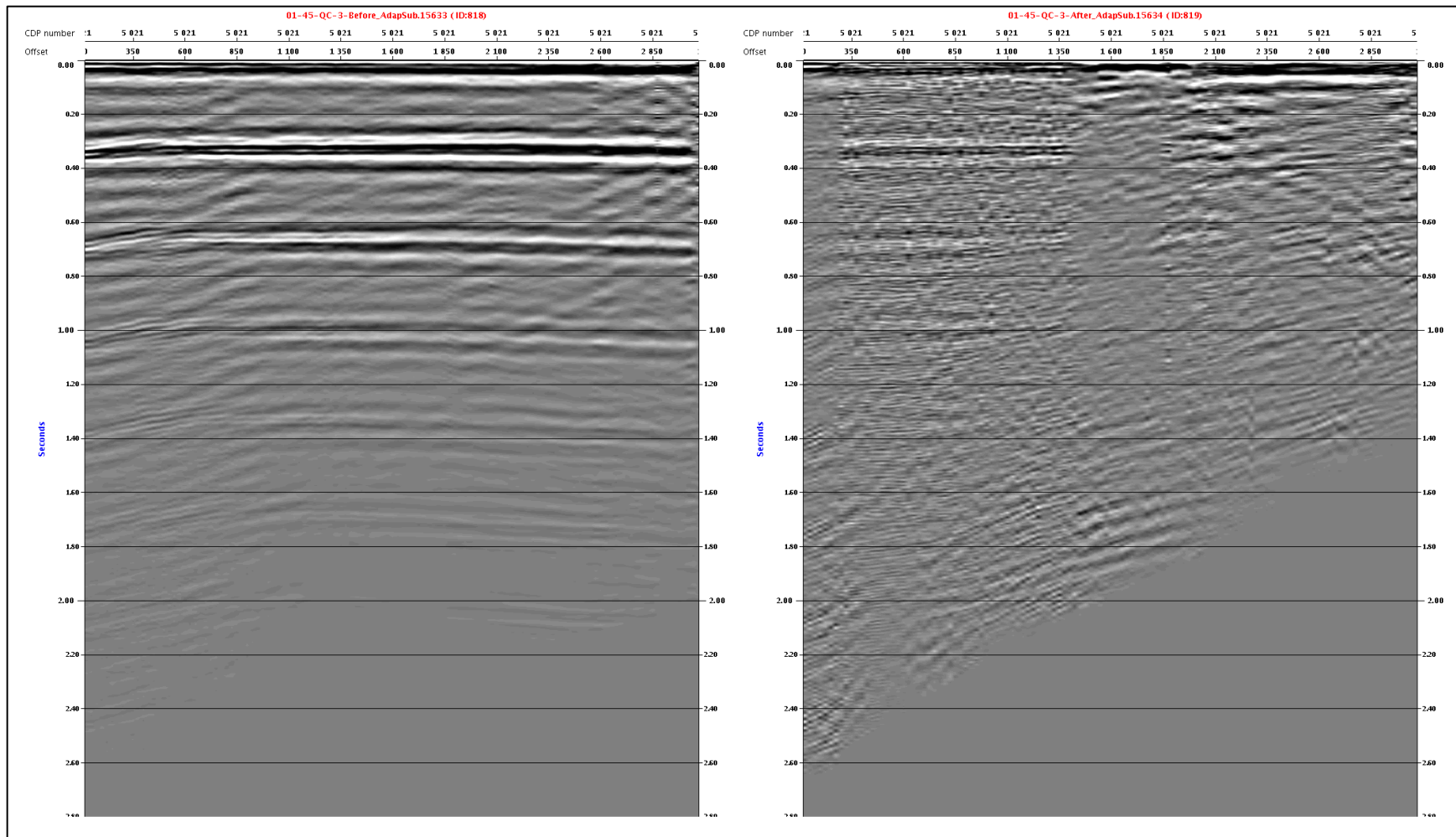


Figure A. 25 Autocorrelation section after the subtraction with the applied velocity percentage 80%.



### A.2.3.3 Adaptive Subtraction Results with 70% Velocity from seismic line 8

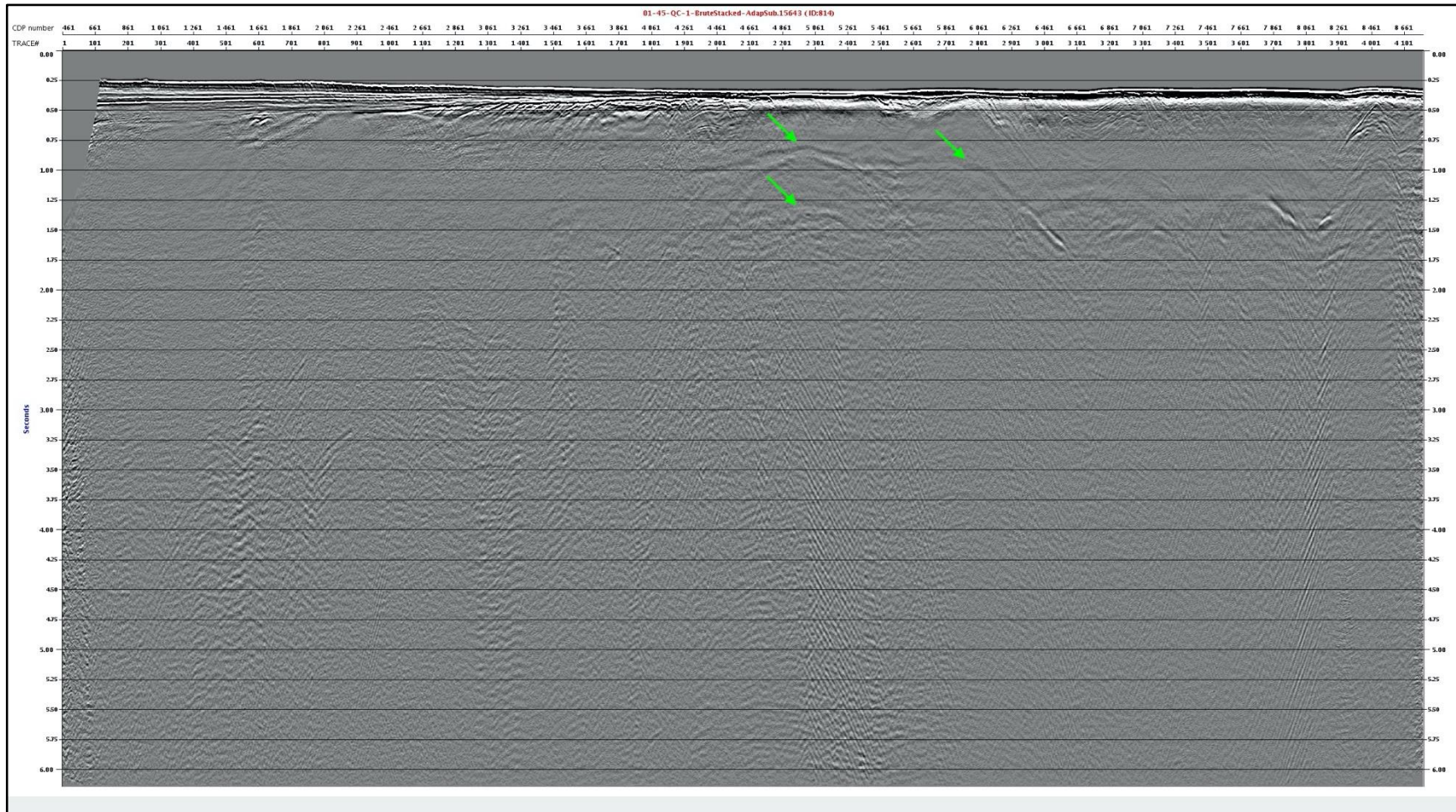


Figure A. 26 Brute-stack section after the subtraction with the applied velocity percentage 70%. Green arrows show the interbed multiples which could not be completely attenuated by the multiple extraction & adaptive subtraction.

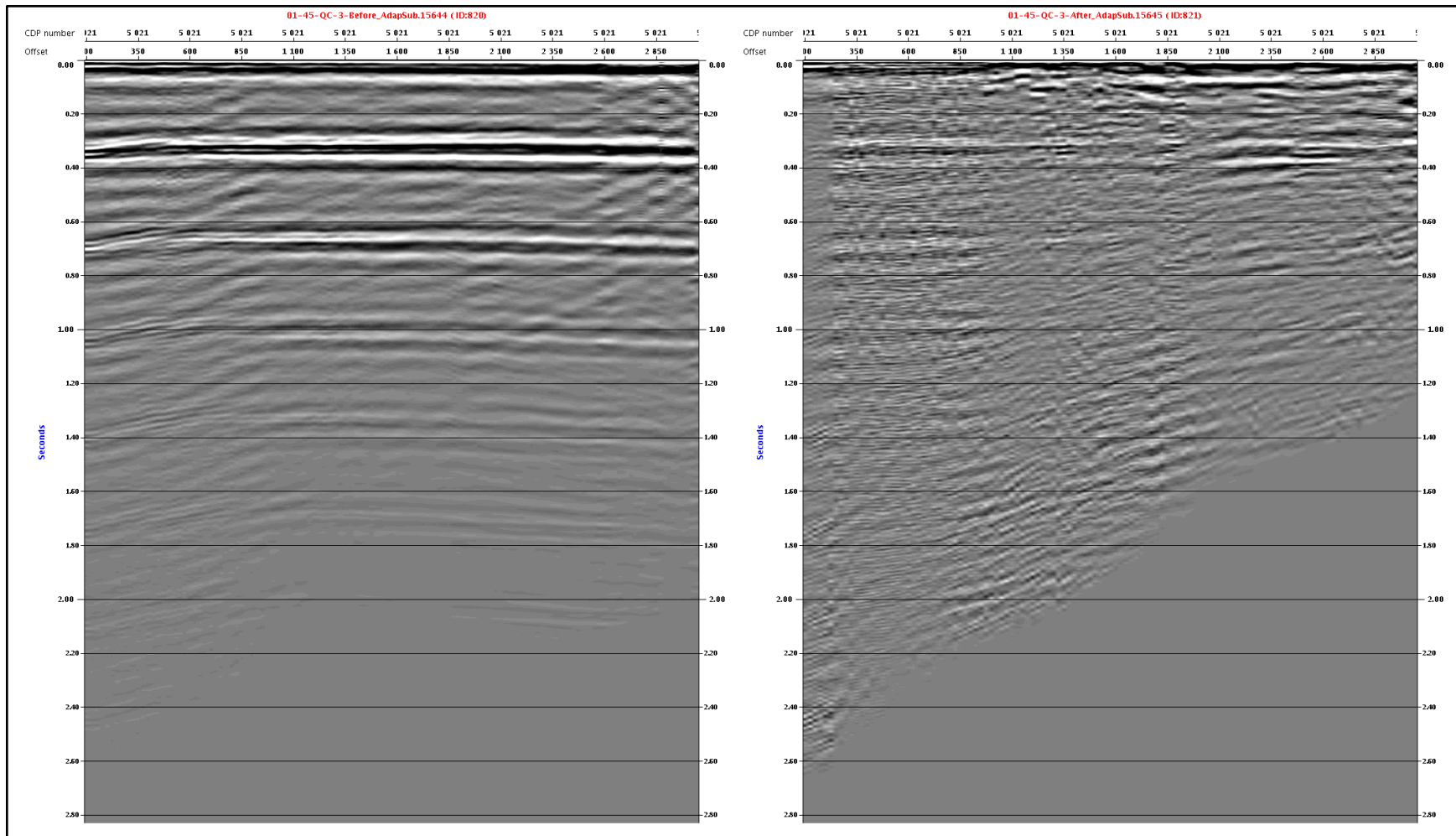


Figure A. 27 Autocorrelation section after the subtraction with the applied velocity percentage 70%.



### A.2.3.4 Adaptive Subtraction Results with 60% Velocity from seismic line 8

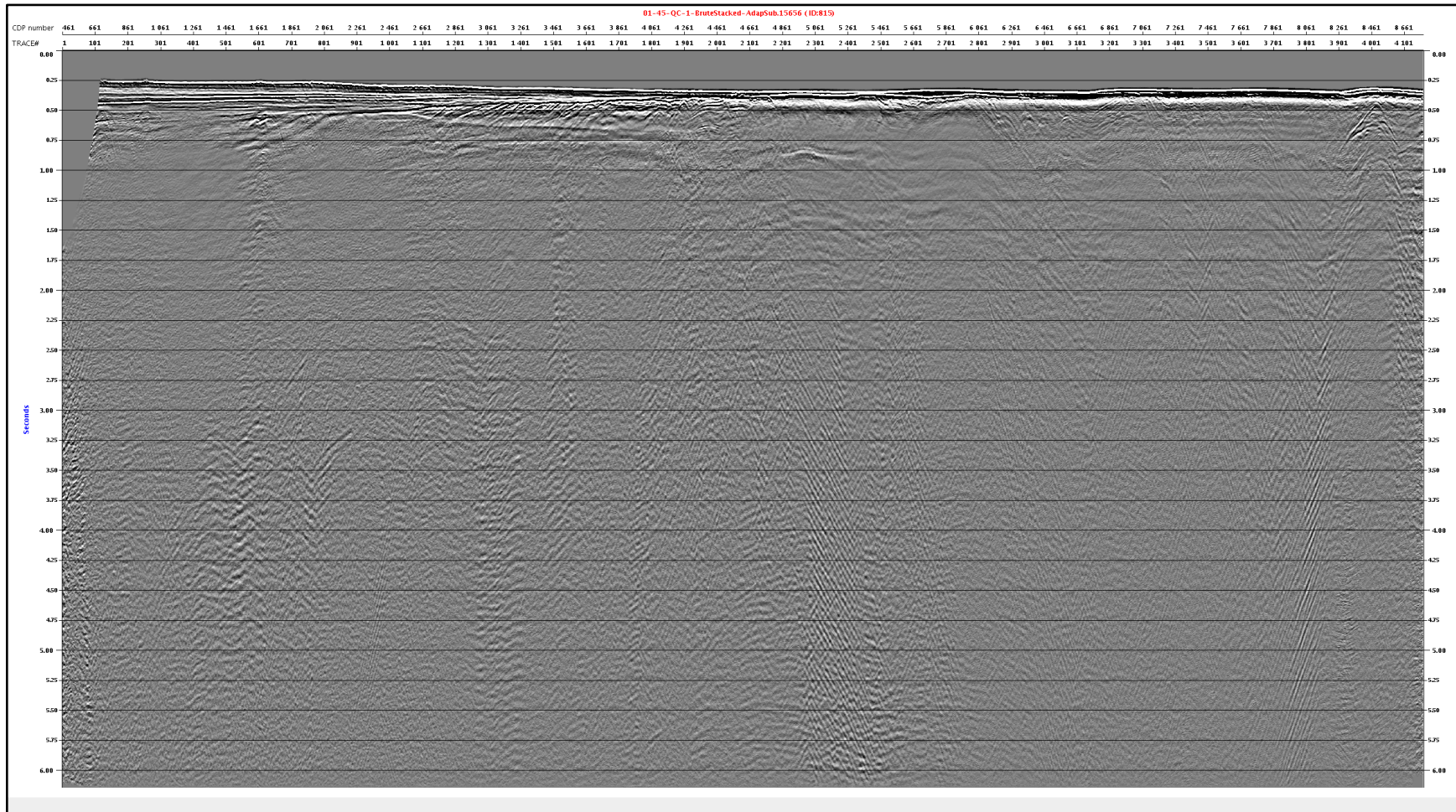


Figure A. 28 Brute-stack section after the subtraction with the applied velocity percentage 60%.

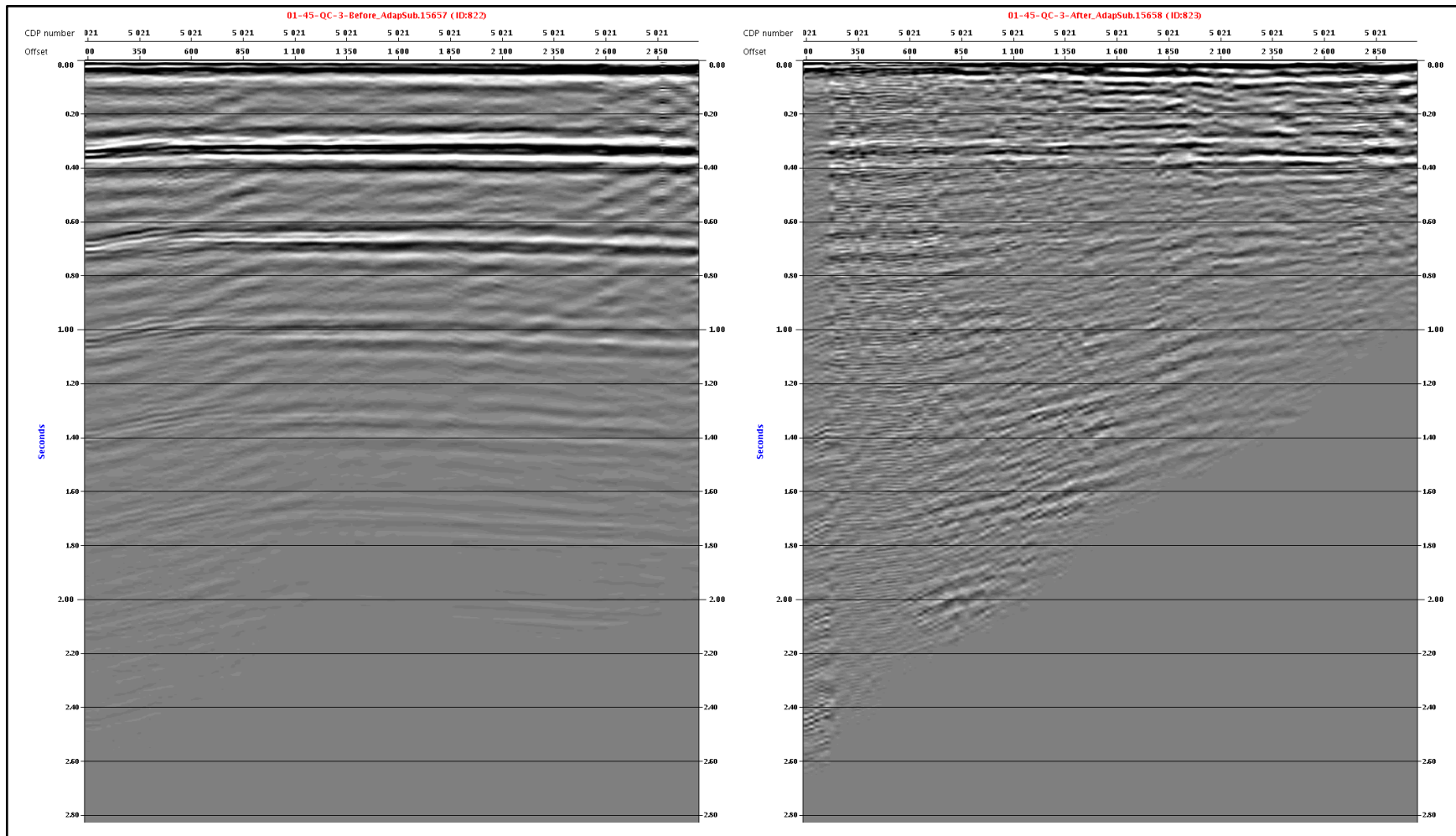


Figure A. 29 Autocorrelation section after the subtraction with the applied velocity percentage 60%.



### A.2.3.5 Adaptive Subtraction Results with 70% Velocity from seismic line 7

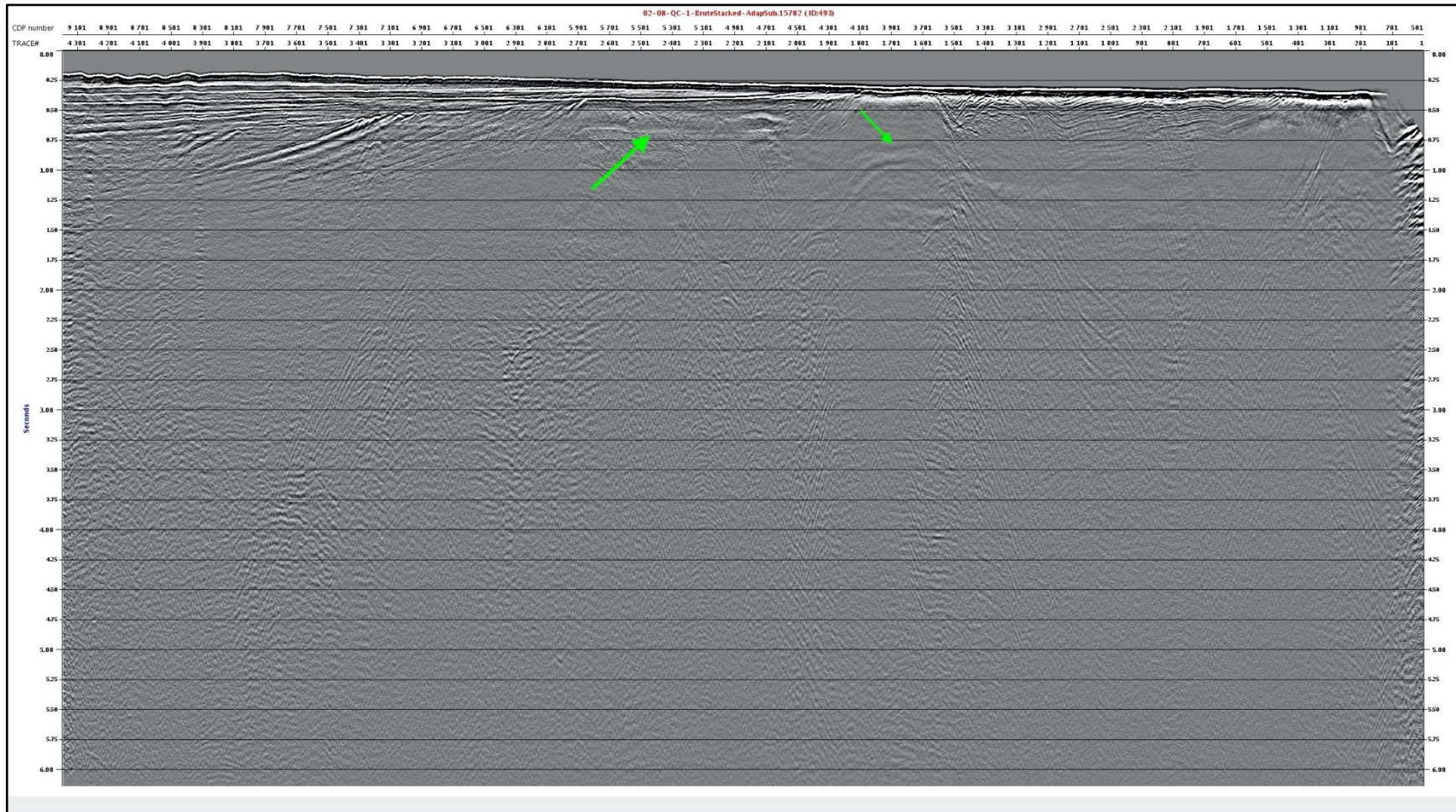


Figure A. 30 Brute-stack section of seismic line 7 shows the results after the subtraction applied with the velocity percentage of 70% from the 1st velocity analysis. Green arrows show the interbed multiples which could not be completely attenuated by the multiple extraction & adaptive subtraction.

### A.2.3.5 Adaptive Spectrum analyzed in the brute-stack section from seismic line 7

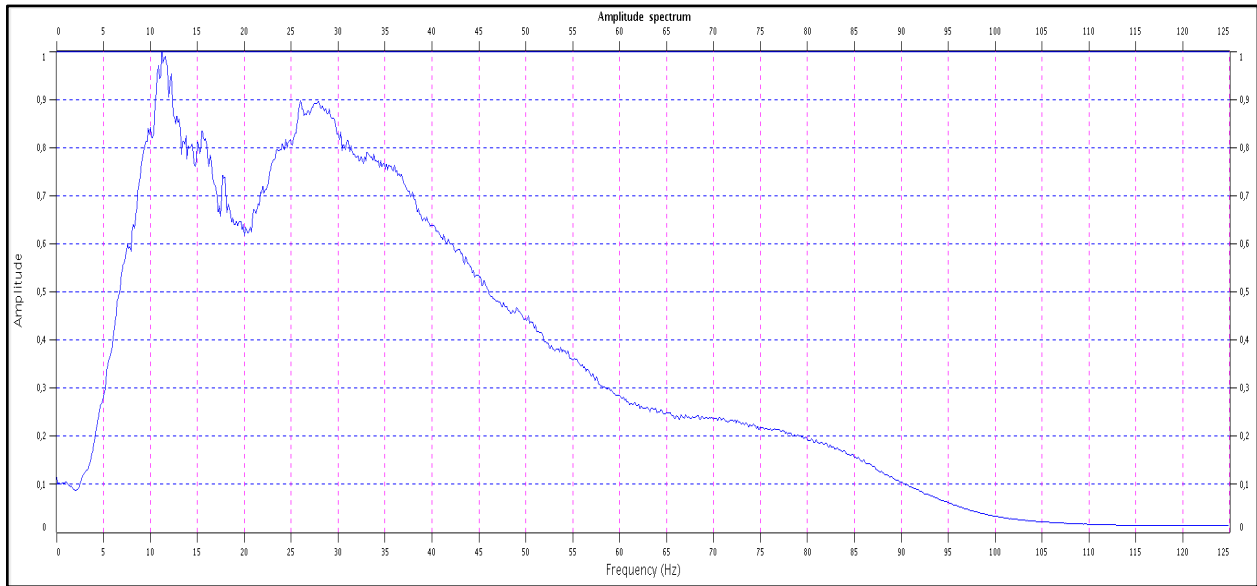


Figure A. 31 Amplitude Spectrum from the brute-stack section of line 7 after the adaptive subtraction with the applied velocity percentage 70%. The spectrum was used to determine the limits of the bandpass filtering before the DMO correction.

A.2.4 Results from 2nd Velocity Analysis After the Subtraction with 70% Velocity  
Different Velocity Analysis Results from seismic Line 8.

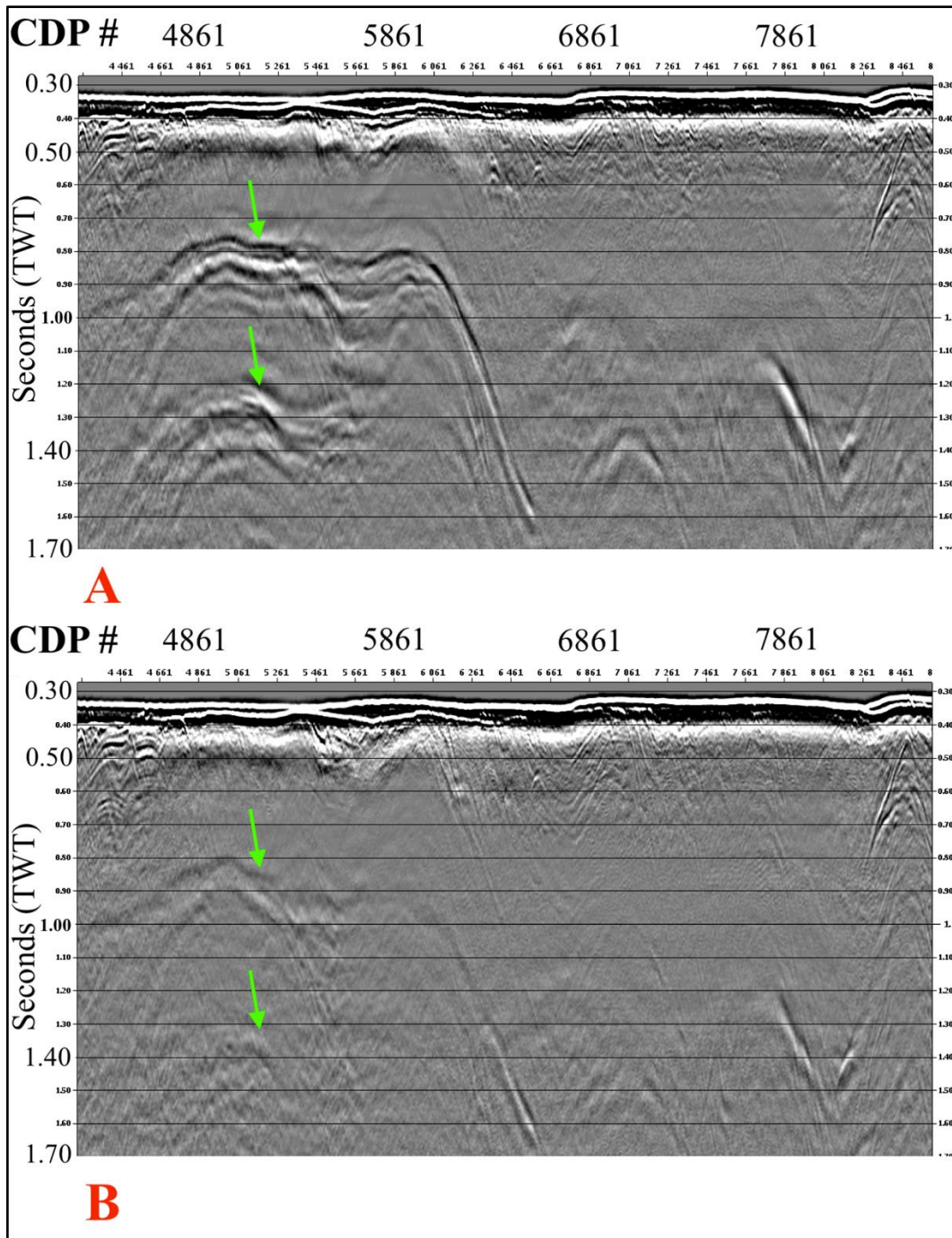


Figure A. 32 The brute-stack section showing the impact of the velocity analysis on the adaptive subtraction. The velocity analysis done with 4 km CDP interval (A) and with 2 km CDP interval (B). Green arrows show the interbed multiple which could not be completely attenuated by the adaptive subtraction but suppressed by the 2nd velocity analysis with the shorter CDP interval (B).



## A.2.5 Stacking Results

### A.2.4.1 Seismic Line 2

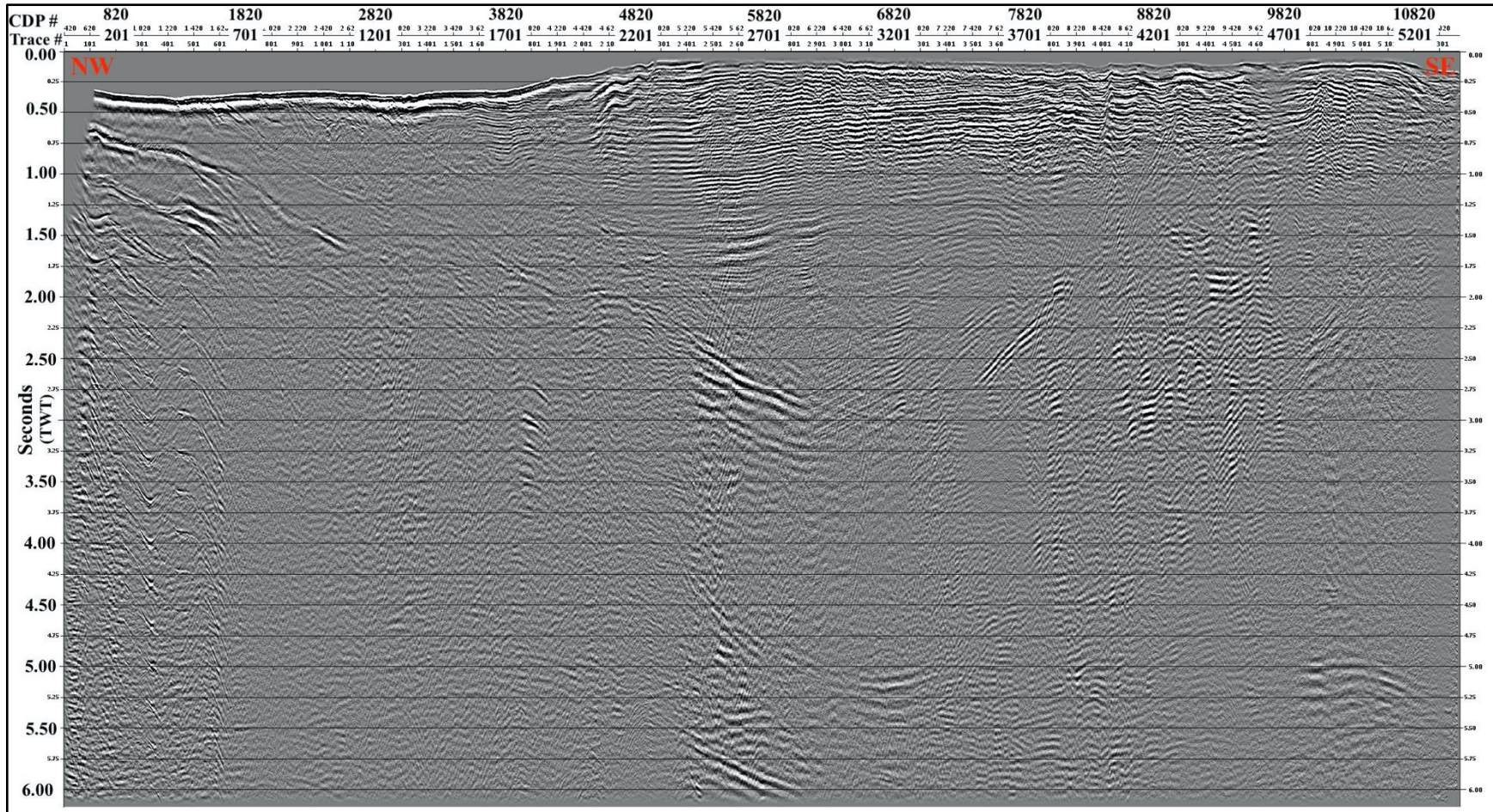


Figure A. 33 shows the stacked section of seismic line 2.



### A.2.4.2 Seismic Line 6

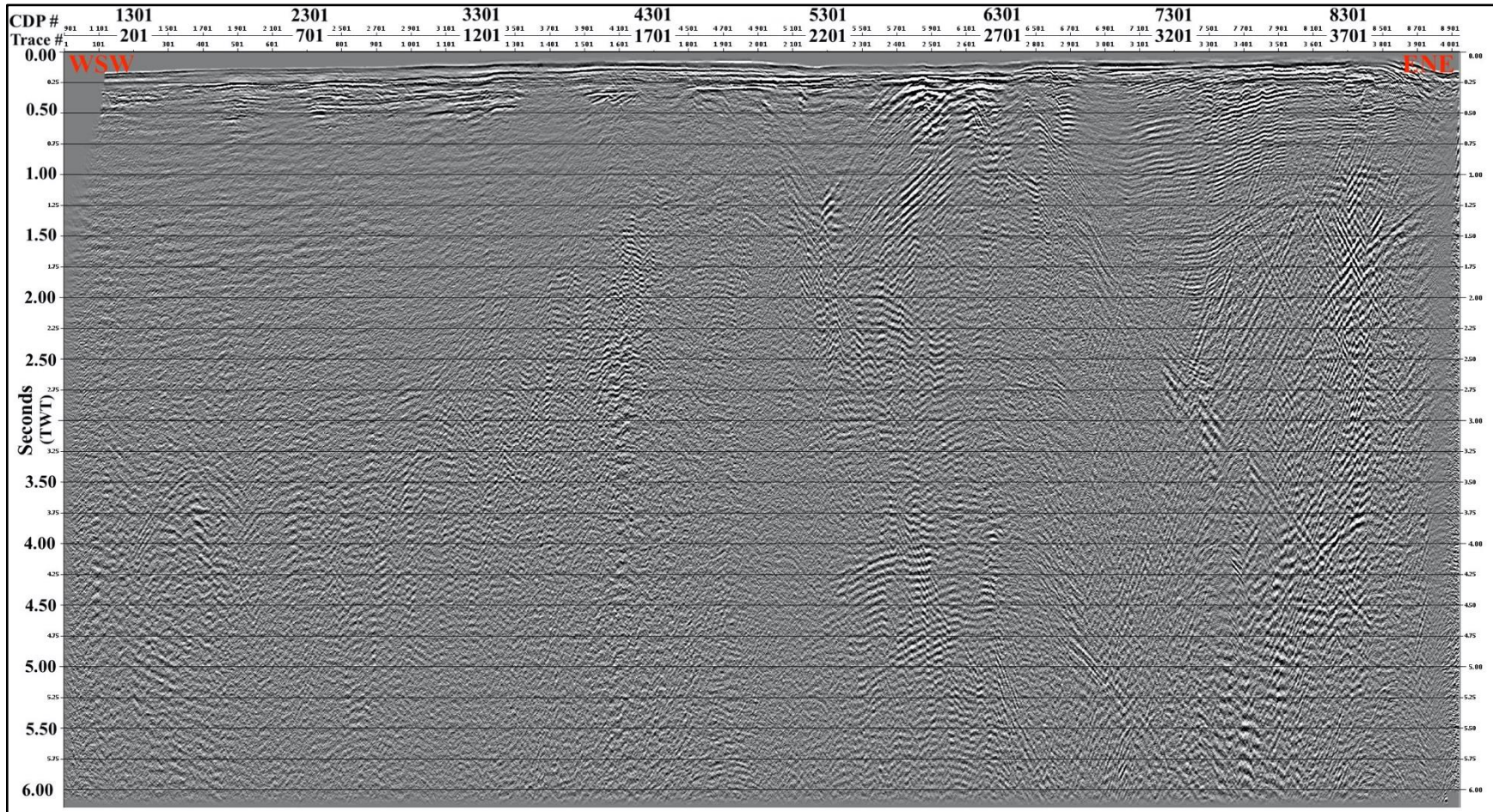


Figure A. 34 shows the stacked section of seismic line 6.



### A.2.4.3 Seismic Line 7

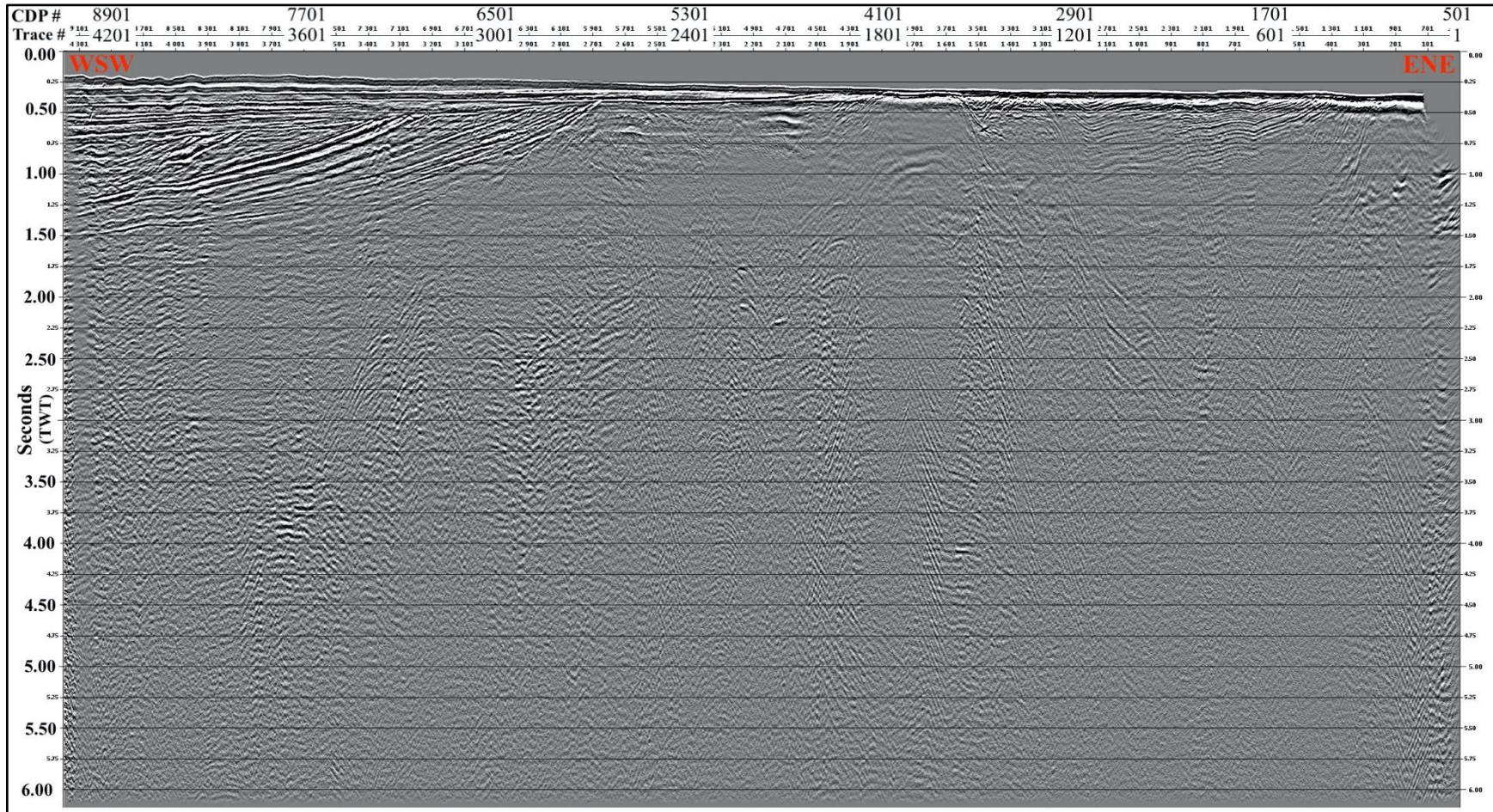


Figure A. 35 shows the stacked section of seismic line 7.



### A.2.4.4 Seismic Line 8

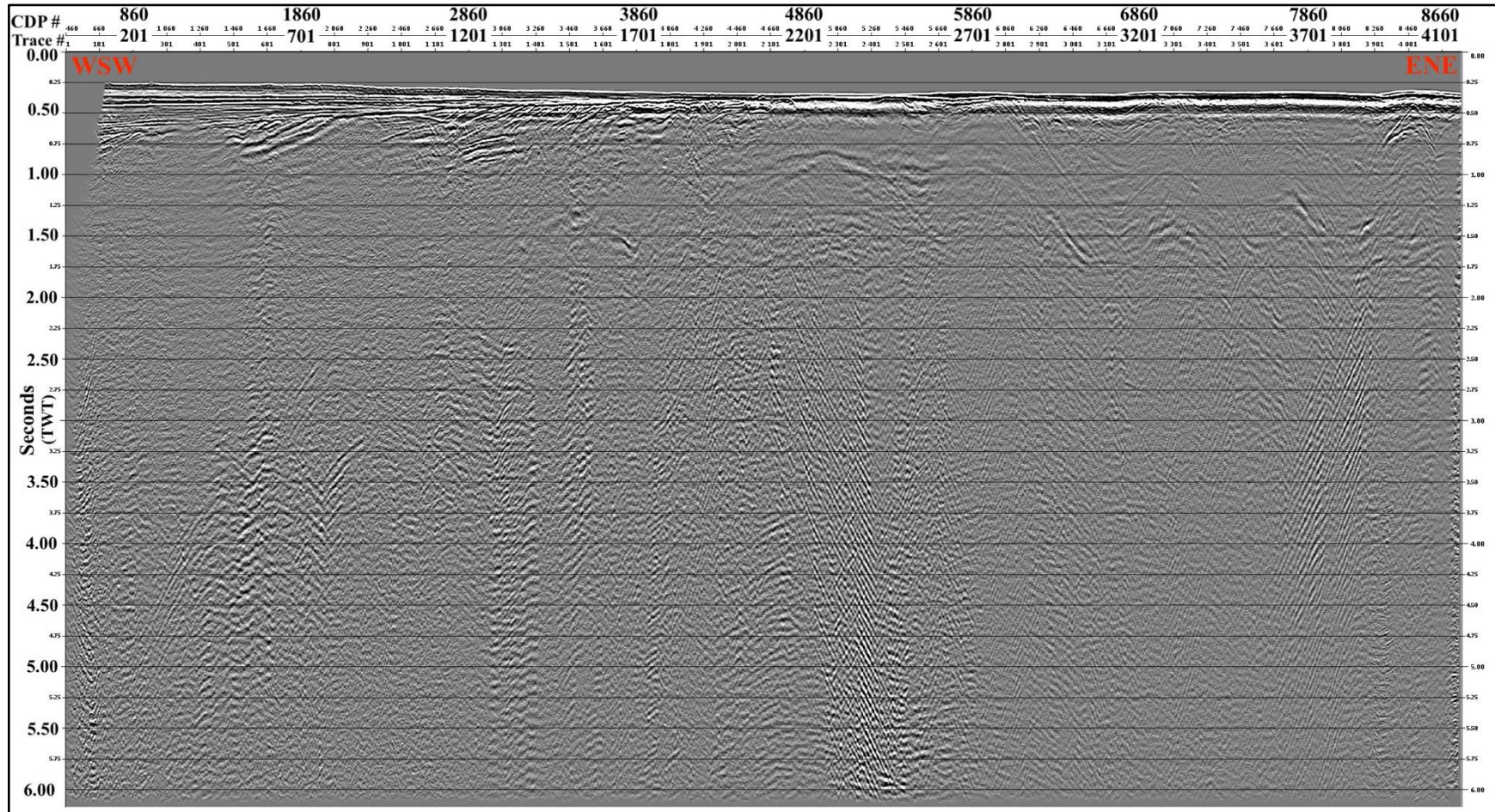


Figure A. 36 shows the stacked section of seismic line 8.



## A.2.6 Results from Post-Stack Processing Sequences Before Migration

### A.2.6.1 Band-pass Filtering

Comparison of the different limits for the band-pass filtering are presented from seismic line 7.

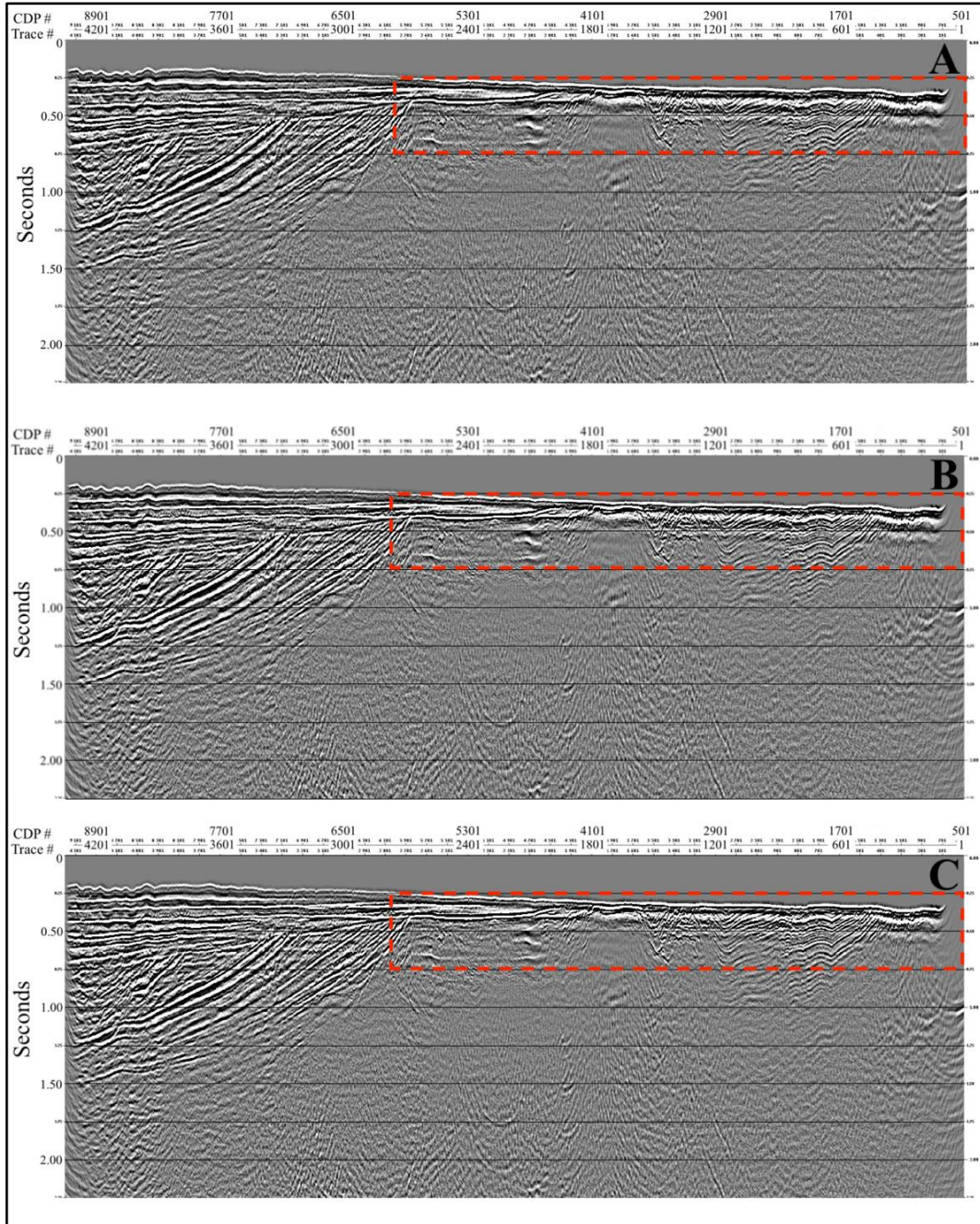


Figure A. 37 shows the comparison of the tested band-pass filtering limits on the migrated section. The 1st band-pass filtering limits are [5-11.5-48-80] Hz and its impact (red dashed-polygon) in A. The 2nd band-pass filtering limits are [5-13-48-80] Hz and its impact (red dashed-polygon) in B. The 3rd band-pass filtering limits are [5-15-48-80] Hz and its impact (red dashed-polygon) in C.



### A.2.6.2 *f-k* Filtering

Comparison without and with different *f-k* limits are presented from seismic line 7.

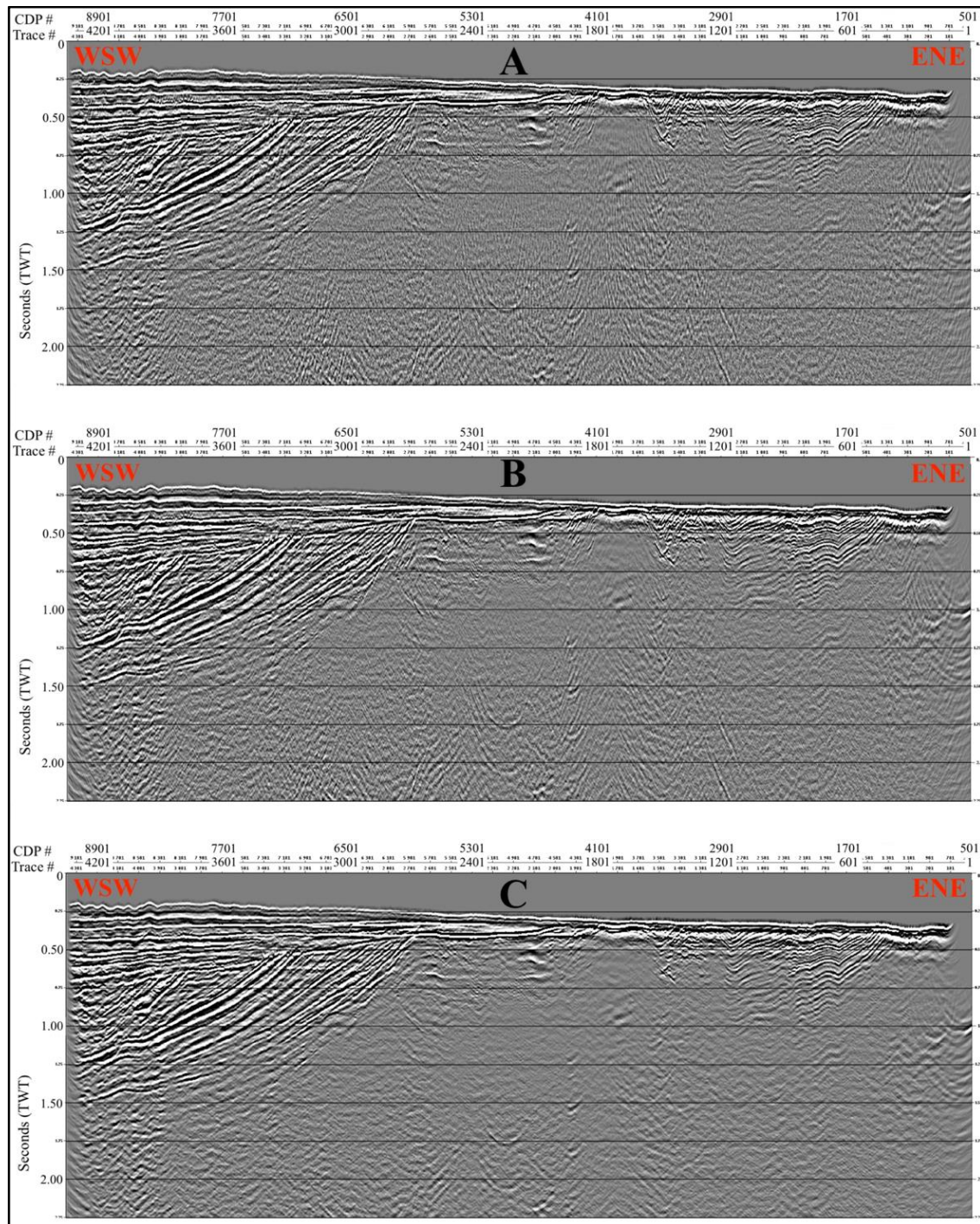


Figure A. 38 shows the comparison of the tested *f-k* filtering limits on the migrated section. There is no applied *f-k* filtering before the migration in figure A. The 1st filtering limits are [-7500, -4500, 4500, 7500] m/s in B and smiling effects are getting shorter. The 2nd filtering limits are [-10000, -5500, 5500, 10000] m/s in C; diffractions are mostly disappeared, while there are still smiling effects left.



# APPENDIX B

This appendix presents the applied methods and results of the other multiple elimination approaches tested in first four workflows besides the chosen one, which is the multiple extraction and adaptive subtraction approach. The comparisons between the different multiple attenuation approaches have been done in seismic line 8 since the data processing had begun performing with this line first. Once the decision was made for the ideal multiple elimination method between them, then the chosen method was applied to all seismic lines as part of the main processing workflow.

## B.1 XJOB FOLDERS

The screen captures of the Xjobs from CGG Geocluster shows the different multiple attenuation approaches applied to seismic line 8.

### B.1.1 Xjob Folder - Deconvolution

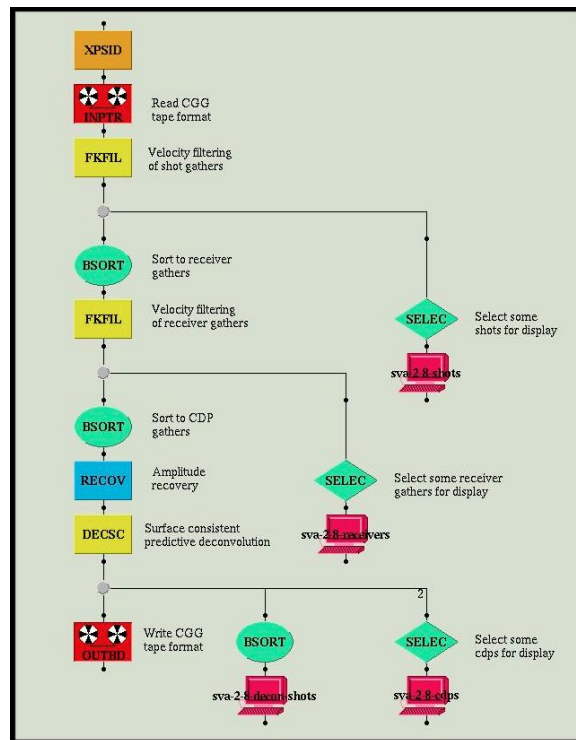


Figure B. 1 Deconvolution Xjob folder applied to original and interpreted CMP gathers, extracted from CGG Geocluster.



### B.1.2 Xjob Folders - Deconvolution in the $\tau$ -p domain

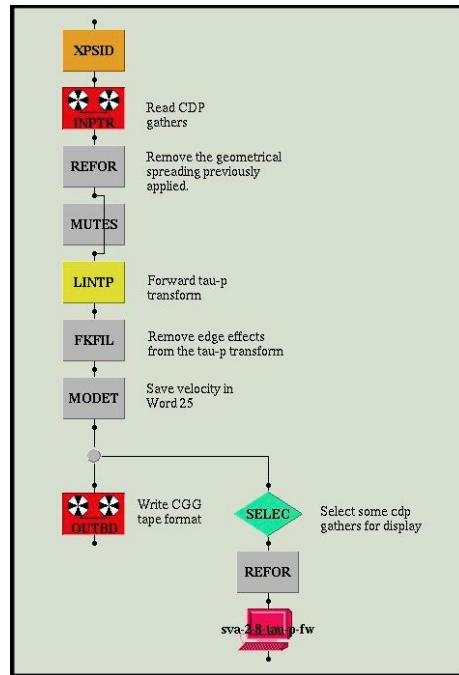


Figure B. 2 Xjob folder converting the CDP gathers to the  $\tau$ -p domain as 1st, extracted from CGG Geocluster.

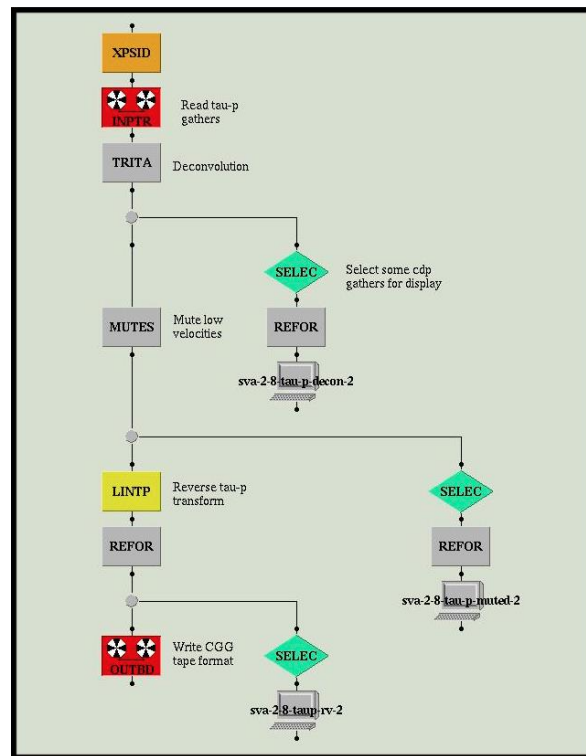


Figure B. 3 Xjob folder applying the deconvolution in the  $\tau$ -p domain and then converting the gathers to the CDP gathers as 3rd step, extracted from CGG Geocluster.

### B.1.3 Xjob Folder - $f-k$ filter

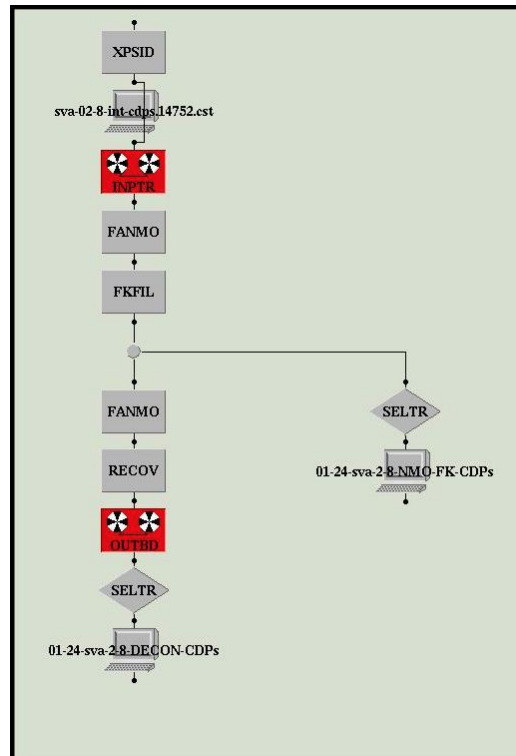


Figure B. 4  $f-k$  filter Xjob folder applied to NMO overcorrected CMP gathers, extracted from CGG Geocluster.

## B.2 METHODS

The traces in the CMP gathers have been interpolated for the following processing methods besides the multiple attenuation by deconvolution. It is beneficial for the processing sequences such as the  $f-k$  filtering and  $\tau-p$  transform due to reducing the truncation effects. Another reason to apply these methods to the CMP gathers instead of the shot gathers is to have independent results regardless of the acquisition direction of the lines.

### B.2.1 Deconvolution applied to the original CMP gathers

The multiple attenuation has been computed is deconvolution applied to the CMP gathers (without interpolation). Deconvolution method is commonly used for broadband seismic data to enhance to temporal (vertical) resolution while removing the source signal, consisting of multiples, from the seismic trace (Dondurur, 2018). Since the 2D reflection seismic data collected

in SVALEX 2002 is broadband (including both low and high frequencies), this method was aimed to apply in this research.

### B.2.2 Deconvolution applied to the interpolated CMP gathers

The same deconvolution approach has been also tested on the interpolated CMP gathers in order to compare the multiple attenuation results between the original and interpreted CMP gathers.

### B.2.3 Deconvolution in the $\tau$ - $p$ domain applied to the interpolated CMP gathers

The deconvolution in the  $\tau$ - $p$  domain has been applied to the interpolated CMP gathers, which has been the main aim to suppress the velocity of the linear events in the  $\tau$ - $p$  gathers which are direct, refracted, and guided waves.

Refractions or head waves, travelling horizontally in the subsurface sediments with the velocity of subsurface sediment units, always have higher velocity and lower dip than direct waves on the shot records. To investigate them during the processing is crucial as they carry velocity information of the topmost sedimentary unit. Guided waves, also travelling horizontally in the subsurface sediments like the refracted waves, reach to the receivers right after they are reflected *repeatedly* in the water column. Although amplitudes of the guided waves are mostly attenuated by the CMP stacking, suppressing them by  $f$ - $k$  and band-pass filtering may be challenging in earlier processing steps. Because the guided waves with high frequency components, caused by a hard seafloor at shallow waters, are mostly in the same frequency band of the primary reflections in the far offsets. The  $\tau$ - $p$  transform (slant stacking) is used to identify and attenuate the amplitude of the guided waves in the  $\tau$ - $p$  gathers. The  $\tau$ - $p$  transform can be applied to the shot or CDP gathers to transfer the traces from  $t$ - $x$  domain to the  $\tau$ - $p$  domain (Figure B. 5). The  $\tau$ - $p$  transform decomposes the shot and CDP gathers from spherical wave fields into the plane waves. Therefore, the linear events (refracted waves, direct waves, guided waves, etc.) in the CDP gathers appears as single points in the  $\tau$ - $p$  gathers (Dondurur, 2018).

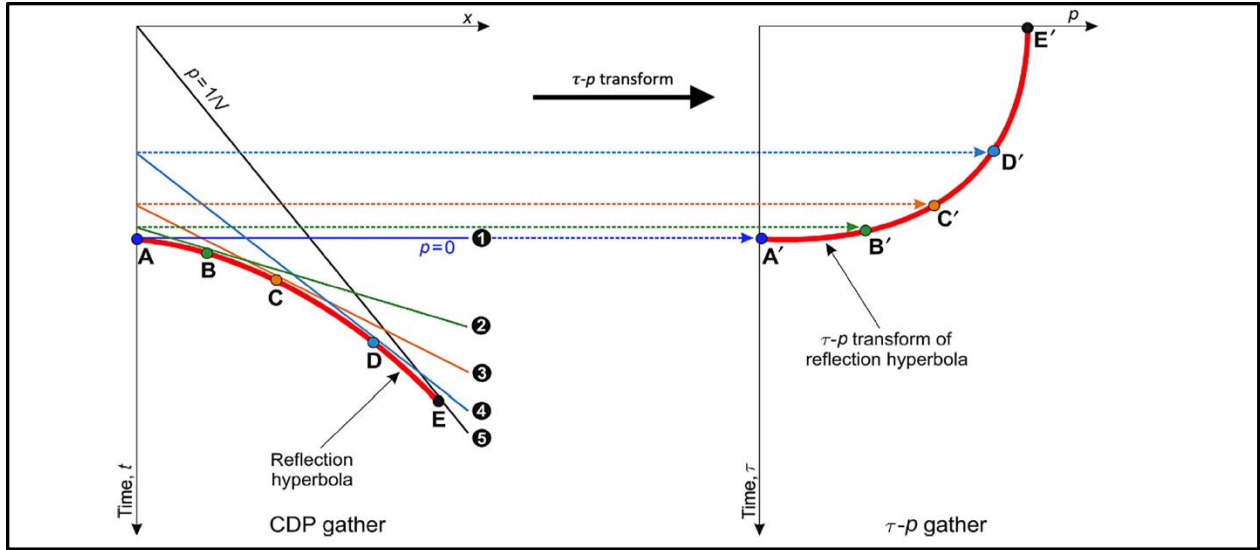


Figure B. 5 The schematic illustration of the  $\tau$ - $p$  transform where the traces are converted from the  $t$ - $x$  domain (CDP gather) to the  $\tau$ - $p$  domain ( $\tau$ - $p$  gather), modified from Dondurur (2018).

Predictive deconvolution in the  $\tau$ - $p$  domain tries to estimate and remove the long period multiples from data. Since the  $\tau$ - $p$  gathers lack of spherical divergence effects in the plane wave components, there must not be a spherical divergence correction in the input data before the deconvolution in the  $\tau$ - $p$  domain (Dondurur, 2018). Once the linear events and the multiples are attenuated in the  $\tau$ - $p$  domain, the traces are returned to the CDP gathers by the inverse  $\tau$ - $p$  transform.

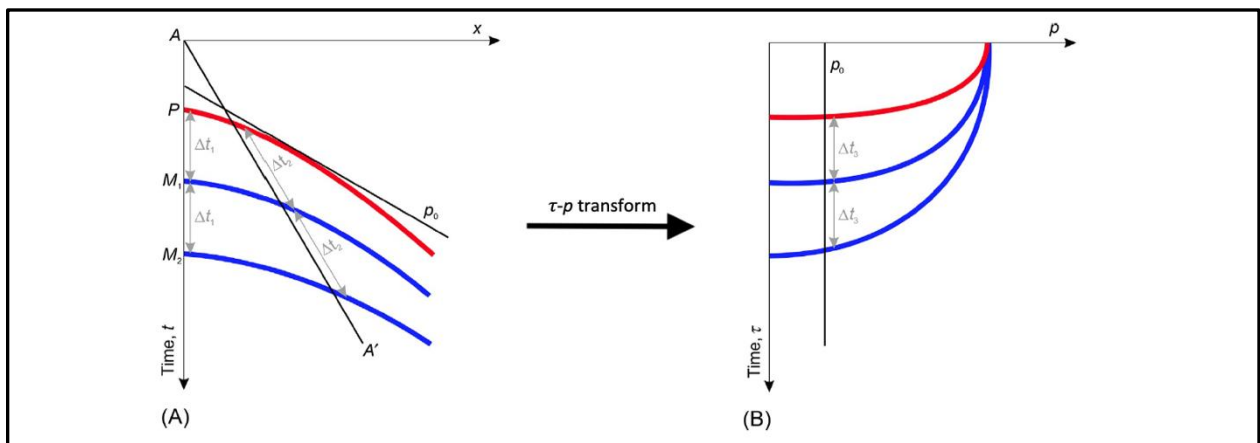


Figure B. 6 The schematic illustration of the hyperbolas of a primary reflection (red) and the multiples (blue) in  $t$ - $x$  domain (A) and the  $\tau$ - $p$  domain (B). Multiples are periodic for  $\Delta t_1$  at  $x = 0$  m offset;  $\Delta t_2$  along the radial line  $A$ - $A_0$  in the  $t$ - $x$  domain;  $\Delta t_3$  at along the constant  $\rho_0$  in the  $\tau$ - $p$  domain. modified from Dondurur (2018).

### B.2.4 $f$ - $k$ filter applied to the NMO corrected CMP gathers (interpolated)

As primary and multiple reflections propagate with different velocities, moveouts of their reflection hyperbolas are different (Figure B. 7.A). As it has been described earlier (NMO Correction chapter) that if the velocity functions used with lower than true values of primaries in NMO correction, the hyperbolas of primary reflections will bend upwards, while the hyperbolas of the multiples are flattened, called overcorrected NMO (Figure B. 7.B). NMO corrected CMP gathers are converted to the  $f$ - $k$  domain (Figure B. 7.C) by the 2D Fourier transform in order to apply the  $f$ - $k$  filter to mute the dips of multiples. The dips of the primaries can be aligned onto positive or negative side of the panel relying on their dips in the  $t$ - $x$  domain. Multiples are only gathered around the center of the panel ( $k=0$ ) since their hyperbolas became flatten after the NMO over-correction. After muting dips of the multiples, data is transferring back to the  $t$ - $x$  domain from  $f$ - $k$  domain (Figure B. 7.D). Then, overcorrected hyperbolas are bent downwards by inverse NMO correction (Figure B. 7.E). Therefore, multiple-free CMP gathers are obtained (Dondurur, 2018).

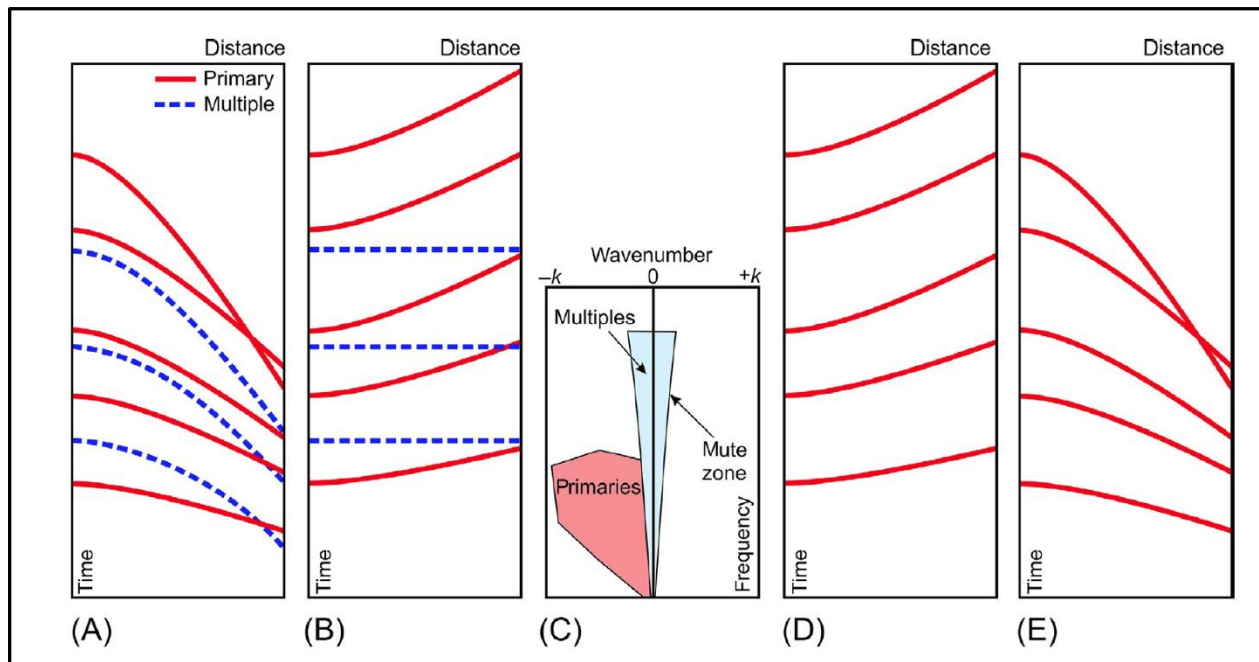


Figure B. 7 Schematic illustration of the steps of multiple attenuation by  $f$ - $k$  filter applied to the NMO overcorrected CMP gathers, extracted from Dondurur (2018).



## B.3 RESULTS

This chapter shows the autocorrelation results from the tested multiple elimination approaches in 4 different workflows and their further results from the CMP stacking and post-stack time migration in seismic line 8. The pre-processing steps for these completed four workflows is the same as the one distinguished in 4.2.1.

### B.3.1 Deconvolution applied to the original CMP gathers

After the pre-processing in the 1st workflow, the  $f-k$  filtering by FKFIL module and the surface consistent predictive deconvolution by the module DECSC was applied to the CMP gathers (without interpolation). The operator length ( $L$ ) was set as 300 ms. The autocorrelation section (Figure B. 8) for the QC purpose has revealed the efficiency of the method.

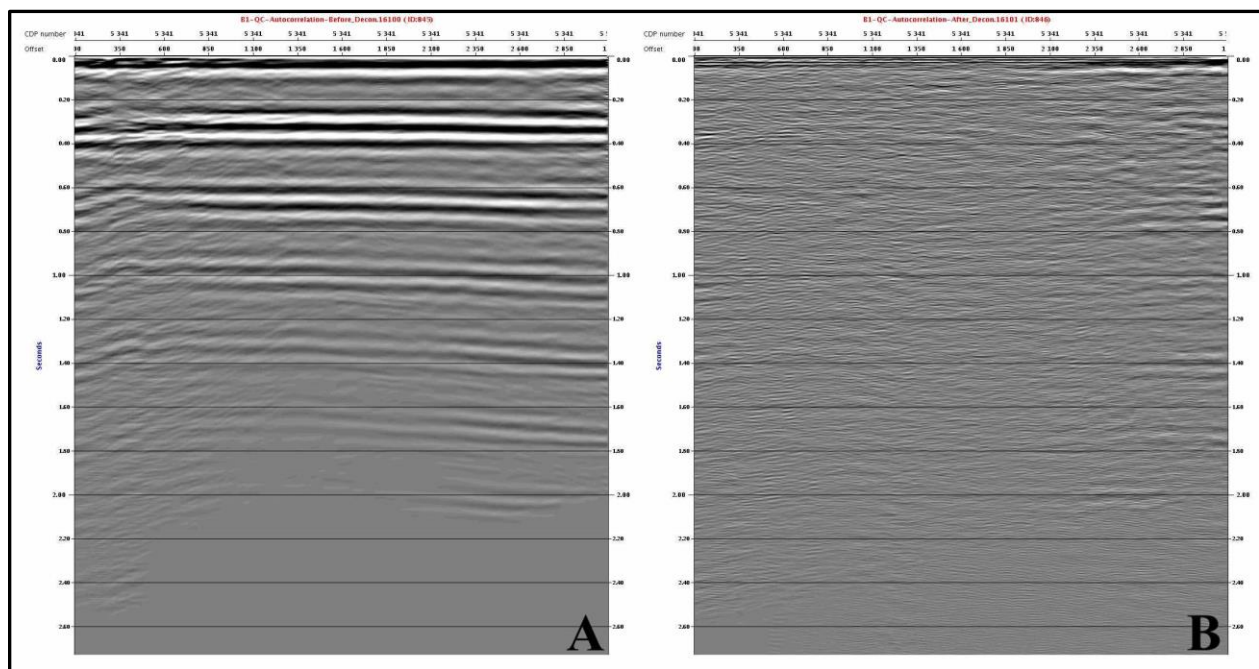


Figure B. 8 The autocorrelation sections from CDP #5501 before (A) and after (B) the deconvolution applied to original CMP gathers. The results have revealed that the multiples were attenuated downwards from 300 ms for every  $\Delta t=300$ ms, however primary reflections have been disappeared.

After this processing step, velocity analysis was done to use  $V_{RMS}$  for NMO and DMO correction. Then, CDP gathers were stacked, and post-stack time migrated. The stacked and migrated

sections have been presented (Figure B. 9 & Figure B. 10, respectively). The multiples were eliminated over the westward dipping layers in the western part of the area, while from the center to the eastern part of the area and shallow parts are in overall have lost the signal quality unfortunately.

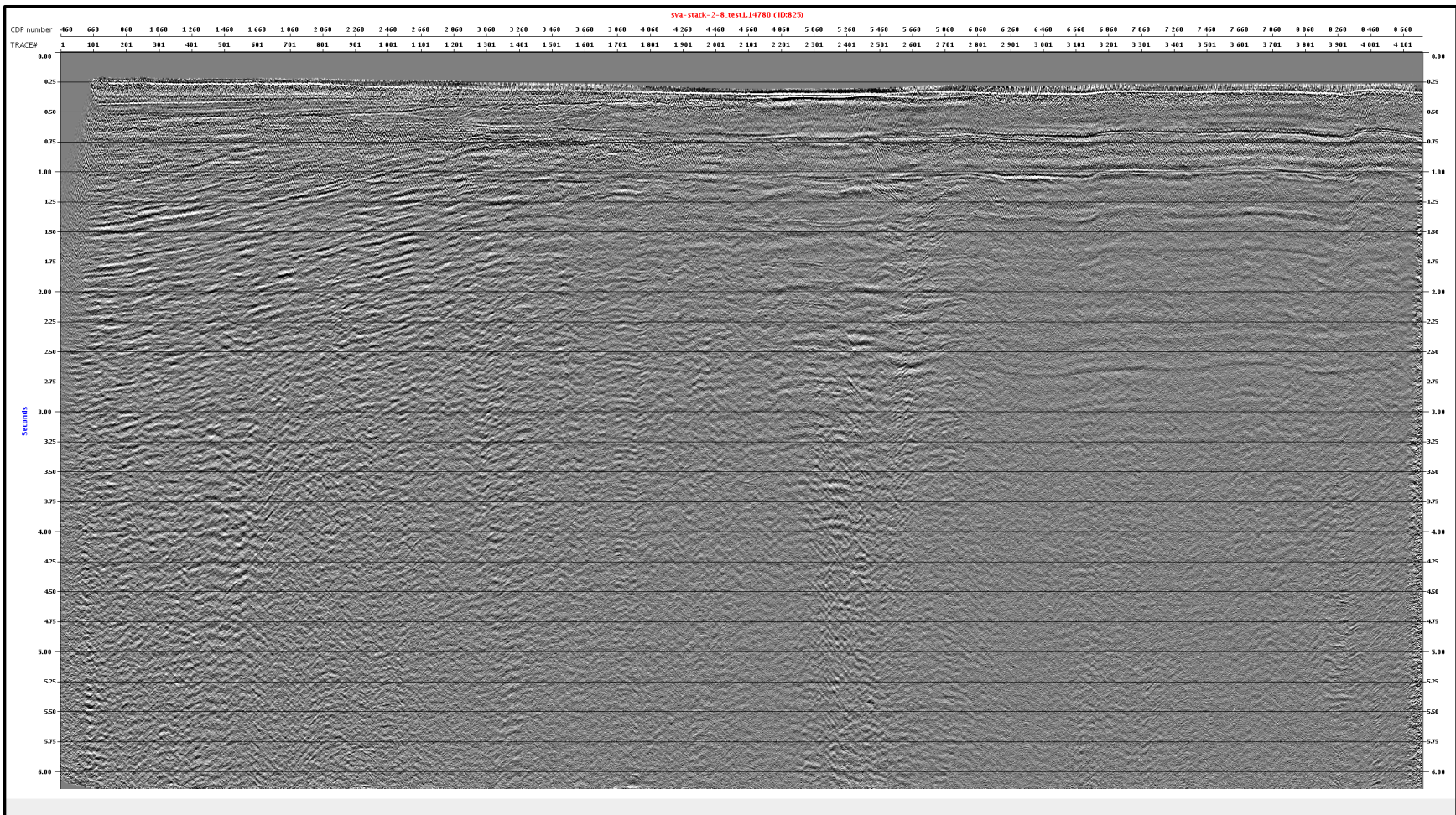


Figure B. 9 shows the stacked section of seismic line 8 from the 1st workflow including the multiple attenuation by the deconvolution applied to the original CMP gathers.



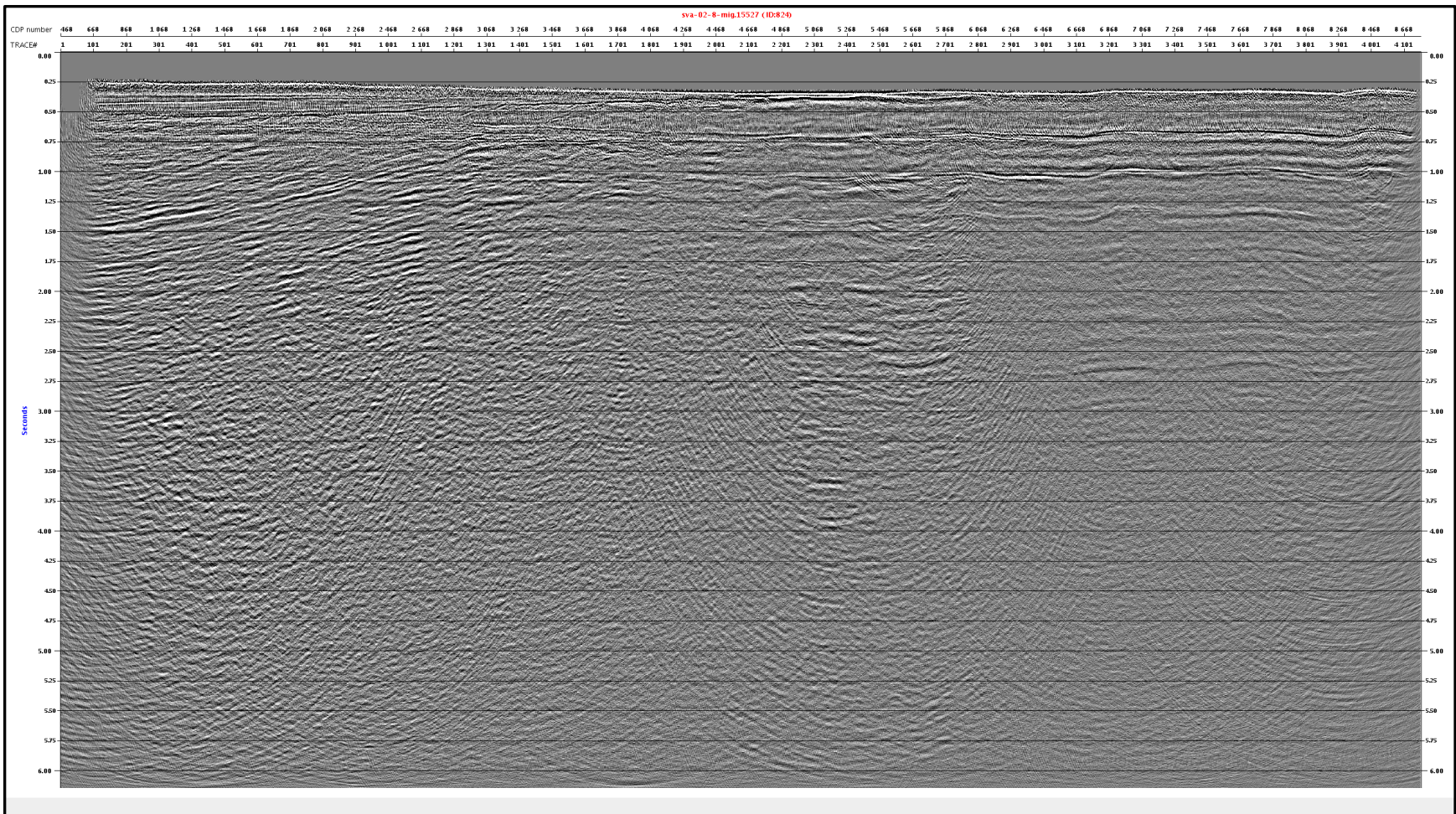


Figure B. 10 shows the post-stack time migrated section of seismic line 8 from the 1st workflow including the multiple attenuation by the deconvolution applied to the original CMP gathers.

### B.3.2 Deconvolution applied to the interpolated CMP gathers

After the pre-processing and trace interpolation steps in the 2nd workflow, the same  $f-k$  filtering and the surface consistent predictive deconvolution sequences in the 1st workflow were repeated but they were applied to the interpolated CMP gathers this time. The autocorrelation section (Figure B. 11) has been investigated for the QC purpose to compare the difference with and without the trace interpolation.

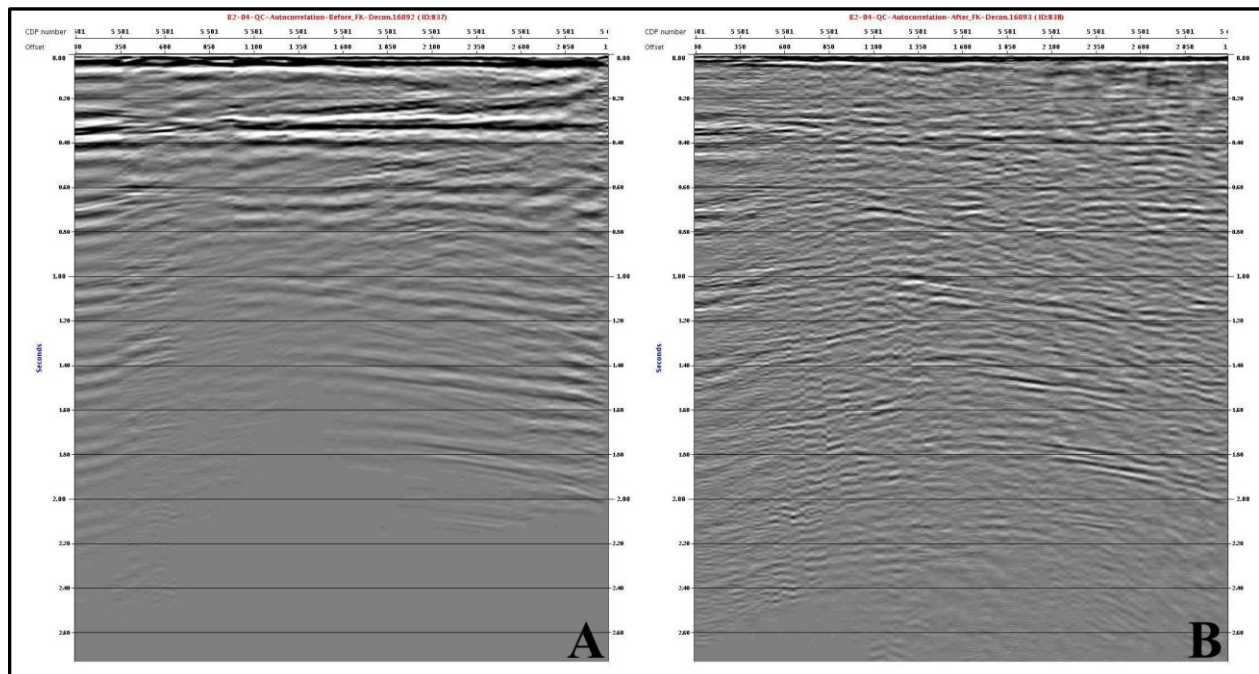


Figure B. 11 The autocorrelation sections from CDP #5501 before (A) and after (B) the deconvolution applied to interpolated CMP gathers. The results have revealed that the multiples could not be attenuated downwards from 300 ms for every  $\Delta t=300ms$ .

After this processing step, velocity analysis was done to use  $V_{RMS}$  for NMO and DMO correction. Then, CDP gathers were stacked, and post-stack time migrated. The stacked and migrated sections (Figure B. 12 & Figure B. 13, respectively) have revealed that the same attenuation method applied to the interpolated CMP gathers have attenuated the seabed multiples over the westward dipping layers in the western part but it was not efficient in the horst and graben structures.



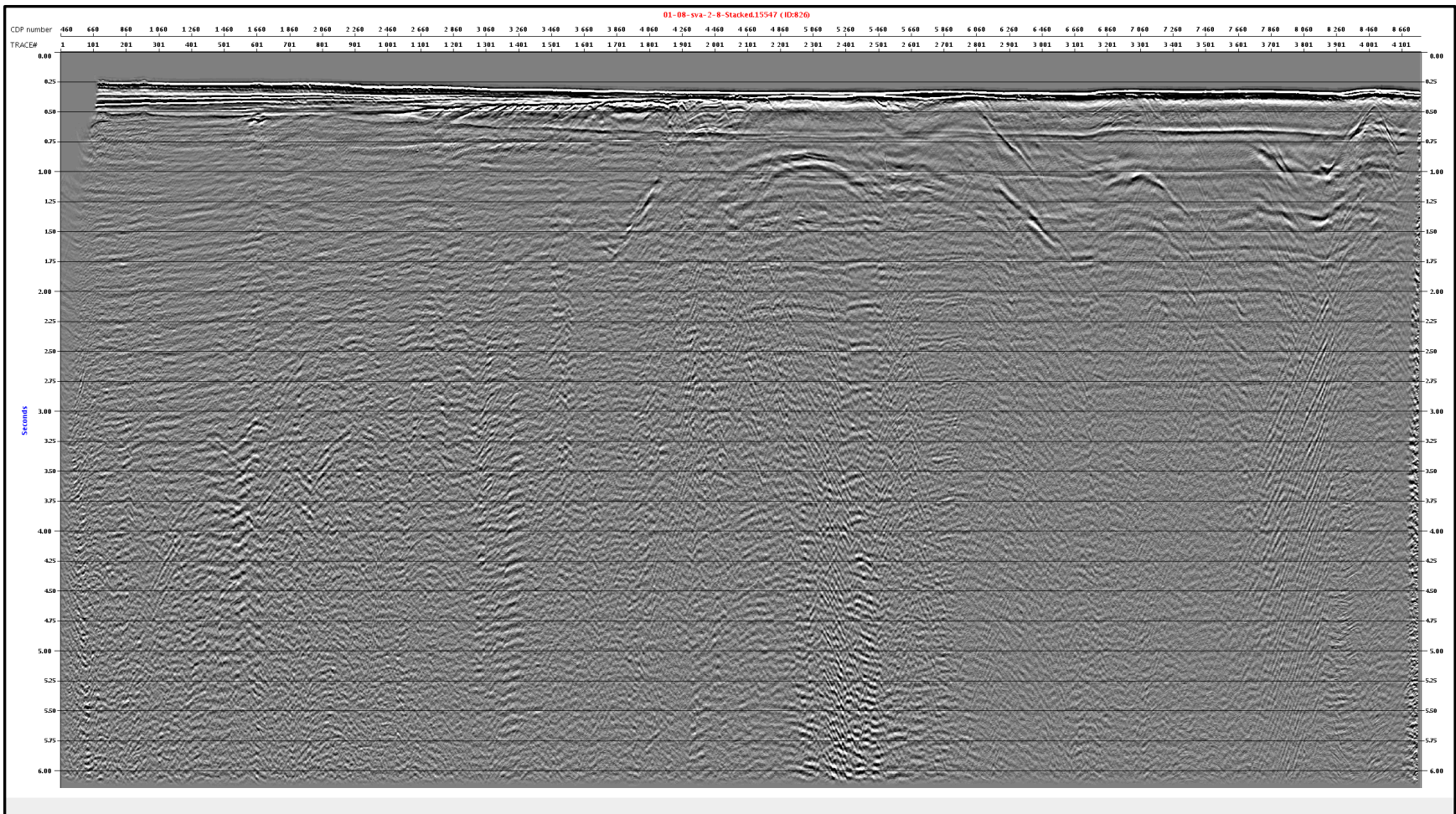


Figure B. 12 shows the stacked section of seismic line 8 from the 2nd workflow including the multiple attenuation by the deconvolution applied to the interpolated CMP gathers.



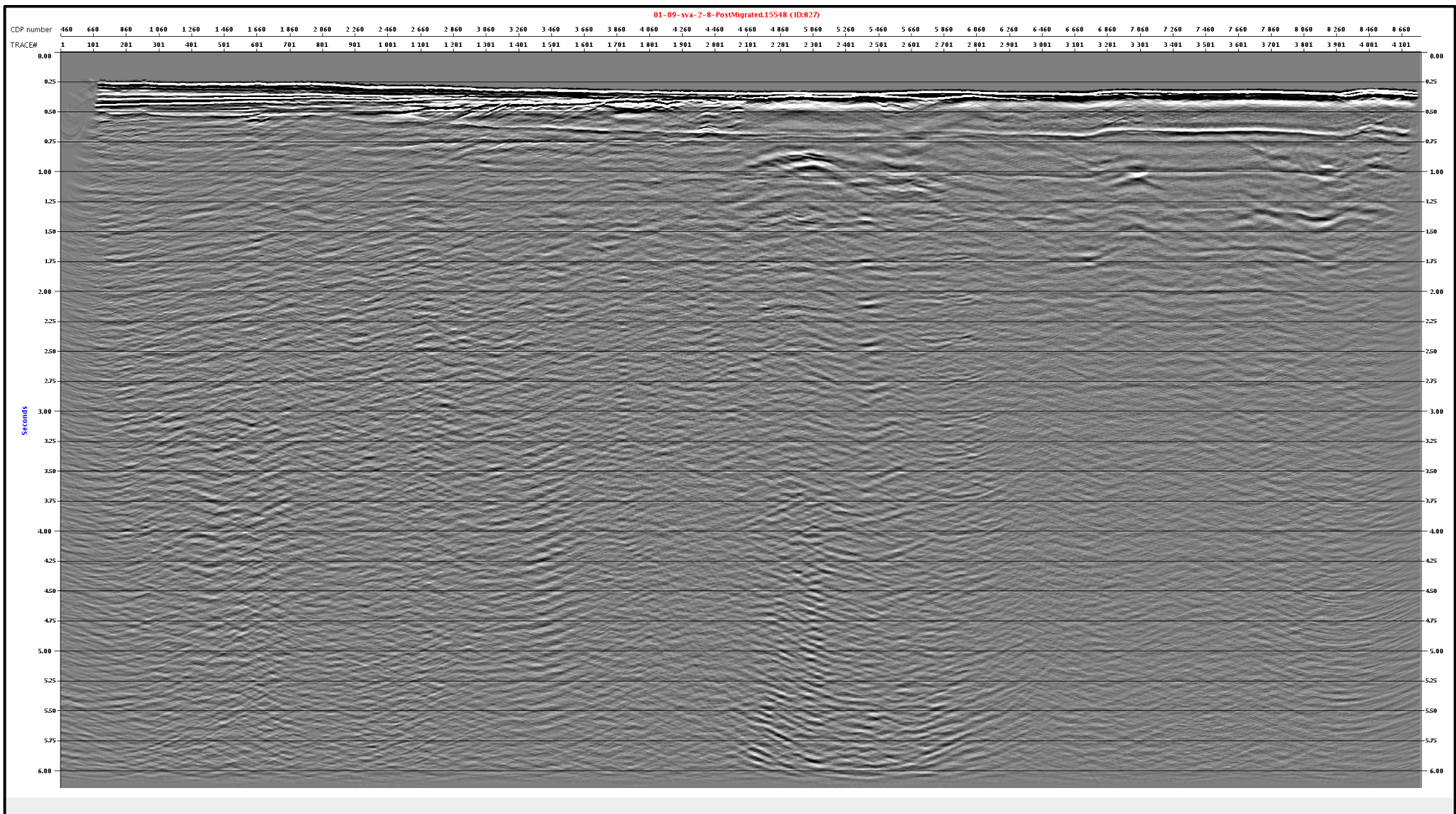


Figure B. 13 shows the post-stack time migrated section of seismic line 8 from the 2nd workflow including the multiple attenuation by the deconvolution applied to the interpolated CMP gathers.

### B.3.3 Deconvolution in the $\tau$ - $p$ domain applied to the interpolated CMP gathers

As difference beginning of this approach, the spherical divergence correction had not been applied during the pre-processing in the 3rd workflow. Then, interpolated CDP gathers were transformed from the  $t$ - $x$  domain to the  $\tau$ - $p$  domain by the module LINTP (forward) in Xjob folder. The edge effects by the  $\tau$ - $p$  transform were removed by an additional  $f$ - $k$  filter by the module FKFIL. Then, the  $\tau$ - $p$  gathers were displayed in the TeamView to pick the apparent velocities ( $1/p$ ) of the refracted waves. They were picked in all displayed gathers in TeamView (varying from 4500 to 6000 m/s in the shallow layers) and a new velocity library has been created (Figure B. 14). During the velocity picking, shot gathers were also observed at the same time to determine the accurate velocity values of refracted waves (Figure 4.7). The velocity library was created by this picked points. Predictive deconvolution was applied by the module TRITA to remove the multiples. The operator length ( $L$ ) was given as 300 ms. Then, the velocity library was used by the module MUTES to mute lower velocities. Finally, multiple attenuated  $\tau$ - $p$  gathers were converted to the CDP gathers by the reverse  $\tau$ - $p$  transform, the module LINTP. The autocorrelation section (Figure B. 15) has been investigated to analyze the efficiency.

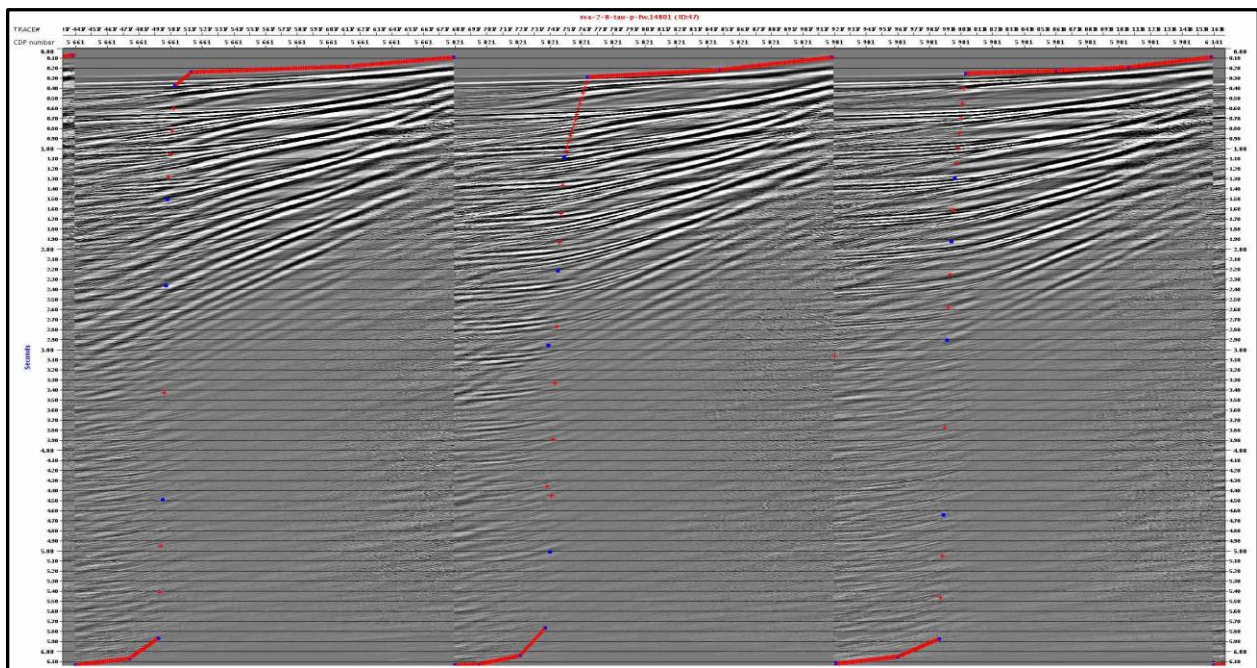


Figure B. 14 The  $\tau$ - $p$  gathers and picked apparent values (blue points) in TeamView. From left to right, apparent velocities are decreasing. The muting zone is formed by the extrapolated values (red plus signs) between the pick values, which is the right side of the red plus signs.

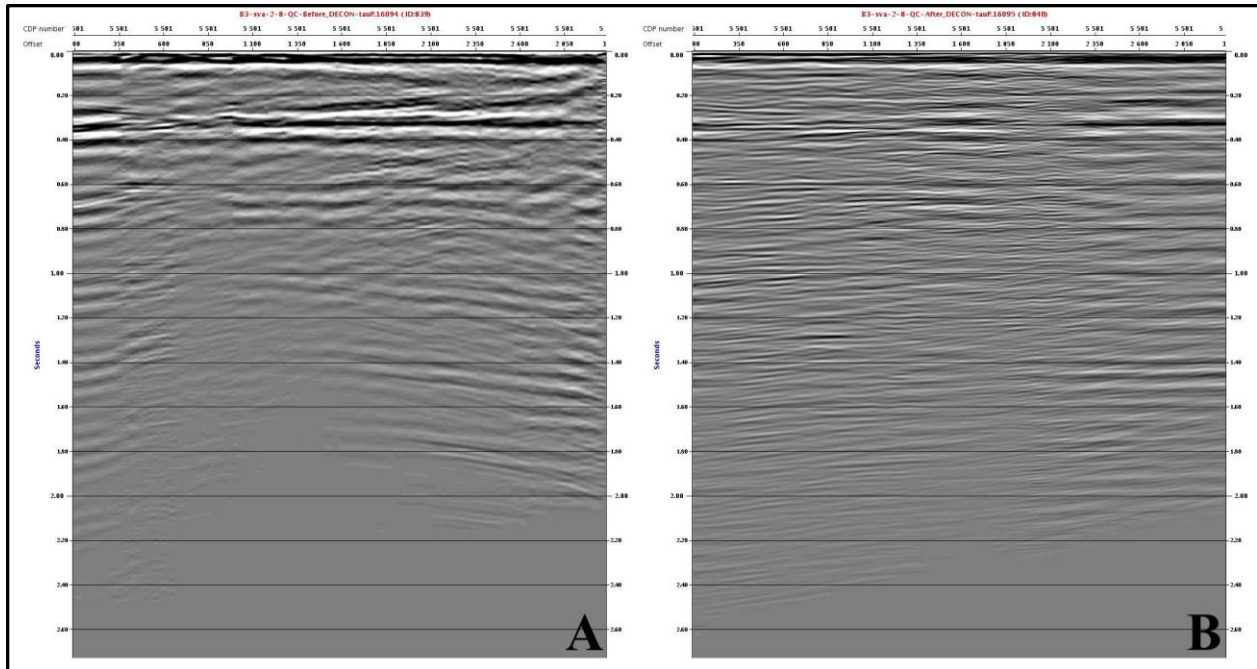


Figure B. 15 The autocorrelation sections from CDP #5501 before (A) and after (B) the deconvolution in the  $\tau$ - $p$  domain. The results have revealed that the multiples could not be attenuated downwards from 300 ms for every  $\Delta t=300$ ms.

After this processing step, velocity analysis was done to use  $V_{RMS}$  for NMO and DMO correction. Then, CDP gathers were stacked, and post-stack time migrated. The stacked and migrated sections have been presented (Figure B. 16 & Figure B. 17, respectively). The results have revealed that 1st order of the surface-related multiples could not be suppressed at all, while the following multiples in the deeper parts of the sections have been attenuated.



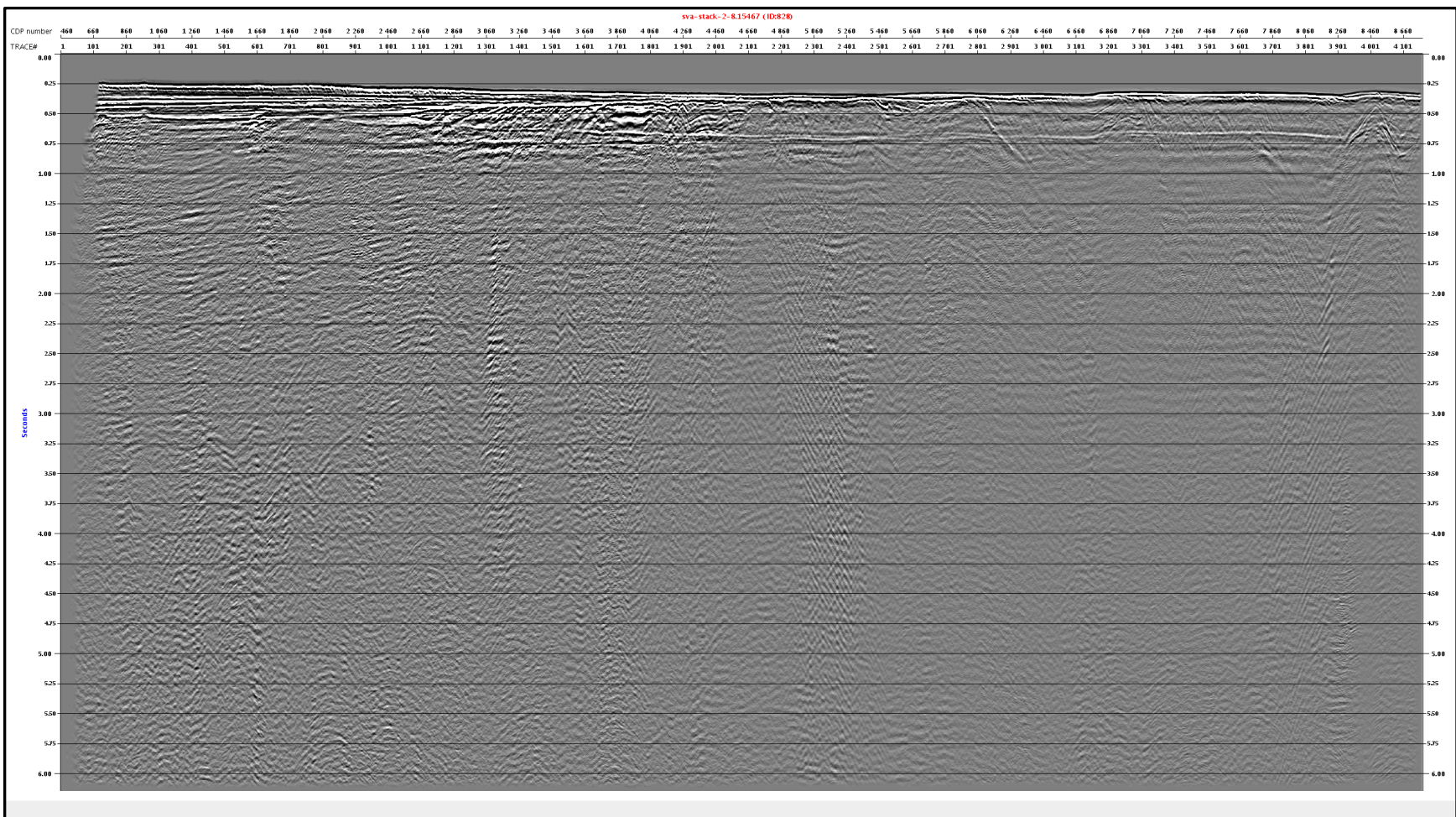


Figure B. 16 shows the stacked section of seismic line 8 from the 3rd workflow including the multiple attenuation by the deconvolution in the  $\tau$ - $p$  domain applied to the interpolated CMP gathers.



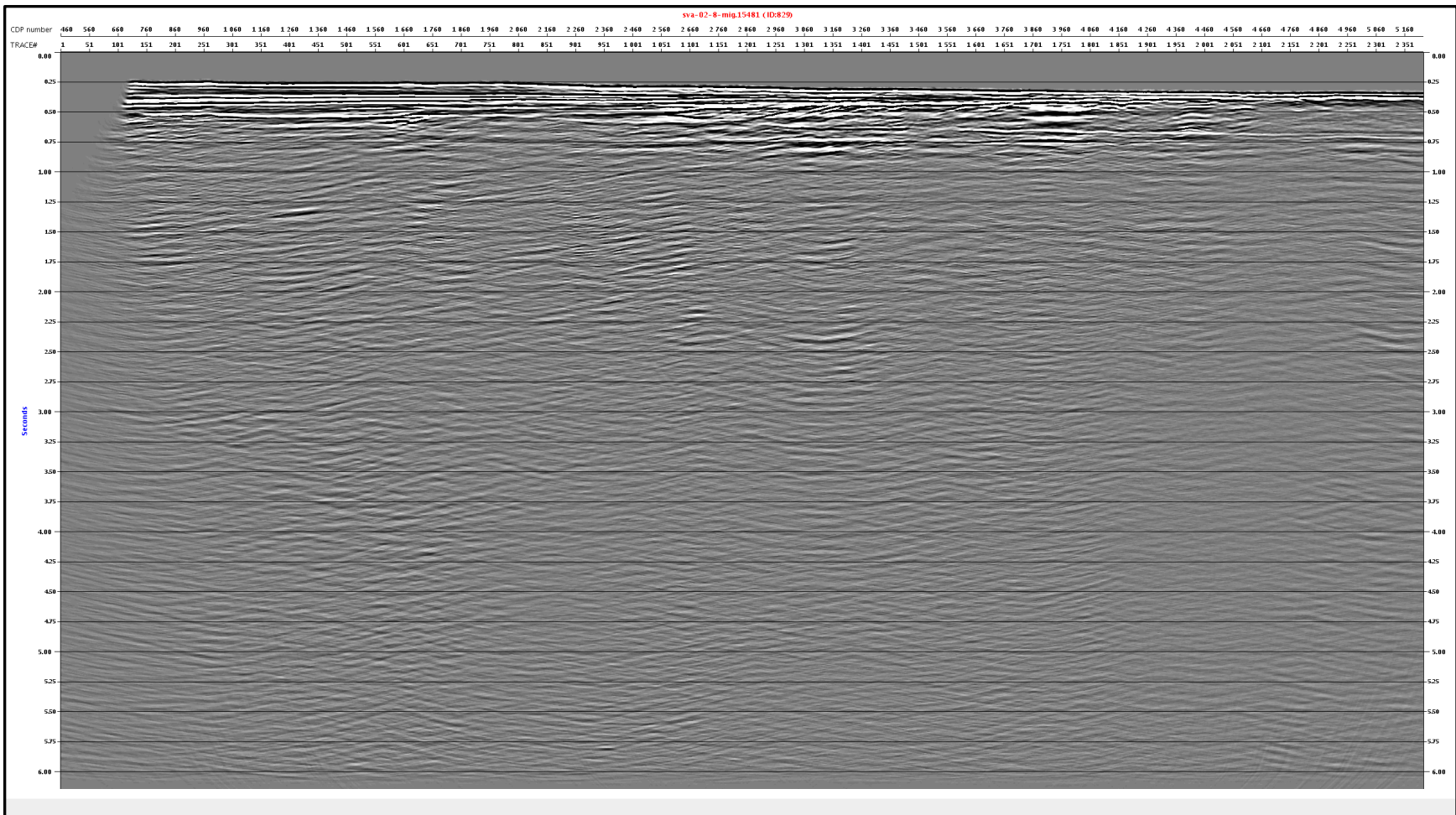


Figure B. 17 shows the post-stack time migrated section of seismic line 8 from the 3rd workflow including the multiple attenuation by the deconvolution in the  $\tau$ -p domain applied to the interpolated CMP gathers.

### B.3.4 $f$ - $k$ filter applied to the NMO corrected CMP gathers (interpolated)

After the pre-processing and trace interpolation steps in the 4th workflow, NMO correction was applied by the module FANMO with the velocity library from the 1st velocity analysis. The velocity percentage in the module was set extremely low in order to bend upwards the hyperbolas of primary reflections, while the hyperbolas of the multiple reflections were flattened in the CMP gathers. Then,  $f$ - $k$  filtering applied to the over-corrected CMP gathers by the module FKFIL. Then, the band-pass filter for velocity limits were set as -150000 and 1750 m/s in the  $f$ - $k$  spectrum to attenuate the velocity of multiples, while passing the velocity of the primary reflections. Then, the multiple-free CMP gathers were inverse NMO corrected by the module FANMO to bend downward the hyperbola of the primary reflections. In order to observe the result, the autocorrelation section has been displayed in Figure B. 18.

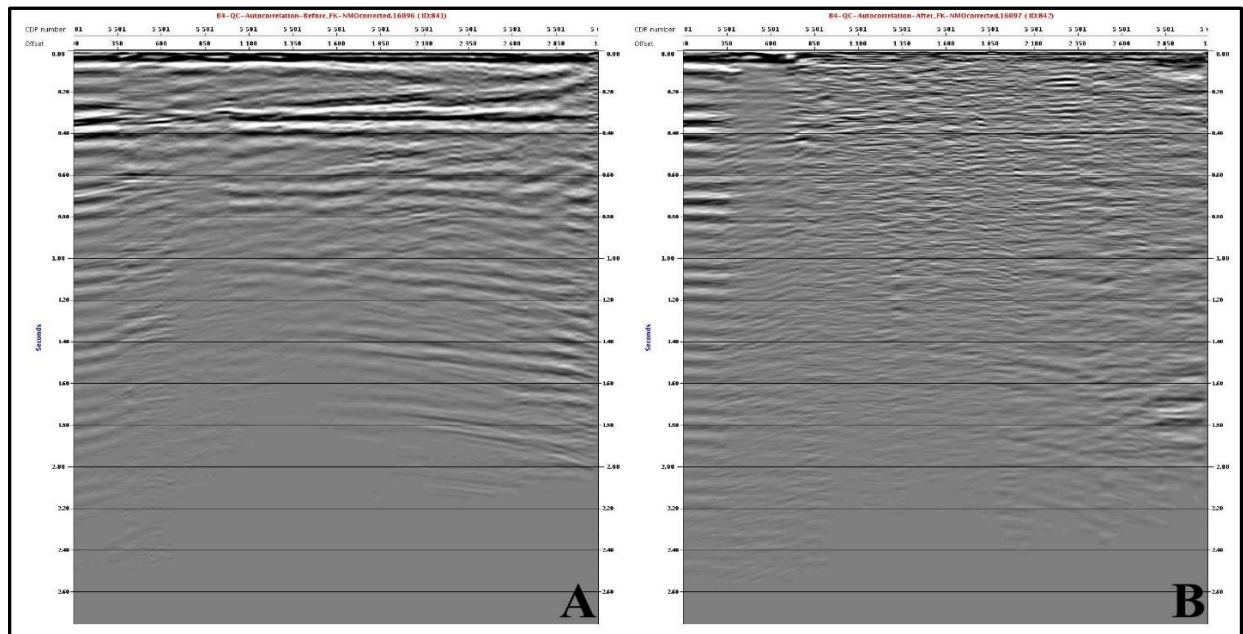


Figure B. 18 The autocorrelation sections from CDP #5501 before (A) and after (B) the  $f$ - $k$  filter applied to NMO over-corrected CMP gathers (interpolated). The results have revealed that the multiples were barely suppressed downwards from 300 ms for every  $\Delta t=300$ ms. However, the primary reflections have been lost as well.

After this processing step, velocity analysis was done to use  $V_{RMS}$  for NMO and DMO correction. Then, CDP gathers were stacked, and post-stack time migrated. The stacked and migrated sections have been presented (Figure B. 19 & Figure B. 20, respectively).



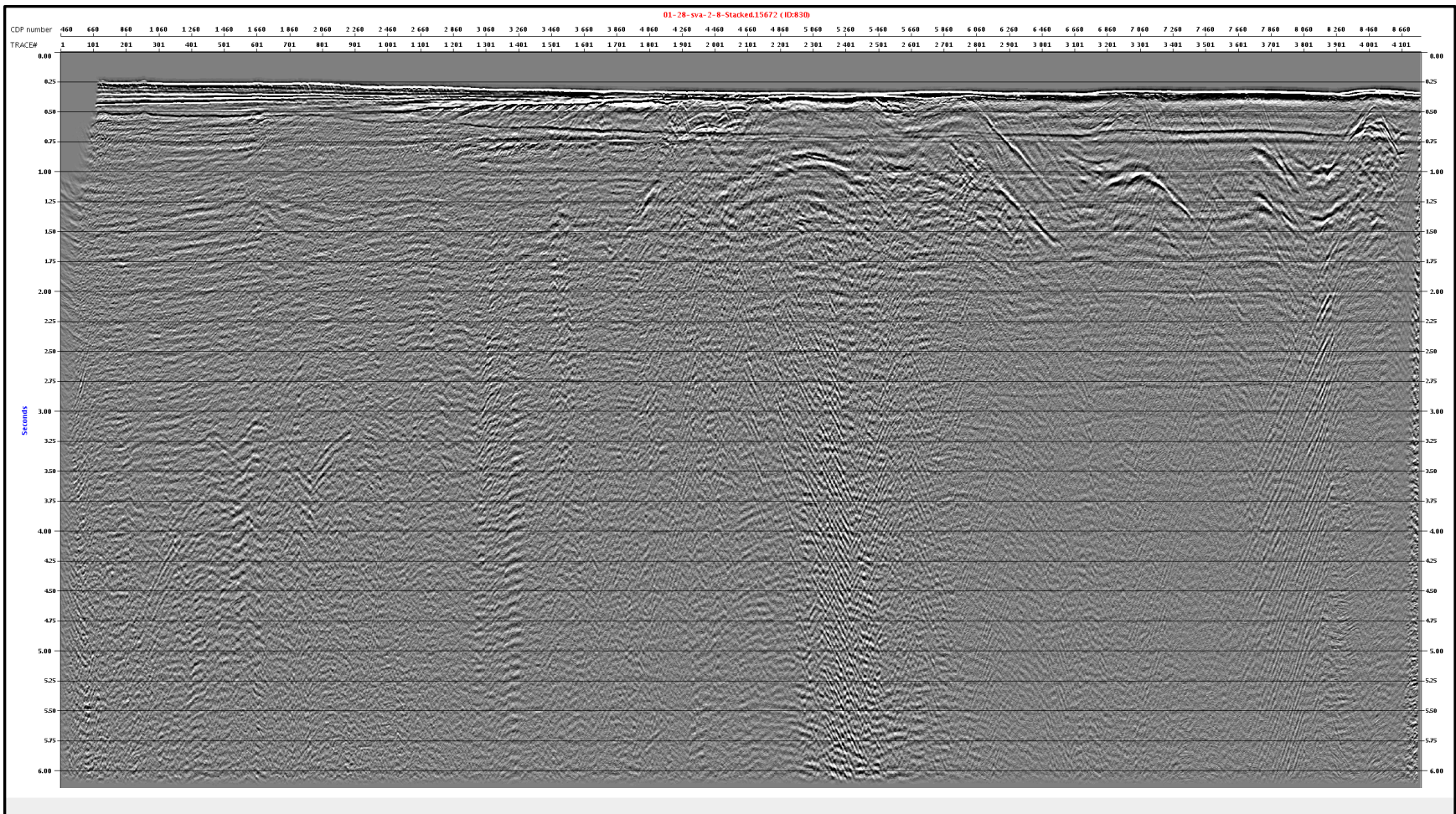


Figure B. 19 shows stacked section of seismic line 8 from the 4th workflow including the multiple attenuation by the f-k filter applied to NMO over-corrected CMP gathers (interpolated).



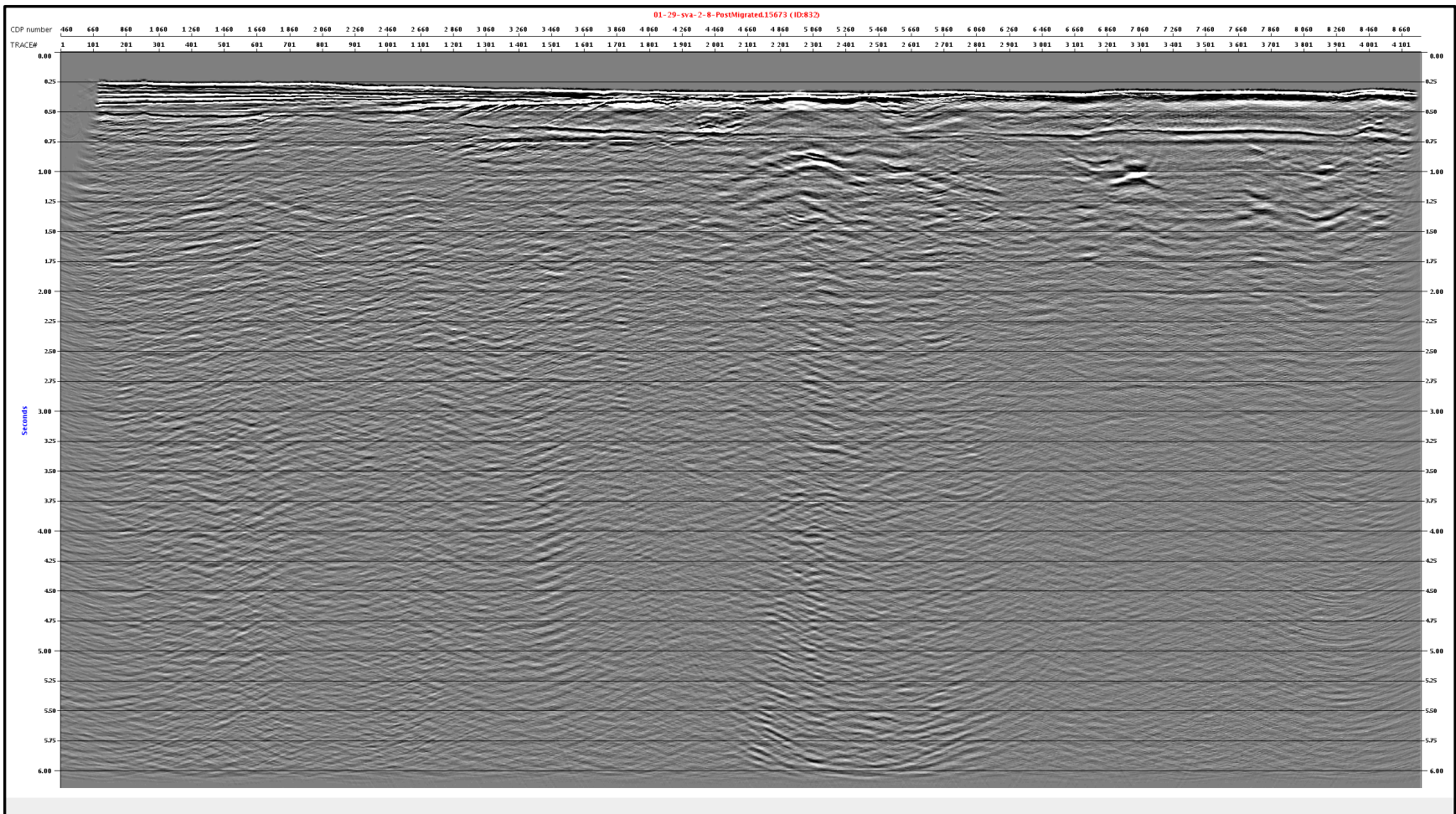


Figure B. 20 shows post-stack time migrated section of seismic line 8 from the 4th workflow including the multiple attenuation by the f-k filter applied to NMO over-corrected CMP gathers (interpolated).

### B.3.5 Multiple Extraction & Adaptive Subtraction

This additional QC result from the main multiple attenuation method from the line 8 has been presented additionally in (Figure B. 21) in order to compare the other multiple elimination QC results from seismic line 8.

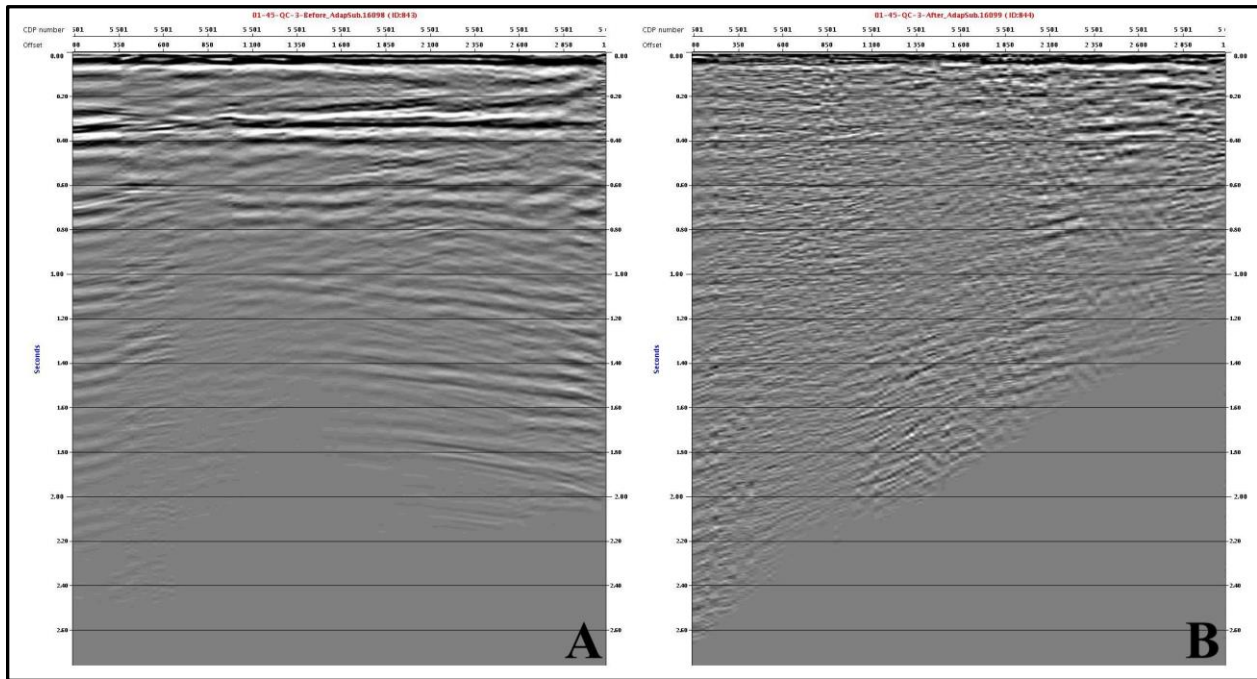


Figure B. 21 The autocorrelation sections from CDP #5501 before (A) and after (B) the multiple extraction & adaptive subtraction method. The results after the subtraction have revealed that the multiples were attenuated overall downwards from 300 ms for every  $\Delta t=300\text{ms}$ .





## APPENDIX C

The alternative seismic interpretation results can be seen in this chapter.

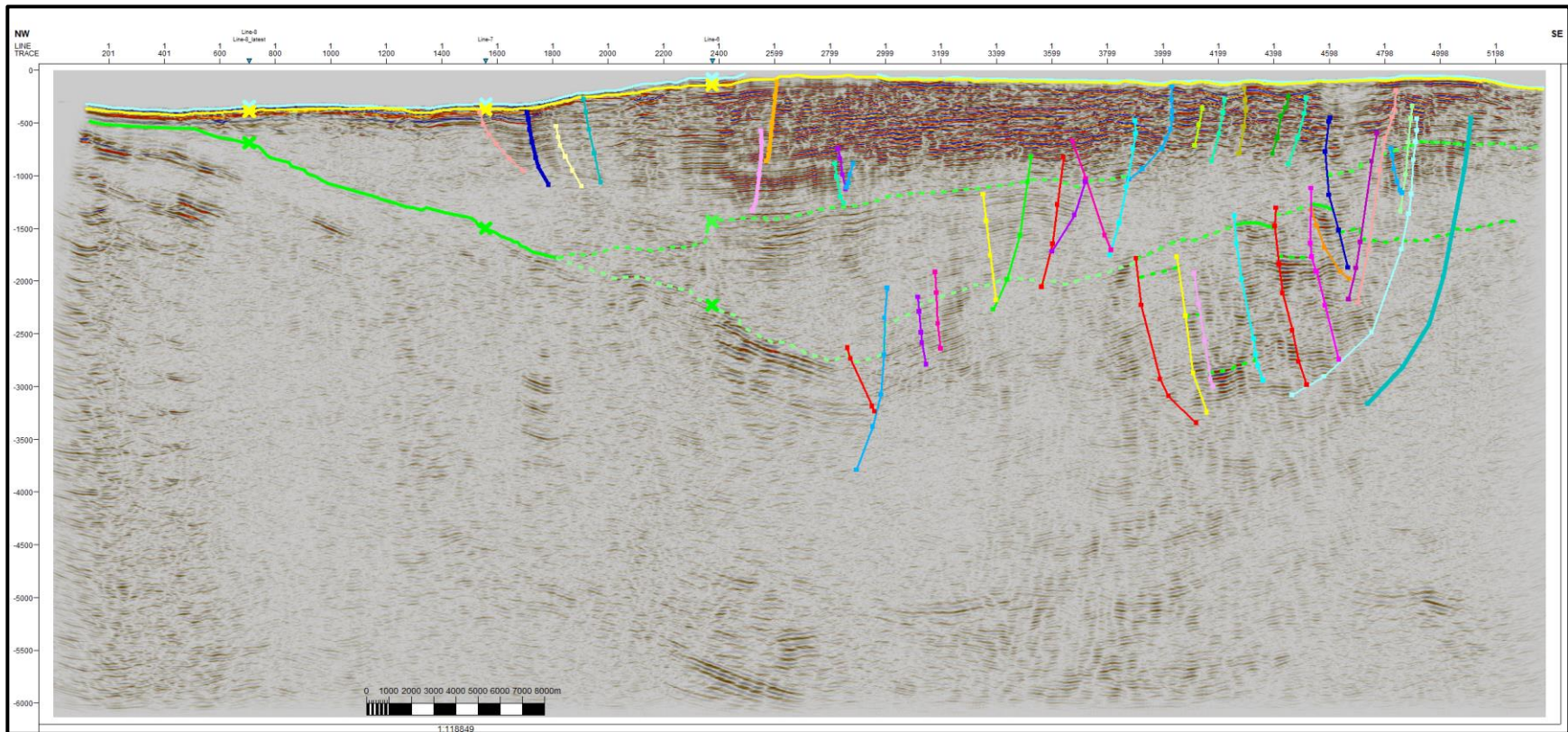


Figure C. 1 Alternative top Hecla Hoek horizon interpretation (green dashed lines) in seismic line 2 due to the uncertainties of the reflection character and discontinuity. Seabed (turquoise blue), URU (yellow), and Certain reflections indicating the Hekla Hoek (green straight line). All major-minor eastward and westward dipping faults alternatively interpreted to correlate the top Hecla Hoek possibilities (represented by multiple colors). The symbol X indicates the horizons at their intersecting points with seismic lines 6,7 and 8.



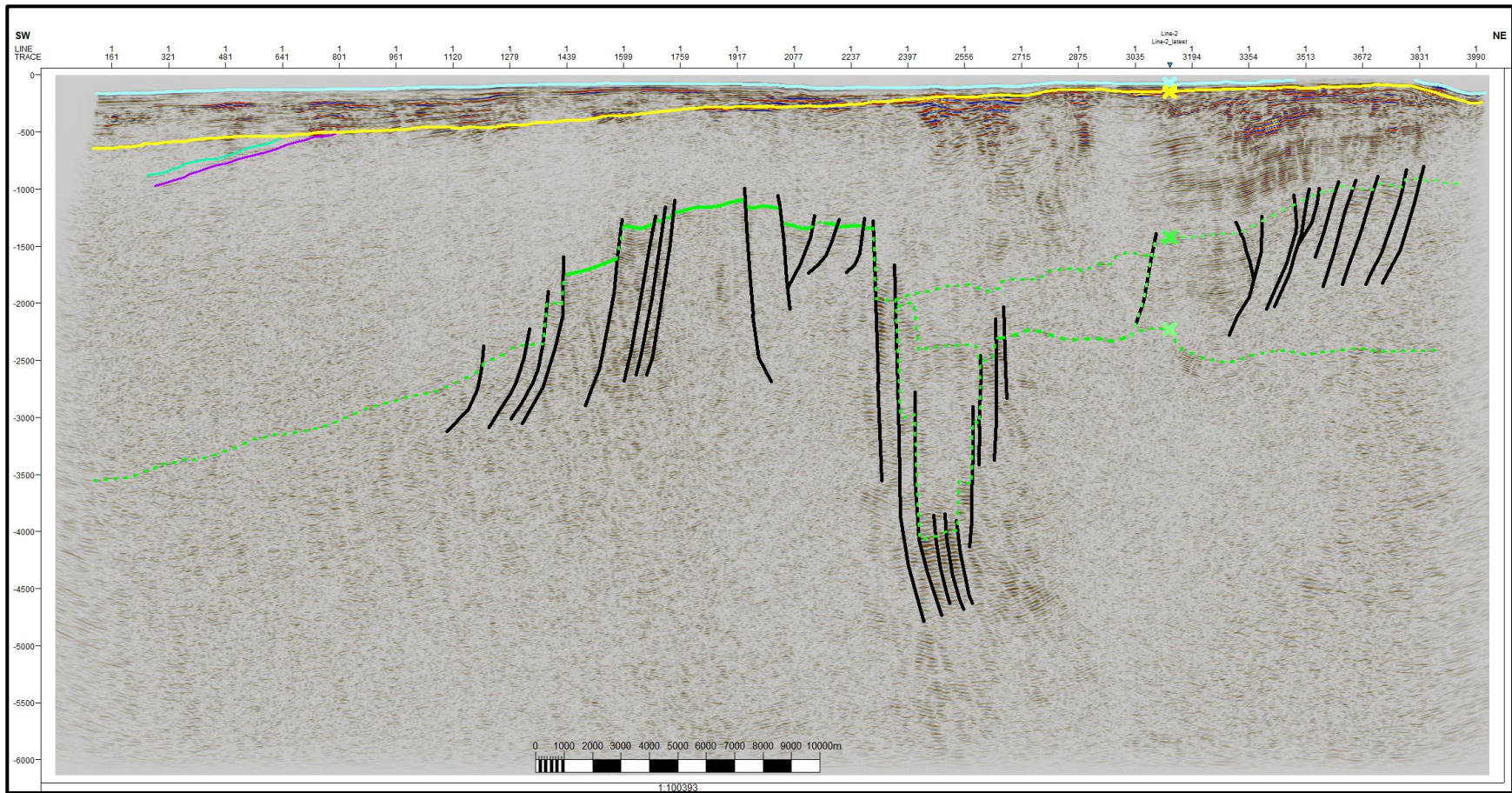


Figure C. 2 Alternative top Hecla Hoek horizon interpretation (green dashed lines) in seismic line 6 due to the uncertainties of the reflection character and discontinuity. Seabed (turquoise blue), URU (yellow), the HFZ dipping layers 4-5 (turquoise green and purplish red lines, respectively), and Certain reflections indicating the Hekla Hoek (green straight line). The black lines present the faults. The symbol X indicates the horizons at their intersecting points with seismic line 2.